

University of Strathclyde

Doctoral Training Centre in Medical Devices

Department of Biomedical Engineering

**Development of a multi-axial load
distribution measurement device**

By

Hin Chung Lau

A thesis presented in fulfilment of the requirements for the degree of

Doctor of Engineering.

2013

Declaration of Rights

This thesis is the result of the author's original research. It has been composed by the author and has not been previously submitted for examination which has led to the award of a degree.

The copyright of this thesis belongs to the author under the terms of the United Kingdom Copyright Acts as qualified by University of Strathclyde Regulation 3.50. Due acknowledgement must always be made of the use of any material contained in, or derived from, this thesis.

Signed:

Date:

Acknowledgement

To the Doctoral Training Centre in Medical Devices (University of Strathclyde) for supporting my education and research, to EPSRC for funding this research.

To Ben Stansfield and Stephan Solomonidis for bringing me into this research, it was everything I could have dreamed of wanting for my education and more. To Scott Wearing for his endless encouragement and guidance throughout the years. I am honoured to have done my doctorate research with you all.

To John MacLean for his advice and his time in helping me to solder hundreds of wires, not to mention his company in the laboratory throughout the years. To David Robb, Stephen Murray, Duncan Lindsay and Bob Baird for their help in producing bits and pieces that made this research possible.

To Matthew Pepper and Eric Geng at University of Kent, for sharing their knowledge and experience, and provided me the opportunity to evaluate their piezoelectric triaxial force transducers.

To Sue Hopper at Queensland Academy of Sports, and Lance Wilson at Queensland University of Technology, for providing support and equipment for material testing.

To Bill Taylor at Silicone Engineering Ltd, Marina Fernando and Paul Gladwin at the Tun Abdul Razak Research Centre (TARRC), for generously provided advice and samples of their silicone/rubber products.

To Nicole for the cup cakes! To my cute little baby niece, for the joy and laughter you bring during the preparation of this thesis.

To my parents and family for their eternal support and encouragement.

And, to Frances, I dedicate this thesis to you.

Publications from this thesis

Hin Chung Lau, Benedict Stansfield, Stephan Solomonidis, Scott Wearing, Matthew Pepper, “Time dependent characteristics of the "Kent" triaxial force transducer system for in-shoe load distribution measurement”, 11th EMED Scientific Meeting (ESM2008), July 2008, Dundee.

Hin Chung Lau, Benedict Stansfield, Scott Wearing, Stephan Solomonidis, William Spence, “A low-cost tri-axial load sensor system: design, characteristics and its potentials”, XXII Congress of the International Society of Biomechanics (ISB2009), July 2009, Cape Town.

Hin Chung Lau, “Development of a 3D load distribution measurement device”, Research Presentation Day (RPD2010), Faculty of Engineering, University of Strathclyde, January 2010, Glasgow.

Hin Chung Lau, Benedict Stansfield, Scott Wearing, Stephan Solomonidis, William Spence, “Low-cost shear stress distribution measurement: is it possible?”, 6th World Congress on Biomechanics (WCB2010), August 2010, Singapore.

Hin Chung Lau, Scott Wearing, Benedict Stansfield, Stephan Solomonidis, William Spence, “Low-cost bi-axial shear stress transducer: a step closer to shear distribution measurement”, 2nd congress of the International Foot and Ankle Biomechanics Community (i-FAB 2010), September 2010, Seattle, USA.

Hin Chung Lau, *Benedict Stansfield*, Scott Wearing, Stephan Solomonidis, William Spence, “An economical way to measure plantar shear distribution.”, Clinical Applications of Foot Pressure Measurement User Group Meeting (IPEM), February 2011, Sheffield.

Abbreviations

%FSO	% Full-scale output
%RC	% Rated Capacity
ADD	Active area depth
AG	Air gap
AP	Anterior-posterior
DAQ	Data acquisition system
DMA	Dynamic mechanical analysis
FBG	Fibre Bragg Gratings
FFT	Fast Fourier Transform
FSR	Force-sensing resistors
GRF	Ground reaction force
IC(s)	Integrated circuit(s)
IPA	Isopropyl Alcohol
LED(s)	Light-emitting diode(s)
MEMS	Micro-electromechanical transducer system
ML	Medial-lateral
Op-Amp	Operational amplifier
PCB	Printed circuit board
PVC	Polyvinylchloride
RC circuit	Resistor-capacitor circuit
RMSE	Root mean squared error
TC	Time constant
TEAG	Total effective air gap

Abstract

Diabetic foot ulceration is a global health problem that often leads to amputation. While peripheral vascular disease and neuropathy are common risk factors for foot ulcers, excessive mechanical stress would directly cause the breakdown of plantar tissue. Once the skin is broken, many factors may contribute to defective healing and putting one at greater risk for ulceration. Clinical measurement of plantar pressure distribution, therefore, is commonly used to identify feet at risk of ulceration. However, plantar pressures are poor predictors and there is evidence that shear load is at least equally important in ulcer development. Compared to the numerous commercial systems available for plantar pressure distribution measurement, only a few experimental devices exist for shear distribution measurement. These are typically either too large for high spatial resolution measurement or expensive to manufacture, limiting their suitability for routine clinical use.

The aim of this study was to develop a low-cost multi-axial load transducer array to measure the distribution of stress beneath the human foot during walking. A pre-existing piezoelectric-based load transducer and several novel transducer designs using hydraulic, optoelectronic and magnetic-based technologies were manufactured and their performance relative to 29 criteria evaluated. The magnetic-based design was found to possess the highest performance (accuracy <3%RC, hysteresis <4%RC, non-linearity <2%RC) and physical characteristics (sensing area 10×10mm). Subsequently, an array consisting of 20 discrete magnetic-based transducers was constructed. In a single subject trial, the total shear load measured by the array was <2N of that measured by a Kistler® force platform. Although the array was capable of measuring biaxial shear load distribution, further work is required to expand the current design to measure load distribution beneath the entire plantar surface. Once realised, such a system has the potential to provide valuable biomechanical data that may help clinicians identify diabetic feet at risk of ulceration.

Contents

Declaration of Rights	i
Acknowledgement	ii
Publications from this thesis	iii
Abbreviations.....	iv
Abstract.....	v
Contents	vi
Chapter 1 Thesis overview	1
1.1 Thesis statement	1
1.2 Motivation	2
1.3 Thesis organisation.....	3
1.4 Summary of contributions.....	4
Chapter 2 Background.....	5
2.1 Clinical need – diabetic foot	6
2.1.1 A global problem	6
2.1.2 The pathway to foot ulceration	7
2.1.3 Care of the diabetic foot.....	10
2.2 Methods of load measurement during gait.....	11
2.2.1 Uniaxial and multi-axial load measurement	11
2.2.2 Differences between force and pressure measurement	12
2.2.3 In-shoe and floor platform data collection methods	13
2.2.4 Device configuration - discrete or multiple transducer array	17
2.3 Diabetic foot biomechanics and foot ulcers	19
2.3.1 Frequency content of plantar load profile	19
2.3.2 Ground reaction forces and forces inside the shoe	20
2.3.3 Shear load under our feet	23
2.4 Project aim and objectives	28
2.4.1 System design requirements.....	29
Chapter 3 Existing methods for load sensing	36
3.1 What is a load measurement device	37
3.2 Electrical resistive based transducers.....	38
3.2.1 Principle of operation.....	38

3.2.2	Signal conditioning	41
3.2.3	Transducer construction	42
3.2.4	Current state-of-the-art.....	42
3.2.4.1	AMTI strain gauged systems	45
3.2.4.2	Davis' strain gauged system.....	45
3.2.4.3	Goodyear's strain gauged systems	48
3.2.4.4	Chen's strain gauged system.....	49
3.2.4.5	Molton Corp.'s strain gauged device	50
3.2.4.6	FSR-based systems.....	50
3.2.4.7	Noda's piezoresistive-based system.....	52
3.2.5	Critical review	53
3.3	Piezoelectric based transducers	54
3.3.1	Principle of operation.....	55
3.3.2	Signal conditioning	58
3.3.3	Transducer construction	62
3.3.4	Current state-of-the-art.....	63
3.3.5	Critical review.....	66
3.4	Capacitive based transducers	68
3.4.1	Principle of operation.....	68
3.4.2	Signal conditioning	69
3.4.3	Transducer construction	70
3.4.4	Current state of the art.....	70
3.4.5	Critical review	73
3.5	Optoelectronic based transducers.....	74
3.5.1	Principle of operation.....	74
3.5.2	Signal conditioning	77
3.5.3	Transducer construction	79
3.5.4	Current state-of-the-art.....	81
3.5.5	Critical review	86
3.6	Magnetic based transducers	87
3.6.1	Principle of operation.....	87
3.6.2	Signal conditioning	89
3.6.3	Transducer construction.....	90
3.6.4	Current state of the art.....	92

3.6.5	Critical review	94
3.7	Pneumatic and hydraulic based transducers	95
3.7.1	Principle of operation	95
3.7.2	Signal conditioning	96
3.7.3	Transducer construction	96
3.7.4	Current state of the art	97
3.7.5	Critical review	98
3.8	Alternative methods for triaxial load sensing	100
3.8.1	Using several measurement systems	100
3.8.2	Computer modelling	101
3.8.3	Critical review	101
3.9	Discussion	102
3.10	Conclusion	108
Chapter 4	Calibration Methods	110
4.1	Primary and secondary force calibration standards	111
4.2	Static, dynamic and multi-axis calibration	111
4.3	Differences in pressure and force calibration	113
4.4	Existing calibration methods	113
4.5	Calibration apparatus for this study	116
Chapter 5	Development of triaxial load transducers	120
5.1	Evaluation of a piezoelectric based triaxial load transducer	121
5.1.1	The ‘Kent’ triaxial force transducer system	121
5.1.2	Data acquisition	122
5.1.2.1	Transducer calibration	123
5.1.2.2	Calibration results	126
5.1.3	Discussion	129
5.2	Development of a hydraulic based triaxial load transducer	133
5.2.1	Design concept	133
5.2.2	Proof of concept prototype	134
5.2.2.1	Hydraulic pressure sensors	134
5.2.2.2	Hydraulic environment	135
5.2.2.3	Transducer structure	136
5.2.2.4	Circuit design	138
5.2.2.5	Prototype calibration	138

5.2.2.6	Prototype calibration results.....	140
5.2.3	Discussion	143
5.3	Development of an optoelectronic based triaxial load transducer	146
5.3.1	Design concepts	146
5.3.2	Proof of concept prototype.....	148
5.3.2.1	Photo sensors.....	149
5.3.2.2	Light emitters	150
5.3.2.3	Elastomeric material.....	151
5.3.2.4	Transducer structure.....	156
5.3.2.5	Circuit design	161
5.3.2.6	Prototype calibration	162
5.3.2.7	Prototype calibration results.....	163
5.3.3	Discussion	165
5.4	Development of a magnetic based triaxial load transducer.....	170
5.4.1	Design concept.....	170
5.4.2	Proof of concept prototypes	172
5.4.2.1	Hall-effect sensor ICs.....	173
5.4.2.2	Permanent magnets	174
5.4.2.3	Transducer structure.....	184
5.4.2.4	Circuit design	186
5.4.2.5	Prototype calibration	186
5.4.2.6	Prototype calibration results.....	187
5.4.3	Discussion	190
5.5	Conclusion.....	193
Chapter 6 Further improvement of two different biaxial shear transducers. 196		
6.1	Transducer designs	197
6.1.1	Optoelectronic based biaxial shear transducer.....	197
6.1.2	Magnetic based biaxial shear transducer	199
6.2	Calibration method.....	200
6.2.1	Experimental setup.....	201
6.2.2	Loading protocols	203
6.2.3	Data Reduction.....	204
6.3	Results & Discussion	205
6.3.1	Transducer performance	205

6.3.2	Hardware	217
6.3.3	Physical requirements	219
6.3.4	Manufacturing requirements	222
6.4	Conclusion.....	223
Chapter 7 Development of a biaxial shear distribution measurement system		225
7.1	System design and construction	226
7.1.1	Transducer design	226
7.1.2	Batch production of discrete transducers	228
7.1.3	Hardware and Electrical implementation.....	231
7.1.4	Software implementation	232
7.2	System calibration.....	233
7.2.1	Results and discussion	235
7.2.1.1	Transducer performance.....	238
7.2.1.2	Hardware	248
7.2.1.3	Physical requirements	250
7.2.1.4	Manufacturing requirements	252
7.3	Preliminary subject trial	252
7.3.1	Method	252
7.3.2	Results and discussion	254
7.4	Conclusion.....	256
Chapter 8 Conclusions and future work.....		258
8.1	Overall project discussion	259
8.2	Recommendations for future Work.....	265
8.2.1	Further evaluation of the magnetic-based transducer	265
8.2.2	Batch production of the transducers.....	265
8.2.3	Clinical trials	266
8.2.4	Elastomeric material testing.....	267
8.2.5	Construction of triaxial load transducer	268
8.2.6	Potential of an hydraulic-based triaxial load transducer	269
8.2.7	Potential of the optoelectronic-based biaxial transducer	270
8.2.8	Methods for the calibration of a large transducer array.....	271
8.3	Using the devices in other applications.....	272
References		275
Appendix A- Terminology		298

Appendix B- Technical drawings of equipment components	301
Appendix C- Piezoelectric-based triaxial load transducer evaluation results	326
Appendix D- Rubber manufacture	333
Appendix E- Optoelectronic-based triaxial load transducer calibration results.....	334
Appendix F- Evaluation of permanent magnets.....	337
Appendix G- Magnetic-based triaxial load transducer calibration results.....	342
Appendix H- Screenshots of the shear distribution measurement system software	344

Chapter 1

Thesis overview

1.1 Thesis statement

The goal of this thesis was to design, manufacture, evaluate and identify the most suitable transducer design for low-cost multi-axial load distribution measurement under the plantar surface of the foot. The device was designed to collect data in a walking environment and was built from an array of discrete multi-axial load transducers mounted as a floor platform. Each transducer in the array was calibrated and the calibrated data were analysed for information about the performance of the system. Results of the preliminary gait analysis using the system were compared to those from a conventional Kistler® force plate. A miniaturised version of the discrete shear transducer was also built demonstrating the potential of the transducer for in-shoe measurement.

1.2 Motivation

The burden of diabetic foot disease cost health care systems around the world billions of dollars each year. Foot ulceration is a common complication of diabetes that often leads to infection and subsequent amputation resulting in prolonged hospitalisation and the need for extensive rehabilitation and home care. The prevalence of diabetes is increasing along with increasing longevity. Therefore, foot ulceration in diabetes will continue to have a heavy social impact, both in terms of quality of life to the patients and their families, as well as economic costs worldwide.

Clinical care of the diabetic foot is of paramount importance in the management of diabetic foot disorders and the prevention of amputation. Early identification is the key to allow prompt healing of any lesion on the foot, and once healed, to prevent its recurrence. Excessive mechanical loading is thought to result in tissue damage and ulceration. Consequently, the measurement of plantar pressure distribution beneath the foot has been advocated and is currently a well established technique for identifying feet that may be at risk for ulceration.

Many scientists believe foot ulcers can be managed better by offloading the affected sites on the foot. However, there is emerging evidence in the literature that suggest plantar pressures are suboptimal predictors of foot ulcers. Some studies have shown that foot ulcer occurs at sites of high plantar pressure, while others have shown it was not the case and suggested shear load would be at least equally relevant in determining potential trauma at the plantar surface of the foot. These hypotheses can only be investigated in greater detail using information gained from a multi-axial load distribution measurement device.

Compared to the numerous commercial systems available for plantar pressure distribution measurement, only a few experimental devices exist at present for shear measurement. All of these devices were either too large for high spatial resolution measurements or they were too expensive to be incorporated in clinical laboratories. Therefore, there is a need for a low-cost device for measuring multi-axial load at the foot-ground interface as well as at the foot-shoe interfaces. The development of a

multi-axial load distribution measurement device in the current study has been greatly enabled by the many recent and on-going advances in sensor technologies and miniature integrated circuits that have resulted in transducers which are small and inexpensive.

1.3 Thesis organisation

This study sought to create a low-cost device capable of measuring multi-axial load distribution beneath the human foot during the most common task; walking. Such a system has the potential to be highly informative by allowing data collection during gait under the plantar surface of the diabetic foot, thus providing valuable biomechanical data for identifying feet that may be at risk of ulceration.

This thesis contains 8 chapters. Chapter 2 outlines the clinical need for multi-axial load distribution measurement (Section 2.1) and extensively reviews current methods of load measurement used during gait analysis (Section 2.2). Finally, our current understanding of the effect of diabetes on foot biomechanics is reviewed (Section 2.3) and a comprehensive list of the requirements of a system for multi-axial load distribution measurement outlined (Section 2.4.1).

Chapter 3 reviews the basic principles underlying the operation of the many load sensing methodologies currently available. This review leads to the identification of 4 technologies that showed most promise and could potentially be used in the construction of multi-axial load transducers (Section 3.10). The 4 technologies are piezoelectric, hydraulic, optoelectronic and magnetic-based load sensing technologies. Chapter 4 outlines methods of evaluating the technical performance of multi-axial load transducers and describes an effective calibration rig for the calibration of multi-axial load transducers (Section 4.5).

Chapter 5 describes the design, development and preliminary evaluation of various multi-axial load transducers based on the 4 different load sensing technologies. This evaluation identifies the design of the optoelectronic and magnetic-based transducers

showing the best potential to satisfy the requirements of the current study. Chapter 6 outlines the further development of these 2 transducers and reports in detail their technical performance relative to the system requirements outlined in Section 2.4.1. The most appropriate transducer, the magnetic-based design, was subsequently identified (Section 6.4). Chapter 7 discusses the design and manufacture of a small magnetic-based biaxial shear transducer array. The device was evaluated (Section 7.2) and the results from a preliminary subject trial were validated against data from a conventional Kistler® force plate system (Section 7.3).

Chapter 8 discusses the overall strength and limitations of the developmental process and highlights areas for further research. Future potential development of the device for triaxial load distribution measurement has been proposed (Section 8.2.5). The use of the transducers developed during the current study in other clinical and industrial applications has also been recommended (Section 8.3).

1.4 Summary of contributions

The work completed for this thesis has resulted in the following:

1. The development of techniques for calibration of multi-axial load measurement systems under static and dynamic conditions.
2. The design, manufacture and evaluation of a discrete triaxial load transducer using hydraulic-based load sensing technology.
3. The design, manufacture and evaluation of a discrete biaxial shear transducer using optoelectronic-based load sensing technology.
4. The development of a miniature discrete biaxial shear transducer using magnetic-based load sensing technology.
5. The development and preliminary evaluation of a robust biaxial shear distribution measurement device using the magnetic-based transducer above.
6. Proposed implementation for a triaxial load distribution measurement device.

Chapter 2

Background

This chapter outlines the clinical need for a multi-axial load distribution measurement device to identify feet that may be at risk for ulceration. First, the literature exploring the global burden of diabetic foot disease and the pathological mechanisms underpinning diabetic foot ulcers are summarised. Current methods of load measurement used during gait and our current understanding of the effect of diabetes on foot biomechanics are then discussed. Finally, the aim and objectives of this research are presented with a comprehensive list of system design requirements for the development of a multi-axial load distribution measurement device.

2.1 Clinical need – diabetic foot

The current study emphasises on one particular area where load distribution measurement might be beneficial for clinical diagnosis and exploration in diabetic foot ulceration. In the diabetic population foot ulceration is a possible complication and presents difficulties for the patient in terms of pain, reduced mobility and infection risk. The following sections highlight the global concern in diabetic foot problems. The pathway to foot ulceration and possible strategies for tackling the problem are discussed.

2.1.1 A global problem

The problem of diabetic foot ulceration has been researched previously by many investigators around the globe (Gefen, 2007, Gordois et al., 2003, Jeffcoate and Harding, 2003, Abbott et al., 2002, McAlpine et al., 2005, Boulton, 2006). Foot disease and ulceration is a major global burden associated with diabetes and has been estimated to cost billions to health care systems worldwide (Boulton et al., 2005). In Scotland alone, there were around 247,000 people diagnosed with diabetes in 2011 and has been estimated to increase by around 10,000 each year (NHS, 2011). Diabetes prevalence was as high as 20% in regions of South and Central America as well as in the Caribbean (Boulton et al., 2005). It was estimated 16 million persons in the United States had diabetes in 1984 (Frykberg, 1998) and a more recent study in 2005 estimated the overall prevalence had increased to 20.8 million, or 7% of the nation's population (Frykberg et al., 2006). As the sixth leading cause of death in the US, diabetes contributes to more than 224,000 deaths per year (Frykberg et al., 2006).

Foot ulceration accounts for more hospital admissions in the diabetic population than any of the other long-term complications (Young et al., 1993, Cheer et al., 2009, Kengne et al., 2009). In the UK alone, the total annual costs of treating people with diabetic peripheral neuropathy and its associated complications was estimated to ~£252 million in year 2001, of which 90.4% was attributable to foot ulceration (Gordois et al., 2003). In a Barbados hospital 75% of its surgical beds were occupied

by patients with diabetic foot lesions (Boulton et al., 2005). Diabetic foot ulcers have resulted in almost 10,000 hospitalisations during year 2004 to 2005 in Australia (AIHW, 2008). Diabetic foot ulceration and amputations were estimated to cost US healthcare payers \$10.9 billion in 2001 (Boulton et al., 2005).

Foot ulceration is a diabetic complication that often leads to infection and subsequent amputation resulting in prolonged hospitalisation, need of rehabilitation and home care (Boulton et al., 2005, Anichini et al., 2007). The presence of foot ulcers could increase the risk of lower extremity amputations by six-fold and therefore at the same time increase the risk of cardiac death (Davis et al., 2006). Amputation rate is also higher in the diabetic population than those without diabetes (Williams and Airey, 2002). Of those who have an amputation, about 30% will experience a progression to a higher level of limb loss or subsequent amputation of the other limb (Dillingham et al., 2005). They also have a mortality rates ranging from 39 to 80% at 5 years (Reiber and Ledoux, 2003, Moulik et al., 2003). It has been estimated that every 30 seconds a lower limb is amputated somewhere in the world as a consequence of diabetes (Boulton et al., 2005).

The lifetime risk of a person with diabetes developing a foot ulcer could be as high as 25% (Singh et al., 2005), and it is likely to become more common since the prevalence of diabetes is increasing along with increased longevity (Anichini et al., 2007, Frykberg et al., 2006). Moreover, as many as 2% of patients with a history of foot ulceration may develop new foot ulcers each year (Abbott et al., 2002) and the rates of recurrence of existing ulcers can be greater than 50% after 3 years (Boulton et al., 2005). As a result, foot ulceration in diabetes will continue to have a heavy social impact, both in terms of quality of life to patients and to their families, as well as economic costs worldwide.

2.1.2 The pathway to foot ulceration

This section will cover the major routes to foot ulceration and provide a brief overview of the development of the disorder. Interested readers are directed to other literature detailing the background on diabetes and other mechanisms underlying foot

complications associated with diabetes (Levy and Valabhji, 2004, Levy and Valabhji, 2008, Guyton and Saltzman, 2001, Jeffcoate and Harding, 2003).

Foot ulcers can occur in anyone, they are defined as lesion on the skin or open sores that will not heal or often keep returning. There are many risk factors that contribute to the formation of foot ulcers (Figure 1). Both intrinsic factors, such as neuropathy, vascular disease and structural deformity as well as extrinsic factors such as high mechanical impact, high pressures, thermal and chemical injury have been identified (Frykberg, 1998, Leymarie et al., 2005, Gefen, 2007). As the investigators have suggested, it is often a combination of factors that ultimately lead to ulceration and eventual amputation. Since ischaemia and neuropathy are common complications of diabetes underlying foot ulcers, they are often defined as two types: neuropathic ulcers and ischemic ulcers.

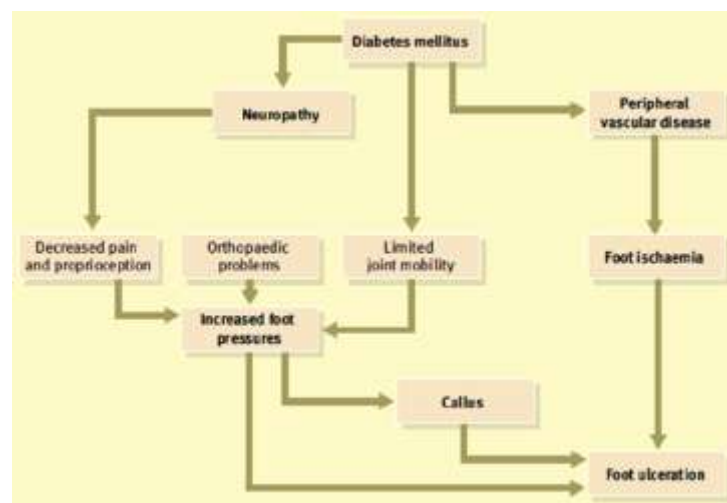


Figure 1 - Pathways to diabetic foot ulceration. (Modified diagram from Boulton, 2006)

The diabetic population is at an increased risk for developing foot ulcers. There are two major types of diabetes mellitus: Type 1 describes an autoimmune disease that destroys beta cells in the pancreas hence the body cannot produce insulin to help glucose get into the cells of our bodies; Type 2 describes a metabolic disorder in which body cells fail to use insulin properly or unable to produce enough insulin, causing elevated sugar levels in the bloodstream. Foot ulcers occur in both Type 1 and Type 2 diabetes, and it has been well established that improved glucose control

can be effective in reducing the risk of the development or progression of numerous diabetic complications (DCCT, 1993, NHMRC, 2005, Frykberg et al., 2006). The consequences of poorly controlled hyperglycemia could lead to ischaemia and neuropathy (Figure 1), which are the most common complications of diabetes that cause foot deformities and ulceration (Clayton and Elasy, 2009). As such, foot ulcers are often defined as two types: neuropathic ulcers and ischemic ulcers.

Ischemic (or neuroischaemic) ulcers are caused by peripheral vascular disease (Figure 1) and often occur when already ischemic tissues are exposed to prolonged occlusion, either partially or fully, of the underlying blood vessels. Continuous occlusion of blood would cause deficiency of oxygen and nutrient supply and waste removal from the tissue. Consequently, the tissue would degenerate and eventually dies due to the accumulation of toxic metabolic by-products produced by the cells (Chang and Seigreg, 1999).

As many as 90% of diabetic foot ulcers are caused by neuropathy alone or in combination with ischaemia. The incidence of neuroischaemic ulceration has increased to become the most common cause of lesions seen in many foot clinics in the UK (Boulton, 2006). Neuropathic ulceration is a common end-result of peripheral neuropathy which is frequent in diabetic patients (Boulton, 2006, Watkins, 2003). In the absence of pain sensation, patients with neuropathy are unable to sense high pressure areas under the foot when walking. The resultant repetitive mechanical loads cause the plantar tissues of the foot to breakdown (Gefen, 2007). As a result, the development of calluses at high pressure locations would eventually result in the breakdown of tissues and therefore ulceration (Figure 1), which may occur without the patient noticing any pain.

Other investigators reviewed that the time required for skin ulceration was inversely related to the level of pressure with a parabolic relationship (Chang and Seigreg, 1999), and neither high pressure values nor abnormal shear forces are necessary to cause ulceration (Guyton and Saltzman, 2001). So perhaps there is not one threshold level of load that would lead to foot ulceration (Armstrong et al., 1998), and that the load duration may be more important. Patients without neuropathy who are able to

sense pain are likely to reposition their foot to provide intermittent mechanical relief (Guyton and Saltzman, 2001). Those who cannot feel pain or are physically disabled, repeated or prolonged exposure to ordinarily tolerable loads could lead to ulceration (Guldmond et al., 2007a). Section 2.3 will discuss in more details these results reported in the literature. To characterise all relevant elements of mechanical loading, the magnitude of the load, its variation with time and its direction would have to be characterised. Vertical and horizontal load components are referred as plantar pressure and shear, respectively. If both direct pressure and shear loading were important factors in the generation of ulcers then both these load components would have to be measured.

2.1.3 Care of the diabetic foot

While clinical care of the diabetic foot remains the mainstay in the management of diabetic foot disorders, early recognition of individuals at risk of ulcerations has been widely advocated as a key preventative strategy in combating the financial and personal burden associated with diabetic foot ulcerations (Anichini et al., 2007, Frykberg, 1998). The National Health Service in Scotland recommends that all patients with diabetes should be screened to assess their risk of developing a foot ulcer (SIGN Guideline 116: Management of diabetes, March 2010, Scottish Intercollegiate Guidelines Network). It has been estimated that an effective risk identification and education program could reduce the formation and recurrence of foot ulcers by up to 50%, thereby negating the need for, and high costs associated with, amputation (Boulton et al., 2005, Boulton, 2006).

It is generally considered appropriate to manage foot ulcers by offloading the affected sites and redistributing the load to other foot regions (Boulton, 2006, Bus et al., 2009, Boffeli et al., 2002, Frykberg et al., 2006, Owings et al., 2009, Cavanagh et al., 2000). Section 2.3.3 discusses how it is believed the role of plantar shear load and its relief would be important in the treatment of diabetic foot problems. The utilisation of a triaxial load distribution measurement device in the clinic settings would allow a quantitative analysis for identifying the specific regions of a patient's foot at risk of ulcer formation.

2.2 Methods of load measurement during gait

Loading on the foot appears to have a role in the process of neuropathic ulcer formation in diabetes. Being able to measure this loading in a quantitative manner across a number of sites beneath the foot would allow examination of the important factors that lead to ulcer formation. Moreover, information about the triaxial load distribution could also be used to direct treatment and intervention strategies (Section 2.1). This section provides an overview of the current state-of-the-art in methods for measuring load under the plantar surface of the foot. An understanding of the limitations of these methods is necessary to compare biomechanical data collected using these techniques (Section 2.3) and provides fundamental information on the physical requirements of a multi-axial load distribution measurement system for gait analysis (Section 2.4.1).

2.2.1 Uniaxial and multi-axial load measurement

Mechanical stresses are generated on our feet with each walking step. The mechanical stress vector can be decomposed into three components, namely vertical (pressure) and two horizontal (shear) components. To fully assess the role of mechanical load in the formation of diabetic foot ulcers, both the vertical and shear force components beneath the plantar surface of the foot should be measured. The ideal measurement device would allow simultaneous measurement of triaxial load; vertical (Z) and two shear (X and Y) components. An alternative would be a compound instrument constructed by superimposing a uniaxial load (Z) measurement device on a biaxial shear (X and Y) measurement device (Giacomozzi and Macellari, 1997, Giacomozzi et al., 2000, Giacomozzi et al., 2008, Heywood et al., 2004). A more time consuming alternative would be to record biaxial shear and vertical load separately using different system in separate trials (Laing et al., 1992).

As summarised in previous reviews of the topic (Cobb and Claremont, 1995, Urry, 1999, Gefen, 2007), vertical load beneath the foot has been researched extensively, largely because there are numerous commercial systems and experimental techniques available for measuring the distributional of vertical load under the foot. However,

the study of plantar shear distribution has lagged behind primarily due to the lack of technology for its measurement. There are only a few experimental devices in existence at present that are capable of measuring the distribution of shear loads beneath the human foot. The many commercial systems for uniaxial load measurement and other experimental devices for multi-axial load measurement will be discussed in more details in Chapter 3. However, some discussion regarding fundamental aspects of force and pressure measurement is warranted, prior to a more in depth discussion of current measurement systems and their limitations.

2.2.2 Differences between force and pressure measurement

‘Load’ can be referred to as friction, moments, pressure or any other type of force. Although ‘force’ and ‘pressure’ are related to one another, they are not the same. It is important to distinguish between the terms force and pressure in order to categorise a load measurement device. Both classifications, however, may be valid in a system that uses different methodologies for multi-axis load detection. For example, a triaxial load measurement system (Davis et al., 1998) can be designed to measure axial pressure and two shear forces. Certain types of transducers, such as some force-sensitive resistors (Urry, 1999), fall between these two categories and are sensitive to force and the area of contact independently.

The concept of pressure can be observed if one is asked to press both ends of a pencil with equal force. The sharp end with smaller surface area results in a greater pressure and therefore more pain to a finger. This means pressure takes into account the area over which the force is acting. The bigger the force, the bigger the pressure for a given contact area, hence $\text{Pressure} = \text{Force} / \text{Area}$. It is obvious that the same force applied to the foot may or may not damage its tissue depending on the area over which the force is acting. Therefore, care should be taken when comparing plantar pressure and plantar force data, such as those discussed in Section 2.3. The area of the surface being loaded must be known in order to perform conversion between the two terms.

Depending on the method used in the calibration of the transducer and hence its intended use, a transducer can be classified as a force or pressure measurement device. Force transducers are often calibrated by applying loads through a rigid structure. An ideal force transducer would respond identically to two equal loads regardless of the area or the location of the applied force. Whereas the output from an ideal pressure transducer, under constant force conditions, would be inversely proportional to the area over which the load was applied. Calibration loading to a pressure transducer is usually applied via a compliant structure, such as an air-filled membrane, to ensure an evenly distributed load across the transducer's sensing surface. Transducer calibration methods are discussed in more detail in Chapter 4.

In most clinical and engineering literature, pressures are specified using standard international (SI) units. The SI unit for force is the Newton (N), and for pressure the Pascal (Pa), which is equal to one Newton per square meter (N/m²). However, other units are often found in the literature for reporting pressures, such as kg/cm² and millimetres of mercury (mmHg). All pressure data given throughout this text include the original units reported within the literature, as well as the equivalent measure in Pascal (Pa) for standardisation and convenience.

2.2.3 In-shoe and floor platform data collection methods

There are two distinctive methods for collecting plantar load data: 1) inside a shoe, and 2) barefoot on the floor. People from different cultural backgrounds may prefer to walk barefoot or with shoes. Force plates or force platforms, are large commercially-available floor-mounted load measurement devices, which are widely adopted for gait analysis to provide independent measurement of total vertical and shear forces. Although they are not capable of measuring the distribution of triaxial load beneath different sites of the foot, they have been developed to a high level of performance and therefore are often regarded as the 'gold standard' against which other load measurement systems are evaluated (Cobb and Claremont, 1995, Catalfamo et al., 2008). Force plate manufacturers include the Kistler Group (Switzerland), AMTI Inc (USA) and Bertec Corp. (USA). A typical force plate has a sensing area of 600×400mm, non-linearity and hysteresis $\leq \pm 0.5\%RC$ (Rated

Capacity), crosstalk between output channels $<\pm 2\%$, sampling frequency 1000Hz, rated capacity of typically 20kN for vertical forces and $\pm 10\text{kN}$ for shear forces (Kistler Group, Switzerland).

The limitations of these force plates are their size, costs and inability to measure distribution of load beneath different parts of the foot. To overcome this limitation, devices have been developed to measure load distribution by the use of an array of small transducers - effectively an array of miniature force plates. The most successful example of this is the experimental platform developed by Davis et al. (1998) capable of triaxial load distribution measurement. Due to the relatively large number of elements included in their array, this device can be seen as the current 'gold standard' in triaxial load distribution measurement. A more in-depth description of the device is given in Section 3.2.4.2. Briefly, the platform device consisted of 16 transducer elements, with non-linearity $\pm 5\% \text{RC}$, hysteresis $\pm 7.5\% \text{RC}$, accuracy of $\pm 5\%$, crosstalk between shear channels 5% and 13% between vertical and shear channels, sampling frequency 37Hz, rated capacity of typically 165N for vertical forces and $\pm 67\text{N}$ for shear forces.

Since the introduction of electronic plantar pressure distribution measurement platforms (or pressure plates) at relatively lower cost, the majority of research involving the diabetic foot has been focused on plantar pressure measurement during bare foot walking (Guldmond et al., 2007a). Examples of manufacturers of pressure plates are Novel GmbH (Germany) and RSscan International (Belgium). Although the devices can only measure uniaxial (vertical) pressures, some systems have more than 6000 transducer elements for high-resolution load distribution measurement – covering an area of around $470 \times 320\text{mm}$, with up to 4 sensor elements/cm². While the performance of these devices does not match that of 'gold standard' force plates, a typical pressure plate has a hysteresis $< 3\% \text{RC}$, accuracy $\pm 5\%$, sampling frequency up to 400Hz, with a rated capacity of typically about 1300kPa (Novel GmbH, Germany).

The major limitation of all platform systems is that they can only measure load during a single step and training may be required for the subject to walk naturally in

a restricted path and onto the sensing area of the device (Guldemon et al., 2007a, Gefen, 2007, Colin E. Thomson, 2002). This may be particularly problematic in the high risk diabetic foot where multiple trials may result in ulceration (Bus and Lange, 2005). Data collection using single step trials is more time consuming and the data may not truly reflect the loading conditions beneath the foot, due to inter-walk or step-to-step variability within or between subjects (Hosein and Lord, 2000).

While several consecutive strides may be examined by using triaxial force measurement treadmills (Kram et al., 1998), treadmill locomotion is known to induce small difference in kinetic, kinematic and electromyographic data compared to over-ground locomotion (Prosser et al., Rosenblatt and Grabiner, 2010, Parvataneni et al., 2009, Riley et al., 2008, Riley et al., 2007, Warabi et al., 2005, Wank et al., 1998), raising questions as to its validity for plantar pressure measurement. An alternative would be to attach discrete multi-axial load cells beneath the shoe (Faber et al., 2010). However, additional devices are needed to accurately detect the position and orientation of the system, if force data are required relative to a ground-reference system (Liedtke et al., 2007). The same applies to in-shoe measurement systems.

Commercial devices for in-shoe pressure distribution measurement (or pressure mats) became available from the 1990s (Guldemon et al., 2007a) and have provided researchers with the opportunity to collect data from multiple steps per trial. Manufacturers of in-shoe pressure systems include Novel GmbH (Germany) and Tekscan Inc. (USA). As demonstrated by these manufacturers, the same load sensing technology used in an in-shoe measurement system can also be used to form a platform system. A commercially available in-shoe pressure mat typically has an insole thickness of <2mm, an allowable bending radius of ~20mm, contains around 80 sensors per insole depending on shoe size, has a non-linearity $\pm 3\%RC$, hysteresis $\sim 7\%RC$, sampling frequency <100Hz, and a rated capacity of about 800kPa.

Despite the fact that a large amount of research has been conducted with these pressure measurement devices, the method by which the data are collected are not standardised and often vary between investigations (Chevalier et al., 2010). Different pressure distribution systems, both platforms and in-shoe type devices, have different

sensor characteristics, spatial resolution and sampling frequency. Differences in measurements may also be found even when the systems are from the same company and based on the same load sensing technology (Chevalier et al., 2010). Therefore, interpretation of the absolute pressure values should take into account the potential influence of different load sensing technology (Bosch et al., 2007).

Comparison of data should also be made based on the same reference axes system, because the alignment of the insole device to the subject's foot may vary between investigations (Lord and Hosein, 2000, Chesnin et al., 2000). It should also be noted that the operating temperature inside the shoe is different to that of barefoot testing on force platform systems. A typical commercially available pressure platform has a working temperature range of 10°C to 40°C, while the operating temperature inside the shoe may vary between 30°C to 40°C (Razian and Pepper, 2003) and beyond after running (Cruickshank et al., 2007). The performance of in-shoe measurement devices may be influenced by temperature (Razian and Pepper, 2003, Cavanagh et al., 1992), and therefore the characteristics of the devices must be taken into account when comparing results between in-shoe devices or data measured from platform systems.

There are other challenges associated with in-shoe load measurement methods. The more obvious reason is the restriction of space within a shoe. The spatial resolution of in-shoe systems are generally lower than those of a platform system (Gefen, 2007). There are also general restrictions on the thickness of the device with researchers typically using transducers with thickness ranging between 1mm and 4mm (Akhlaghi and Pepper, 1996, Razian and Pepper, 2003, Tappin et al., 1980, Lord et al., 1992, Laing et al., 1992, Lebar et al., 1996, Wang et al., 2005, Kärki et al., 2009). While a more recent study successfully mounted several transducers of thickness 10mm into female high heel shoes (Cong et al., 2011). However, uneven surfaces inside the shoe and bending forces, resulted in crosstalk between elements, raising questions as to the accuracy of the data may lead to erroneous outputs (Cobb and Claremont, 1995, Razian and Pepper, 2003).

Correct fitting and alignment of the instrument can be physically challenging (Hosein and Lord, 2000) and ill-fitting transducers may adversely alter gait patterns and hence the load distribution beneath the foot (Kong and De Heer, 2009). Structural and musculoskeletal differences found between subjects and variations in footwear designs would also affect the loading conditions inside the shoe (Hosein and Lord, 2000, Chevalier et al., 2010). Some investigators have questioned whether in-shoe data measured during walking in a laboratory settings on level ground were representative of plantar loads during daily activities (Guldemon et al., 2007a, Kong and De Heer, 2009), while others believed pressures at the foot-shoe interface is the one that most resembles real life walking (Colin E. Thomson, 2002). Nonetheless, the current study aims to identify a method for load measurement inside the shoe because the same transducer design could also be used to form a platform system.

2.2.4 Device configuration - discrete or multiple transducer array

Commercially available pressure distribution measurement devices (Section 2.2.3) are configured using an array of transducer elements that is capable of covering the whole plantar surface of the foot. One could imagine the large volume of data contained in each trial from a pressure distribution measurement device, let alone a system that could measure triaxial load distribution. Some may argue (Nevill et al., 1995) that plantar load should only be measured at selected anatomical sites to reduce the amount of redundant information and to simplify the analytical task to be carried out by the clinicians.

Discrete in-shoe transducers can be placed at specific locations to allow localised load measurement under regions of the foot (Razian and Pepper, 2003, Hosein and Lord, 2000, Lord and Hosein, 2000, Akhlaghi and Pepper, 1996, Nevill et al., 1995, Razian and Pepper, 1998, Cong et al., 2011). However, prior knowledge regarding the area of interest is required in order to determine placement of each individual transducer. The use of a pressure mat to locate the site of peak pressure beneath the feet for the purpose of subsequently locating the discrete transducers has been tried (Hosein and Lord, 2000, Lord and Hosein, 2000).

The mounting of each discrete transducer within the shoe to allow reliable data collection could be physically challenging. Each transducer would ideally be as small as possible to allow them to be placed side-by-side if necessary (Hosein and Lord, 2000). A relatively large transducer would require extra-depth shoe or inlay area for mounting (Hosein and Lord, 2000, Cong et al., 2011). As reviewed previously (Urry, 1999), the locus of the peak load on the foot may displace by at least 7mm during walking. Therefore the position of the transducer with respect to the peak load is important, to avoid erroneous reading when the peak load is situated at the junction of two or four adjacent transducers.

A study (Lord, 1997) suggested the peak pressure measured by a transducer with an area of 10×10mm can be underestimated by as much as 70% of the true peak, depending on the sharpness of the peaks. However, the pressure measurement device used in the study suffered from poor accuracy (~10% error) and creep (5% error in 30seconds). Another study estimated a 10×10mm transducer could measured peak pressure almost as well as those with 5×5mm (Davis et al., 1996). In the study, a commercial pressure distribution measurement system (EMED, Novel GmbH, Germany) comprised an array of 5×5mm transducers was used, each transducer with an accuracy rated better than 5%. A more recent study (Pataky, 2012), conducted based on the modelling method presented in Lord (1997), suggested that the critical sensor widths required to achieve 90% accuracy ranged from 1.7mm to 17.4mm. However, measurement accuracy is also dependent on the positioning of the sensor and as such there is no particular spatial resolution can yield a constant measurement accuracy across common plantar load measurement tasks.

Platform systems constructed from a single or multiple discrete transducers can also be found in the literature (Davis et al., 1998, Chen et al., 2010). The advantage of these systems is that each transducer can be detached from the assembly for calibration or repair when necessary. Localised load measurement under specific regions of the foot is also achievable on a platform system by the addition of a video system (Chen et al., 2010). However, studies conducted using multiple triaxial load transducers have shown that peak plantar pressure and peak shear sites may differ in diabetic patients (Yavuz et al., 2007b, Cong et al., 2011, Hosein and Lord, 2000).

Since pressure distribution measurement systems are readily available, therefore, there is a need for a transducer array capable of biaxial shear distribution measurement before one can confidently select and eliminate anatomical sites for evaluation.

2.3 Diabetic foot biomechanics and foot ulcers

A summary of current methods of measuring load under our feet has been discussed together with suggestions on how the measured data should be interpreted (Section 2.2). The volume of biomechanical studies of the foot in diabetes continues to grow, but as highlighted earlier (Section 2.2.1), there is relatively little published research regarding plantar shear data, presumably due to a lack of technology for its measurement. Nonetheless, the following sections provide a summary of our current understanding of the loading patterns beneath the human foot during walking, with or without shoes. The differences in loading patterns between normal and the diabetic population are discussed. This review would provide the information to assess the technical requirements for the design and development of a triaxial load distribution measurement system (Section 2.4.1).

2.3.1 Frequency content of plantar load profile

Any load transducer will have a natural frequency of oscillation. Large dynamic measurement error will occur if a dynamic load is applied to a transducer with a frequency component at the natural frequency of oscillation of the transducer. It is important that the frequency content of the loading patterns under the feet is taken into account when selecting or specifying a measurement device. The transducer must not have a natural frequency within the expected input signal range. Moreover, based on the Nyquist sampling theorem, the sampling rate of the measurement device should be at least twice the highest significant frequency contained within the plantar loading signal.

During barefoot walking, Antonsson and Mann (1985) found that 98 % of the signal power in the vertical load was contained in the range 0 to <10 Hz. The researchers used a Kistler force plate system with a high sampling rate (2kHz) to measure the frequency content of the load beneath the entire foot during barefoot walking. Similar findings have been reported elsewhere (Kram et al., 1998, Harris et al., 1996). There are, however, components of the loading on the foot that exhibit higher frequencies. For example the heel strike transients have been reported to contain frequency components at around 75Hz for barefoot walking and 60 Hz for shod walking (Harris et al., 1996).

Dominant frequencies of <4Hz were found in the shear load directions, both during barefoot and shod walking (Harris et al., 1996). Higher dominant frequencies in the shear axes of <9Hz was reported in another study with the subject walked on an instrumented treadmill (Kram et al., 1998). The latter study did not indicate whether the subjects were wearing shoes, and peak ground reaction forces measured in treadmill gait tend to be less than those measured during overground walking (Riley et al., 2007, Parvataneni et al., 2009). Nonetheless, it appears that a sampling frequency of approximately 50Hz would be adequate to characterise the majority of the foot-floor interactions during walking (Kärki et al., 2009, Orlin and McPoil, 2000). However, for full characterisation of hard foot impact, such as during running, a sampling rate of up to 200Hz or more would be required (Nevill et al., 1995).

2.3.2 Ground reaction forces and forces inside the shoe

Ground reaction forces (GRF) are equal in magnitude but opposite in direction to the forces the body exerts on the supporting surface through the foot. Force plates (Section 2.2.3) are widely used to measure GRF during barefoot and shod trials. Figure 2 illustrates typical GRF data measured by a force plate during normal barefoot gait. Vertical and shear forces of up to 110% and 20% of body weight, respectively, can be expected during barefoot gait (Harris et al., 1996, Keller et al., 1996), whereas forces of up to 3 times the body weight could occur during barefoot running (Nilsson and Thorstensson, 1989, Kram et al., 1998, Keller et al., 1996).

GRF measurements provide an indication of the magnitude of load that a measurement device may need to withstand.

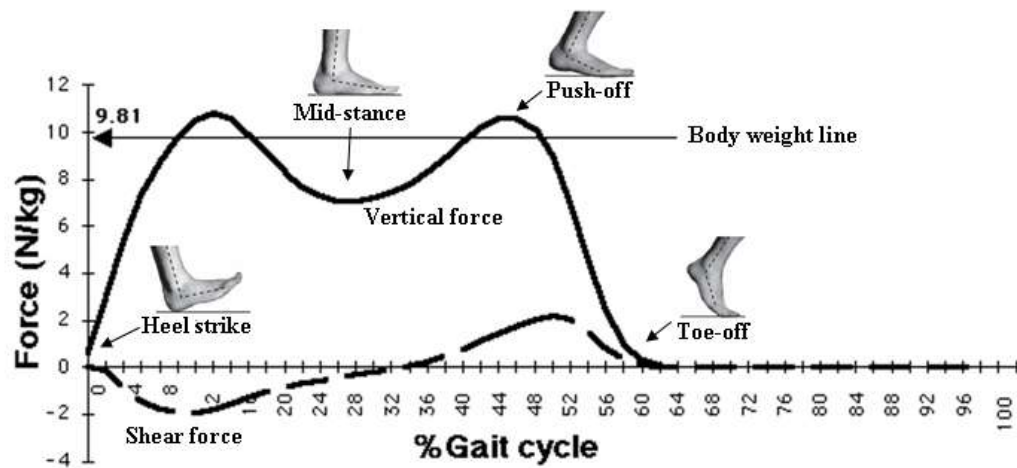


Figure 2 - Ground reaction forces measured during normal gait. Vertical force and anterior-posterior shear force are illustrated. Force data are normalised to body mass. (Modified diagram from Kirtley, 2005)

It is recognised that biomechanical factors, both load and its distribution, play an important role in the development of diabetic foot ulcers. Since force plates can only measure the overall GRF on the foot, pressure plates and in-shoe pressure mats are commonly used to identify high pressure regions within the foot which are considered to be at high risk for foot ulceration (Section 2.2.3).

During barefoot walking at a preferred speed, peak pressures between 165kPa to 1100kPa have been reported in individuals with diabetes (Drerup et al., 2008, Armstrong et al., 1998, Bus et al., 2005). Barefoot peak pressure as high as 1253kPa have been recorded in one particular diabetic patient (Guldmond et al., 2007b). However, peak pressures reported during barefoot walking were not apparent during shod gait. Lord and Hosein (2000) found in-shoe peak pressure values during gait were slightly higher in their diabetic patient group but not significantly when compared to a healthy control group (diabetes 273kPa vs. normal 228kPa). Another in-shoe study also found a small overall mean differences of 28kPa in forefoot plantar pressures between patients with or without neuropathy (Guldmond et al., 2007a). In-shoe peak pressure in patients with per cavus was found at the forefoot region to be about 40N/cm² (or 392kPa) (Crosbie and Burns, 2008).

The wide spectrum of pressure values found in the literature between normals and patients, as well as between patient groups, may be caused by several factors. Pressure measurement devices from different manufacturers have different spatial resolution, thus absolute pressure values recorded are likely to vary between systems. The maximum value recorded would depend on the spatial resolution and whether the sensing element was placed precisely at the high pressure point, otherwise underestimation of the true maximum value would result (Section 2.2.4). Between-subject differences in walking speed would affect their plantar pressure values. Reducing the walking speed would cause a reduction of peak pressures in all plantar regions (Drerup et al., 2008, Rosenbaum et al., 1994). Patients with diabetic neuropathy may have used a more cautious gait pattern due to reduced feedback (Eils et al., 2002, Guldmond et al., 2007a) therefore making it difficult to compare between groups. Alternations in the movement or position of different parts of the foot in diabetes, for example clawtoes, which result in depressed (relatively plantarflexed) metatarsal heads, might contribute to altered pressure patterns beneath the foot (Gefen, 2007, Boffeli et al., 2002). Peak pressure have been found to be nearly two times higher in diabetic patients with toe deformity compared to those without toe deformity (Bus et al., 2005). Footwear has also been shown to moderate plantar foot pressures, with loose fitting shoes found to decrease peak pressures (Fiedler et al., 2011), while sports shoes with soft midsoles may reduce loading rates due to better cushioning (Hagen and Hennig, 2009).

While results published previously have suggested that patients with diabetic neuropathy typically experience higher plantar pressure and that increased peak pressure would increase the likelihood of ulceration (Veves et al., 1992, Shaw et al., 1998, Stokes et al., 1975, Frykberg et al., 1998, Uccioli et al., 2001, Pataky et al., 2005), researchers are currently unable to identify a critical magnitude of peak plantar pressure that can predict with certainty when soft tissue ulceration will occur. Studies have attempted to establish an injury threshold: Armstrong et al. (1998) established one at about 700kPa with sensitivity of 70.0% but may be only 65% specific; while Lavery et al. (2003) suggested the threshold at 87.5 N/cm² (or 873kPa) yielding a sensitivity of 63.5% and a specificity of only 46.3%. In a large

study of 251 diabetic patients, 42% of the ulcerated patients did not have high foot pressure (Frykberg et al., 1998) and in another study only 38% of the ulcers developed under peak pressure locations (Veves et al., 1992).

When used in isolation, foot pressures have been suggested by to be poor predictor of plantar foot ulcers (Cavanagh et al., 2000, Lavery et al., 2003) as it does not provide sufficient information to differentiate between neuropathic and non-neuropathic diabetic feet (Hayes and Seitz, 1997). Researchers have suggested other factors; such as the accumulation of pressure with time (pressure-time integral) (Hayes and Seitz, 1997, Lavery et al., 2003, Maluf and Mueller, 2003) and shear load (Lavery et al., 2003, Cavanagh et al., 2000) might also be implicated in the development of foot ulcers. While further research on pressure-time integral in diabetes can be conducted using commercial pressure measurement systems (Section 2.2.3), a multi-axial load distribution measurement device that can measure load continuously throughout the gait cycle would be necessary to fully assess the role of shear load in the formation of foot ulcers.

2.3.3 Shear load under our feet

Although the measurement of plantar pressure distribution is currently well established, the link between the resultant pressure profiles and foot ulceration is not clear (Section 2.3.2). This has led researchers to investigate other factors, specifically plantar shear loading. The topic of shear force in the formation of ulcer is increasingly being discussed at healthcare conferences (congresses of the International Foot & Ankle Biomechanics (i-FAB) community) and special interest groups such as the National Pressure Ulcer Advisory Panel (NPUAP). In 2005, an international consensus group, the Shear Force Initiative (SFI) was created by NPUAP together with the European Pressure Ulcer Advisory Panel (EPUAP) and Japanese Society of Pressure Ulcers (JSPU) to help shape future research. The NPUAP has also updated their definition of ulcer based on current research to include the term shear: “A pressure ulcer is localized injury to the skin and/or underlying tissue usually over a bony prominence, as a result of pressure, or pressure in combination with shear and/or friction” (Black et al., 2007).

Shear stress in the plantar tissue can be caused by various loading methods including direct shear or pressure applied perpendicular to the plantar surface. The application of a force parallel to the plantar surface (direct shear) would cause shear stresses and deformation in the plantar tissue (Figure 3a). Pressure and shear are intimately linked hence pressure applied on the plantar surface alone would also cause some degree of shear through tissue distortion (Figure 3b). The relative movement of the skin and underlying tissues causes shear stresses to develop in the soft tissues overlying bony prominences. The compression of the tissues would also distort adjacent tissues causing pinch shear (Figure 3b).

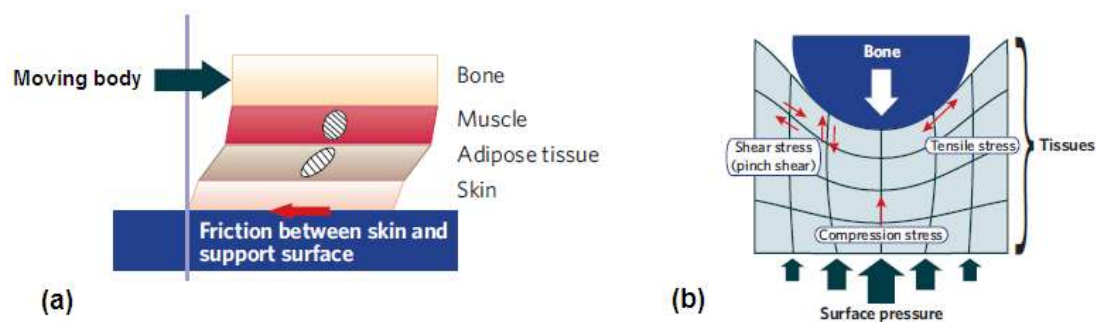


Figure 3 – The deformation and stresses in plantar tissue due to the application of direct shear load (a), or pressure on the plantar surface (b). (Diagrams adapted from Wounds International, 2010)

A steep pressure gradient across a small plantar surface area is likely to produce high shear stresses that may exceed tissue tolerance causing deep tissue injuries. This leads to many researchers to hypothesize that it is also likely for ulcers to initiate from deeper tissue layers (Lott et al., 2007)(Wounds International, 2010). However, internal stresses are difficult to predict by means of interface pressure measurements alone (Gefen, 2009a, Gefen, 2009b). Perhaps measuring the displacement change of the skin in combination with pressure could be one solution. However, methods for measuring skin deformation are beyond the scope of the current project. With today's technologies, it is only realistically possible to measure the shear load being applied at skin surface interfaces. Internal stresses are difficult and unethical to measure directly in vivo, but based on load transfer principles, these stresses will be distributed over the plantar surface of the foot. As such, computer models could be used to estimate internal stresses from load measurement data obtained at the plantar surface (Atlas et al., 2009, Lott et al., 2008, Mueller et al., 2008). Therefore,

measuring shear load (or in combination of pressure) over the plantar surface could further assist in solving the link between tissue stresses and the development of foot ulcers.

The hypotheses that shear load at the skin surface interfaces also have an important role in ulcer formation can be supported by studies conducted on animals. Excessive shear forces have previously been shown to cause hyperkeratosis in mice tissues that could lead to ulceration (Mackenzie, 1974). While another study conducted on rat forepaws has been shown that repetitive loading of ordinarily tolerable shear forces could also lead to ulceration (Brand, 1991). Studies on pigs has demonstrated that with the present of shear load, the pressure necessary to occlude blood vessels was almost half (Bader et al., 2005) and tissue breakdown would occur earlier when shear forces were increased (Goldstein and Sanders, 1998).

Similarly in studies on human, as referenced in Chang and Seigreg (1999), a study conducted in 1968 (Palmer et al., 1968) found that adding shear force after long periods of exposure to pressure, reduced the pressure threshold that causes tissue damage. Another study has also found that with the presence of a shear stress as little as 10kPa, the pressure required to produce ischemia of the skin reduces by a factor of up to two (Bennett et al., 1979). This shear-induced effect was apparent even in young healthy adults (Goossens et al., 1994).

Compared to the numerous commercial systems and experimental techniques available for plantar pressure distribution measurement, only a few experimental devices currently exist for shear measurement. Prototype devices consisting of an array of transducers for measuring shear distribution have been reported previously (Christ et al., 1998, Davis et al., 1998, Mackey and Davis, 2006), as well as discrete transducers for shear measurement on the ground or inside the shoe (Akhlaghi and Pepper, 1996, Razian and Pepper, 2003, Tappin et al., 1980, Chen et al., 2010, Lord et al., 1992, Laing et al., 1992, Lebar et al., 1996, Wang et al., 2005). All of these devices were either too expensive (B.Davis, Cleveland USA, pers. comm.) or too large (>10mm²) to be incorporated in a large array for a high spatial resolution load distribution measurement device. As a result, none of these devices is currently

capable of measuring the distribution of shear forces over the entire plantar surface of the foot. Moreover, each of these experimental devices employed a different load sensing technique, and hence they possessed very different system characteristics in terms of transducer dimensions and measurement accuracy.

Studies employing floor mounted shear distribution measurement systems to evaluate walking in healthy adults have found that the highest shear loadings occurred beneath the metatarsal regions of the foot (Davis et al., 1998, Chen et al., 2010). The maximum shear load was found to be about 5% of body weight (~88kPa) in one study (Chen et al., 2010), and approximately 25% (~92kPa) of the applied vertical pressure in another (Davis et al., 1998). Similar results have been reported in-shoe, where shear loads were 30% of vertical pressures on average in healthy individuals walking at their preferred speed (Laing et al., 1992). However, in-shoe shear values as high as 75% to 100% of vertical pressure have been reported by others when testing healthy individuals under similar conditions (Razian and Pepper, 2003).

Average maximum shear of ~73kPa was found in a group of patients with diabetic neuropathy, with the highest reading of 122kPa for an individual in the group (Lord and Hosein, 2000). With the same device in a separate study with normal subjects (Hosein and Lord, 2000), the average maximum was found to be higher at ~87kPa shod walking without hose or ~31kPa when wearing nylon hose. Others measured shear load between 6kPa to 52kPa at various regions of the foot (Perry et al., 2002); (Lebar et al., 1996) and up to 200kPa was found in the metatarsal and hallux regions (Akhlaghi and Pepper, 1996). However, the latter results suffered from error due to bending of the transducer (Section 5.1). Some researchers attempted to calculate shear from plantar pressure data (Lott et al., 2008) and from finite element modelling (Dai et al., 2006). Computational models are often based on the theory of elasticity and assuming subsurface tissues to be homogeneous, isotropic and linear elastic (Lott et al., 2008, Zou et al., 2007), but they all should be verified with real-life measurements.

Since there is no standard practices in shear measurement, devices from different manufacturers have different characteristics and spatial resolution, hence the absolute

shear value may vary between systems. Researchers could easily underestimate shear loads if discrete transducers were not located precisely at the region of interest on the foot, which may be due to relatively large transducer size (Hosein and Lord, 2000). Due to technical limitations, some devices could only record <5 seconds of data (Lord and Hosein, 2000, Hosein and Lord, 2000, Davis et al., 1998). Some investigators may have had their transducers orientated referring to the foot and not to the walking direction (Lord and Hosein, 2000), which can make comparison between studies difficult. The speed of walking, shoe design and its fitting could also influence shear measurement during gait (Lord and Hosein, 2000, Hosein and Lord, 2000).

As well as the peak load measurement, it is also important to consider the loading profile and time of load application. Diabetic subjects who walked slower were found to have higher shear-time integral values than non-diabetic subjects (Yavuz et al., 2008). The location of high shear value in relation to high pressure values should also be examined. Skin breakdown and the reduction in skin blood flow likely occur at far lower loads, when pressure is simultaneously applied with shear (Pinzur, 2004, Parish et al., 2007, Ming and Roberts, 1993). Researchers have also suggested that the direction of shear force should be investigated to examine whether plantar tissues are being tensioned (stretched) or compressed (bunched) during walking (Davis et al., 1998).

A critical review of the articles discussed above would reveal that the real clinical need for a shear load distribution measurement device can only be identified if there is more significant data available on interface shear and its relationship to ulcer development. From our understanding of the physical and mechanical principles, it is a fact that the shear component is always present when the foot is mechanically loaded. It is unfortunate that there is currently not a well accepted or validated device for measuring shear distribution over the plantar surface, and researchers were therefore not able to fully evaluate this variable. However, animal models (Mackenzie, 1974, Brand, 1991, Bader et al., 2005, Goldstein and Sanders, 1998) have provided some level of evidence that the presence of shear would increase the risk of ulcer formation. Studies conducted on other parts of the human body (Palmer

et al., 1968, Bennett et al., 1979, Goossens et al., 1994) also demonstrated similar evidences that the presence of shear load at the skin interface would increase the risk of tissue damage. Once the skin is broken, many factors may then contribute to defective healing and putting one at greater risk for ulceration.

On the other hand, reports of the distribution of shear load under the foot and the interaction of these to ulceration are very limited or non-existent. Several studies have used different experimental devices to measure interface shear during gait. Some studies were conducted on a single (Chen et al., 2010, Akhlaghi and Pepper, 1996, Razian and Pepper, 2003), or up to ten non-diabetic subjects only (Laing et al., 1992). The purposes of these trails were only to show the utility of the devices and provide representative normal subject data in addition to their calibration data. One research group has utilised the same device on nine normals (Hosein and Lord, 2000) and six diabetic patients (Lord and Hosein, 2000). However, the subject group is too small to give truly representative data, and the discrete transducers are limited to certain sites on the foot which cannot provide a full picture of what was occurring on the plantar surface of the foot. Nonetheless, these preliminary results provide some indication of the main characteristics and magnitude of shear load under our feet, which is valuable for constructing the design requirements for the current project to develop a new multi-axial load transducer. Once realised, such a system has the potential to provide valuable biomechanical data that may help improve our understanding of the role of mechanical load in the formation of foot ulcers.

2.4 Project aim and objectives

This chapter has highlighted the global concern in diabetic foot ulceration. Neuropathic ulcers are widely believed to occur in response to the mechanical overloading of plantar tissues and the measurement of plantar pressure distribution has become a well established clinical technique to aid in the identification of individuals at risk of ulceration. However, scientific support for this premise is controversial. While early studies indicated that foot ulcers occur at sites of high

plantar pressure, more recent studies as well as studies conducted on other animals have shown this is not the case and proposed that plantar shear and the duration of exposure to both pressure and shear may be more useful in identifying people at high risk of developing diabetic foot ulcers. Such hypotheses can only be scientifically tested with the aid of a multi-axial load distribution measurement device that can measure load continuously throughout the gait cycle.

The ideal device should be capable of triaxial load distribution measurement, both inside or outside the shoe. However, since various pressure distribution measurement devices are commercially available, there is specific need for a device that is capable of biaxial shear measurement. Such a device would ultimately improve our understanding of the role of mechanical load in the formation of diabetic foot ulcers.

The aim of this research, therefore, was to develop a novel, low-cost multi-axial load transducer that can be used in-shoe or incorporated in an array for measurement of the distribution of load beneath the human foot during gait.

To fulfil this aim, the following objectives needed to be met:

Objectives:

1. To identify essential and desirable system design requirements for the development of a multi-axial load distribution measurement device.
2. To identify load sensing technologies with the greatest potential to meet the requirements outlined in Objective 1.
3. To establish an efficient and effective method of calibrating multi-axial load transducers.
4. To identify the optimal transducer design to be incorporated in a multi-axial load distribution measurement device against the design requirements in Objective 1.
5. To design, manufacture and evaluate a multi-axial load distribution measurement device against the design requirements in Objective 1.

2.4.1 System design requirements

To achieve the aim of the current study, the design and development of the multi-axial load distribution measurement device was required to meet certain physical and technical requirements. The minimum requirement of being capable of measuring biaxial shear load had to be met. Additionally, there were 28 specific design requirements which had to be met to make the system of practical use. Most of these design requirements can commonly be found in technical specifications of other commercially available force measuring systems, while other requirements have been developed based on previous literature and considerations for the practical implementation of a load distribution measure system for the foot (Sections 2.2 and 2.3). The requirements are detailed within four categories in Table 1 below:

Table 1 - System requirements for a multi-axial load distribution measurement system.

<u>Essential requirement:</u>			
Transducer must be capable of biaxial shear measurement or triaxial load measurement continuously over the time of one gait cycle.			
<u>Category A: Transducer performance</u>			
#	Requirement	Condition	Description/Information
1	Rated Capacity	Vertical load: 2500kPa Shear load: 300kPa	The rated capacity of the load transducer must be equal to or greater than the largest load expected during walking. Commercially available pressure platforms have a rated capacity of typically up to about 1300kPa (Novel GmbH, Germany) (Section 2.2.3), and previous work has shown highest pressure can be expected about 1250kPa (Guldemon et al., 2007b) (Section 2.3.2). Shear load ~122kPa can be expected (Lord and Hosein, 2000) (Section 2.3.3). The device must withstand the weight of a person (780N). Potential mechanical abuse was also considered and a safety

			<p>factor of >2 was preferred.</p> <p>Conditions are given in unit of pressure (kPa), which should be converted to Force (N) in respect to transducer surface area (#19) for force transducers.</p>
2	Resolution	<10kPa	This is the ability of the device to distinguish between two load levels. Commercially available pressure platforms have a pressure resolution typically about 10kPa (Novel GmbH, Germany) (Section 2.2.3).
3	Accuracy	<±5% RC	The accuracy of the system should be comparable, if not better, than those typically found in commercially available pressure plates (Novel GmbH, Germany) (Section 2.2.3).
4	Frequency Response	Error of <±5% RC below 75Hz	<p>The frequency response of the sensor should reflect the ability to adequately pass the frequency content of the input load signal in walking with minimum error – accuracy not less than that stated in #3 above.</p> <p>Data previously reported has indicated that foot contact transients were reported to be around 75 Hz (Harris et al., 1996) (Section 2.3.1).</p>
5	Hysteresis	<±3% RC	Comparable to commercially available pressure plates of 7%RC (Tekscan Inc., USA). (Section 2.2.3).
6	Non-linearity	<3% RC	Comparable to commercially available pressure plates of <3%RC (Novel GmbH, Germany) (Section 2.2.3).
7	Combined error	<3% RC	Hysteresis and non-linearity (see definition in Appendix A).
8	Signal noise	<10kPa	<p>Error caused by electromagnetic interference and other noise sources.</p> <p>Signal noise should not deteriorate the measurement resolution (#2) of the device.</p>
9	Cross-talk	<5%RC between all channels	Comparable to the triaxial load distribution measurement device current found in literature (Davis et al., 1998) (Section 2.2.3).
10	Error due to off-	<5%Reading	Comparable to the triaxial load

	axis loading		distribution measurement device current found in literature (Davis et al., 1998) (Section 3.2.4.2).
11	Repeatability	<10kPa	Agreement between the readings of successive measurements of the transducer output. This should agree or better than the measurement resolution (#2) of the device.
12	Drift/Creep	<5% Reading in 10 seconds	The device is intended for gait analysis. However, potential static loading conditions would be likely if subjects were to stand on the device before each walking trial. The author foresees a static condition of ~10 seconds before/after each trial. Moreover, rapid creep characteristics of commercially available pressure measurement systems tend to occur within 10 seconds after the load was applied (Hachisuka et al., 1998). This value should be comparable to other sources of error, such as #10 Error due to off-axis loading.
13	Temperature sensitivity	<10% Reading between 10°C to 40°C	A working temperature range of 10°C to 40°C is typically found in commercially available pressure plates (Novel GmbH, Germany)(Section 2.2.3). Temperature effect of up to 10% error was considered to be acceptable for in-shoe force measurement (Razian and Pepper, 2003). 1% error per 1°C increase in temperature can be expected from a commercial pressure system (Hachisuka et al., 1998) and more than 10°C change inside the shoe may be expected (Cruickshank et al., 2007).
<u>Category B: Hardware</u>			
14	Sampling frequency	≥200Hz	Commercially available pressure mats can sample up to 100Hz (Section 2.2.3). Ideally, sampling frequency should

			exceed 200Hz to capture loading transients associated with foot impact activities (Nevill et al., 1995) (Section 2.3.1).
15	Power consumption	<22W	<p>This requirement is more specific in the design of in-shoe load transducers. For safety, it should be noted that large currents should be avoided for in-shoe transducer systems. Power consumption should be kept as low as possible for mobile devices.</p> <p>The device should continuously operate for at least 30 minutes. A typical 9V, 1200mAh Lithium battery estimated to provide about 11W per hour, therefore 22W for 30 minutes.</p>
16	Multiplexing capability	1:1 raw output to load output	<p>720 transducer elements (each with a sensing area of 10×10mm) are required to cover an sensing area of 300×240mm. Visual targeting a force measurement platform of this size had minimal effects on force parameters (Wearing et al., 2000).</p> <p>The outputs from each transducer element in the array must be multiplexed to minimise the final size of the device. Ideally the transducer should only produce 1 voltage output for 1 axis load reading, so the number of multiplexer circuits can be minimised.</p> <p>If software processing is required instead of electronic hardware, computation of load should be manageable via a laptop computer with typical specifications.</p> <p>A complete pressure distribution platform costs around £65000 (Novel GmhH, Germany). Therefore, each transducer element should cost <£18 for an economically desirable multi-axial system (assuming 80% cost towards external electronics and computers, and total 720 elements in an array).</p>
17	Computational requirements	Laptop friendly	
18	Hardware Cost	<£18 per transducer element	

<u>Category C: Physical requirements</u>			
19	Transducer sensing surface area	$\leq 10 \times 10\text{mm}$	Previous study have shown that minimal underestimation of load can be expected from a transducer size of $10 \times 10\text{mm}$ (Davis et al., 1996)(Section 2.2.4).
20	Transducer thickness	$\leq 5\text{mm}$	Although transducer thickness of 10mm has been used for in-shoe applications (Cong et al., 2011), other experimental transducer designs were no thicker than 4mm (Section 2.2.3). This requirement is more specific in the design of in-shoe load transducers.
21	Suitability for in-shoe applications	YES	An ideal transducer would be suitable for both in-shoe and measurement on the ground. Method for load measurement inside the shoe could also be used to form a platform system (Section 2.2.3).
22	Easy to mount/wear	YES	This requirement is specific to the design of discrete in-shoe load transducers. External signal conditioning circuits that might be required to be worn by the user during use must not affect the gait of the user. Transducer and cabling should allow easy in-shoe mounting.
23	Transducer sensing surface allowable movement	$< \pm 0.75\text{mm}$	This will directly affect the gap size between adjacent transducers in an array configuration. The gap between each transducer, however, should be minimised to avoid pinching of the plantar tissue (for user's safety and comfort) and to allow good spatial resolution in the load data. The current 'gold standard' device for triaxial load distribution measurement (Davis et al., 1998) (Section 2.2.3) has a spacing of 1.5mm between adjacent transducers, and did not have the problem of pinching the skin during use (B.Davis, Cleveland USA, pers. comm.). Hence each transducer could move

			±0.75mm.
24	Spatial Resolution	>1 transducer per 11.5×11.5mm area	This condition directly relates to #19 and #23. Currently, pressure plates have a spatial resolution from 1 to 4 elements per 10×10mm area (Novel GmbH, Germany) (Section 2.2.3).
25	Reusability and Life span	Year(s)	Life span of the device should be more than a year if the chosen load sensing technology is not economically desirable to be disposable after >1 use. Some commercial pressure distribution measurement system was found to have a life span of only 30 gait cycles (Nicolopoulos et al., 2000)
<u>Category D: Manufacturing requirements</u>			
26	Batch production	Fast and low-cost	Cost and time required to manufacture and assemble a large transducer array is important. It is not desirable to have each transducer element manufactured by hand.
27	Matrix arrangement capability	YES	For load distribution measurement, transducer elements should be mountable next to each other.
28	Cabling	≤5 wires per transducer	This condition directly relates to #16. Ideally each transducer should have less than 5 wires (1 wire per load output plus 2 wires for power), unless the multiplexing technique (#16) allow overall fewer wires.
Note: RC = Rated Capacity			

Chapter 3

Existing methods for load sensing

In developing a load measurement device, it is useful to understand the basic operation of the load sensing technologies to be used, their advantages and their limitations. This chapter presents a literature review of current methods used in load sensing with specific emphasis on the area relevant to this research, particularly in electronic technologies for the measurement of plantar foot forces. Given the system design requirements (Section 2.4.1), approaches that cannot record temporal loading events were not considered. Interested readers are directed to a comprehensive review of non-electronic load measurement methods (Urry, 1999). There are many techniques for load sensing and they are used with instrumentation of varying complexity. Although it is not within the scope of this thesis to provide a comprehensive description of all load sensing principles, relevant background is given when appropriate. The purpose of this chapter is to explore, review and thereto identify potential techniques that could be used to develop a low-cost multi-axial load measurement system.

3.1 What is a load measurement device

‘Load’ is a term frequently used in engineering to refer to ‘any type of force’ exerted on a surface or body (Section 2.2.2). A load measurement device, or load ‘transducer’, is a device that provides an output quantity that is directly related to the parameter being measured, force or pressure in this case. When external load is applied to a stationary object, stress and strain are the result. Stress is the object’s internal resisting forces, and strain is the amount of deformation per unit length of the object when a load is applied. Therefore, by definition, any matter can be calibrated as a mechanical load transducer if one is able to measure its deformation under loading conditions.

Unfortunately, minute deformation (submillimeter) can be physically challenging to quantify. However, some materials when subjected to load would change other physical quantity other than its physical dimensions. For example, the electrical resistance of copper wire is directly related to its dimensions, thus copper can be seen as an electrical resistive-based load transducer. Materials which have a physical quantity that is easier to detect than its deformation may only withstand very small load before failing. However, it might be possible to develop a new load transducer by combining different transducers with these attributes as one. For example, copper wire could be bonded on a stiffer load-responsive material to be used as an electrical load transducer - provided there is a mean to measure the changes in its electrical resistance as the combined transducer is subjected to load.

A transducer may have a physical quantity that may not be understandable to the user. In that case, a ‘sensor’ is required to measure such physical quantity and converts it into a signal that is readable by the observer or by an instrument. Typically, such a signal is electrical, but optical, hydraulic, and auditory signals are not uncommon and they all, in turn, could be converted to electrical data.

As the current study was aimed at developing a novel device, it was necessary to keep an open mind and considered any approach that could potentially allow continuous load measurement. For the purpose of this thesis, a load measurement

device was operationally defined as any physical quantity detection device, comprising of a transducer or a combination of transducers, that is sensitive to said load-responsive physical quantity, and if necessary with a sensor, connected to the output of said transducer as input and converts it into an electrical signal which can be read and stored by an instrument continuously.

3.2 Electrical resistive based transducers

This section explores and provides a critical assessment of load measurement techniques that use electrical resistive-based components.

3.2.1 Principle of operation

Load measurement devices based on electrical-resistive principles are often classified into two categories: 1) strain gauges, and 2) force-sensing resistors. All strain gauges are piezoresistive – their resistance changes in response to mechanical stress. To avoid confusion, the term "strain gauges" is used throughout the text to refer to foil strain gauges only; the term "piezoresistive" is used to refer to any other devices or material that exhibit the same behaviour.

Strain Gauges

There are various types of resistive strain gauges that can be used to measure the strain experienced by an object with the application of load. Fundamentally, all resistive strain gauges are designed to convert mechanical motion into an electronic signal. Foil strain gauges are based on Ohm's law and consist of metallic wire in a zigzag grid pattern (Figure 4). A tensile strain would cause the wire to elongate and become thinner, and consequently increases its resistance. Conversely, a compressive strain causes a decrease in resistance. If such a metallic wire grid is typically bonded to an elastic structure element under strain then the change in resistance could be measured and be calibrated to measure load. The zigzag grid pattern maximises the

amount of wire subject to strain parallel to the grid length (Figure 4). As such, accurate positioning of strain gauges is paramount to accurate load measurement.

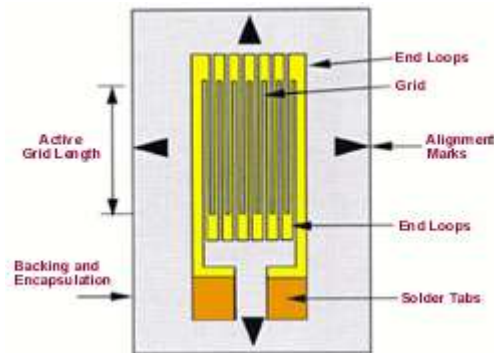


Figure 4 - A typical foil type strain gauge. (Image reproduced from <http://www.sensorland.com/HowPage002.html>)

A foil strain gauge usually consists of a metal foil pattern on an insulating flexible backing (Figure 4). Usually the backing is marked to allow the gauge to be installed appropriately aligned with the strain field. Typical backing materials include epoxy, which also provides electrical insulation between the foil and the elastic structure element. Gauges are usually manually bonded to structures using adhesives, but some are manufactured backed with an adhesive layer to reduce time in assembling. The use of a bonding agent, however, unavoidably influences the strain transmission from the structure to the gauge.

Thin-film strain gauges are a type of resistive strain gauge that eliminates the need for adhesive bonding. The strain gauge is molecularly bonded to the underlying deformable structure directly by thermal evaporation or sputtering techniques (Witt, 1974). The manufacture of thin-film strain gauges may be accomplished by laying down many layers. In its simplest form, an electrical insulation layer would first be deposited onto the structure's surface, and then a thin-film of metal is deposited onto this insulating layer. Thin-film strain gauges are relatively more cost effective in batch productions than foil gauges due to the manufacturing techniques involved.

In contrast to other resistive strain gauges, semiconductor strain gauges are based upon the piezoresistive effects of the gauge material, such as silicon. The bulk resistivity of a piezoresistive material is influenced by the applied mechanical stress.

Hence, when a semiconductor strain gauge is unloaded, its resistance is very high. This type of gauge is relatively small and less expensive than foil-type gauges, and they exhibit higher unit resistance and sensitivity. The gauge factor (K) is a measure of the change in resistance (R) for a given strain: $K = \frac{\Delta R/R}{\Delta L/L}$, where ΔR is change in resistance from its unstressed resistance value (R), and ΔL is change in length from its original length (L). The gauge factor is typically 100-150 for a semiconductor strain gauge and 2-4 for a foil type strain gauge. Although semiconductor strain gauges exhibit negligible creep and hysteresis, they are non-linear with strain and sensitive to temperature changes (National Physical Laboratory, 2010).

Force-sensing resistors

Force-sensing resistors (FSR) are made of polymers that exhibit the piezoresistive effect. FSRs vary in design, but a typical FSR consists of a polymer that contains both electrically conducting and non-conducting particles which are encapsulated between two electrodes (Figure 5). Applying a load causes the conductive particles to contact each other and the electrodes, thereby decreasing its resistance. The manufacturing of FSR is very cheap as the conductive polymer or ink can be applied to substrates by screen printing. FSRs are also very small in size with thickness typically less than 0.5mm. However, FSRs have low precision (~10% reading) and could be damaged under prolonged loading conditions.

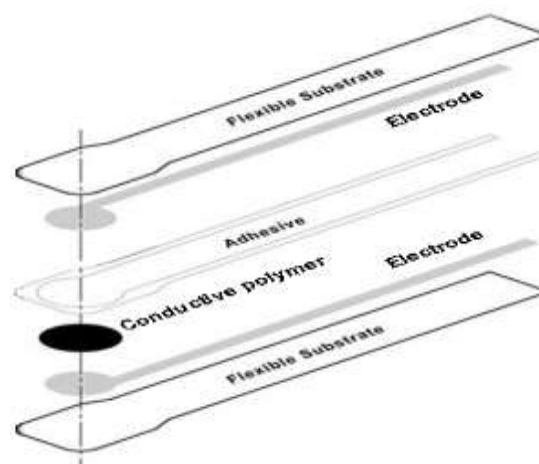


Figure 5 - Typical construction of a force-sensing resistor. (Modified image from www.tekscan.com)

3.2.2 Signal conditioning

As with all resistive based transducers, the change in resistance due to external load is often very small (micro-ohms). Resistive transducers, whether strain gauge-based or FSRs, are often connected to a Wheatstone bridge circuit along with other signal conditioning electronics that provide amplification to convert the resistance change into a voltage output suitable for external data collection systems. Signals from resistive-based transducers are usually small (in millivolts) and their transmitting systems require substantial insulation from external noise. Figure 6 illustrates a typical quarter Wheatstone bridge circuit connected with an active strain gauge. Assuming the resistance value $R = R1 = R2 = R3 = R4$, and that the active strain gauge resistance varies from R to $R + \Delta R$ due to the induced strain, the output voltage ΔV due to the strain is given as $\Delta V = \frac{\Delta R}{4R + 2\Delta R} E$, where E is the excitation voltage. The output voltage is then often fed to a signal conditioning circuit for further amplification.

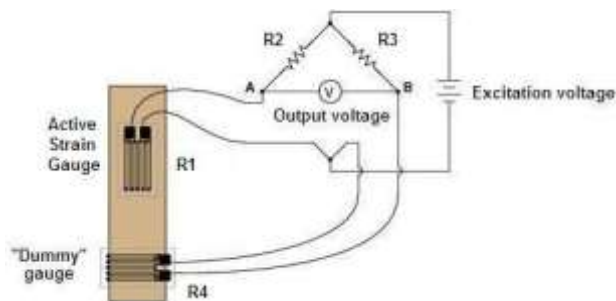


Figure 6 – A quarter Wheatstone bridge circuit to measure strain and provide temperature compensation using the addition of a ‘dummy’ strain gauge. (Modified diagram from <http://www.allaboutcircuits.com/worksheets/bridge.html>)

There are three types of Wheatstone bridge configurations: quarter-bridge, half-bridge, and full-bridge. The number of active gauges, that is 1, 2 and 4 active elements, determines the kind of bridge configuration, respectively. Each configuration has its own advantages and limitations. The quarter-bridge is simple in design and only requires the installation of one strain gauge therefore saving space and installation time. Due to the quarter-bridge circuit arrangement, a load transducer would produce non-linear outputs for the changes in resistance. A ‘dummy’ resistor is required to form a half-bridge for temperature compensation (Figure 6). The active

element should be mounted in the direction along the strain field, whereas the dummy gauge is mounted in close thermal contact but not directly on the specimen or usually mounted perpendicular to the principle axis of strain. Strain gauges are often installed at various locations on the structure specimen, thus wire management could be physically challenging for a full-bridge configuration within a miniature load transducer. That said, full-bridges are often chosen for their superior performance in terms of high sensitivity in strain, allow temperature compensation and can be configured to reject side loads or other loads that are not along the principle axis of strain.

3.2.3 Transducer construction

The construction of a uniaxial load sensing FSR is relatively simple (Figure 5). On the other hand, strain gauges must be bonded or constructed on to the surface(s) of an elastic structure. The geometric shape of the structure and its material properties determine the magnitude of the strain field produced by the external load, hence the sensitivity of the load sensing system. Materials such as steel or aluminium are often chosen for their robustness and their linear relationship between stress and small strain. The design of the structure and the precise locations of the strain gauges are paramount to minimise the effect of cross-talk for accurate load measurement. Precise installation of foil gauges is time consuming and wiring between active gauges could be physically challenging particularly if full-bridge circuits were used (Section 3.2.2). Moreover, bulky amplifier circuits are also required, which are often connected externally to the transducer.

3.2.4 Current state-of-the-art

Strain gauges are frequently found in the heart of commercially available load cells and pressure transducers. These systems typically have a sampling rate greater than 1kHz, and an accuracy and non-linearity better than 0.05% (FUTEK Advanced Sensor Technology Inc. USA). Commercially available triaxial force/moment load cells have previously been instrumented beneath shoes to measure ground reaction forces (Faber et al., 2010, Liedtke et al., 2007, Schepers et al., 2008, Schepers et al., 2009, Veltink et al., 2004, Veltink et al., 2005). The increase in height and the total

weight of the shoe associated with attachment of the transducers, however, represent major limitations of such an approach. Moreover, this technique is not suitable for measuring load distribution (Figure 7).



Figure 7 - Picture of an instrumented shoe with two triaxial force/moment transducers beneath the heel and the forefoot. (Image reproduced from Schepers et al., 2008)

Many experimental transducers designed for specific applications have also utilised strain-gauge technology. The Department of Bioengineering has extensive experience using strain gauges in the construction of 6-components load transducer for the biomechanical analysis of lower limb prostheses (Magnissalis et al., 1992). Similar devices have also been used in full-bridge configuration to measure triaxial force on prosthetics during amputee gait (Berme et al., 1976). Others have instrumented beds and seats (Goossens et al., 1993) as well as robotic grippers (Kim, 2007b, Kim, 2007a, Kim et al., 1999, Kim et al., 2008) with strain gauges to measure interactive forces. These devices tended to be relatively large in size ($>74\text{mm}^2$) and required larger numbers of strain gauges (>8 gauges) for accurate measurement of triaxial load. Despite accurate construction of the transducer structure and precise installation of the gauges, output error from strain gauge-based transducers may increase >16 fold (from 0.2% to 3.3%) when a combined load is applied to the transducer rather than when load is applied along only one axis (Hirose and Yoneda, 1990).

Miniature resistive-based transducers are usually constructed using gauge materials that exploit piezoresistive characteristics (Katragadda and Xu, 2008). These materials have been integrated on cantilever beam structures and connected into Wheatstone bridges for triaxial load measurement (Cranny et al., 2005, Jin and Mote, 1998). A flexible circuit, housing a 2×2 transducer array in a $10\times 10\text{mm}$ space, capable of

triaxial force measurement has been demonstrated (Beccai et al., 2005). Although the device was intended for measurement of triaxial forces at the stump-socket interface of a prosthetic device, it was only tested up to loads of 2N which is significantly lower than the expected load under the plantar surface of the foot (Section 2.3). Others have developed similar piezoresistive-based devices for shear measurement of loads up to 40N (Lin and Beebe, 2002, Wang and Beebe, 2000). However, the size and number of wires required for each transducer element were large in comparison to the sensing surface of the transducers themselves (Figure 8), which would limit the spatial resolution of a potential array of transducers. As a result, the design is not suitable for incorporation with an array for load distribution measurement. Moreover, it can be difficult to avoid exposure to humidity to a piezoresistive micro-electromechanical transducer system (MEMS) during use, in particular for in-shoe applications. Moisture vapour entering through gaps in the transducer could condense as liquid droplets. The capillary force due to surface tension caused by the droplet could cause damage or bending forces to the transducer micro-structure resulting an unacceptable voltage shift (Chiou et al., 2003).

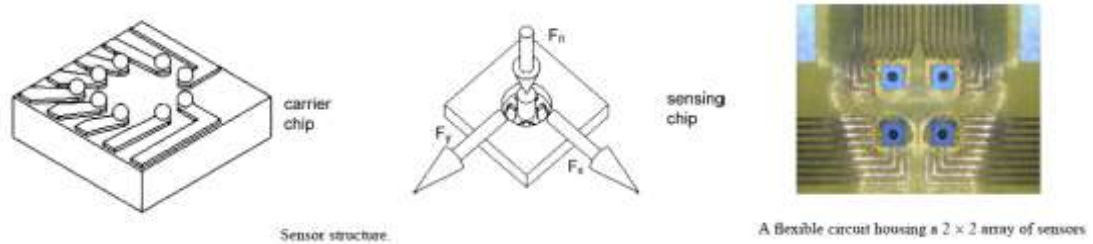


Figure 8 - The piezoresistive based 3-axial force sensor by Beccai et al. (2005).

Conducting polymers which display piezoresistivity have been deposited onto plastic substrates to form FSRs (Section 3.2.1). These polymers can also be used to coat on fabrics (Calvert et al., 2007, Campbell et al., 2007) or can be directly knitted into fabrics (Huang et al., 2008a, Huang et al., 2008b) to measure loading. However, sensing performance of piezoresistive polymers has been shown to be inconsistent due to cracking of the polymer surface and non-predictive contacts between conducting fibres within the textile (Calvert et al., 2007). Moreover, polymer-coated

transducers often display inherent instability with changing environmental conditions such as temperature, humidity and deteriorate following long storage period (>9 months) (Campbell et al., 2007, Li et al., 2005). Nonetheless, polymer-based plantar pressure distribution measurement systems are commercially available for use in gait laboratories. These systems are discussed further in the following sections together with other existing resistive-based devices suitable for multi-axial plantar load measurement.

3.2.4.1 AMTI strain gauged systems

Force platform systems from AMTI Inc. (USA) are capable of measuring 6-component forces and are currently regarded as one of the ‘gold standards’ force measurement tools which have been used extensively to measure ground reaction forces in gait analysis (Bhatt and Pai, 2009, Bisiaux and Moretto, 2008, Yung-Hui and Wei-Hsien, 2005, Tsai et al., 2007). These platform systems use strain-gauge technology for load sensing. These platform systems have often been used as the reference to test the accuracy and reliability of other load measurement systems (Low and Dixon, 2010, Chesnin et al., 2000, Catalfamo et al., 2008, Davis et al., 1998, Veltink et al., 2004, Clark et al., 2010). These force platforms are typically large in size (600×400×83mm) and, as such, are not suitable for in-shoe applications. But because of their build quality, their characteristics would give an indication of the level of reliability that one may expect in a strain gauge-based load measurement device. As specified by the manufacturer, their systems typically can measure shear in the order of 1000N and vertical load of 2000N with <2% crosstalk between all channels and a natural frequency of ~400Hz. Their systems also have minimum hysteresis ($\pm 0.2\%$) and non-linearity ($\pm 0.2\%$).

3.2.4.2 Davis’ strain gauged system

Davis’s group at the Cleveland Clinic Department of Biomedical Engineering (USA), has developed a strain-gauge based device for simultaneous measurement of vertical pressure and the anterior-posterior (AP) and medial-lateral (ML) distributed shearing forces under the plantar surface of the foot (Davis et al., 1998). The

platform measurement system consisted of 16 individual transducers arranged in a 4×4 array to measure the distribution of loads beneath the foot. As with other strain-gauged devices, it relied on a mechanical structure: in this case 16 hollow cylindrical aluminium columns, each fitted with two sets of T-strain gauge rosettes, and within each set four rosettes are equidistantly spaced around the column for AP and ML shear measurement. An ‘S’-shape cantilever instrumented with four rosettes was fitted on top of each column to measure compressive forces (Figure 9). Each transducer was anchored to a 20mm thick aluminium base plate. The sensing surface area of each transducer measured 25×25mm with 1.5mm spacing (Figure 9). The overall thickness of the system was approximately 160mm.

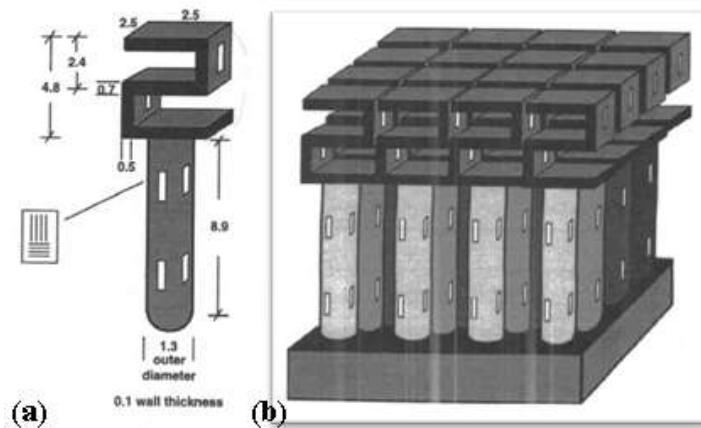


Figure 9 - Davis's pressure and shear measurement device. Schematic representation of the transducer (a), and the fully assembled device consisting of 16 transducers in 4×4 array (b). All measurements are in centimetres. (Images extracted from Davis et al. (1998))

A full Wheatstone bridge configuration was used for all strain gauges, four bridges for shears and two bridges for vertical pressure on each transducer. The authors used 32 multiplexors and 16 analogue-to-digital converters to sample all 96 bridges. The resonant frequency of the unloaded device was reported to be 350Hz. The system had a sampling frequency of 37Hz but could record for 2 seconds only. Although the reason for the short limited recording capacity was not published, it is likely that memory storage and the speed of the electronics used restricted the amount of data that could be acquired. Such limitation restricted the loading responses that could be investigated during gait. Moreover, the size of the external signal conditioning circuit was not published, but is expected to be large and consume considerable power.

The overall sensing surface (105×105mm) of the array was not large enough to cover the entire plantar surface. Recently, the system has been improved and now consists of 80 transducers arranged in an 8×10 array (Figure 10). The structure of the transducers remained the same (Figure 10), but the size of each transducer was decreased from 25×25mm to 10.27×10.27mm (Yavuz et al., 2007a, Yavuz et al., 2007b), thereby improving the spatial resolution of the system. However, the overall size of the device still restricted the area of analysis to only a portion of the foot. Although it was not a critical requirement for a platform system, the overall thickness of their new system was not published. The method of securely mounting each transducer in position within the array was not described. Due to the large number of wire connections required for the many (six) Wheatstone bridges on each transducer, wire management for the system though not discussed was likely to be difficult (Figure 10). Manufacturing time and costs for the construction of the device was “exorbitantly expensive” (B.Davis, Cleveland USA, pers. comm.).



Figure 10 - Davis' new pressure and shear system. The fully assembled device consisting of 80 transducers in an 8×10 array (top left). The wire connections beneath the system are illustrated (top right). A single transducer (bottom). (Images reproduced from Davis (2010))

Each transducer in the array was statically calibrated with compressive and shear loads up to 165N and 67N, respectively. A representative transducer in the array was tested under multi-axial loads against a commercially available strain gauge-based

load cell. On average, a difference of 3N, or 5% of the applied load, was found under dynamic loading conditions. Hysteresis was determined to be $\pm 7.4\%$. Point-loading tests at extreme corners of the transducer resulted in the greatest error (3.8N), which equated to 14% of the applied load measured at the centre of the transducer (27.2N). Average cross-talk in the shear channels was 5.2% (3.2N) of the applied vertical load, while average cross-talk on the vertical channel was 13.3% (4.8N) with AP shear, and 4.3% (2.3N) with ML shear. A maximum error of $\pm 12\%$ was observed on the compression channel when torsion force was introduced. The output of the transducer array was also compared to that of an AMTI force plate (Section 3.2.4.1) during clinical gait trials. Although the force profiles from each system appeared similar, results for each system were obtained from separate gait trials, and consequently could not be directly compared.

3.2.4.3 Goodyear's strain gauged systems

Although not designed for the field of biomechanics and gait analysis, a patent for a triaxial force pin sensor array was filed by The Goodyear Tire & Rubber Company (Triaxial force pin sensor array, US6536292 B1, 2003). Their design utilizes strain gauge technology to measure forces generated at the footprint of a car tyre. The transducer design was somewhat similar to Davis' system, with an 'S' shaped structure on top of a long column (Section 3.2.4.2). The Goodyear system differed primarily in its modular design, where stacks of transducers were combined as one module, to facilitate exchange of faulty transducers.

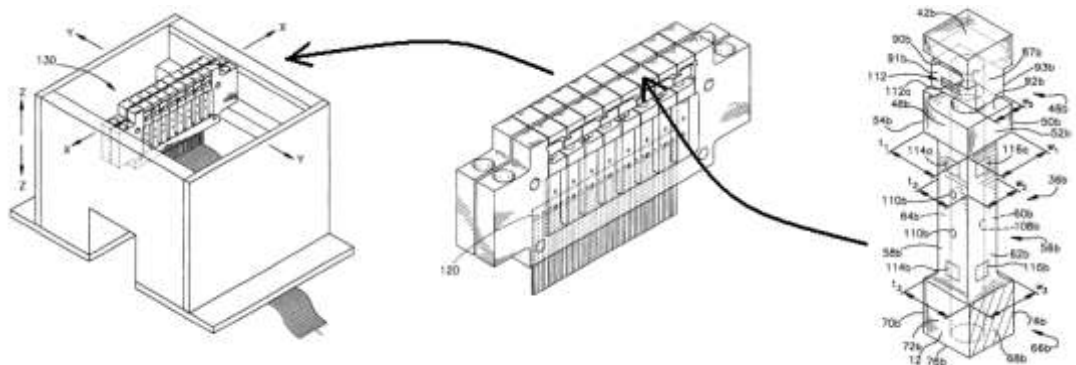


Figure 11: A modular design for a triaxial force distribution measurement system. (Figures extracted from Gary William Richards (2003))

3.2.4.4 Chen's strain gauged system

A gait platform described in Chen et al. (2010) allowed localised measurement of both the vertical and shear forces under any specific region of the foot during barefoot walking. The design principle of the force transducer was identical to that of the Davis' system described earlier (Section 3.2.4.2), and used strain gauges in combination with an 'S' shaped structure positioned on top of a long column (Figure 12). The gait platform had only one triaxial load transducer but incorporated a high-speed camera system, which by identifying a single anatomical landmark on the plantar surface of the foot, allowed for the determination of which part of the foot made contact with the transducer (Figure 12).

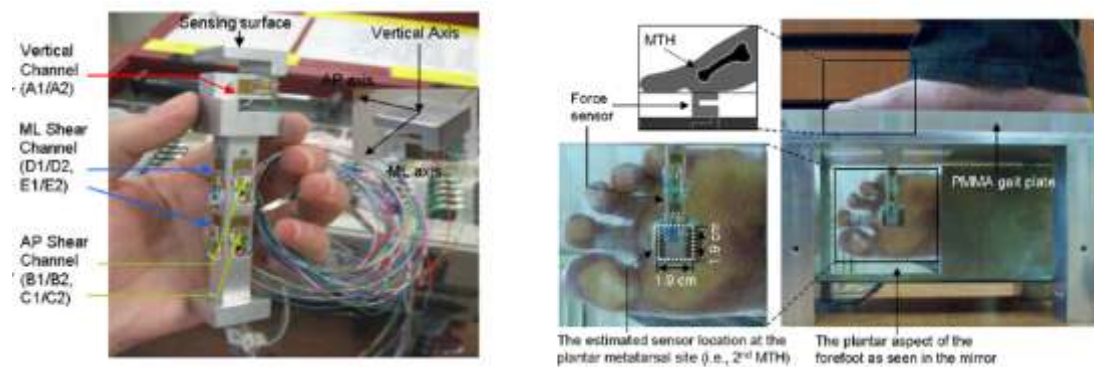


Figure 12 - Gait platform with single triaxial force sensor and high-speed camera. (Images extracted from Chen et al. (2010))

The transducer was fabricated using a single piece of aluminium bar with a flat top sensing surface of 19×19mm. 5 sets of strain gauges rosettes, in temperature compensating Wheatstone-bridge circuits, were bonded onto the sensor body to capture the triaxial forces independently. Transducer outputs were collected at a sampling rate of 100Hz. Calibration of the transducer in the vertical and shear axes was conducted dynamically using a material testing machine (Model 5848, Instron, USA), up to loads of 200N and 50N, respectively. Cross-talk effects were found to be less than 0.6% in all cases. Frequency response analysis revealed that transducer output was within 2% of the applied load up to 50Hz loading conditions.

3.2.4.5 Molton Corp.'s strain gauged device

The PREDIA is a commercially available device from Molton Corporation, Hiroshima, Japan. It is specified by the manufacturer that the PREDIA device is capable of measuring pressure and shear force simultaneously. According to their patent (Bedsores man-factor measuring device, US7090647 B2, 2006) which describes the underlying operation principle, the device is constructed by combining an air-filled pressure transducer on top of a strain gauge-based shear sensing transducer (Figure 13). The application of uniaxial shear load would move the top and bottom substrates of the transducer away from each other therefore pulling on the strain gauge (Figure 13). The concept of biaxial shear measurement using the same shear sensing principle has been described in the patent, however, their product only utilised a single strain gauge for uniaxial shear measurement (Figure 13). In the manufacturer's specifications it is stated that the PREDIA device is capable of measuring pressure from 0 to 150mmHg (± 2 mmHg), or 20kPa over an area of 36 \times 66mm, and 0 to 50N (± 1 N) shear over an area of about 80 \times 40 mm. The device has been used recently to investigate shear and pressure characteristics at the interface of wheelchair seat cushions (Akins et al., 2011). However, there is limited evidence of the characteristics of the system in the literature.

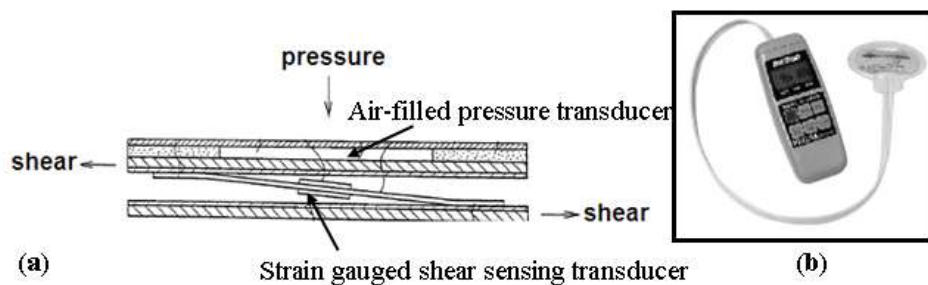


Figure 13 – The pressure and shear force transducer parts (a) and the completed PREDIA system (b).
(Modified images from patent file US7090647B2 and manufacturer's datasheet)

3.2.4.6 FSR-based systems

Force sensing resistors (FSR) are currently employed in numerous commercially available devices, specifically for uniaxial plantar pressure distribution measurement. These companies include, but are not limited to, Tekscan Inc. (USA), RS-Scan

International (Belgium), Paromed GmbH & Co. (Germany), Sensor Products Inc. (USA), and T&T Medilogic GmbH (Germany). The products vary from single discrete transducers to large arrays suitable for uniaxial pressure distribution measurement on chairs. FSR transducers, such as those from Tekscan Inc., are often manufactured using screen-printable polymer inks on substrates that are thin and flexible (Lowe et al., 2007). Large transducer arrays can be multiplexed easily by parallel conductive tracks orthogonally placed one over the other (Macellari and Giacomozzi, 1996). However, due to the total numbers of outputs, pressure distribution measurement systems often have a restricted sampling rate of no greater than 100Hz.

The performance of FSRs that utilise conductive elastomer is subject to mechanical creep (the gradual deformation of the substrate material under constant load) and, therefore, are not suitable for analysing forces under static conditions (Macellari and Giacomozzi, 1996). These transducers have also been shown to underestimate high impact and propulsive forces (Low and Dixon, 2010) due to their poor frequency response at high frequency loads. FSRs that use printable polymers, in contrast, often suffer from poor repeatability (Cobb and Claremont, 1995), poor accuracy (30% error) (Nicolopoulos et al., 2000) and are non-linear and have large hysteresis (Fernandes et al., 2003). Researchers have recommended that FSR users to estimate and calibrate the transducer with similar pressure level for more accurate results. Errors in measuring peak pressures, as large as 33.9%, have been shown with FSRs, leading some to suggest that calibration at the specific pressures to be recorded is required (Hsiao et al., 2002). Moreover, shear loading has been found to affect the accuracy of FSRs, with errors in the vertical pressure values increasing from 5.1% to 92% with prolonged shear loading (20N for 20 hours). This error could be reduced to only 2.8%, if compressive calibration of the transducer is done following the prolonged application of shear load (Hall et al., 2008). The elimination of shear sensitivity was believed to be caused by the permanent deformation of the polymer during prolonged shear loading (Hall et al., 2008). The sensitivity to compressive loads would also degrade after prolonged use of the transducer hence FSRs usually have a short life span of typically 30 gait cycles (Nicolopoulos et al., 2000). It should

be noted that these limitations apply to pressure mats and in-shoe systems for those manufacturers who utilities the same FSR technologies in both product range. To the best of the author's knowledge, there is no other document reporting any improvement on the life span typically experienced with FSR after Nicolopoulos' paper.

3.2.4.7 Noda's piezoresistive-based system

In theory, any uniaxial vertical load measurement device could be used to measure shear load instead if the device was placed on its side. In fact, this was recently demonstrated in a biaxial shear measurement system (Noda et al., 2006). The system had piezoresistive material deposited on silicone substrates, which essentially mimic devices for commonly used for vertical load measurement (Cranny et al., 2005, Jin and Mote, 1998). However, the substrates were then etched and fabricated as standing cantilevers. Orthogonally arrayed standing cantilevers were embedded in an elastic material (20×20×1.5mm) to allow biaxial shear measurement (Figure 14). A similar design was also used in a triaxial load measurement device (Huang et al., 2010), where the cantilevers were curved rather than straight. The sensitivity of such a transducer design would be heavily dependent on the characteristic of the elastic material (Noda et al., 2006, Huang et al., 2010). Moreover, the life span of such devices would be questionable due to the constant deformation of the cantilevers under loading conditions. It has been estimated that the transducer could be damaged after 300 times of repeated load or is subjected to stress above 150kPa (Huang et al., 2010), therefore the design is currently not suitable for gait analysis.

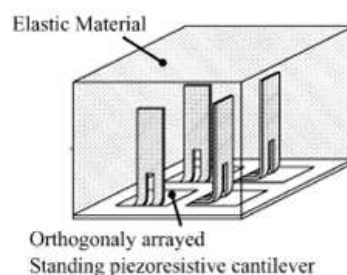


Figure 14 – Standing cantilevers with piezoresistor arrayed orthogonally for shear load measurement. (Image reproduced from Noda et al. (2006))

3.2.5 Critical review

As demonstrated previously in various experimental transducer designs and Molton Corp.'s commercially available device, it is clear that strain gauge technologies could be used in the design of a transducer that would meet the essential requirement of the current study – the ability to measure biaxial shear or triaxial load (Section 2.4.1).

In terms of transducer performance, strain gauge-based transducers constructed using metallic materials are robust, can withstand high loads and can perform linearly with load with low hysteresis and non-linearity. High levels of accuracy are also achievable even at high frequencies. Performances of piezoresistor or FSR-based systems, in contrast, are very much dependent on the substrate material on which the resistive substance is deposited and often have performance characteristics inferior to strain-gauged devices. While FSRs can be multiplexed easily, thus substantially reducing hardware costs, FSRs tend to suffer from poor repeatability, accuracy (~30% error) and exhibits nonlinear relationship with high hysteresis ($\pm 5\%$) compared to strain-gauged devices ($\pm 0.2\%$).

On the other hand, strain-gauged devices connected in Wheatstone bridge circuits may require relatively bulky external circuits. More physical space would be required for electrical connections between gauges to complete each Wheatstone bridge and routing to the amplifier circuits. The lower sensitivity of strain gauges compared to FSR systems may require higher quality amplifiers and higher power consumption. Although surface mount amplifier technologies may be available, the provision of power may be an issue for in-shoe measurement. However, the foil gauges themselves must not be permitted to bend during in-shoe measurement, otherwise there could be an output due to bending which will combined with that caused by the vertical or shear loads. This is true for all resistive based technologies including FSR.

In terms of the physical requirements, FSR or piezoresistor-based transducers can be readily made into miniature sizes suitable for in-shoe applications. Transducer sensing surface dimensions of less than 10×10mm would be readily achievable,

yielding a system with good spatial resolution. Although foil strain gauges are often installed on bulky structures for load detection, the dimensions of the gauges themselves are small and thin. A novel way of installing foil strain gauges would be required if it were to be used for in-shoe applications, otherwise, the thickness of the transducer would only be suitable for incorporation within a platform system. That said, relatively large transducers could facilitate easy handling and mounting. A modular system approach, such as that used in the Goodyear system, has the advantage of allowing rapid replacement of defective transducer elements and easy detachment for cleaning the gaps between elements to prevent dirt or contamination from affecting force measurement. Foil-gauged metallic transducers usually have a long life span. But due to constant deformation under loads, piezoresistor or FSR-based sensing elements are not suitable for prolonged load measurement and are subject to premature degradation in performance due to physical deterioration with repeated loading.

FSRs' suitability of being incorporated into arrays and the fact that they can be batch produced at low-cost matches the manufacturing requirements of the current study, but as mentioned above, they perform poorly in comparison to other resistive-based technologies. The transducer structure which the strain gauges or piezoresistors are adhered to has to be designed as to allow easy access and easy alignment during the installation of these sensing elements. Manual application of gauges is time consuming and therefore costly. Thin-films may be an alternative method but still would require complex wiring between gauges within the transducer structure and therefore would not be ideal for volume production. Therefore, strain-gauge technologies are not realistic alternative for the development of transducer array and are not suitable for in-shoe applications.

3.3 Piezoelectric based transducers

This section explores and provides a critical assessment on load measurement techniques that use piezoelectric-based components.

3.3.1 Principle of operation

In 1880, Pierre Curie and Jacques Curie demonstrated that surfaces of certain crystalline material will become electrically charged when subjected to mechanical stress (Arnau, 2008). These piezoelectric materials, therefore, can be used as a load transducer, if the electric charge generated with the application of load can be measured.

The ability of certain non-symmetric dielectric materials to generate an electric charge in response to applied mechanical stress is called the piezoelectric effect. The application of force to a piezoelectric material deforms its lattice structure. For example, in a quartz crystal, such deformation will result in a shift of its positively charged silicon and negatively charged oxygen ions. The shift in the centre of positive and negative charges, in turn, results in the generation of an electric charge between opposite faces of the crystal. The density of the charge generated on the surfaces of the crystal is proportional to the force exerted, and would disappear with it (Arnau, 2008). When tension changes to compression, the external electrical field changes sign (Figure 15).

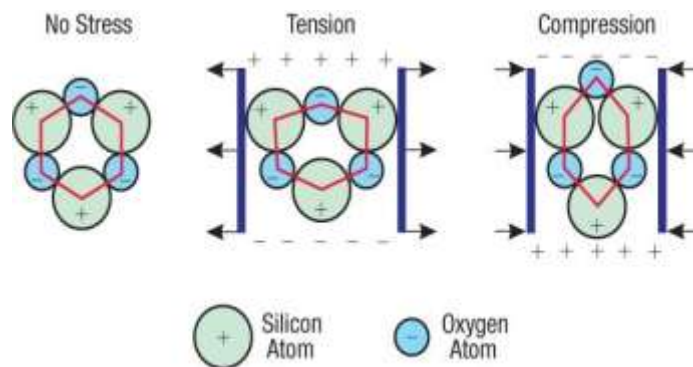


Figure 15: Piezoelectric effect in quartz. (Image reproduced from Brown (2001))

The piezoelectric effect only takes place if the applied stress acts along the polar axes of the piezoelectric material. For example in the case of a Quartz, depending on how it is cut or manufactured (Figure 16), three main modes of operations can be distinguished (Kistler.com, 2010):

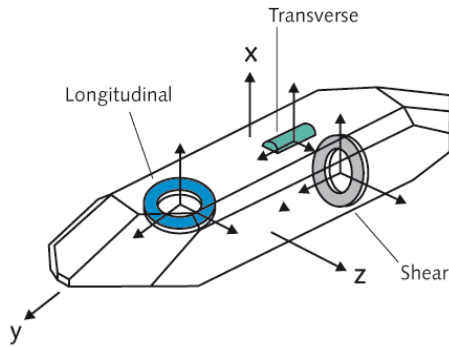


Figure 16: Ways of cutting a Quartz piezoelectric crystal. (Image reproduced from Kistler.com (2010))

Transverse effect: The charge output develops on the unloaded surfaces of the piezoelectric element, which is perpendicular to the direction of the applied force (Figure 17). The amount of charge generated is dependent on the geometrical dimensions of the piezoelement.

Longitudinal effect: The charge output occurs and can be measured from the surfaces to which the force is applied (Figure 17). The amount of charge produced depends only on the amount of force applied and not the dimensions of the crystal. Several piezoelements can be connected mechanically in series and electrically in parallel in order to increase the charge output.

Shear effect: The charge output develops on the loaded surfaces of the piezoelement (Figure 17). The amount of charge generated is dependent on the amount of force applied and not the dimensions of the piezoelement.

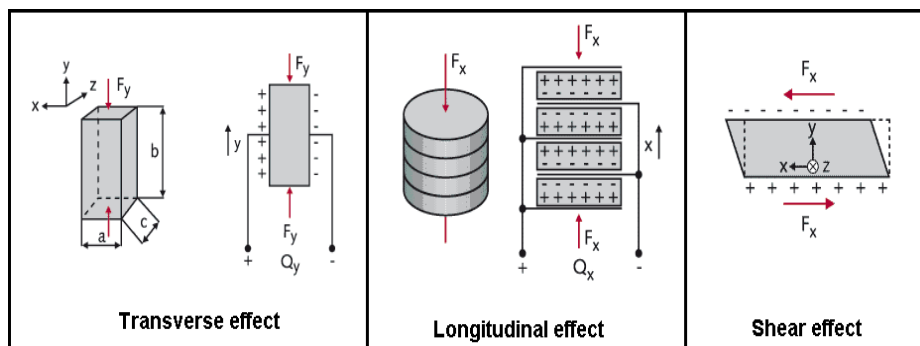


Figure 17: The three main modes of operation in piezoelectric material. Illustration of electrodes on the surfaces of the piezoelement where charges are generated and arrows indicates the directions of applied load. (Images extracted from Kistler.com (2010))

The Curie brothers first demonstrated that quartz crystal and Rochelle salt exhibited the most piezoelectricity ability. Naturally grown quartz crystals were the first commercially exploited material used in transducers for measurement, while scientists continued to search for materials with higher performance. Today, there are two main groups of materials used in piezoelectric transducers: 1) natural single crystal materials, and 2) man-made piezoelectric materials (Wharton, 2006). More detailed information on the different groups of piezoelectric materials can be found elsewhere (Barron, 2009).

Briefly, man-made crystals such as Gallium orthophosphate are similar to natural crystals in that sensing elements of different modes of operations can be manufactured out from a single crystal (Figure 16). Compared to natural crystals, man-made materials such as polycrystalline piezoceramics and polymers can be manufactured easily, in large quantities, and at low cost with an unlimited availability of sizes and shapes. However, they must undergo the poling process for the piezoelectric phenomenon to occur. An unpoled material consists of many randomly orientated domains and thus has no net polarisation. Application of a high electric field would force each dipole to orient in the field direction and the dipoles remain fairly aligned after the electric field has been removed leading to a permanent polarisation of the material (Sirohi and Chopra, 2000).

Piezoceramics can produce higher charge output since their sensitivity can be two times higher than those of single crystal materials (Wharton, 2006). Moreover, man-made piezoelectric polymers, such as polyvinylidene fluoride (PVDF), can be readily manufactured with mixed composition suitable for multi-axial load sensing (Kärki et al., 2009, Razian and Pepper, 2003, Sirohi and Chopra, 2000). On the other hand, natural single crystal materials have a much higher, almost infinite, long term stability and excellent temperature behaviour. Curie temperature for Quartz is about 550°C, whereas it is about 120°C for PVDF. Curie temperature is the temperature above which the material loses its piezoelectric behaviour.

Piezoceramics and piezoelectric polymers are not only piezoelectric but are also pyroelectric. The pyroelectric effect reflects the deformation of the lattice structure

of the material caused by a change in temperature. The additional charge associated with change in temperature, therefore, may confound load measurement. When comparing the potential performance of different piezoelectric materials it is therefore necessary to take into account both effects: quartz crystal does not exhibit pyroelectric effect like piezoceramics and polymers if they are cut in the appropriate way to avoid the axes that exhibit the pyroelectric effect, but piezoceramics and polymers exhibit greater (>100 times) piezoelectricity ability than quartz (Razian, 2000, Wharton, 2006).

3.3.2 Signal conditioning

Piezoelectric materials are active sensing elements – they required no power supply to operate and the electric charge generated can be collected via electrodes attached to the sensing element. Piezoelectric materials generate a charge only when force is applied to or removed from them. The amount of electric charge generated is proportional to the force acting on the material. The charge output is required to travel through the piezoelectric measurement chain before reaching a read-out device, such as a computer screen or a data recording device. The measurement chain consists of the actual piezoelement, a charge amplifier and the connection cables between these components.

Because no material can offer infinite electrical insulation, the charge output from the piezoelement that travels through the measurement chain would eventually leak to zero. In effect, when a static force is applied to a piezoelectric force sensor, the charge output initially generated will eventually leak back to zero yielding an inaccurate signal. The rate of this drift, or time constant, in the output signal is dependent on the lowest insulation resistance path in the measurement chain. It is also possible that a slow speed dynamic force becomes quasi-static and the charge leakage is faster than the rates of charge build up due to the changing force. Therefore, the time constant that determines the measurement limit or the low cut-off frequency of the device could deteriorate due to insufficient insulation. Environmental contaminants such as moisture or grease can reduce the insulation

resistance of connection sockets, therefore all cable connections must be kept as clean as possible.

Piezoelectric materials themselves are insensitive to electromagnetic fields and radiation, enabling measurements under harsh conditions. However, the electronics required for these materials to work can be sensitive to noise. In many cases, high impedance cables are required to minimise noise in the signal. Piezoelectric sensors require no offset even after frequent load cycles. The sensing element can be reset to zero prior to each new measurement process by discharging any electric charge generated by factors such as initial load. This automatically eliminates the effect of any static or slow changing mounting conditions without affecting the measurement accuracy.

There are two circuits commonly used for signal conditioning in piezoelectric sensors: 1) Voltage mode, and 2) Charge Mode. Both circuit designs serve the same general functions, which include: 1) conversion of the output to a useful low impedance voltage signal and 2) signal amplification. While more detailed comparison between the two modes of operation can be found elsewhere (Dytran.com, 2011, Karki, 2000). Table 2 summaries the typical configuration, advantages and limitations of each operation mode:

Table 2 - Typical configuration, advantages and limitations of charge mode and voltage mode piezoelectric systems.

<u>Charge mode system</u>	<u>Voltage mode system</u>
<p><u>Configurations:</u></p> <p>Output from the piezoelement is a charge and is routed to the signal conditioning circuits placed externally to the transducer via low-noise cables.</p>	<p><u>Configurations:</u></p> <p>Output from the piezoelement is modelled as a voltage source. Amplification and signal conditioning circuits are set close to the piezoelement, often built within the transducer housing.</p>
<p><u>Advantages:</u></p> <p>1. All electronics are placed externally to the transducer housing, allowing:</p> <ul style="list-style-type: none"> • The piezoelectric material to operate in harsh environments or at high temperatures 	<p><u>Advantages:</u></p> <p>1. High impedance circuitry is protected within the transducer, ensuring:</p> <ul style="list-style-type: none"> • Low impedance output signal from the transducer can be transmitted over long cables

<p>(>500°C is possible).</p> <ul style="list-style-type: none"> • Selective system characteristics, such as sensitivity and frequency range, via external switching components. • Dimensions of the transducer to be minimised. • Minimisation of the amount of cables. 	<p>through harsh environments with no loss in signal quality.</p> <ul style="list-style-type: none"> • Can function with ordinary cables eliminating the need for expensive low-noise cabling.
<p><u>Disadvantages:</u></p> <ol style="list-style-type: none"> 1. High impedance signal output <ul style="list-style-type: none"> • Requires signal conditioning prior to being recorded/analysed. • Greater potential to be contaminated by noise (includes triboelectric effect by cable movement, electro-magnetic and radio interference). 2. Requires external signal conditioner. 3. Requires high quality low-noise cabling. <ul style="list-style-type: none"> • Often cannot be repaired but must be replaced if damaged. • Expensive. 	<p><u>Disadvantages:</u></p> <ol style="list-style-type: none"> 1. Built-in electronics are sensitive to shocks; care must be taken to ensure they are not damaged due to high mechanical shocks at heel strike. 2. Electronics are within the transducer. <ul style="list-style-type: none"> • Increasing the overall dimensions of the transducer. • Requires power supply to the transducer – increasing the amount of cabling. • The characteristics of the transducer are fixed and are independent of supply voltage.

Although it is beyond the scope of this thesis to describe the different circuit configurations possible in different modes of operation (Karki, 2000), both voltage mode and charge mode transducers are essentially resistor-capacitor (RC) circuits. The schematic (Figure 18) indicates a simple RC circuit in charge mode.

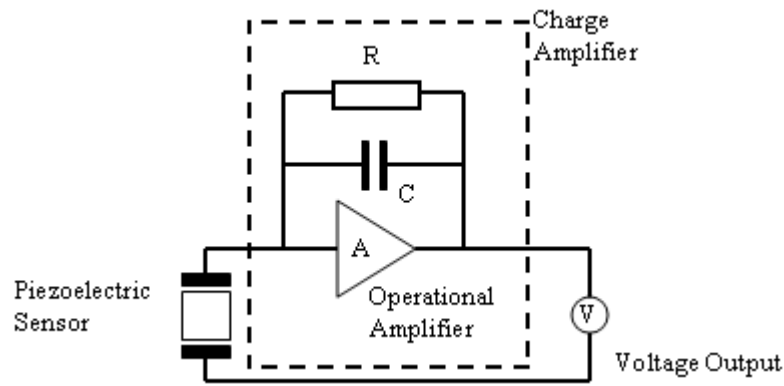


Figure 18 – A simplified model of a typical charge amplifier circuit.

The time constant (TC) of a RC circuit is determined by the product of the capacitor and the resistor: $TC = RC$. TC is defined as the time (in seconds) required for the transducer system to discharge its signal output to 37% of its original value. After a step input applied to the transducer, the charge across the capacitor immediately begins to discharge through the resistor and then follows the exponential RC discharge curve as shown in Figure 19. Typical values for the time constant range from less than 1 second to up to 2000 seconds (PCB Piezotronics, 2010).

$$q = Qe^{-t/RC}$$

where:
 q = instantaneous charge (pC)
 Q = initial quantity of charge (pC)
 R = resistor value (ohms)
 C = capacitance (pF)
 t = any time after t_0 (s)
 e = base of natural log (2.718)

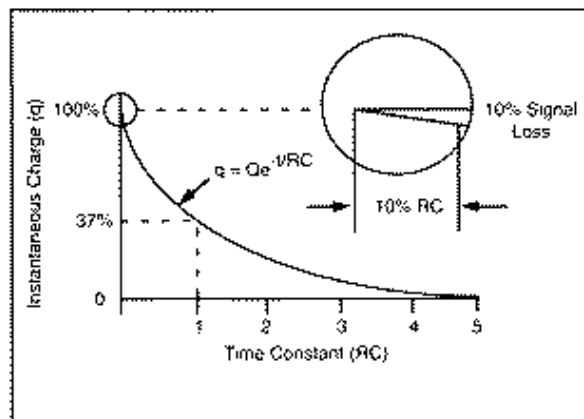


Figure 19 - The basic RC discharge curve. (Figures extracted from PCB Piezotronics (2010))

Due to the actual RC characteristics of an amplifier circuit, it can be understood that piezoelectric force transducers are not ideal for static load measurements (Mack, 2007). The general rule of thumb is that output signal loss and time elapsed over the first 10% of a TC have a one to one relationship. For a transducer with TC of 100 seconds, 10% of the original signal will have decayed over the first 10 seconds. For

1% accuracy, data should be taken in the first 1% of the TC, or 10% of the TC if 10% accuracy would be acceptable. Figure 20 graphically demonstrates the event with a square waveform input. If the static load was held, the signal output would naturally decay towards zero in approximately 5 TC. If the load was removed, the output signal would fall below the initial baseline reference point and eventually decay upwards toward zero until equilibrium in the circuit was observed (Figure 20). The magnitude of the fall below the initial reference point would be the same as the decay that occurred during static loading. This would result in a constantly changing baseline and therefore the absolute transducer output value could not be used as a direct measure of the applied load, unless an expensive charge amplifier and conditioning circuit was used to lengthen the TC thereby allowing quasi-static load measurements (Lord and Smith, 1983).

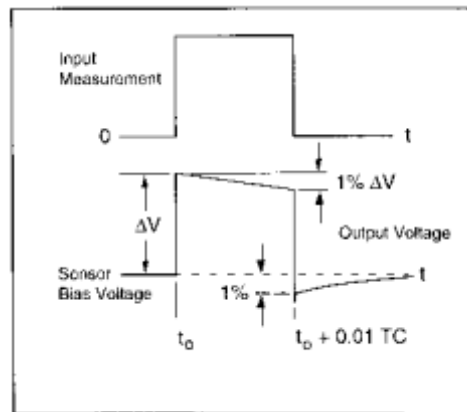


Figure 20 - Typical square function response from a piezoelectric-based transducer. (Figure reproduced from http://www.pcb.com/techsupport/tech_force.php)

3.3.3 Transducer construction

The construction of a piezoelectric load transducer can be very simple. A structure or a thin membrane could be used to guide and transmit the external load to the piezoelement (Figure 21). Since piezoelectric materials are active sensing elements they required no power supply to operate, but a power supply to the transducer housing would be required if it were to operate in voltage mode with electronics built within the transducer (Section 3.3.2). The electric charges generated are collected via electrodes attached on the piezoelement and fed to the amplifier and other electronic

circuits (Figure 21). The attachment locations of the electrodes on the piezoelement depend on the mode of operation of the piezoelectric material, whether the transverse effect, longitudinal effect or shear effect is utilised (Section 3.3.1). The active elements and electrodes are usually enclosed and protected from electromagnetic noise in a metallic housing (Figure 21).

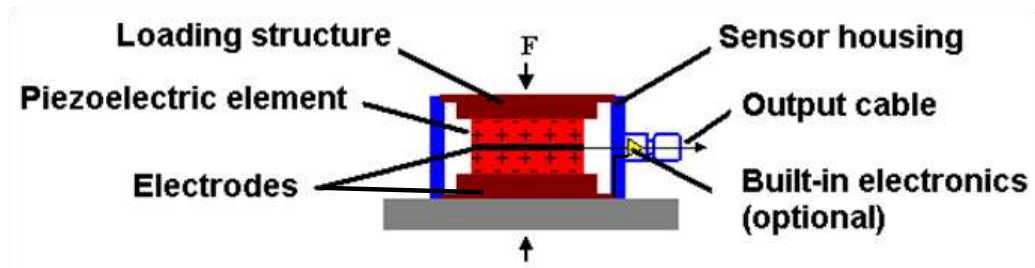


Figure 21: An example of the construction of a piezoelectric force sensor. (Modified diagram from Wharton (2006))

Although brittle, piezoelectric materials typically have a high modulus of elasticity and stiffness – in the order of $104e^9N/m^2$ (Wharton, 2006). In other words, piezoelements show very small levels of deformation when subjected to external load. However, as piezoelements are often thin in comparison to their cross sectional area, care must be taken when bending moments or other external load exists, otherwise the system would be prone to mechanical induced error (HBM, 2010). The high natural frequency and high load capacity enabled by the stiffness of piezoelectric material makes it ideally suited for dynamic measurements (National Physical Laboratory, 2010). However, charge leakage associated with piezoelectric circuits renders them less suitable for static measurements. While this effect can be negated, to some extent electronically, it requires expensive amplification and conditioning circuits (Section 3.3.2).

3.3.4 Current state-of-the-art

In 1969, Kistler Group (Switzerland) introduced the world's first piezoelectric 3-component force transducer. Triaxial force transducers can be manufactured by stacking a piezoelement sliced to exploit the longitudinal effect, together with two elements sliced to exploit the shear effect (Section 3.2.1). The charge from each

element is then collected via their individual electrodes inserted into the stack. Each piezoelement must be aligned precisely so that the orientation of the active axis coincides with the axis of the force component to be measured. Each piezoelement will produce a charge proportional to the force component specific to that particular element. Kistler's force platforms are capable of measuring 6-components of force and are currently regarded as one of the 'gold standard' devices. These systems have been used extensively to measure ground reaction forces in gait analysis (Shaw et al., 1998, Antonsson and Mann, 1985, Gefen et al., 2000, Giacomozzi et al., 2000) and have often been used as the reference to test the accuracy and reliability of other load measurement systems (Sumiya et al., 1998, Nicolopoulos et al., 2000).

Due to high stiffness of the piezoelectric crystal and the metallic transducer housing, the typical natural frequency of a Kistler transducer is of the order of 1000Hz, as specified by the manufacturer. The rated capacity of the transducers for vertical load is typically 17kN and ± 8 kN in shear loading. The cited non-linearity and hysteresis of the transducer is $< \pm 0.5\% RC$. However, like any piezoelectric-based system, outputs from Kistler's transducers exhibit drift even when connected to expensive charge amplifiers. The cited maximum drift in Kistler's amplifiers is 10mN/s and 5mN/s for the vertical and shear axes, respectively. Other commercially available piezoelectric transducers also exhibit output drift. Quartz-based transducers from HBM GmbH (Germany) have a maximum drift of 25mN/s (HBM, 2010). Triaxial piezoelectric force transducers from PCB Piezotronics (USA) have previously been used to measure pedal forces during recumbent cycling (Johnston et al., 2008). These typical transducers can typically measure 6kN vertical and 3kN shear forces, with a resolution of about 0.6mV/N and a time constant of 1000 seconds.

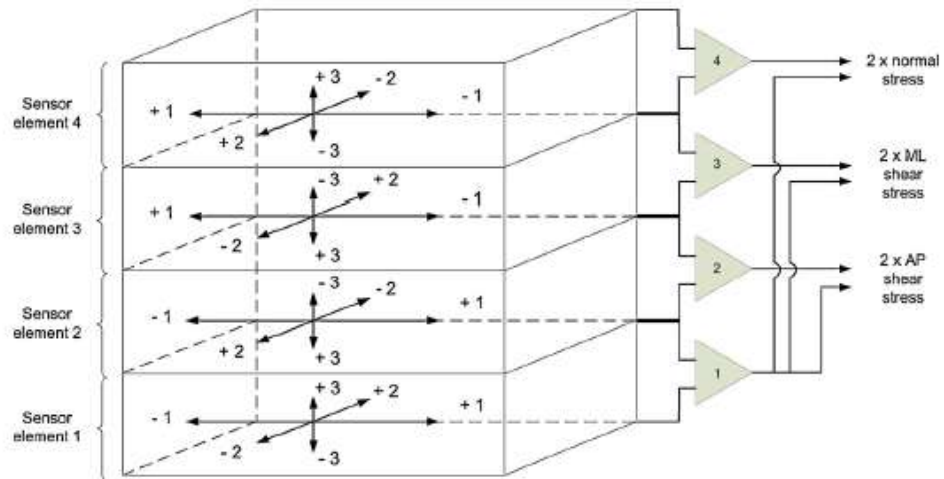


Figure 22 - Triaxial load transducer consists of 4 separate PVDF sensing elements. (Image reproduced from Kärki et al. (2009))

Quartz-based triaxial load transducers that use stacks of crystals can be used to measure heavy loads (3000kN) in applications such as shipbuilding (Li et al., 2009a, Li et al., 2009b, Li et al., 2009c). Large transducers and commercially available devices mentioned above usually have the piezoelement enclosed in a metallic housing for adequate protection from electromagnetic noise. Experimental miniature transducers that use a stack of four PVDF elements covered with plastic sheeting, also exist for triaxial load measurement (Kärki et al., 2009). The desired triaxial force signals, both vertical and two shear components, were obtained as difference signals between PVDF elements (Figure 22). The overall dimensions of the transducer were 30×30×2.4mm, and it was calibrated up to 4.5N (~5kPa) and 1.15N (~1.3kPa) in the vertical and shear directions, respectively. However, the calculated sensitivity values from the calibration were used to calculate the measurement at higher load (~165kPa vertical load and ~50kPa shear) in a preliminary subject trial. However, it was a preliminary prototype transducer with poor manual construction. Double-sided tape was used to attach each PVDF element together. Moreover, the accuracy of the measured data was not validated against a reference load measurement standard.

A flexible plantar pressure distribution measurement system consisting 64 piezoelectric sensing elements has also been demonstrated previously at the

Biomechanics Institute of Valencia (Martínez-Nova et al., 2007, Martínez-Nova et al., 2010). While each of the circular sensing elements was 5mm in diameter and 0.5mm thick, no published information is available regarding the characteristics and the construction of the device.

A more developed and reported in-shoe triaxial load transducer has been demonstrated by the research group at the University of Kent (Razian and Pepper, 1998, Razian and Pepper, 2003). The potential of an in-shoe uniaxial plantar pressure measurement system, utilising a single element of piezoelectric film, was first reported by the group (Nevill et al., 1995). The design was then modified for biaxial shear measurement (Akhlaghi and Pepper, 1996) and advanced to a tri-axial force transducer using a single copolymer film (Razian and Pepper, 1998, Razian and Pepper, 2003). The copolymer film had a mixed composition of PVDF and trifluoroethylene (TrFE) and was sandwiched between three printed circuit boards to form a complete transducer. The triaxial load transducer measured 13×13×2.7mm and operated in charge mode with an external charge amplifier (Nevill et al., 1995). To the best of the author's knowledge, the Kent's system is currently the only piezoelectric-based device consisting of multiple triaxial load transducers for measuring triaxial load under various discrete locations beneath the foot. The system was calibrated up to 700N for vertical and 400N for each shear axis under quasi-static loading condition. The average full-scale non-linearity was found to be of the order of 1%, hysteresis <2%, average crosstalk ~2%. Variation in temperature ranging between 30°C and 40°C was expected to introduce a maximum measurement error of about 2% (Razian and Pepper, 2003). The performance of Kent's system has been evaluated in the current study and is discussed further in Section 5.1.

3.3.5 Critical review

The utilisation of piezoelectric material in multi-axial force transducers have been well established for over 40 years. While quartz has been traditionally used, triaxial force measurement was only possible by using three piezoelements, each cut according to an identified crystal axis direction. Recently, however it has been shown that piezoelectric copolymers have properties that provide the potential to develop

triaxial load transducers with a single piezoelement. Although thin film of piezoelement may be difficult to mount or manually handle, transducer dimensions of around 13×13×3mm which is suitable for in-shoe applications have been demonstrated. Due to the stiffness of the piezoelectric material, negligible deformation of the transducer can be expected. Therefore, the gap between adjacent transducers can be minimised, potentially allowing high spatial resolution load distribution measurement from a transducer array. However, care must be given when working with PVDF and its copolymer. Copolymer is brittle and could shatter if bent. Additional bending will also introduce deformation which will in turn develop charge therefore generating false outputs.

The relatively stiff piezoelectric material would also ensure the system has a high natural frequency (of the order of 1kHz) that is suitable for measuring the foot strike transients. Other transducer performance requirements such as hysteresis (<2%), non-linearity (1%) and rated capacity (700N vertical, 400N shear) could also be easily achievable in a piezoelectric-based transducer. However, the accuracy of the device is highly dependent on the amplification circuit, as well as the quality of the transducer construction. Piezoelectric materials theoretically display zero cross-talk, however, imperfections in transducer construction could potentially lead to other stress being transmitted to the active element thereby causing erroneous results. Moreover, charge leakage associated with all piezoelectric systems requires relatively expensive amplifier circuits. The amplification circuit maximise the decay time constant and directly influences the low pass frequency response of the device. Although a relatively short time constant may be sufficient in a platform system for dynamic load measurement over the period of a single gait cycle, the time constant should be as long as possible for in-shoe applications when quasi-static conditions may be possible during testing. Moreover, sufficient insulation and protection from environmental contaminants along the whole piezoelectric measurement chain is paramount to avoid signal noise and deterioration in the time constant value.

In terms of hardware and manufacturing requirements, cables required per transducer can be minimised if the system was to operate in charge mode. However, the cost per transducer is typically very high due to the need for expensive low-noise cables.

Suitability for low-cost batch production and the capability for the transducers to be incorporated in an array are unclear and would require some novel solutions. Manual fixation of the piezoelement on the transducer structure and precise attachment of electrodes may be necessary. As such, the reliability and life span of the system would depend on the quality of the bonding of the piezoelement and the installation of wires. Any environmental contaminants such as dust and moisture could potentially alter the intended load transmission to the piezoelement thus causing output errors. Due to the RC characteristics of an amplifier circuit, the constantly changing baseline in the signal means that the absolute output value could not be used as a direct measure of the applied load. A circuit with a long TC (2000 seconds) would be possible but likely to be expensive.

3.4 Capacitive based transducers

This section explores and provides a critical assessment of load measurement techniques that use capacitive-based components.

3.4.1 Principle of operation

Capacitance has a unit of Farad (F) and is a measure of the ability of a system to store electric charge. A basic system consists of two conductive and electrically charged plates (electrodes) that are parallel and separated by an insulating dielectric medium (Figure 23). The capacitance C is given by $C = \epsilon A/d$, where ϵ is the permittivity of the dielectric, A the area of the overlapping area of the plates and d their distance. Therefore, there are three basic factors that determine the amount of capacitance in a system: 1) overlapping area of the plates, 2) the gap distance between the plates, and 3) the dielectric material used.

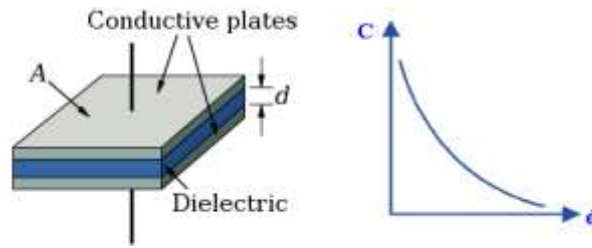


Figure 23 - A basic capacitor with a dielectric medium between two conductive plates, each of area A and with a separation of d . Graph showing the non-linear relationship between capacitance (C) and distance (d).

A simple load transducer can be realised by using an elastic material as the dielectric medium which separates the electrodes. With all other factors unchanged, when external load is applied to the assembly, the elastic layer deforms, which decreases the distance between the electrodes and results in a capacitance change proportional to the magnitude of the applied load. A load transducer could also work by allowing one of the electrodes to move with external load, thereby altering the overlapping area of the plates. In this case, the variation in the overlapping area of the plate would change the capacitance of the system. Alternatively, the dielectric material could be made movable between the two electrodes while other variables remain constant.

3.4.2 Signal conditioning

There are many circuit designs suitable for measuring capacitive change and it is beyond the scope of this thesis to describe the many possible configurations. Briefly, an AC circuit is typically used to measure the change in capacitance in a transducer. Greater sensitivity to changes in any two of the three basic factors (area, gap space and dielectric material of the capacitor system) can be achieved in a transducer working in differential mode (Figure 24). The 'twin-T' circuit configuration can be used as the measurement circuit for differential capacitive transducers and is less influenced by the effect of stray capacitance (Kuphaldt, 2002), which may be due to undesirable capacitance between wires or between electronic components and the transducer chassis. Otherwise, compensatory measures, such as the use of a Faraday shield, are required to minimise the effect of stray capacitance in the system (Guinta, 1996).

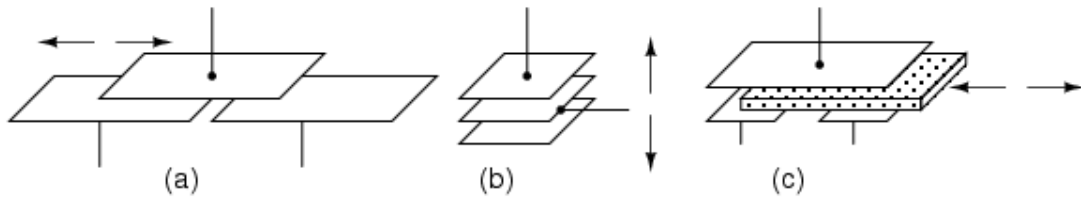


Figure 24 - Differential capacitive transducer varies its capacitance by changing: area of overlapping electrode (a), distance between electrodes (b), or dielectric between the electrodes (c). (Diagrams extracted from Kuphaldt (2002))

Capacitance measurement is also possible using circuits based on the charge-balancing principle as described elsewhere (Zhu et al., 1991, Zhu and Spronck, 1992). However, regardless of the capacitance sensing circuit used, additional linearization techniques would be necessary to convert the non-linear capacitance change (Figure 23) to a linear load-capacitance output if desirable (Yamada et al., 1992).

3.4.3 Transducer construction

As mentioned above (Section 3.4.1), a basic uniaxial load transducer can be constructed with two parallel electrodes that are separated by an insulating elastic material (Figure 23). Moreover, it is obvious that a differential capacitive transducer, such as those shown in Figure 24a and c, are suitable for shear load measurement. It can be understood that capacitive transducers can be extremely thin (<2mm) and theoretically be made into any shape. The electrodes need not to be bonded to the dielectric material allowing easier and quicker manufacturing. However, the electrodes would then need to be encapsulated within an elastic housing. Such housing should also provide adequate shielding to minimise the effect of stray capacitance and possible influence in the capacitance output due to the conductive property of the plantar skin (Lee, 2006).

3.4.4 Current state of the art

Capacitive-based uniaxial pressure distribution measurement devices are not new. Novel GmbH (Germany), founded in 1978, developed the world's first commercially available device for the measurement of plantar pressure distribution. Today, capacitive-based plantar pressure distribution measurement systems are available

from other manufacturers, such as AmCube (UK). Fundamentally, their systems are based on two parallel plates of fixed area with a gap space that will vary with the load applied. The dielectric in Novel GmbH's systems is a rubber-like elastomer. Platform devices as well as in-shoe transducers are currently available from Novel GmbH, and have been used extensively in gait analysis (Bertsch et al., 2004, Bosch et al., 2007, Drerup et al., 2008, Chen et al., 2007) and for evaluating plantar pressure distribution in the diabetic population (Armstrong et al., 1998, Bacarin et al., 2009, Bus et al., 2006, Bus et al., 2005, Guldemond et al., 2007a, Guldemond et al., 2007b, Hayes and Seitz, 1997). Novel GmbH's platform system has a spatial resolution of 4 sensing elements per cm² and is capable of sampling at up to 400Hz. However, the company has not specified the frequency response of their system.

Novel GmbH's in-shoe systems displayed good accuracy and precision with error less than 3%, but only when the system was: 1) less than 1 year old, 2) measurements were taken shortly after calibration of the system, and 3) measurements were taken within a few seconds after pressure was applied (Hsiao et al., 2002). It is not recommended that a subject stands on the device for a prolonged period either before or after measurements are taken. While the manufacturer specifies that the transducers are not designed to measure pressure less than 15kPa (Novel 2010 product catalogue), due to poor accuracy (up to 57% error), measurement below 35kPa was not recommended by others (Hsiao et al., 2002). Long-term (hours) plantar load measurement may be required to monitor patient's daily activities, but prolonged use of the system resulted in 9.6% drift after 20 minutes of static load (50kPa). Prolonged cyclic load also resulted in error up to 8% and as much as 22% for loads under 300N (Hurkmans et al., 2006). The visco-elastic properties of the dielectric elastomer used in the transducer is likely to blame for such time-dependent characteristics of the system. However, these errors did not appear to affect outcomes in clinical measurement when tests lasted less than 10 minutes.

Commercial capacitive-based devices were compared to commercial resistive-based pressure distribution measurement systems described earlier (Section 3.2.4.6). In terms of linearity, hysteresis and measurement error, Novel GmbH's capacitive-based system had the highest performance (Giacomozzi, 2010), and the capacitive-

based system from AmCube suffered from low performance on all of these parameters. The reliability of Novel GmbH's platform system in repeated plantar pressure measurements during gait across multiple testing sessions over >5 days was found to be satisfactory with a coefficient of variation of <10% for peak pressure measurements (Gurney et al., 2008, Maetzler et al., 2010).

Based on the differential capacitive principle (Section 3.4.2), Chu et al., (1996) demonstrated a transducer capable of measuring triaxial load. Their prototype device was a 10mm² chip containing 3×3 triaxial load sensing elements, with overall accuracy of 2% and non-linearity of 1% but could only measure forces up to 1g (0.01N). A transducer based on the same triaxial load sensing principle, but on a larger scale, has been reported by Novel GmbH (Christ et al., 1998). Their system consisted of 64 sensing elements, each with an area of 15×15mm, in an 8×8 matrix configuration. The principle of the transducer is illustrated in Figure 25. The vertical load (F_v) was measured by the increased capacitance due to the decrease in distance between plates 1&2 and plates 1&3. The shear load (F_h), directed towards the right as illustrated, would have led to an increase in capacitance between plates 1&3 but a decrease between plates 1&2, thus shear (F_h) could be calculated by finding the differences in capacitances between the two pairs of plates.

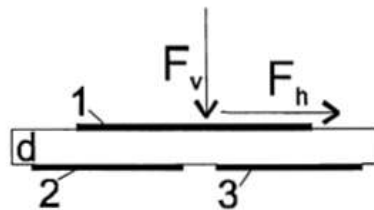


Figure 25 - Principle of measuring vertical and horizontal forces with the capacitor plates 1,2 and 3.
(Diagram reproduced from Christ et al. (1998))

The device had a thickness of approximately 1mm, and is 1mm thinner than their commercial in-shoe uniaxial pressure system. The company proposed that hysteresis would be <2% but did not provide data to support the claimed performance. No further updates on the progress of this triaxial measurement systems have been published by Novel GmbH since the document by Christ et al. (1998).

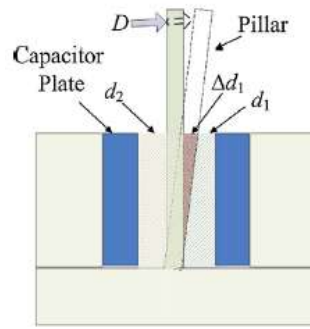


Figure 26 - The end view of the structure of a capacitive-based shear force sensor showing the displacement of the pillar when shear force is applied. (Diagram reproduced from Tiwana et al. (2011))

Other experimental devices (Heywood et al., 2004) have attempted to measure shear loads by effectively placing a vertical differential capacitive system in a sideways position. The device could measure up to 15N shear, with a non-linearity of 8.3% and hysteresis <12%. The same design concept (Figure 26) was also found in the work of Tiwana et al. (2011) but their system could only measure shear load of up to 4N. Due to height, and therefore area, of the capacitive plates, the capacitance of the transducer was relatively low and would require circuits with high resolution to detect the relatively small changes in capacitance (Tiwana et al., 2011).

3.4.5 Critical review

Capacitive-based pressure distribution measurement is now a well established technique in the field of biomechanics. However, because commercial capacitive-based transducers employ an elastomeric medium as the dielectric layer, the frequency response of the transducer is anticipated to be less than other load sensing technologies, such as piezoelectric-based transducers (Sections 3.3). Accuracy was found to be poor for low load measurement (up to 57% below 35kPa) and in some cases it was not possible to measure pressure less than 15kPa. Due to the non-linear nature of capacitive sensing, additional linearization circuitry or software compensation techniques are required for optimal measurement performance.

Compared to strain-gauge-based technologies (Section 3.2), capacitive-based transducers have potentially superior physical characteristics, such as minimal transducer thickness (<2mm) and high spatial resolution (5×5mm sensing area)

making them suitable for in-shoe applications. Batch production of capacitive-based transducers and their ability to be incorporated within an array has been proven. However, these were only true for systems capable of uniaxial pressure measurement. A novel method of identifying the location of the capacitive plates would be required for a combined pressure and shear measurement device to have the same physical characteristics.

Moreover, it is questionable whether capacitive load sensing technology could be used for biaxial shear or triaxial load measurement. Although various experimental triaxial designs have been investigated, more than 10 years after the publication from Novel GmbH, there is still currently no commercially available system capable of measuring shear. It was believed the concept of shear measurement using parallel plates separated with an elastomeric material poses many technical problems. One could imagine that if a load were applied to the side of such transducer it would cause the top electrode plate to tilt at an angle thereby causing erroneous output. The problem cannot be solved even if the top electrode was in a circular shape, but then in theory the transducer would not be sensitive to torsion caused by off-axis shear loading. Accurate shear measurement using capacitive-based sensing technology would be challenging.

3.5 Optoelectronic based transducers

This section explores and provides a critical assessment on load measurement techniques that use optoelectronic-based components.

3.5.1 Principle of operation

Light, in the visible or invisible spectrum, exhibits many properties such as intensity, wavelength and interference. As such, there are various methods for the manipulation of light appropriate for load sensing. Nonetheless, all optoelectronic-based transducers consist of a light source and a light (or photo) sensor. The purpose of the photo sensor is to convert the optical signal to an electrical signal that can be read

and stored by an instrument continuously. Examples of some methods for the manipulation of light are discussed below:

Light intensity

One of the most obvious and best understood methods for the manipulation of a light source is the shutter method. The movement of a load-sensitive membrane or structure could be used to convert the load into a mechanical displacement, which in turn could be used to drive a shutter that blocks the light from reaching a photo sensor (Figure 27a). Other simple light source and photo sensor configurations, as proposed by Hirose and Yoneda (1990) could also be used to change the light intensity due to applied load, these includes: 1) the change in light intensity due to the relatively movement of the light source and the photo sensor (Figure 27b), 2) the installation of multiple photo sensors to measure X and Y direction movements by determining the ratios of the light intensity received by the photo sensors (Figure 27c), 3) the use of a mirror to increase the light intensity due to movement of the mirror, which effectively represents the opposite of the shutter method (Figure 27d), and 4) the use of a converging lens or pinhole set in front of the light source to allow increased sensitivity in the Z-directional distance (Figure 27e). Fundamentally, all these optical configurations are displacement sensors but a load transducer can be materialised when holding such an optical unit within elastomeric members. Minute displacements produced by external load, therefore, could be measured and calibrated.

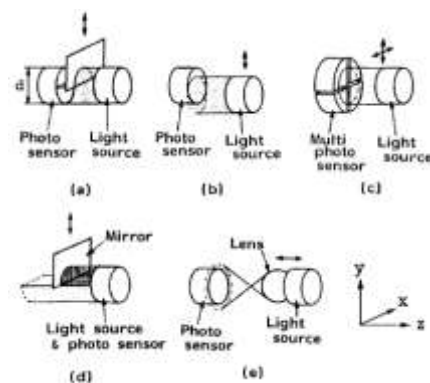


Figure 27 - Several types of optical sensor proposed by Hirose and Yoneda (1990). (Image reproduced from Hirose and Yoneda (1990))

The light intensity in an optical fibre can also be altered. Optical fibres rely on total internal reflection to confine light to their core, which is only valid if the propagation of light in the fibre hits the boundary of the fibre at an angle larger than the critical angle for the boundary. Scattered light within the fibre is more likely to exceed this critical angle once the fibre is bent (Figure 28). If an external load results in bending of a fibre, the change in intensity received at one end of the fibre could be calibrated to measure such a load.

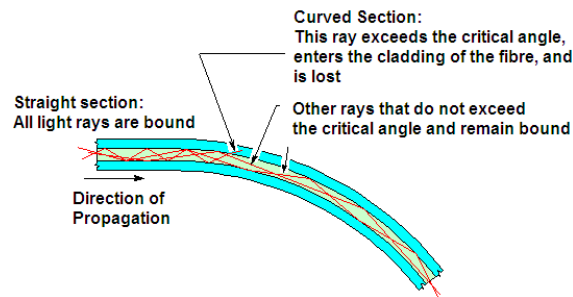


Figure 28 - Light loss in an optical fibre due to bending. (Modified diagram from http://faxswitch.com/Definitions/telecom_dictionary_m.html)

Wavelength

Fibre Bragg Gratings (FBG) are fringes in the core of an optical fibre created by intensive UV light. The periodic spacing structure of these fringes result in the reflection of light at a specific narrow band wavelength, called the Bragg wavelength (Figure 29). All other wavelengths are transmitted through the grating without being reflected. An external load or stress applied to the fibre causes the period of the grating to shift, and so the peak reflected wavelength is shifted too. Therefore, a load transducer can be realised by detecting the shift of the Bragg wavelength.

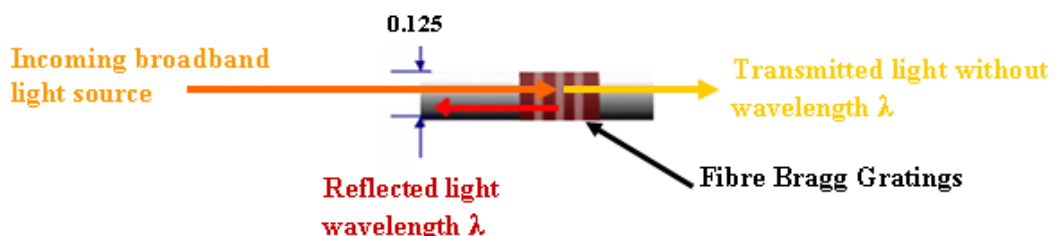


Figure 29 – Fibre Bragg grating schematic. Typical fibre diameter of 125 μ m and the reflected Bragg wavelength (λ). (Modified diagram from Kreuzer (2007))

Optical interference

Optical interference is a phenomenon whereby two light waves interact. When two light waves interact the resultant wave may be of greater or lower amplitude depending on the type of interaction, either constructive or destructive interference, respectively. This property of light waves has the potential to be put in use for load detection. For instance, photoelasticity is one of the many possible methods based on optical interference, which allows the stress distributional in a material to be graphically represented (Figure 30). The light transmitted is altered based on the deformation of the material. The resultant light pattern could be captured via a video recording device, thus studying the light pattern one could determine the state of stress across the whole surface of the material.

Alternatively, video recording devices could be used to track the changes in colour from a stress sensitive material that would change colour depending on the load being applied (Stucke et al., 2012)



Figure 30 – Stress patterns visualised using optical interference in a plastic model of a crane hook with hanging weights and photographed through polarised white light. (Credit: Peter Aprahamian, Sharples Stress Engineers Ltd, Science Photo Library)

3.5.2 Signal conditioning

The simplest optoelectronic circuit would be for the measurement of light intensity. A photodiode is usually used for such a purpose. The design of a photodiode circuit is beyond the scope of this thesis. For more details, interested readers are referred to a textbook dedicated for the design of photodiode circuits (Graeme, 1995). One could see a photodiode as a solar cell, which requires no power to operate but is

capable of converting light energy into either current or voltage, depending upon the mode of operation (Graeme, 1995). Photodiode circuits are commonly used in a wide range of applications, including precise laser or mirror alignment and inside laser printers for precise detection of the printer head location. Figure 31 illustrates a typical quad-photodiode amplification circuit used for precise detection of the X and Y position of a laser source. Circuit boards with built-in quad-photodiode arrays with sum and difference amplifiers are commercially available. Circuit boards of sizes no larger than the photodiodes themselves (about Ø10mm) are available and have a typical bandwidth of more than 150kHz for high speed detection.

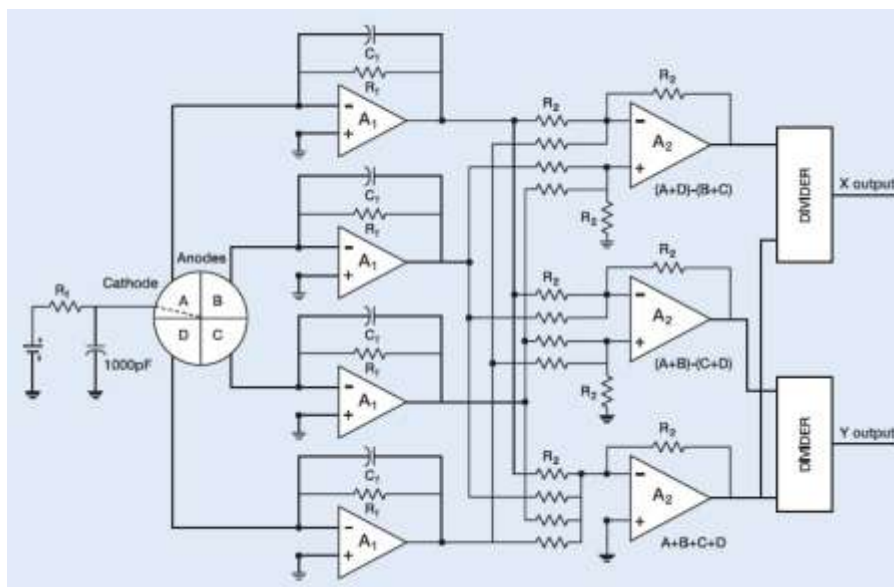


Figure 31 - Typical circuit used with multi-element photodiodes for detecting the X and Y position of a light spot with respect to the centre of the multi-element photodiode. (Figure reproduced from OSI OptoelectronicsInc (2010))

Fibre Bragg Gratings (FBG) systems usually work by injecting light from a broadband source into the fibre. The grating reflects a narrow spectral component at the Bragg wavelength, or in transmission this component is missing from the observed spectrum. The detection of change in wavelength from a light source is relatively complex than measuring light intensity and there are several different principles for analysing such optical variable. The reader is directed to other literature for an in depth description on the operating principle of some wavelength interrogators (Kreuzer, 2007). Most optical interrogators consist of multiple

photodiodes and mathematical algorithms are then applied to interpret the shift in wavelength and relate it to the applied load.

For systems based on optical interference or photoelasticity, a video camera would be necessary. The image sensor within a video camera is simply a large array of photodiodes (or pixels) multiplexed together. If colour detection was desired, such as in the case of photoelasticity, an array of colour filters that passed the three primary colours to selected photodiodes would be used. Today, low-end image sensors typically contain 1280×720 pixels with speeds of up to 60 frames per second in continuous recording mode. High-end cameras with speed in the order of >500 frames per seconds are commercially available but are expensive, with fewer pixels and in some cases can only record a few seconds worth of data.

The same multiplexing circuit used in video cameras, such as active-matrix addressing, is also applicable in transducers that are based on detecting the changes in light intensity. Hence, the construction of a load distribution measurement system containing large numbers of photodiodes would be possible. The multiplexing capability of FBG systems is discussed in the next section (Section 3.5.3).

3.5.3 Transducer construction

The construction of an optoelectronic based transducer differs dramatically depending on its operating principle. Light-emitting-diodes (LEDs) are often selected over incandescent light sources because they are relatively cheap, consume relatively little power, have a longer life span and are available in various sizes. A simple uniaxial load transducer, for example based on the shutter method (Section 3.5.1), could be constructed with a LED and a photodiode enclosed in an elastic structure. A multi-axial load transducer could potentially be realised using multiple photodiodes. The LED and photodiodes need not to be placed within the transducer housing. Instead, fibre optics could be used to guide the light into and out of the transducer part to photodiodes located externally from the transducer structure. This would further increase the resistance to electromagnetic noise making the transducer suitable for load measurement in a magnetic resonance imaging facility, for example.

In fact, the transducer structure could simply be the fibre optic cable itself if the principle of fibre bend loss could be utilised in a multi-axial load transducer design. As such, the thickness of an optoelectric-based transducer would likely be suitable for in-shoe applications. For platform systems, photodiode amplifier and data processing circuits are commercially available and they are no larger than the photodiode chips, hence all the electronics could be embedded within the transducer housing without compromising the spatial resolution of the system.

The construction of a load transducer using optical fibres with Fibre Bragg Gratings would be very similar to using resistive strain gauges (Section 3.2.3). The bonding of FBG on surface(s) of an elastic structure for vertical or shear load sensing would be time consuming. Similarly, the design of the structure and precise locations of the FBGs would be paramount to minimise the effect of cross-talk for accurate load measurement. In contrast to strain gauges, a bridge circuit configuration is not necessary for FBG systems. Also, more than one FBG could be integrated in a single optic fibre. 13 sensor points per fibre are currently recommended by a FBG manufacturer (HBM GmH, Germany). In other words, a 4-channel FBG interrogator (Section 3.5.2) could measure the change in wavelengths in as many as 52 sensor points along 4 separate FBG optic fibres. This multiplexing capability of FBG is attractive for a load distribution measurement system where wires, or in this case the number of fibres, could be minimised. However, FBG technology is relatively new and the interrogators are currently very bulky in size and expensive to operate (>£14000, PXIe-4844 interrogator, National Instruments Corps., Ireland). Theoretically, a single fibre with numerous FBGs could be used to form a layer of distributed shear transducers large enough to cover the entire plantar surface of the foot. However, a typical fibre would suffer from a loss in light intensity, hence signal intensity, if the fibre were bend with a radius <10mm.

A load transducer that was based on optical interference would only be suitable as a platform system. The construction of which would require a video camera to be situated beneath the platform, unless a mirror configuration was to be used.

3.5.4 Current state-of-the-art

The shutter method has been used in an experimental miniature force transducer for an advanced computer pen (Clijnen et al., 2003b, Clijnen et al., 2003a). The transducer consisted of a mechanical shutter structure which converts the applied load into linear displacement of the shutter, which in turn blocks the LED-photodiode pair. Three LED-photodiode pairs were used to measure triaxial load. The overall transducer dimensions were $\text{Ø}12 \times 45.6 \text{mm}$, with a rated capacity of only $\pm 2 \text{N}$, accuracy of 1%, but with a high resonance frequency of 360Hz. A non-shuttered LED and photodiode pair was also situated in the transducer to compensate for potential thermal effects

A low-cost miniature optoelectronic-based transducer ($\text{Ø}15 \times 3.8 \text{mm}$) has also been demonstrated previously but was only capable of uniaxial shear measurement (Lebar et al., 1996). The thickness of the transducer was largely determined by the dimensions of the photodiode ($5 \times 2.5 \times 0.6 \text{mm}$), but it was not clear why the width was relatively large, when the LED was small ($3 \times 1.5 \times 1.5 \text{mm}$). The transducer relied on a spring structure made of naval bronze material, which was specifically selected for its non-reflective characteristics. The spring and silicone adhesive used in the construction of the transducer provided the restoring force for the moving shutter situated between the LED-photodiode pair. The transducer was calibrated up to 91N in shear and hysteresis was found to be different between opposite shear directions. The authors hypothesised the different performance between shear axes was caused by poor construction of the spring structure. At worst, average non-linearity was 7.6% and hysteresis was 21%. Temperature sensitivity was 3.5% full scale/ $^{\circ}\text{C}$, but could theoretically be eliminated using a dummy pair of LED-photodiode as mentioned above. The inherent speed of optoelectronic circuits allowed the transducer to have a sampling frequency of 500Hz.

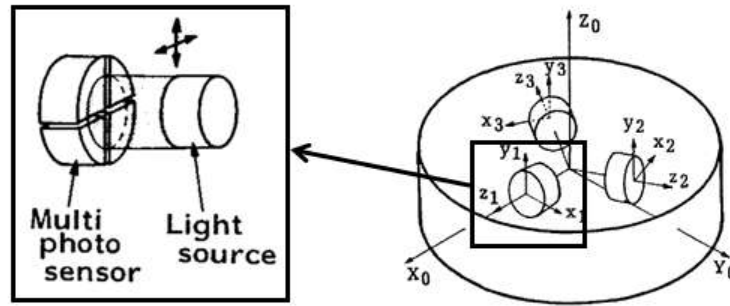


Figure 32 - The use of 3 LED & quad-photodiode pairs in a 6-channel force transducer Hirose and Yoneda (1990).

Hirose and Yoneda (1990) described a 6-channel force transducer based on 3 pairs of LED & quad-photodiode pairs and evaluated the transducer against a resistive strain gauge-based transducers. The authors found the compliance of the transducer (100 μ m at rated capacity) was not as good as strain gauge type transducers (typically 20 to 100 μ m at rated capacity) due to the need for greater displacement change when load was applied. Measurement accuracy (0.3%), however, was comparable to strain-gauged transducers, whereas the weight was as much as 5 times less even with the amplifier electronics built inside the transducer. Moreover, the authors estimated the cost of the overall system to be at least 15 times cheaper than strain-gauged transducers. While the size of the transducer was large ($\text{\O}76 \times 40$ mm), it highlighted that the single LED-quad-photodiode pair could potentially be used for accurate measurement of triaxial load in a small transducer package.

The concept of triaxial load measurement based on bend loss in optical fibres has been demonstrated previously (Wang et al., 2005). The conceptual design consisted of a mesh of optic fibres orthogonal to each other (Figure 33), which allowed pressure measurement. The location of the applied load could be tracked by measuring the loss of light from each x-axis and y-axis fibres. For shear measurement, two of these fibre meshes were aligned and bonded on top of each other. The location of the load measured by the top and bottom mesh would be different when shear load was applied due to the displacement change of the top mesh relative to the bottom mesh. The authors constructed a prototype consisting a 2×2 array of fibres. However, it is questionable whether this concept could be expanded to an array of more than 2×2 because the location of the applied load could

not be tracked if multiple locations of the mesh were loaded simultaneously. However, FBGs have the potential to overcome this limitation.

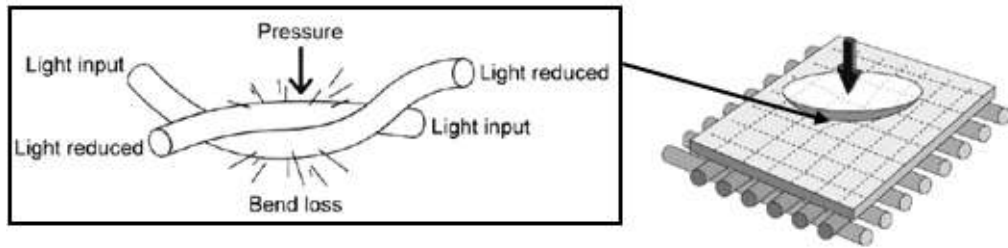


Figure 33 - The principle of pressure measurement based on bend loss in optic fibres (Wang et al., 2005).

A high spatial resolution uniaxial pressure transducer array using FBGs has been described (Heo et al., 2006). The 3×3 transducer array covered a sensing area of 10×10mm. The transducer consisted of 3 optic fibres each with 3 FBGs, each 5mm apart. Vertical load was measured via a bridge-like structure that would extend the FBG with the application of load (Figure 34). The transducer displayed linear response, high accuracy (99.9%) and had a resolution of about 0.001N. An additional dummy FBG along the fibre was used to compensate for any temperature change in the system. This feature might be viewed as a disadvantage, since measuring the change in wavelength is currently very expensive. Moreover, FBGs post other design challenges (Heo et al., 2006), namely: 1) light loss caused by bend loss of fibre that are within or outside the sensing area has the potential to decrease the intensity of the reflected light to the point when the Bragg wavelength cannot be measured, 2) chirping is when a non-uniform load is distributed along the fringes of one FBG which causes distortion of the Bragg signal, and 3) more design effort is required to ensure the load that is applied to a specific FBG must not affect other FBGs along the same fibre.

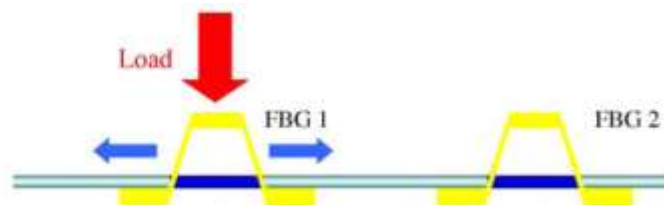


Figure 34 - Bridge-like structures that can be extended symmetrically in the optical fibre direction when a vertical load was applied. (Diagram extracted from Heo et al. (2006))

Shear measurement using FBG in conjunction with another transducer design was details by Suresh et al. (2004). In contrast to the mesh design discussed above, the optical fibre was bonded to two carbon composite materials (CCM) with the FBG embedded in a deformable silicon rubber layer at an angle of $\sim 1^\circ$ (Figure 35). The transducer ($50 \times 20 \times 1.8\text{mm}$) only had one FBG and was tested for measuring uniaxial shear up to 40N. It displayed good linear response ($R^2 = 0.997$) but failed at shear load of 67N due to the bonding of the fibre on the CCM.

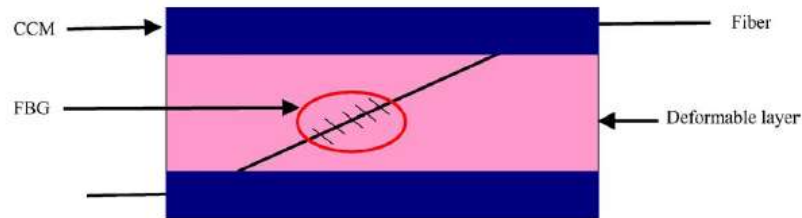


Figure 35 – Deformable layer between two layers of CCM to increase the shear force sensing range using FBG. (Diagram extracted from Suresh et al. (2004))

High-resolution pressure distribution measurement was possible with a platform system based on the interferometry technique (Hughes et al., 2000). A camera of 500×700 pixels and a speed of 25fps, was used to obtain images of an area of $60 \times 90\text{mm}$ at a spatial resolution of $70\text{pixel}/\text{cm}^2$. The camera was located on the side of the platform and imaged the underside of a Perspex plate via a mirror. An interferometry pattern of the Perspex plate was taken prior to the application of any pressure was applied. The original pattern was then compared to the changing interferometry pattern when the subject walked across the platform. The platform was designed to measure pressure of up to 1MPa, however, the authors did not report the measurement resolution and the accuracy of their image processing software. Their results appeared that the measurements were not linear and suffered from hysteresis. Perhaps, with more advanced camera systems available today, such a pressure distribution measurement systems could potentially be upgraded to include a faster camera with higher pixels count ensuring the whole plantar surface of the foot is captured. However, image processing would require heavy computational effort, thus such a method is unlikely to provide real-time load data to the user if

required. A novel technique would be required to obtain an interferometry pattern that could be used for shear measurement.

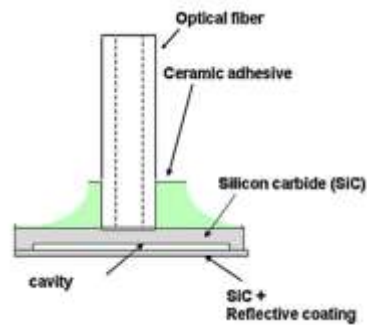


Figure 36 - Schematic view of the membrane-based pressure transducer using an interferometry load sensing technique. (Diagram extracted from Ceyssens et al. (2008))

Instead of using a video camera, a simple LED-photodiode pair was used to construct a discrete pressure transducer based on the principle of interferometry (Ceyssens et al., 2008). The LED and photodiode were located outside the transducer housing, light was directed to and from the sensing structure which consisted of a light reflection membrane that deformed when subjected to pressure (Figure 36). Optical interference occurred in the cavity formed by the optical fibre and the reflective silicone, therefore changing the intensity received by the photodiode. The membrane was of the size of 2mm² but the overall transducer dimensions and response characteristics were not reported.

It should be noted that the optoelectronic sector is still growing fast, with vast potential for more novel techniques in load measurement. Manufactures claimed that photonic devices such as light emitters and detectors can be printed onto bendable, disposable and ultra thin surfaces (Nanoident Technologies AG, 2006). These miniature components could potentially be inkjet printed using liquid conductive and semi-conductive materials making a cost-effect way to manufacture large transducer arrays for load distribution measurement. Also, advances in the development of stretchable substrates for optoelectronics may allow the construction of flexible in-shoe transducers. The researchers have embedded miniature inorganic LEDs and photo-detectors in waterproof substrates which allowed them to be flexed and stretched while maintaining their electrical connection (Kim et al., 2010).

3.5.5 Critical review

Simple light intensity based multi-axial load transducers have been previously developed by using multiple light emitter and photodiode pairs. Although the stiffness of an optoelectronic-based transducers may not be as good as strain-gauged transducers, their measurement accuracy, linearity and other characteristics are comparable if not superior to any other load sensing technologies. However, care must be taken when selecting the material for the construction of the transducer, which would affect the frequency response and temperature sensitivity of the system. Temperature effects, on the other hand, could be compensated but at the cost of using an additional dummy optical sensor part.

In terms of hardware requirements, LED and photodiode circuits are low-cost and have relatively low power consumption. The fast response time with optoelectronics allow high sampling frequency (>500Hz) and high multiplexing capability has been previously demonstrated with video camera systems. However, computational requirements would be high for a load distribution measurement system that contains numerous photodiodes or consists of a video recording system with large pixel values at fast frame rates.

The size of the light emitter and photodiode determines the overall physical dimensions of the transducer. But the size of the sensing structure can be miniaturised by using optical fibres or potentially with the advancement in print-able optoelectronics. FBG transducer may be thin and small but wavelength interrogators are big and expensive, making this approach not fit for purpose. Similarly, high-speed video-based systems are also expensive and are not suitable for in-shoe applications. However they would likely have the highest spatial resolution. Transducer thickness and sensing surface area could be kept to a minimum by using a load-sensitive optical fibre, such as those based on bend-loss or FBG. However, optic fibres cannot be bent to a small radius without significant intensity loss and so would be difficult to be incorporated inside a shoe where space is limited. The concept of using a single FBG fibre to cover the whole plantar surface area of the foot would be extremely challenging or impossible with today's fibre technology.

Moreover, the reliability and life span of optic fibres under repeated stress during gait would require further research.

FBG may be batch produced and be incorporated in a matrix arrangement for load distribution measurement. However, as mentioned above, routing the fibres across the whole sensing area would be physically challenging. Moreover, adhering the FBG to transducer structures would be time consuming and costly. Using LED-photodiode pairs may be an alternative method and batch production would be relatively easy with commercially available amplifier and signal processing circuits. These circuit boards are small and can be incorporated within the transducer, but additional cabling would be required in comparison to FBG-based systems. Nonetheless, low-cost batch production of miniature optoelectronic device can be expected in the near future, especially given the rapid technical advancement of this sector.

3.6 Magnetic based transducers

This section explores and provides a critical assessment of load measurement techniques that use magnetic-based components.

3.6.1 Principle of operation

There are several means of using the phenomena of magnetism in load sensing and some common techniques are outlined below:

Magnetoelasticity

The magnetoelastic Villari effect describes the change in the magnetic properties when a ferromagnetic material is subjected to mechanical stress. The technology is often used in displacement transducers (MTS Systems Corp., USA). For more information on the principle and the use of the Villari effect in transducers, the reader should refer to the documentation available on the manufacturer's website (MTSsensors.com). Ferromagnetic materials such as iron, nickel and cobalt exhibit

the Villari effect. A load transducer can be realised if one could measure the change in magnetic field of such material under loading conditions.

Magnetoresistance and Hall-effect

Magnetoresistance and the Hall-effect are different but two related phenomena that could be used for magnetic field sensing. Magnetoresistance (MR) involves the change in electrical resistance of a conductive material within an applied magnetic field. The change in resistance of the conductive material is proportion to the square of the sine of the angle (θ) between the magnetisation vector and the direction of current flow (Figure 37a). The Hall-effect is characterised by the production of a voltage in a conductive material that is perpendicular to both the current flow through the material and the direction of the magnetic field applied across the material (Figure 37b).

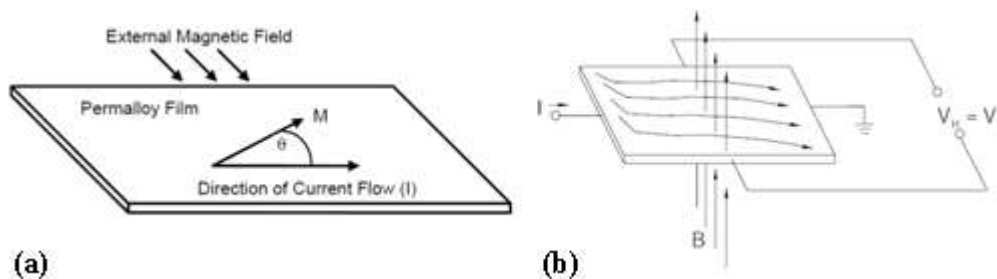


Figure 37 – The magnetoresistance principle (a) with the magnetisation vector (M) and direction of current flow (I); and the Hall-effect principle (b) with magnetic field (B) applied perpendicular to the current (I) passing through the conducting material causing a voltage output (V) across the orthogonal axis. (Diagrams reproduced from Honeywell-Inc. (2011a) and Honeywell-Inc. (2011b))

For maximum sensitivity in the change in magnetic field, the active element and the magnetic field should be aligned as shown in Figure 37. The MR active element responds to parallel fields, while the Hall-effect element responds to perpendicular fields. Therefore, the mounting of each sensing element in relation to a magnet would be different (Figure 38).

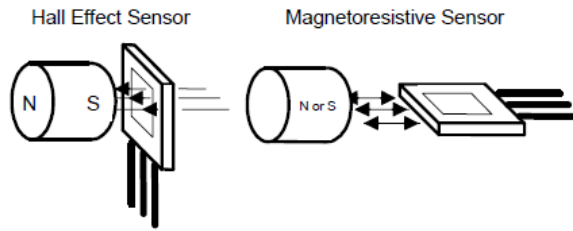


Figure 38 - The physical application differences between Hall-effect and magnetostrictive sensors. (Diagrams reproduced from Honeywell-Inc. (2011b))

MR devices are roughly 200 times more sensitive than silicon Hall-effect devices (Honeywell-Inc., 2011a). However, MR devices have a non-linear response and saturate with a high magnetic field strength. Outputs from Hall-effect devices, in contrast, are typically low (of the order of microvolts) but the voltage signals that are generated can be easily amplified. Moreover, Hall-effect devices are known to have a highly linear response to magnetic field strength, with negligible saturation effects even in high-strength magnetic field (Honeywell-Inc., 2011a). However, the output voltage of Hall-effect devices is also sensitive to the strain experienced by the active element, known as the Kanda effect (Kanda and Yasukawa, 1981). Therefore, care is required to ensure Hall-effect devices are not subject to mechanical stress or thermal stress if its intended purpose is to measure fluctuations in magnetic field strength. Fortunately, both MR and Hall-effect technologies are compatible with integrated circuit processing, thus many commercial Hall-effect devices (Honeywell Sensors, USA; Allegro MicroSystems Inc., USA; and Melexis Microelectronic Systems, Belgium) have built-in circuits to compensate for the effect of mechanical stress and temperature.

3.6.2 Signal conditioning

Custom signal conditioning for the design of a magnetic-based transducers is not necessary, given the availability of commercial sensor chips. Miniature ICs (around $3 \times 3 \times 1$ mm) with built-in signal amplification capability and temperature compensating circuitry are available at low-cost from various microchip manufacturers. As discussed above (Section 3.6.1), the output from a Hall-effect active element does not saturate even within strong magnetic fields. However, due to the amplifier circuits typically used in a commercial Hall-effect IC, its output would

saturate if the magnetic field was higher than the started maximum rating specified by the manufacturer. Multiplexing voltage outputs from an array of sensor ICs would be relatively easy with the same active-matrix addressing approach used for optoelectronic-based devices, which also produce a voltage output (Section 3.5.2).

3.6.3 Transducer construction

The magnetic flux produced by a material that exhibits magnetoelasticity or from a permanent magnet at any point in space is affected by many factors including its length, cross-sectional area, shape and composition. Magnetic flux can also be affected by other substances placed within the path of the flux. Although a complete discussion on designing magnets is beyond the scope of this thesis, it is important to understand that the physical configuration of a magnetic system can influence the output of a magnetic sensor..

When working with magnetoelastic materials, the magnetic sensor must be located as close as possible to the material for maximum sensitivity. Ideally, the sensor should be bonded to the surface of the magnetoelastic material. The orientation of the magnetic sensor would depend on the type of sensor used and the flux lines produced by the material during loading conditions. For systems with permanent magnets, an elastic structure would be required to hold the sensor IC and the magnet. Ideally, the elastic structure should also allow relative movement between the components under load conditions. Magnetic-based load sensing is a contactless technique hence the electronic components are not subjected to damage associated with wear and tear. Thus, magnetic-based transducers can be expected to have a long life span.

The following discussion focus on the use of Hall-effect sensor ICs, but the same operating principles are also applicable to MR-based sensor ICs. Although the sensor IC used may produce a linear output proportional to the applied magnetic field, the field produced by a permanent magnet is not linear, hence the output from a sensor IC may be considered linear only for relatively small movement of the magnet (Figure 39). The output voltage from the IC is directly related to the total effective air gap (TEAG), which is the gap between the face of the magnet and the active

element inside the IC. The TEAG is the sum of the active area depth (ADD), the depth of the active element below the face of the IC and the air gap (AG), the distance between the IC and the face of the magnet (Allegro Micro Systems Inc., 2011).

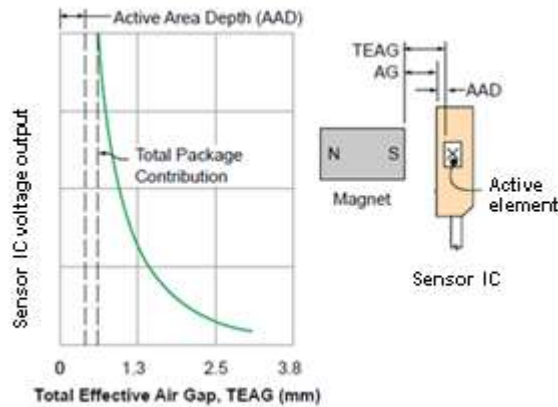


Figure 39 - Definition of total effective air gap (TEAG), active area depth (AAD), air gap (AG) and demonstration of the effect of a permanent magnet on the output signal from a Hall-effect sensor IC. (Diagram reproduced from Allegro Micro Systems Inc. (2011))

There are many possible paths of motion, or modes of operation, for a magnetic-based sensor system. Figure 39 illustrates the output from the sensor IC with the magnet moving in ‘head-on’ mode, where the poled face of the magnet moves perpendicular to the face of the IC (Figure 40a). Another common operating mode is the ‘slide-by’ mode (Figure 40b), which provides relatively steep output slopes compared to ‘head-on’ mode and is very linear around the centre portion of the magnet. The use of more than one magnet can further enhance the sensitivity of the system. For instance, the ‘push-pull’ approach is when two magnets with opposite poles facing each other, whereas the push-push approach has the same magnetic pole facing each other. They can be used to provide greater field strength than a single magnet for a steeper voltage output slope. Both arrangements can be applied in the head-on or slide-by mode (Figure 40c and d) but are less-sensitive to lateral motion.

Flux concentrators can be used to provide a low reluctance path for the magnetic field thereby increasing the flux density at the active element. Although a complete discussion on the design of flux concentrators is beyond the scope of this thesis, the

reader is directed elsewhere for a more detailed discussion of the characteristics of the different modes of operations and the use of flux concentrators (Allegro Micro Systems Inc., 2011).

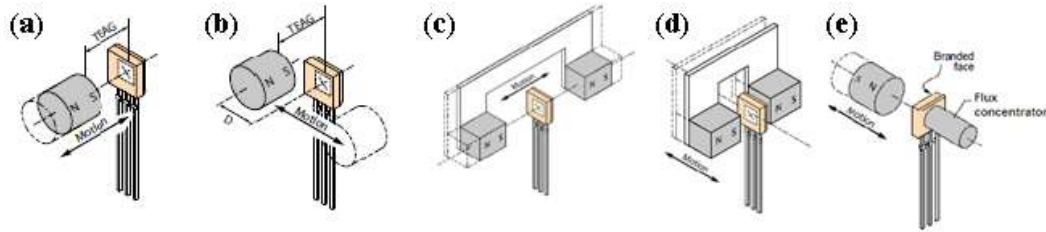


Figure 40 - Demonstration of head-on mode (a), slide-by mode (b), push-pull head-on mode (c), push-pull slide-by mode (d) and the use of a flux concentrator in the head-on mode (e). (Diagrams extracted from Allegro Micro Systems Inc. (2011))

3.6.4 Current state of the art

Displacement transducers based on magnetoelastic principle are commercially available from MTS Systems Corp. (USA). The use of the same principle in load sensing has been demonstrated in the work of Garshelis and Tollens (Garshelis and Tollens, 2010). Their experimental transducers were constructed using 60mm long tubular beams of a magnetoelastically active material with outside diameter 15.9mm and inside diameter 12.7mm. A commercial Hall-effect integrated circuit was cemented to the surface of the centre of the tube and was oriented for maximum sensitivity to the magnetic field. Calibration loads of up to 1500N were applied to the centre of the tubular transducer structure. The output response from the Hall-effect IC displayed good linearity (1.4%) and hysteresis (2.2%). Although the dimensions of their transducers were large in size, the same load sensing principle could potentially be applied on miniature transducers.

Magneto-resistive-based transducers, designed for the measurement of uniaxial shear on the sole of the foot have been reported previously (Tappin et al., 1980, Laing et al., 1992). The design were later expanded and modified for biaxial shear (Lord et al., 1992) and triaxial load measurement (Williams et al., 1992). However, vertical load measurement was only made possible by integrating a strain-gauged diaphragm

on top of the biaxial shear transducer. The need for an alternative load sensing technique for measurement of vertical load is not clear. However, it is possible that either the magnetoresistive-based sensor was not sensitive to vertical movement of the magnet or that the vertical movement of the magnet was limited, resulting in minimal change in magnetic field strength. Nonetheless, the work has demonstrated the potential of a hybrid transducer design that combines various load sensing technologies in one transducer for multi-axial load measurement. Given that load measurement using strain-gauges has been previously discussed, this section will concentrate on the magnetic-based shear measurement capability of the system.

The biaxial shear transducers constructed by the researchers mentioned above were based on the same hardware design but in different sizes. Each transducer consisted of 3 disks separated by an elastic material, such as silicone or rubber (Figure 41). The direction of movement of each disk was constrained by ridges and corresponding grooves that were etched on the adjacent surfaces of the disks. The middle disk housed a magnet at its centre, and each of the outer disks contained a magnetoresistive-based sensor. Stainless steel and aluminium were used for the disks for their strength and non-magnetic properties.

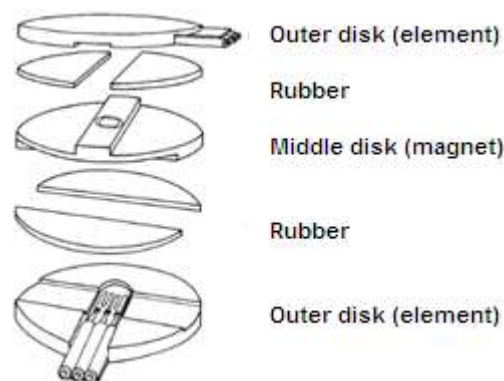


Figure 41 – Exploded assembly of the biaxial shear transducer. (Diagram extracted from Williams et al. (1992))

The dimensions of their transducer were $\text{Ø}16\text{mm}\times 3.8\text{mm}$ with the additional vertical load sensing structure. Shear load was calibrated up to 50N and transducer response appeared to be linear but with 8% hysteresis. Natural rubber was used as the elastic

medium in the transducer, which resulted in a 5% creep during static loading (30N for 30 seconds). The magnetoresistive sensing elements were not an integrated circuit chip, but were connected in a bridge circuit, similar to those described earlier for resistive-based transducers (Section 3.2.2). The voltage outputs from the bridge circuit were then fed to a custom built amplifier circuit. The measurement resolution of the transducer was 0.2N but was reported to be limited only by the signal-to-noise ratio of the output signal. Although the authors published only limited performance characteristics of the transducer (Williams et al., 1992), the work demonstrated that magnetic-based transducers could have high sampling frequencies (in the order of 1000Hz) making them suitable for dynamic gait measurement. Moreover, it should be noted that the magnetoresistive sensing elements used by the investigators could be easily be replaced by the use of more-linear Hall-effect sensor ICs.

3.6.5 Critical review

As demonstrated by several research groups, biaxial shear measurement can be readily achieved using a magnetic-based sensing technique. However, alternative load sensing technologies may be required for triaxial load measurement. This would depend on the movement of the magnet and the sensitivity of the sensing element, hence whether the changes in magnetic field were large enough to be detected. Alternatively, the magnetic field in the vertical direction could potentially be enhanced by using more than one magnet or adding a flux concentrator to the magnetic system. However, this could increase the overall dimensions of the transducer. Depending on the construction of the transducer, a material that exhibit magnetoelasticity could possibility be used. However, this would depend on the amount of flux that could be ‘generated’ under load.

A linear response can be expected from a magnetic-based load transducer with good measurement resolution (~0.2N). The performance of experimental transducers developed previously has suffered from creep and hysteresis, but these effects could likely be minimised by selecting materials with more appropriate mechanical properties. Magnetic-sensors may include temperature compensation circuits, but the

temperature sensitivity of systems that utilise elastomeric materials in their construction would need to be investigated.

In terms of hardware requirements, a linear output can be expected from magnetic field sensor circuits. High sampling rate ($>1000\text{Hz}$) has also been demonstrated. Hardware costs could be minimised by using commercial magnetic sensor ICs. Given analogue voltage output is commonly found in magnetic-based circuits, they could be multiplexed with ease using methods such as active-matrix addressing.

The physical dimensions of a magnetic-based transducer would depend on the arrangement of the magnet(s) and sensor(s) but transducers with a thickness of $<4\text{mm}$ have been demonstrated previously and would be suitable for in-shoe application (Williams et al., 1992). Relatively small transducer sensing surface area would be possible with miniature commercial magnetic sensor ICs (about $3\times 3\times 1\text{mm}$ each), thus the arrangement of multiple transducers could be optimised for high spatial resolution load distribution measurement. A magnetic-based transducer would also be expected to have a long life span (years) since it involves non-contact load measurement.

Moreover, low-cost production would be possible using off-the-shelf sensor ICs. Minimum cabling would be necessary since each sensor IC would have a single output. That said, the amount of outputs per transducer would depend on how many ICs are required for triaxial load measurement. Nonetheless, multiple sensor ICs have the capability of being multiplexed allowing transducers to be incorporated in a matrix arrangement for load distribution measurement.

3.7 Pneumatic and hydraulic based transducers

This section explores and provides a critical assessment of load measurement techniques that use pneumatic-based or hydraulic-based components.

3.7.1 Principle of operation

A hydraulic-based load transducer typically consists of a liquid concealed within an elastic structure. The application of load to the structure would increase the fluid pressure which would be measured, often with a pressure transducer. The pressure transducer could be based on any of the load sensing technologies discussed previously throughout this chapter. The operating principles of a pneumatic-based load transducer would be the same as those a hydraulic-based load transducer, but with gas instead of liquid. However, gas is much more easily compressed than liquid, hence hydraulic-based transducers would be inherently stiffer than pneumatic ones.

3.7.2 Signal conditioning

Amplification circuits and signal conditioning requirements for a hydraulic-based transducer would depend on the chosen pressure sensing technology. Alternatively, commercial pressure sensors with integrated amplifier circuits can be used. Dimensions of commercial pressure sensor ICs vary dramatically depending on their rated capacity and whether integrated signal conditioning circuits are included. A pressure transducer with rated capacity ranging from 50mmHg (7Pa) to 500psi (3450kPa) with built-in amplification typically measures about 13x11x10mm (40PC-250G1A, Honeywell, USA). These transducer ICs can provide an analogue voltage output that is linearly related to the applied pressure with high degree of accuracy (~0.2%). Sampling frequencies in the order of 1kHz is also possible. Voltage outputs could be multiplexed easily as discussed earlier (Section 3.5.2).

3.7.3 Transducer construction

Theoretically, any structure containing liquid or gas can be used as a load transducer, provided the compartment is connected to a pressure transducer. Because any material would deform when subjected to load, a load transducer is realised if the pressure sensor is sufficiently sensitive to detect the changing pressure within the structure. If a special liquid or gas filled hose is used, the pressure transducer used to monitor the change in pressure can be located away from the sensing structure. The sensing part of a hydraulic or pneumatic-based load transducer can be self-contained and would require no external power. Consequently, they can be used in a magnetic resonance imaging facility. However, care would be required to ensure any

movement or external load applied to the hose would not confound pressure measurement.

3.7.4 Current state of the art

Hydraulic based force transducers are commercially available from various companies (such as TST Instruments Ltd, Canada; MGS Ltd, UK; Procter & Chester Measurements Ltd, UK) with typical accuracy <1%RC but are typically large in size (Ø50×30mm) for high load applications (>250kN). A miniature device for measuring interface pressures was previously available from Talley Oxford, UK. The system had been used for the assessment of contact pressures on a mattress (Buckle and Fernandes, 1998). The system consisted of multiple fluid filled bags that could be mounted separately. The fluid in each bag was channelled to its pressure transducer via hoses. Although the performance characteristics of the system were not published within the literature, the instrument could measure pressures at least up to 246mmHg (~32kPa).

A commercial hydraulic-based system (Paromed GmbH, Germany) is currently available for in-shoe plantar pressure distributional measurement and has been used in several published gait studies (Bisiaux and Moretto, 2008; Luninghake et al., 2002). Depending on the size of the shoe, the system from Paromed GmbH consists of up to 36 measuring points across the plantar surface of the foot and has a thickness of 3.5mm. Each measurement point consists of a fluid-filled cell embedded with a micro-pressure transducer. The transducer converts the measured pressure to an electrical signal routed to a recording unit strapped on the waist of the user. The relatively small numbers of transducers in comparison to other commercial plantar pressure systems (Sections 3.2.4.6 and 3.4.4), and the speed of the measurement circuits allowed the Paromed system to have a sampling frequency of up to 300Hz. The hydro-cells, theoretically, are sensitive to both vertical pressure and shear load. However, the system could not be used to differentiate the individual force components. The performance of the system was assessed and measurements compared to a 'gold standard' force platform (Section 3.2.4.1). Chesnin et al. (2000) reported that the device could measure stresses of up to 625kPa with accuracy of

$\pm 2\%$ full scale at a resolution of 2.5kPa. Minimum hysteresis (0.05%), non-linearity ($\pm 0.42\%$) and no apparent drift was observed. The overall centre of pressure data calculated from the Paromed system had good correlation with, and small RMS error ($\sim 1.4\text{cm}$) compared to, a strain gauge-based reference force plate system.

Previous researchers has used hydraulic-based load transducers to measure interface pressure on mattresses (Clark and Rowland, 1989) and hand-grip force (Liu et al., 2000). A pneumatic-based transducer has also been used to measure hand-grip force, by connecting an air-filled elastomeric tube to a commercial piezoresistive pressure sensor IC (Del Maestro et al., 2011). Liu et al. (2000) demonstrated the remote sensing capabilities of these sensors by employing a 9 metre nylon hose ($\text{\O}3\text{mm}$ diameter) between the sensing structures to the pressure transducer, which allowed measurement of handgrip force during a magnetic resonance scan. The design used distilled water as the fluid medium and air bubbles were removed to avoid measurement error. The handgrip measurement device consisted of a handgrip device linked to a piston which would compress the liquid in the tube leading to the pressure transducer. Highly linear output was observed ($R^2=0.999$), but only over a force range of 80N to 800N. The authors hypothesised that the friction between moving parts of the handgrip device might have introduced the error and non-linearity at the low force range ($<80\text{N}$).

3.7.5 Critical review

The measurement of uniaxial load could be achieved easily with a hydraulic-based transducer design. A simple load transducer could be realised using a deformable tube filled with liquid or gas connected to a commercial pressure transducer. Current systems based on this design are sensitive to both vertical pressure and shear load. However, the design does not allow individual force components to be differentiated. Therefore, a novel transducer structure would be required to measure multi-axial load using hydraulic-based components. For example, three deformable tubes filled with liquid could be positioned within a transducer structure to measure each individual force components.

There are currently a large number of commercial transducers available for accurate (~0.2%) measurement of pressure over a range as low as 7Pa to as high as 3450kPa. These transducers are simple to operate and often come with built-in amplifier circuits that will provide a voltage output that is linearly proportional to the applied pressure. However, it should be noted that the characteristics of the load transducer would be highly dependent on the elastic material used to construct the transducer structure. Further research is required to evaluate the frequency response of pneumatic or hydraulic devices for gait laboratory applications. Nonetheless, commercial plantar pressure measurement systems have been demonstrated using hydraulic devices can provide minimum hysteresis, non-linearity and drift. The expansion of gas or liquid due to temperature changes would affect measurement accuracy, but the principle of using a dummy transducer would be sufficient to negate this confounding effect (Sections 3.2.2 and 3.5.4).

In terms of hardware requirements, linear output can be expected from commercial pressure sensor ICs. High sampling rate (>1000Hz) is also possible. Hardware costs would be relatively low by using off-the-shelf components but would depend on the numbers of ICs required for multi-axial load sensing. Analogue voltage output from these circuits could be multiplexed with ease, using methods such as active-matrix addressing, but will also depend on the total number of channels.

Commercial multi-sensor pressure measurement systems have demonstrated that hydraulic-based transducers with minimum thickness (<3.5mm) are suitable for in-shoe applications. In theory, the sensing surface area of the measurement device could be as small as desired (~1mm), provided the applied load to the structure would cause a pressure change detectable via the pressure transducer. Consequently, high spatial resolution (>1 transducer per 11.5×11.5mm area) of an array of hydraulic transducers would be feasible. The movement of the transducer sensing surface may be relatively large if a compliant structure were used to contain the liquid or gas.

Although a load transducer could be realised by simply connecting a commercial pressure transducer to a gas or liquid filled structure, seals must be applied carefully

during production to avoid leakage. Air bubbles in any hydraulic systems should also be avoided. Minimum cabling would be required and each sensor IC would be likely to have a single voltage output that could be multiplexed. Incorporation of special hoses to route the gas or liquid to the transducer, however, could be physically challenging when creating an array of transducers.

3.8 Alternative methods for triaxial load sensing

Some load sensing technologies discussed above in this chapter may not be suitable or practically impossible to be used for triaxial load measurement under the plantar surface of the foot. This section explores alternative methods for triaxial load measurement

3.8.1 Using several measurement systems

A particular load sensing technology may be suitable for load sensing in one particular direction, vertical or shear. A compound instrument constructed by combining two transducers as one could be possible in order to accomplish the ultimate goal of triaxial load measurement. This approach has been adopted by several researchers previously.

As described earlier (Section 3.6.4), a magnetoresistive-based transducer suitable only for shear measurement has been previously combined with a strain-gauged transducer to measure the additional vertical load. In another example, a miniature pressure transducer was placed on top of a capacitive shear transducer (Heywood et al., 2004). A pressure distribution measurement platform was secured on the surface of a ‘gold standard’ force platform during several studies (Macellari and Giacomozzi, 1996, Giacomozzi and Macellari, 1997, Giacomozzi et al., 2000, Giacomozzi et al., 2008). The force platform provided the resultant triaxial load and the pressure distribution measurement device provided the contact area and additional pressure data during gait. Consequently, this compound instrument allowed the researchers to estimate the triaxial load on sub-areas of the foot.

However, the misalignment between the measurement axes of the two systems would increase measurement error.

In one case, the recording of shear and vertical load were conducted in separate trails (Laing et al., 1992). Plantar shear measurement was measured using a magnetic-based transducer during one trial, and pressure distribution measurement was recorded in a separate trail using a capacitive-based device.

3.8.2 Computer modelling

Many researchers have attempted to estimate plantar shear load using mathematical computer modelling. Shear stress is often predicted based on plantar pressure distribution data because they are readily available (Chen et al., 2003, Lott et al., 2008, Dai et al., 2006). Some also attempted to estimate local triaxial load acting on the foot based on the local plantar pressure distribution data and the global ground reaction force obtained from a force plate (Giacomozzi et al., 2008). However, as much as 28% error was observed when comparing real pressure data with those predicted using this technique (Bullimore and Burn, 2007, Fong et al., 2008). As pointed out by many researchers (Sanders, 1995, Yavuz et al., 2007a, Gefen et al., 2000), any mathematical models must first be proven valid against experimental measurements before they can be considered accurate predictors of the loads under the foot.

3.8.3 Critical review

It would be ideal to use the same load sensing technology in a single transducer to measure triaxial load. If not possible, a hybrid transducer combining two or more load sensing technologies to measure multi-axial load would be an alternative. The likely disadvantages of developing a compound transducer includes: 1) the final transducer would be larger in size, 2) more cabling would be expected because different power supply input and transducer output may be required for each technology, 3) precise alignment of the loading axes is required, and 4) manufacturing a combined transducer would likely require more time and incur

greater costs. Computational models should be verified with real-life measurements. Therefore, a multi-axial instrument is needed to develop and validate such models.

3.9 Discussion

The basic operation of 7 different load sensing technologies has been explored, namely: resistive, piezoelectric, capacitive, optoelectronic, magnetic, pneumatic and hydraulic-based technologies. The signal conditioning and electronic circuit requirements that are likely to be required in each technology were considered. This provided an indication of the complexity of utilising a particular technology in a load measurement system. Possible ways of constructing a load transducer based on any one particular technology were also discussed. Some of the existing load measurement devices were explored to provide an insight into how each load sensing technologies can be utilised and the possible characteristics of the transducers. Alternative methods of combining two load measurement systems to measure multi-axial loads were also explored. The advantages and limitations of each method have been critically reviewed.

This section will summarise the findings and compare all 7 technologies against the requirements of this study (Section 2.4.1) with the aim to identify those appropriate for the development of a low-cost multi-axial load distribution measurement device.

A scoring system is used to compare the potential of each technology to meet each of the requirement categories (Section 2.4.1): ranked from 1 to 7, where 7 is scored to the technology with the highest potential and 1 to the least. The scores from each requirement category are summed to identify the technologies with high potential. The scoring process inevitably involved a degree of subjective judgement. The author has given the scores with minimum impact from any potential bias. However, higher scores have been awarded in favour to technologies that could perform well in an in-shoe measurement system.

- **Essential requirement: biaxial shear or triaxial load measurement**

Resistive-based and piezoelectric-based force platforms are currently regarded as the ‘gold standard’ in triaxial load measurement and have been used extensively in gait analysis. However, resistive-based device often require large transducer structures which are unsuitable for in-shoe measurement. Although miniature transducers have been demonstrated, their sensing elements are subjected to mechanical wear and tear. Thus, the life span of these devices was expected to be relatively low. In comparison, negligible deformation can be expected in piezoelectric-based devices. But piezoelectric materials are relatively more sensitive to bending forces and edge loading effects which would affect the accuracy of triaxial load measurement, especially during in-shoe measurement. Capacitive-based devices are also sensitive to off-axis loading or unevenly distributed load. Such a problem could potentially be solved by strategically mounting piezoelectric materials that are only sensitive to a particular load axis in a transducer. However, currently there are no potential solutions for capacitive-based devices. Simple optoelectronic-based triaxial load transducers have been demonstrated by using multiple light emitter and photodiode pairs. Their performance was found to be comparable to resistive-based devices but with the advantage that they could be miniaturised. Miniature biaxial shear transducers based on magnetic-based technology have been previously used for in-shoe applications and when combined with other load sensing technology have the potential for in-shoe triaxial measurement. There is currently no pneumatic-based or hydraulic-based transducer capable of multi-axial load measurement. However, the simplicity of using a gas or liquid filled deformable tube as the sensing element makes it an attractive option for multi-axial load sensing.

Technology	Resistive	Piezoelectric	Capacitive	Optoelectronic	Magnetic	Pneumatic	Hydraulic
Score	2	5	1	6	7	3	4

- **Category A: Transducer performance**

Performance of resistive-based devices is very dependent on the sensing element used for load sensing: high accuracy (~3%), low hysteresis (~2%) and non-linearity (~2%) can be expected from strain gauge-based transducers, but this is not necessarily the case for FSR-based devices. Frequency response in strain gauge-based device was high (~400Hz) provided the transducer was constructed from

material with high stiffness. This is also the case in piezoelectric-based devices, where the active element is typically stiff, making it suitable for measuring high frequency loads ($\sim 1000\text{Hz}$). However, the inherent charge leakage that is characteristic of piezoelectric-based systems render them less suitable for static load measurements. Piezoelectric-based devices can perform well in terms of hysteresis, non-linearity ($\sim 0.5\%$) and rated capacity ($\sim 17\text{kN}$ vertical load, $\sim 8\text{kN}$ shear load), but measurement accuracy is highly dependent on the design of the amplifier circuit. Without expensive circuit components, the drift in signal would severely affect the accuracy and usefulness of the absolute measurement output from the device. Capacitive-based devices were found not suitable for low load measurement ($< 15\text{kPa}$), and the output response is inherently non-linear and requires compensation via circuitry or software. It is likely that an elastomeric medium would be required between the capacitor plates. Therefore, the frequency response of the transducer would be inferior to other load sensing technologies. Like any other method, performance of optoelectronic-based devices are dependent on properties of the materials used in the construction of the transducer structure. The compliance of optoelectronic-based devices may be inferior to strain-gauge-based devices but may still be sufficiently stiff to ensure a high frequency response. Accuracy ($\sim 0.3\%$) and linearity of optoelectronic-based devices can potentially be better than other load sensing technologies with careful transducer design and selection of transducer structure material. The same is also true for magnetic-based transducers, where linear response and high measurement resolution ($\sim 0.2\text{N}$) can be expected when appropriate structural materials are used. Commercially available magnetic field and pressure sensor chips can provide easy and accurate measurement of these physical quantities. As such, pneumatic-based and hydraulic-based devices can also benefit from these commercial sensors for accurate ($\sim 0.2\%$) load measurements. Pneumatic-based transducers, however, are more likely to suffer from low frequency response than hydraulic-based transducers due to the compressible nature of gas. Although resistive and piezoelectric-based systems are the current gold standard for platform systems, their performance may not be retained in a system for in-shoe measurement, hence their lower scores below.

Technology	Resistive	Piezoelectric	Capacitive	Optoelectronic	Magnetic	Pneumatic	Hydraulic
Score	5	2	1	7	6	3	4

- **Category B: Hardware**

The sampling frequency of the system is independent of the technology used for load sensing. It depends on the total number of transducers in the system, the number of signal outputs from each transducer and the sampling rate of each transducer. Existing devices have demonstrated that sampling frequency adequate for gait analysis ($\geq 200\text{Hz}$) is achievable using resistive-based or FSR-based technology. However, depending on the characteristics of the strain gauges used, power requirements and hardware costs may be high for strain gauged devices. The provision of power may also be an issue for in-shoe measurement. Although piezoelectric-based sensors may not require a power source and may reduce cabling requirements, expensive low-noise cable connections are necessary between piezoelectric circuit components. Expensive charge amplifiers are also required to minimise error caused by the inherent drift in the signal output. Capacitive-based transducers, in comparison, are theoretically cheap to make just requiring two conductive and electrically charged electrodes. The signals from capacitive-based transducers can also be multiplexed easily as demonstrated by commercial devices capable of load distribution measurement. Similarly, multiplexing capability for optoelectronic-based transducers is also assured by using the same technique used in video camera sensors. Depending on the number of photodiodes, high sampling frequency is possible with optoelectronic circuits. Considerable computing power for data processing would be required if a high-pixel count video technique is used for load measurement. LEDs and photodiodes, in contrast, are relatively low-cost and would consume relatively low power in comparison to strain-gauged devices. Power consumption can be expected to be even lower if commercially available magnetic-field and pressure-sensor chips are to be used. These chips can be used in magnetic-based transducers and pneumatic-based or hydraulic-based devices, and in addition to being low-cost, they provide high sampling rates and their voltage output can be multiplexed. Although pneumatic and hydraulic systems may still require the use of

resistive-based transducer to convert pressure changes to an electrical signal, they do not necessarily carry the same disadvantages of these technologies. That is because the electronics used to monitor the change in pressure can be located away from the sensing structure.

Technology	Resistive	Piezoelectric	Capacitive	Optoelectronic	Magnetic	Pneumatic	Hydraulic
Score	2	1	7	3	6	4	5

- **Category C: Physical requirements**

Miniature FSR or piezoresistive-based transducers already exist, but strain gauge-based designs are unlikely to be suitable for in-shoe applications. That said, strain gauge-based transducers that are long but with relatively small sensing surface area (10.27×10.27×160mm) have been demonstrated previously in platform-based systems with good spatial resolution (1.5mm spacing between transducer). While strain gauges are bonded to structures that often show little deformation, piezoresistors or FSRs would be subjected to wear and tear, thus their life span would be expected to be relatively low (~30 gait cycles). Piezoelectric-based transducers displayed negligible deformation, so adjacent transducers could be placed near each other for high spatial resolution measurement. Small and thin transducers (13×13×2.7mm) based on one or several piezoelectric materials have been demonstrated previously. Due to their small dimensions, manual handling and manufacture of the transducer may be difficult. The reliability and life span of the system would depend on the quality in the manufacturing process - bonding the piezoelement and electrode connections. In contrast, capacitive-based transducers have superior physical characteristics because they can have a very simple structure, where two thin electrode plates would be sufficient. As such, capacitive-based transducers could potentially be very thin (1mm) with small sensing surface area that would allow high spatial resolution measurement (5×5mm sensing area). The advancement in flexible miniature optoelectronic components or the use of optical fibres may allow the manufacture of miniature transducer for in-shoe applications. However, optic fibres cannot be bent to a small radius (<10mm) and the life span of flexible circuits under repeated stress during gait would require further research. LEDs and photodiodes themselves are small in size (~2mm), thus transducers with

small sensing surface areas and transducer arrays with good spatial resolution could potentially be developed. Magnetic-based transducers with minimal thickness (3.8mm) suitable for in-shoe application have been demonstrated previously. Small transducer sensing surface area (~10mm²) would be possible with miniature magnetic sensor ICs that are commercially available. Also, a relatively long life span would be expected from a magnetic-based transducer because it is a contactless load sensing technique. Hydraulic-based transducers that are suitable for in-shoe applications are currently commercially available. The design of pneumatic or hydraulic-based transducers could be customised and adopted easily for high spatial resolution measurement because they could perform similarly to optical fibres if the gas or fluid-filled structures were small deformable tubes.

Technology	Resistive	Piezoelectric	Capacitive	Optoelectronic	Magnetic	Pneumatic	Hydraulic
Score	1	2	7	6	5	3	4

- **Category D: Manufacturing requirements**

The time consuming process of adhering strain gauges makes these types of transducer relatively expensive to manufacture. Thin-films may be an alternative method, but the many wire connections necessary for a resistive-based transducer would also make the construction of an array time consuming. FSR-based systems, in contrast, are suitable for low-cost batch production. The manufacturing of piezoelectric-based transducers, however, could be expensive as precise bonding of the piezoelement and precise attachments of electrodes are required. On the other hand, piezoelectric-based transducers are different from other sensing techniques in that they are active sensing elements and require no power supply, hence cabling time could be minimised. Batch production of capacitive-based transducer arrays can be achieved. However, this may only be applicable to systems capable of uniaxial pressure measurement, unless a novel way of arranging the capacitive plates for shear measurement could be developed. The same applies to FBG transducers; locating FBG fibres in a transducer structure for shear measurement would require some novel design ideas. However, FBGs can be batch produced and be incorporated in a matrix arrangement with ease. Transducers using LED-photodiode pairs with commercially available amplifier and signal processing circuits would require less

time to manufacture too. These circuit boards are small and could be built inside the transducer, saving space and allowing transducers to be arranged next to each other. Off-the-shelf sensor ICs are available for magnetic-based transducers. These ICs are small in size and require minimum cabling time. Pressure sensor ICs are also available for pneumatic and hydraulic-based transducers. However, care must be taken during the manufacturing of hydraulic-based transducers to avoid air bubbles and leakage, which require extra time for quality inspection.

Technology	Resistive	Piezoelectric	Capacitive	Optoelectronic	Magnetic	Pneumatic	Hydraulic
Score	1	2	6	5	7	3	4

The overall scores for each load sensing technology have been calculated and are further discussed in the next section (Section 3.10) to identify those worth investigating for their suitability for the development of a low-cost multi-axial load distributional measurement device.

3.10 Conclusion

The overall score for each of the load sensing technologies is shown below.

Technology	Resistive	Piezoelectric	Capacitive	Optoelectronic	Magnetic	Pneumatic	Hydraulic
Essential requirement	2	5	1	6	7	3	4
Category A	5	2	1	7	6	3	4
Category B	2	1	7	3	6	4	5
Category C	1	2	7	6	5	3	4
Category D	1	2	6	5	7	3	4
Total	11	12	22	27	31	16	21

It can be seen that several load sensing technologies might be considered to have potential for use in the development of a low-cost multi-axial distribution measurement device. Magnetic-based and optoelectronic-based techniques displayed the highest potential for fulfilling the objectives of this study. Capacitive-based technologies had a relatively high overall score, but failed to meet the essential criteria of being suitable for multi-axial load measurement. Consequently, capacitive-based technologies were not investigated further. Pneumatic-based and hydraulic-based methods were found to have similar characteristics and their design could be interchangeable by replacing liquid with gas or vice versa. However, hydraulic systems are inherently stiffer and hence they possess higher frequency response than

pneumatic systems. The potential for developing a relatively simple load distribution measurement device using hydraulic-based system is clear. This technology was therefore selected for further investigation. Both resistive-based and piezoelectric-based technologies had the lowest scores, partly due to hardware requirements, cost and difficulties associated with batch production. However, piezoelectric-based systems scored reasonably in the pre-condition requirement in that they have one of the highest potentials for development of miniature devices for triaxial load measurement. Moreover, a piezoelectric-based triaxial load transducer was made available during this study which allowed a comprehensive evaluation of such technology. It was concluded that transducers using the following 4 technologies would be investigated further:

1. Piezoelectric-based transducers
2. Hydraulic-based transducers
3. Optoelectronic-based transducers
4. Magnetic-based transducers

Chapter 4

Calibration Methods

Calibration procedures for load transducers have to be accurate and time effective, especially for a load distribution measurement device where hundreds of individual transducer elements may require calibration independently. The basic calibration procedure simply involves taking a measurement while applying a known reference load. However, there are many techniques used in the application of the reference load that could influence the performance of the calibrated transducer. This chapter explores the many standard practices and procedures currently used in the calibration of load transducers. The objective of examining the methods used in the literature was to provide guidance for the current study. Finally, a novel and effective calibration device and its operating procedures for the calibration of multi-axial load transducers has been proposed and utilised in the current study.

4.1 Primary and secondary force calibration standards

Force standard machines are machines for undertaking force calibration on load transducers and can be categorised as either primary or secondary. The performance of a primary standard machine can be verified through physical principles directly to the fundamental base units such as mass (kg) and time (s). For example, a machine that uses deadweight of known mass suspended in the earth's gravitational field to generate a load on the transducer to be calibrated would be a primary standard machine.

Secondary standards are machines which rely on the reproduction of forces that can be compared to primary standards by the use of a calibrated reference force transducer, which are sometimes also referred to as force transfer standards. A reference force transducer is often placed in a materials testing machine in series with the load transducer to be calibrated.

The use of the primary standard and handling of heavy weights could be problematic especially when numerous transducers would require calibration during this study. Therefore, the current study used the secondary standard and calibrated the transducers against reference load cells. The instruments and procedures used will be discussed in the following chapters.

4.2 Static, dynamic and multi-axis calibration

Static and dynamic calibration techniques are both commonly used in the calibration of load measurement instruments. Static calibration, also referred as step loading, is usually achieved by applying known loads using deadweight and recording the transducer output. Whereas dynamic calibration is commonly conducted using material testing machines to apply a loading-unloading cycle to the transducer within a specific time interval. The loading regime should be representative of the loading conditions that the transducer will be subjected to in real-life situations. Material

testing machines can also be instructed to carry out static calibration by applying step loads.

There are various documents and international standards (e.g. ASTM E 74 and BS EN ISO 376) currently available that cover the calibration of uniaxial force instruments in static mode. In the absence of standardised procedures for dynamic force calibration, many of the published plantar load measurement devices were calibrated statically (Davis et al., 1998, Berme et al., 1976, Cong et al., 2011, Heywood et al., 2004) and the results were assumed to be applicable for dynamic force measurements. Very few systems were calibrated under dynamic mode (Chen et al., 2010). A static calibration process would not necessarily require a costly material testing machine and the procedure can be simple for any transducer that has a linear response. However, dynamic calibration is more desirable for systems with time-dependent characteristics. While the ability of a transducer to respond to high frequency loads can be evaluated by analysing its impulse response, care must be taken to avoid damage to the transducer when subjected to large impulse loads.

Multi-axis calibration is usually identical to single axis calibration but done once for each axis. Again, there is no standard currently available for the calibration of multi-axial load instruments in either static or dynamic mode. However, proper mounting for precision alignment and orientation of the transducer is critical to its calibration and performance during use. All multi-axial transducers suffer from crosstalk (see definition in Appendix A), which is the effect on different axis component than the one where the load was applied. Any off-axis load applied along one axis, the other axis component would be subjected to a real load in addition to crosstalk. Therefore, the transducer should be mounted between smooth, flat and parallel surfaces during calibration. The correct alignment between the transducer and the contact surfaces is paramount to prevent non-uniform loading or bending moments. There are many factors that would cause non-uniform loading and thus poor measurement results, these include but are not limited to: 1) surface not parallel, 2) surfaces not flat, and 3) there are surface defects, such as chips, fractures, dimples or spikes on the surfaces.

4.3 Differences in pressure and force calibration

Load measurement devices can be classified as ‘pressure transducers’ or ‘force transducers’, and it is important to distinguish between the two. Although a certain type of transducer may fall between these two categories, their classification is dependent on how they were calibrated and hence their intended use.

Force transducers are often calibrated by applying loads through a rigid structure, thus their output may be considered estimates of force (Urry, 1999). An ideal force transducer would respond identically to two equal loads regardless of the area or the location of the applied load. Calibration load to a pressure transducer is usually applied via a compliant structure, such as an air-filled membrane to ensure an evenly distributed pressure across the sensing surface of the transducer (Urry, 1999). In that case, the transducer output is a reflection of the pressure. An ideal pressure transducer, under constant loading conditions, would produce output that is inversely proportional to the area over which the load was applied.

4.4 Existing calibration methods

This section explores the many methods currently used in the calibration of multi-axial load transducers. The basic calibration procedure for vertical load involves taking a measurement from the transducer while applying known loads directly on top of the transducer. The two outputs would then be used in a mathematical algorithm through a least-square optimisation to estimate the calibration matrix. Crosstalk in the shear axes would be investigated by simultaneously taking the output from the shear channels during vertical loading compared to their corresponding output at its rated capacity. However, as discussed above (Section 4.2), there is currently no international standard for the calibration of shear or multi-axial load transducers in either static or dynamic mode. In contrast to uniaxial vertical loading, it is physically more challenging to conduct tests along the shear axes. As a result, various methods have been used by different investigators.

Pulley systems are widely used to apply shear load during calibration (Laing et al., 1992, Tappin et al., 1980, Lebar et al., 1996, Davis et al., 1998, Cong et al., 2011). A pulley system was also used for in-situ calibration of a force plate system (Hall et al., 1996). In a pulley system, a cord often attached via a cap or directed to the sensing surface of the transducer and aligned along the surface of the transducer would run over the top of a pulley and down where weights are hung. Increasing or decreasing weights are hung from the pulley to perform calibrations. The orientation of the cord would determine the direction of the applied shear load. Sufficient lubrication of the pulleys and the alignment of the cord to transducer axes are important for accurate shear measurement. The pulley system has its advantage being simple and requires only apparatus that are often readily available in the laboratory. However, precise attachment and alignment of the cord to the transducer, and the handling of heavy weights (~350N) in a pulley system would be time consuming when numerous transducers would require calibration during this study.

Ideally, a transducer system intended for multi-axial load distribution measurement during gait should be calibrated in dynamic mode to simulate real-life conditions. Shaker systems (Physikalisch-Technische Bundesanstalt, Germany) have been previously employed in the evaluation and dynamic calibration of a multi-axial force-moment transducer (Park et al., 2002). The shaker system was a primary standard method of calibration based on Newton's law. Figure 42 illustrates the operating principle in uniaxial vertical calibration, but the same applies to shear calibration by mounting the transducer sideways (Park et al., 2002). A mass was attached to the sensing surface of the transducer and the assembly was mounted onto the shaker machine. The shaker, or vibration exciter, was then used to generate dynamic excitation to the transducer base. The inertia of the seismic mass would generate dynamic force to the transducer. A laser-doppler-interferometer was used to detect the acceleration of the known seismic mass, and the force was subsequently calculated using Newton's law (Figure 42).

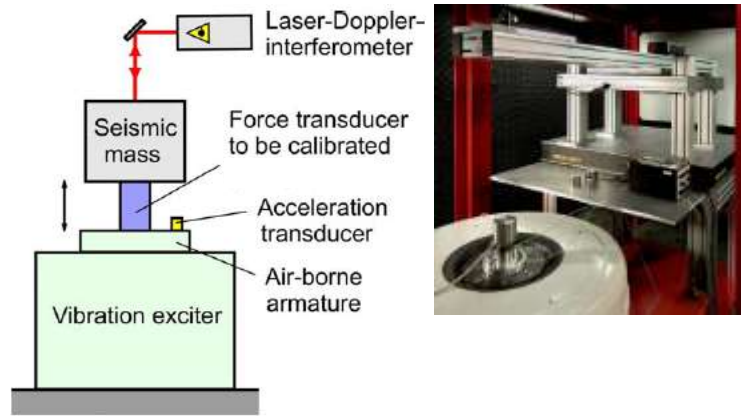


Figure 42 - Shaker system at the PTB for dynamic calibration. (Images from Dr. Andy Knott, National Physical Laboratory (NPL), UK, pers. comm.)

To avoid the costs and technical complication associated with using laser-doppler interferometer (Hoiting, 2005), the calibration procedure could be modified to a secondary standard by using reference load cells instead of measuring acceleration. As demonstrated in Kärki et al. (2009), a shaker or a material testing machine can be used to generate dynamic excitation, but instead of tracking the acceleration of the seismic mass, reference load cells are attached to the transducer and their respective outputs are used for calibration purposes.

Mounting of the transducer in its sideways positions for shear measurement, however, could be challenging especially for miniature transducer that have no mounting mechanisms. Consequently, double sided adhesive tape has been previously used for mounting transducers to the calibration rig (Kärki et al., 2009). Instead of repositioning the transducer between vertical and shear calibrations, an alternative would be to use several actuators/exciter to apply load from different directions. A block on top of the transducer is used to allow forces to be transmitted through to the transducer (Figure 43). Two actuators with built-in load measurement capability were then used to apply each component of forces separately to the block (Li et al., 2009a, Li et al., 2009b, Li et al., 2009c). Similar setup of using multiple actuators to apply multi-axial load is also used by manufacturers (Kistler Group (Switzerland), AMTI Inc (USA), pers. comm.) for calibrating their force plates.

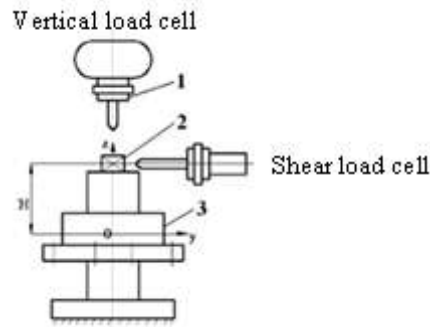


Figure 43 – Diagram of calibration for measuring dynamic vertical load and shear: 1) actuator mechanism with built-in load transducer, 2) detachable block, 3) the transducer to be calibrated. (Modified diagram from Li et al. (2009b))

There are other methods than using a least-squares linear fit of characterising the relationship between the device output and that of the applied load via the calibration instrument. It should be noted, however, that least-squares methods are only suitable for transducers with linear response. Neural-work based calibration methods (Lu et al., 1997) and additional calibration adjustments, such as the use of higher order functions, have been advocated that may bring the transducer into a state of performance more suitable for its use (Hirose and Yoneda, 1990). These methods often require additional tests to be conducted on the transducer and, as such, are more time consuming. Calibration adjustment is specific to the design of the transducer being tested. Extra calibration steps may be time consuming and the improvement in transducer measurement accuracy should be weighed against these extra time and resources implications.

4.5 Calibration apparatus for this study

A custom designed calibration rig was constructed to allow calibration and evaluation of different experimental transducer designs that were manufactured in the current study. The design used in the current study was not too dissimilar to that shown in Figure 43, in that actuators were used to apply static or dynamic load to a stationary transducer. The calibration rig was designed to facilitate transducer calibration in three different conditions: 1) uniaxial vertical calibration, 2) uniaxial shear calibration, and 3) simultaneous application of vertical and shear load (biaxial loading).

Table 3 - Relevant specifications of the Nano25 load cell.

Axis	Vertical load axis (Z)	Shear load axes (X and Y)
Rated Load Capacity	$\pm 500\text{N}$	$\pm 125\text{N}$
Load resolution	0.06N	0.02N
Measurement error	0.05% full scale	0.03% full scale

The aluminium calibration rig was designed to be manually operated and consisted of three main parts (Figure 44): 1) a six-channel reference load cell (Nano25, ATI Industrial Automation, USA) which was mounted onto a translation stage along the base plate of the rig; 2) a vertical linear bearing with a steel rod (Loading rod) installed on a movable tower platform; and 3) a linear bearing (DryLin® RTA-01-20, Igus Ltd, UK) with another steel rod situated on an adjustable tilting platform via two friction window hinge joint. These parts and other components of the calibration rig are listed in Appendix B. The specifications of the reference load cell can be seen in Table 3.

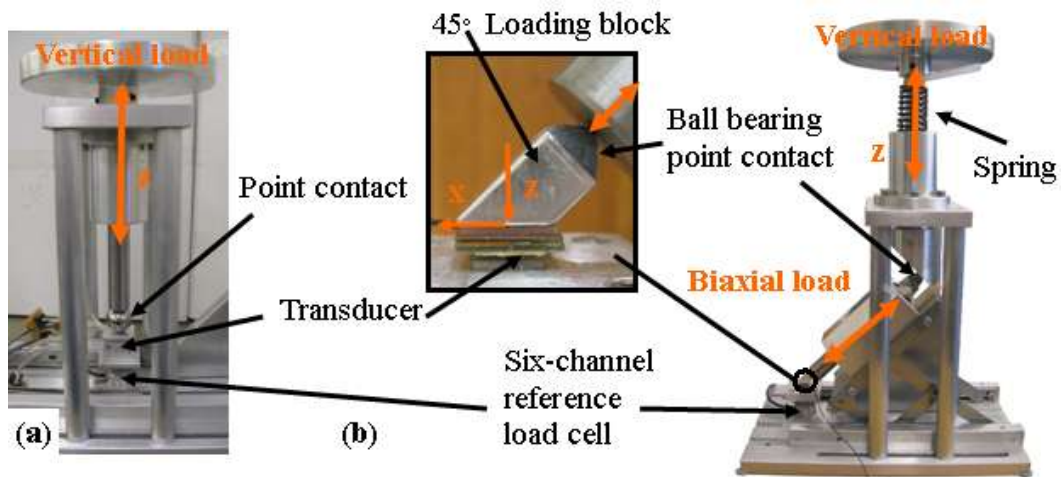


Figure 44 - Adjustable calibration rig for uniaxial calibration in the vertical direction (a) and for simultaneous vertical and shear load (b).

A flat aluminium plate (Mounting platform, 39×39mm) was secured onto the reference load cell to allow transducers of larger sizes to be mounted on its upper surface. During vertical calibration, the vertical loading rod (Figure 44a) was positioned in line with the vertical axis of the reference load cell. A ball bearing attached in series with the loading rod was used to apply vertical load to the transducer. A flat aluminium plate placed in between the ball bearing and the

transducer was used for spreading the load across the effective area of the transducer. Dynamic calibration could be conducted either manually applying load to the top end of the loading rod (Figure 44a), or automatically using an alternative loading mechanism such as a motor-driven actuator. A compression spring allowed the loading rod to recover to its initial position following the removal of load. Dead weights of known mass can be placed on top of the dish for static calibration.

During shear calibration, the adjustable tilting platform was lowered so its linear bearing was aligned along the shear axis of the transducer to be calibrated. Shear load was then applied via the loading rod towards the edge of the transducer or to the sides of the loading block that was attached to the top of the transducer. The transducer was mounted in different orientations allowing calibration of all four shear directions in separate tests. To simultaneously apply vertical and shear load to the transducer, the tilting platform was raised at an angle of 45° (Figure 44b). An angled adaptor was attached to the bottom end of the vertical loading rod. The other end of the tilted rod has a point contact with a 45° loading block that was secured onto the sensing surface of the transducer (Figure 44b). The 45° loading block allowed a combined vertical and shear load to be transmitted to the transducer. Dynamic calibrations were conducted by hand in an uncontrolled manner, but dead weights of known mass can be placed on top of the dish for static shear calibration.

The signal outputs from the reference load cell were fed to a data acquisition (DAQ) system (USB-6225, National Instruments Corps, Ireland) connected to a laptop running LabView software (Version 8.6). The DAQ system was controlled via a LabView program which was provided by the load cell manufacturer to ensure reliable acquisition and accurate voltage-to-force output conversion. The LabView program was modified to allow storage of data from the reference load cell together with any other outputs from the transducers to be calibrated. The calibration rig provided an effective way of generating vertical and/or shear load in a repeatable and controlled manner. The way in which each experimental transducer was secured to the mounting platform during calibration is described in Chapter 5 below.

The calibration rig described above provided a quick and easy method for the calibration and evaluation of transducer prototypes that were manufactured in the current study. While it allowed controlled application of static loads, dynamic calibrations were not well controlled. Consequently, once each prototype design was optimised, a more controlled loading system was employed to provide a more detailed evaluation of transducer performance. A different second-standard material testing machine (ElectroForce3200, Bose Corp., USA) became available during the course of the current study and were used over the calibration rig described here. These will be discussed in later chapters describing the calibration procedures.

It should be noted that due to the mechanical design of the calibration rig, in particular with the tilting platform set at an angle of 45° , the force experienced by the transducer to be calibrated would be less than the magnitude of force being applied to the rig. This would not be an issue because any force experienced by the transducer is transmitted through and detected by the six-channel reference load cell. Calibration tests have been conducted based on the force signal from the reference load cell and not the physical force or dead-weight being applied on the rig. However, if any medium, such as adhesive tape, is placed between the reference load cell and the transducer to be calibrated, it would alter the compliance of the calibration setup and should be taken into account.

Chapter 5

Development of triaxial load transducers

This chapter outlines the development and preliminary evaluation of various novel triaxial load transducer designs based on different load sensing technologies. Piezoelectric, hydraulic, optoelectronic and magnetic based technologies were previously identified (Section 3.10) for their potential to be used in the construction of triaxial load transducers that would satisfy the system requirements described in Section 2.4.1. The current study benefitted from the availability of a pre-existing piezoelectric triaxial force transducer prototype from the University of Kent. The piezoelectric based device and other novel transducer design prototypes based on the other 3 technologies mentioned above were evaluated for their suitability in measuring triaxial load. Prototypes with the potential to satisfy the requirements of the current study would be developed further to achieve the primary goal of the study – namely, the development of a multi-axial load transducer suitable for incorporation in a large array for load distribution measurement.

5.1 Evaluation of a piezoelectric based triaxial load transducer

As discussed in Section 3.3.4, the research group at the University of Kent had described the development of a triaxial piezoelectric force transducer to quantify the triaxial force under discrete location of the plantar surface of the foot within an in-shoe environment. The group at Kent had kindly forwarded some of their transducers together with the charge amplifier circuit to allow a first-hand evaluation of their system. Limited characterization of the device has been presented in their papers (Razian and Pepper, 2003, Razian and Pepper, 1998). This chapter further characterises their piezoelectric system and has been reported elsewhere (Lau et al., 2008). The following sections provide a summary of the evaluation. However, the primary objective of the investigation was not to assess the performance of the ‘Kent’ system. The ‘Kent’ system was taken as a representative piezoelectric based device to evaluate the suitability of piezoelectric material in the design of triaxial load distribution devices.

5.1.1 The ‘Kent’ triaxial force transducer system

The piezoelectric copolymer used in the ‘Kent’ triaxial transducer had a mixed composition of polyvinylidene fluoride (PVDF) and trifluoroethylene (TrFE) (Razian and Pepper, 2003). A 10×10mm element of the piezoelectric film (500µm) was sandwiched between three double sided printed circuit boards (PCB) of 0.7mm thickness (Figure 45). The upper PCB measured 10×10mm and the two lower PCBs measured 13×13mm. The overall transducer dimensions were 13×13×2.7mm.

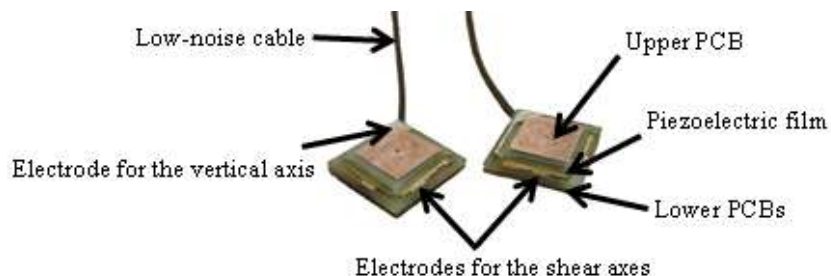


Figure 45 – Piezoelectric triaxial force transducers from the University of Kent.

The PCBs were used to provide electrodes for cable connections as well as electrical shielding. The lower PCBs facilitated cable attachment, provided physical protection to the electrode surfaces and also prevented external load from touching the sides of the piezoelectric film. To avoid soldering and heat exposure to the piezoelectric film, cables were attached to the electrodes by means of silver loaded epoxy adhesive (Razian, 2000). A different silver conductive paint was applied to connect the four sides of the piezoelectric film to the electrodes. A gap at the end of each side was left without paint to avoid shorting (Razian, 2000). A central groove and four small channels in the lower PCBs allowed a low-noise tricoax-cable (1mm diameter) to be embedded between them. The piezoelectric film and the PCBs were bonded using non-conductive epoxy resin. The smooth surfaces of the copolymer film needed to be carefully roughened to improve bonding to the PCBs. Finally, the transducer was covered with PCB lacquer for electrical insulation.

The band pass characteristics of the charge amplifier circuit used in this evaluation had a frequency response of about 0.01Hz to 250Hz (Matthew Pepper, University of Kent, pers. comm.). As with any electrical system for measuring DC charges, high-quality electrical insulation was paramount for the ‘Kent’ piezoelectric transducer which operated in charge mode (Section 3.3.2). The low-noise tricoax-cable used in the ‘Kent’ system was a bespoke product and the manufacturer had minimum order requirements. As a result, low volume production of the transducer would be relatively expensive. An up-to-date quotation from the manufacturer revealed that a two-core low-noise cable of the same type would require a minimum order of £2700 per 400m (Lynda Terry, Habia Cable Ltd, UK, pers. comm.).

5.1.2 Data acquisition

The piezoelectric transducer and the charge amplifiers from the ‘Kent’ research group were evaluated as-is, with no modifications, except the charge amplifier circuit provided was secured in a plastic enclosure for protection. The three cables from the piezoelectric sensor were connected to the charge amplifier circuit using the RS-232 connector on the plastic enclosure. The charge amplifier circuit was powered via the $\pm 5V$ outlets from a bench top power supply. The three outputs channels from the

charge amplifiers were connected to a data acquisition system (DAQ) (USB-6225, National Instruments Corps, Ireland). Data recording was controlled via a custom program written in LabView8.6 (National Instruments Corps, Ireland).

Although it was not the primary goal of this study, it should be noted that a full calibration and characterisation of the ‘Kent’ system was not possible. It was found that the piezoelectric film of the transducer was detached from the PCB assembly during the application of shear loads as little as 40N, which was significantly lower than the rated capacity (500N) of the transducer (Razian and Pepper, 2003, Razian and Pepper, 1998). Similar observations were made by other researchers undertaking calibration testing of the ‘Kent’ transducers (Thornton, 2009). It was possible that aging of the epoxy resin used in bonding the transducer resulted in delamination of the transducer. As a result, limited data were gathered, particularly for the shear axes. Nonetheless, the tests conducted have provided sufficient insight into the usability of piezoelectric material in the design of a triaxial load distribution device.

5.1.2.1 Transducer calibration

Two distinctive calibration configurations were used to evaluate the ‘Kent’ piezoelectric system: 1) pure vertical loading using a computer-controlled material testing machine (Lau et al., 2008), and 2) pure vertical and biaxial loading using a manually controlled transducer calibration rig.

Computer-controlled calibration setup

The piezoelectric transducer and amplifier circuitry were further shielded with aluminium foil (Figure 46) to minimise electrical noise during testing. The transducer was fixed to the mounting plate of the material testing machine with adhesive tape. A 10mm aluminium cube (loading block) with a recess at the top for a steel ball bearing ($\text{Ø}5\text{mm}$) was placed on top of the transducer during vertical loading (Figure 46). Visual inspection indicated that the lacquer coating of the transducer was not uniformly flat. Moreover, initial pilot testing suggested the transducer was sensitive to surface irregularities, thus the transducer was evaluated under different loading conditions:

1. Vertical load applied via the loading block.
2. Vertical load applied via the loading block rotated 90° to test how surface irregularities of the block influenced transducer output.
3. Vertical load applied via the loading block with intervening rubber on top and beneath the transducer to ensure the load was evenly distributed across the transducer surface (Figure 46).

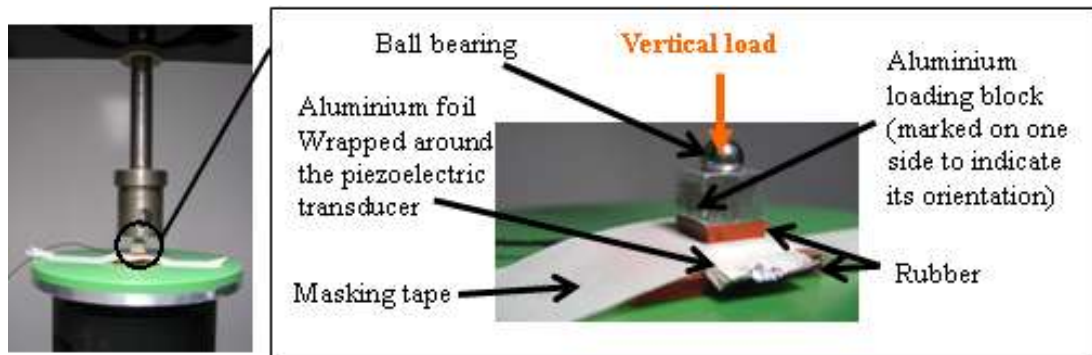


Figure 46 – Calibration setup in the Instron 5800R material testing machine during vertical testing.

A series of pure vertical (Z-axis) loading regimes were applied to the piezoelectric transducer via a uniaxial material testing machine (5800R, Instron, USA) (Lau et al., 2008). Input loadings were implemented including: impulse (rapid loading of 42N and unloading in 2seconds); step load input (42N for 40 seconds); and sinusoidal cyclic loading (2N-42N at 1Hz). Detailed descriptions of the loading sequences have been included in 0. All loading sequences began with a 10s load hold at nominal zero load, ensuring transducer outputs were stable about zero volts. Each sequence finished with a 40s load hold to allow evaluation of the decay in transducer output, which is typically exponential in a piezoelectric system (Lord and Smith, 1983). Force data from the material testing machine and the three voltage outputs from the transducer system were sampled simultaneously at 200Hz using the DAQ system (USB-6225).

Manually controlled calibration setup

Further tests were conducted to evaluate the transducer performance in the shear axes. The transducer was secured to the mounting platform of the calibration rig

described earlier (Section 4.5) to allow manual application of pure vertical load as well as biaxial load (Figure 47) to the transducer. The performance of the piezoelectric transducer was evaluated against a six-channel reference load cell (Nano25, ATI Industrial Automation, USA) (Figure 47). Force outputs from the reference load cell and the three voltage outputs from the transducer system were sampled simultaneously at 200Hz using the DAQ system (USB-6225).

The transducer was carefully aligned to the measurement axes of the reference load cell before it was adhered to the mounting platform using double-sided rubber adhesive (No-more-nails on a roll, UniBond), which ensured a more uniform distribution of load to the transducer surface. As with computer-controlled calibration testing, vertical load was applied to the transducer via a 10mm aluminium cube positioned in series with a steel ball bearing ($\varnothing 5\text{mm}$), however, the transducer and the charge amplifiers were not wrapped with aluminium foil (Figure 46). Dynamic vertical load, over a range of about 0-30N, was manually applied via the calibration rig for 30 seconds at a rate of approximately 1Hz.

The calibration rig was also used to apply biaxial load. Biaxial load was applied via a 45° angled loading block made of aluminium (Figure 47). Dynamic biaxial load was applied manually at about 1Hz over the ranges of $\pm 30\text{N}$ for 30 seconds. Because the loads were applied manually, the actual load could be $\pm 15\%$ of the intended 30N. The $\pm X$ shear axis was tested before the same biaxial tests were conducted with the transducer mounted upside down for testing in the $\pm Y$ shear axis (Figure 47b). The transducer was evaluated upside down to test the hypothesis that the lower PCBs may deform and introduce bending in the piezoelectric material causing erroneous reading. Unfortunately, the piezoelectric film of the transducer was later delaminated from the PCB assembly. As a result, the $\pm Y$ shear axis with the transducer in its original position and the $\pm X$ shear axis with the transducer in an inverted position were not evaluated.

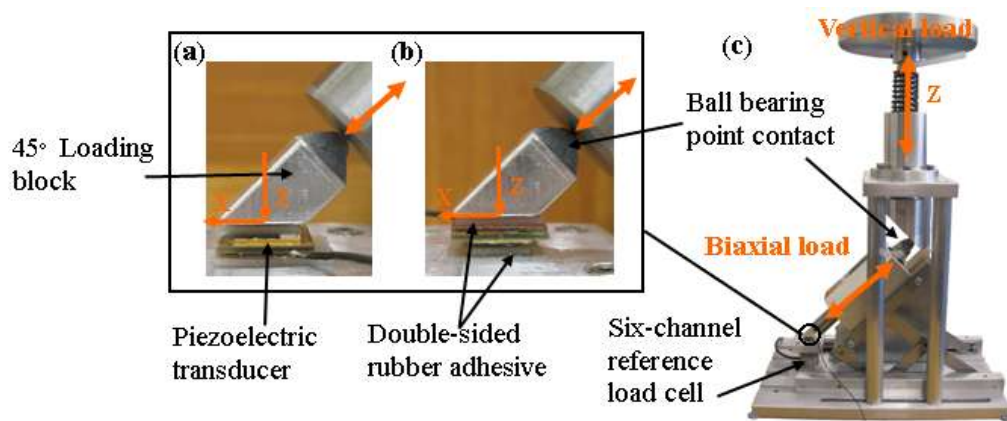


Figure 47 – The piezoelectric triaxial force transducer placed in its intended orientation (a) and up-side down (b) on the calibration rig during biaxial loading (c).

5.1.2.2 Calibration results

It was found that any physical contact with the shear channel electrodes would cause output saturation. Visual checks were performed before each test to ensure the aluminium foil was not in contact with the electrodes. Despite attempts to shield the ‘Kent’ system from electromagnetic influences, the outputs of the transducer were affected by noise during calibration in the material testing laboratory. The transducer and its connections at the charge amplifier were particularly sensitive to electromagnetic noise. Static charge from a plastic ruler, for example, was noted to influence the output voltage dramatically. Consequently, output voltages from the ‘Kent’ system during computer-controlled testing were lowpass filtered (Kaiser Window filter, $F_{pass} = 1.5$, $F_{stop} = 2$) in MATLAB (Version R2007a). While the signal-to-noise ratio of the system was significantly lower (8:1) during manual loading than computer-controlled tests (3:1), signal outputs were also filtered to aid comparison of the system performance during computer-controlled and manual loading tests. 0 contains illustrations of typical transducer output signals before and after filtering.

Results from computer controlled calibration

Figure 48 illustrates a typical filtered system output from the vertical channel when a cyclic load (0) was applied to the transducer. An exponential decay was apparent in the system output. The average time constant was estimated by fitting an exponential curve ($V = V_0 e^{-\lambda t}$) to the peak value from each loading cycle as shown in Figure 48. As a secondary check, the exponential response at the end of the cyclic sequence (Figure 48) and the exponential response during step loading (0) were also evaluated. Average time constant values for each transducer axis have been summarised in Table 4. The average time constant ($\tau = 1/\lambda$) was found to be less than 15s for both vertical and shear axes. However, the time constant in the shear Y axis was found to be about 9s when rubber was used during calibration.

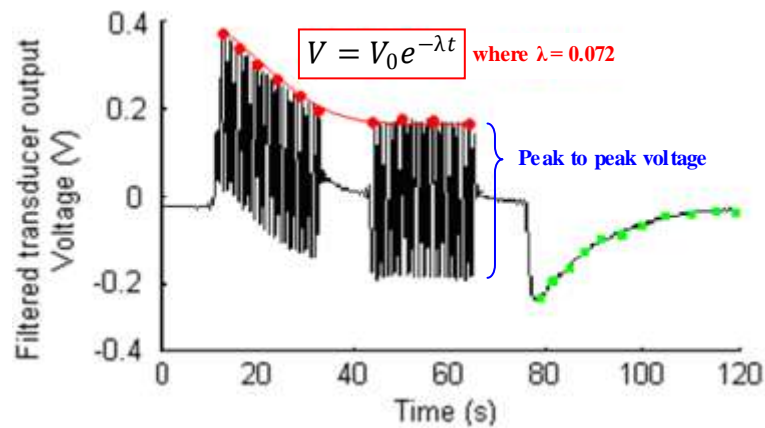


Figure 48 - Voltage-time plot illustrating a typical vertical output response under vertical loading. The exponential decay curves (red and green) were fitted in order to estimate the time constant of the charge amplifier circuit. The signal shown has been low-pass filtered. The typical input load can be seen in 0.

Due to the exponential decay in the transducer response, the absolute output voltages from the amplifier circuit were not directly related to the applied load. However, because the applied loads controlled via the computer were consistent between tests, the peak-to-peak output voltages (Figure 48) from each loading regime were compared with the applied peak-to-peak vertical load (Table 4). To examine the effect of cross-talk, average peak-to-peak voltage outputs from the two shear axes during pure vertical loading have been evaluated (Table 4). The orientation of the loading block was found to have negligible influence on output voltage (Table 4).

Table 4 - Transducer triaxial response under different pure vertical loading regimes.

Loading regime	Loading block orientation	Rubber	Peak-to-peak applied load (N)	Peak-to-peak voltage output (V)			Time constant τ (s)		
				X	Y	Z	X	Y	Z
Impulse	0	Yes	39	0.17	0.15	0.37			
	90		38	0.16	0.13	0.37			
	0	No	40	0.14	0.71	0.21			
	90		40	0.18	0.65	0.21			
Step	0	Yes	44	0.20	0.16	0.42	11.49	9.25	14.30
	90		39	0.19	0.13	0.42	11.33	8.21	15.09
	0	No	41	0.16	0.74	0.25	11.95	13.02	14.76
	90		41	0.22	0.72	0.28	11.52	12.20	14.38
Cyclic	0	Yes	35 (SD 0.13)	0.13 (SD 0.008)	0.13 (SD 0.004)	0.35 (SD 0.006)	11.11	9.37	13.88

Table 5 - Transducer response under pure vertical and biaxial loading regimes.

Applied load	Transducer orientation	Transducer output (Slope of the calibration curve, input load vs. transducer output voltage)		
		Shear X	Shear Y	Vertical Z
Pure vertical load	Normal	undetermined		0.0102
X- biaxial load		0.0157		0.0133
X+ biaxial load		0.0053		0.0118
Pure vertical load	Upside down		0.0174	0.0130
Y- biaxial load			0.0109	0.0130
Y+ biaxial load			0.0097	0.0137

Note: Crosstalk in the shear axes during pure vertical loading and biaxial loading are shown. Please refer to text for explanation why some data were undetermined.

Results from manually controlled calibration

Figure 49b illustrates a typical system output from the vertical channel when a cyclic load (Figure 49a) was manually applied to the piezoelectric transducer. The peak load applied to the transducer was not consistent between loading cycles. As a result, the exponential decay that was characteristic of the system during computer controlled loading (Figure 48) was not evident during manual loading (Figure 49b). Although the absolute output voltages from the amplifier circuit cannot be interpreted directly, the peak-to-peak values should be proportional to the applied load and therefore a consistent slope of the calibration curve. Calibration curves during both pure vertical and biaxial loading tests have been plotted (0) with their slope summarised in Table 5. The vertical and shear (Y) outputs were practically identical during pure vertical and biaxial loading when the transducer was placed up-side-down in comparison to its intended orientation (Table 5).

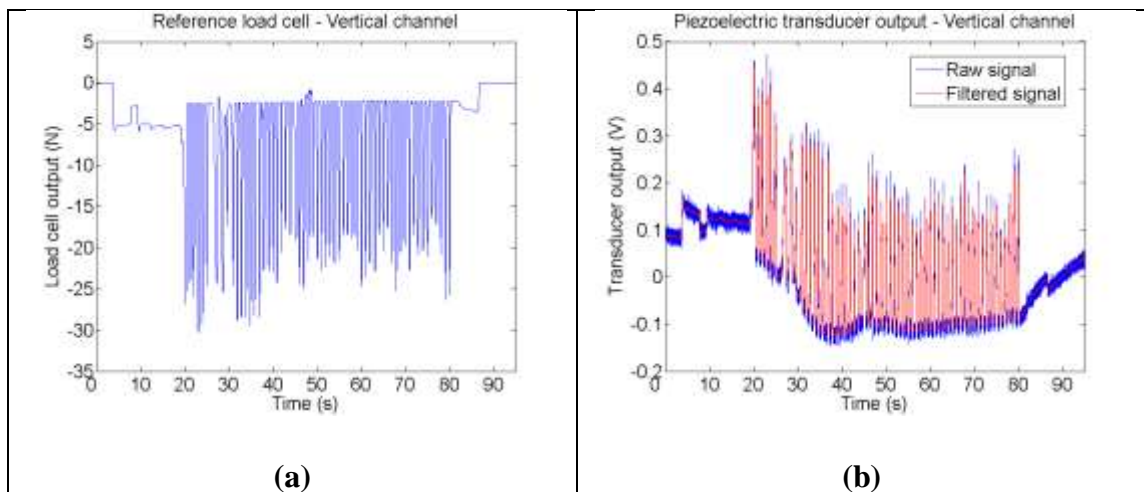


Figure 49 – A typical cyclic load applied manually ($\approx 1\text{Hz}$) using the calibration rig (a) and the corresponding output from the piezoelectric transducer (b). Plots are for the purpose of illustration only and show the application of dynamic load for 60seconds compared to the 30s duration used during calibration.

5.1.3 Discussion

As with all piezoelectric transducer/charge amplifier systems (Lord and Smith, 1983), exponential decay was apparent in the voltage output response of the ‘Kent’ system (Figure 48). Despite this decay, however, peak-to-peak signals were linearly proportional to the applied load and were consistent between cycles during cyclic

loading (Table 4 and Figure 48). The constantly changing baseline in the signal meant that the absolute voltages could not be used. As noted by Lord and Smith, (Lord and Smith, 1983), incorporation of more expensive charge amplifier and conditioning circuits may act to lengthen the decay in the signal, hence the time constant, to allow quasi-static load measurements. The average time constant was estimated to be about 14s in the vertical axis and 11s for the shear axes (Table 4). The time-dependent response reflected the band pass characteristics of the charge amplifier whose low pass frequency response was estimated to be 0.01Hz (Matthew Pepper, University of Kent, pers. comm.), which results in a time constant of 15s.

It is likely that the measured time constants were less than 15s due to drift in the charge amplifier system. Drift will always be observed when using charge amplifiers and both drift and the time constant simultaneously affect the voltage output (Gautschi, 2002). Drift can be caused by low insulation resistance or by leakage current, however it is not a predictable phenomenon (Gautschi, 2002). In fact, the measured time constants were found to be lower in the shear axes when rubber was used during calibration, which was more apparent in the shear $\pm Y$ channel (Table 4). Although not fully tested, it was hypothesised that static charges generated from the deforming rubber via the aluminium foil may have created an electrical field around the shear electrodes which accelerated current leakage during calibration. The aluminium foil might have been relatively closer to the Y-shear electrode than the X-shear electrode, thus the effect was less evident in decay characteristic of the X-shear axis.

As previously reported (Akhlaghi, 1995), baseline drift could occur with degradation of the lacquer that encased the transducer. Such a problem was not apparent in the vertical channel, but a light touch on the shear electrodes on the transducer would cause output saturation. This confirmed that the insulation on the shear electrodes was not adequate and, as such, was prone to error caused by drift. Moreover, despite the use of the expensive low-noise tricoax-cable, the system was sensitive to external electromagnetic influences. In contrast to the 'Kent' system which operated in charge mode, the piezoelectric material could, as an alternative, be made to operate in voltage mode by integrating an amplifier circuit into the transducer. The voltage

signal would be able to transmit longer distances and would have been less sensitive to electromagnetic noise. However, such a design would have significantly increased the overall dimensions of the transducer and, as such rendered it unsuitable for in-shoe applications.

The vertical and shear (Y) outputs were practically identical during pure vertical and biaxial loading when the transducer was placed up-side-down in comparison to its intended orientation (Table 5). This phenomenon suggested that the PCBs used in the construction of the transducer were not sufficiently rigid to prevent bending of the piezoelectric transducer. The lower PCBs were larger than the piezoelectric film and the upper PCB, any load applied to the transducer would cause the lower PCBs to conform and its sides would bend upward. Therefore, even an evenly distributed load on the transducer surface would cause the PCBs to deform concavely causing erroneous outputs in all three axes. This was best demonstrated when the transducer was evaluated up-side-down. Moreover, in contrast to Figure 50a where the transducer was up-side-down, the deforming PCBs were to blame for the irregular response found in the shear (X) axes when vertical load was applied (Figure 50b). This unexpected response renders the shear channels, in the current design, unsuitable for accurate measurement of shear load.

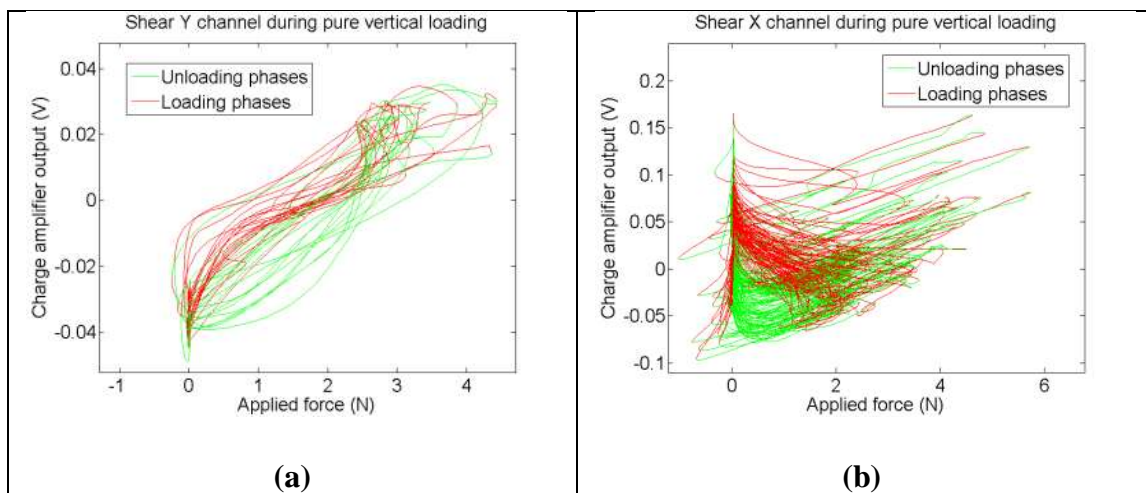


Figure 50 - Transducer response in the shear (Y) channel during application of pure vertical (Z) load (a), and transducer response in the shear (X) channel during application of pure vertical (Z) load (b). These figures are reproduced in Appendix C.

The orientation of the loading block displayed no influence in the performance of the transducer (Table 4), hence the unusual output discussed above was not associated with surface irregularities in the loading block. However, when rubber was not used during pure vertical calibration there was a decrease in signal in vertical (Z) axis, and a corresponding decrease in cross-talk in one shear (X) axis but a five fold increase in crosstalk in the other shear (Y) axis (Table 4). This implies that surface irregularities in the transducer may dramatically affect its performance.

Results from this investigation have indicated that a robust transducer structure with high-quality electrical shielding capability is crucial in the design of a piezoelectric-based load measurement device. Moreover, to avoid erroneous output due to bending of the transducer, housing material with a high bending stiffness would be required to enclose the piezoelectric material. Perhaps the design of the ‘Kent’ transducer was over simplified with only three PCBs enclosing the piezoelectric film. High precision in manufacturing the transducer structure is of importance to avoid any error caused by mechanical cross-talk. Coating the transducer with lacquer should be avoided unless an even finish can be guaranteed. To prevent premature failure of the transducer, a stronger bonding method for the attachment of the piezoelectric film to the transducer structure or a complete enclosed design would be required. Although the surfaces of the piezoelectric film were roughened to improve bonding to the PCBs, it is possible the process may cause surface irregularities resulting in non-uniform loading and erroneous results. Furthermore, a robust design is paramount to avoid injury that might be caused by sudden failure of the transducer during use.

In summary, the ‘Kent’ transducer design was found to be suitable for characterisation of the vertical load. Results from the current study have indicated that, for accurate shear load measurement in gait applications, piezoelectric materials need to be incorporated within a robust transducer structure to avoid bending and other mechanically induced errors. A strong bonding medium is required for mounting piezoelectric material to the transducer structure. High precision control for an even layer of the bonding medium would be necessary. Also, for safety, the piezoelectric material should be enclosed within a housing in case of premature failure of the bonding medium. To keep the dimensions of the transducer to a

minimum, the piezoelectric material should be operated in charge mode, therefore expensive low-noise electrical connections are required to minimise noise in the signals. Costly charge amplifiers are also required for quasi-static load measurement. Therefore, high volume production of piezoelectric transducer would be relatively expensive due to inspection time and hardware facilities required for high-precision manufacturing.

5.2 Development of a hydraulic based triaxial load transducer

The use of hydraulic based technologies in load measurement has been discussed (Section 3.7). This section outlines the development of triaxial load transducers that measures load through pressure by using hydraulic based components. The prototypes were evaluated for their suitability in the design of a triaxial load distribution device.

5.2.1 Design concept

Pressure sensors are widely used in different industries to measure the pressure of gases or liquids. With the advancement in miniature integrated circuits, pressure sensors have become smaller and cheaper. Off-the-shelf pressure sensors with integrated amplifiers or other signal conditioning circuits are readily available. With an appropriate hydraulic environment, these off-the-shelf devices could easily be used to construct a load measurement system. The simplest example of a hydraulic environment would be a liquid filled tube connected to a pressure sensor (Figure 51a). A similar technique has been used to build uniaxial load transducers that are compatible with magnetic resonant imaging (MRI) environment (Liu et al., 2000, Petre et al., 2008) by ensuring the electric pressure sensors can be located outside the magnetic field of the MRI.

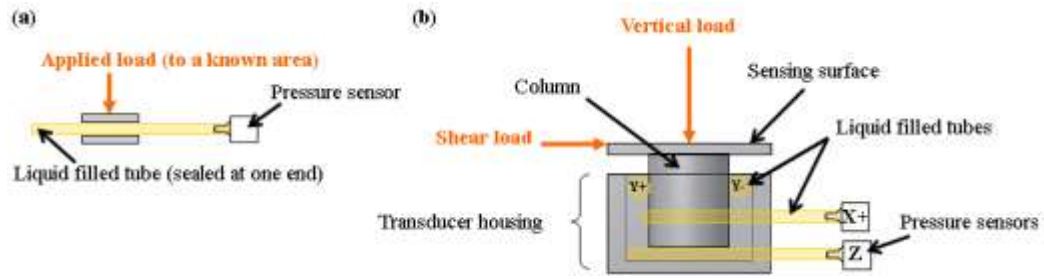


Figure 51 - Illustration of a simple hydraulic based uniaxial load transducer (a) and the multiple of such arrangement used in the construction of a triaxial load transducer (b).

In the case where some liquid is contained in a deformable tube, any load applied on the tube will change the pressure of the liquid within. Thus, based on Pascal's law, the external load can be monitored by measuring the changes in pressure inside the tube. In fact, as demonstrated in Figure 51a, the pressure tube itself can be a simple uniaxial load measurement device or a pressure measurement device if the load was applied to a known area. A simple triaxial load transducer, therefore, could be constructed with as little as five pressure tubes (Figure 51b): one for each of the four shear directions (X and Y) and one for measuring vertical load (Z).

5.2.2 Proof of concept prototype

Two simple prototype transducers (Prototype A and B) were constructed using commercially available pressure sensors and carefully selected tube materials to evaluate the feasibility of triaxial load sensing based on the concept described above (Section 5.2.1). The two prototypes only differed in the material of the pressure tubes.

5.2.2.1 Hydraulic pressure sensors

Different off-the-shelf pressure sensors were identified following extensive searches of product catalogues from hardware suppliers (RS Components Ltd, Northants, UK and Farnell UK Ltd, Leeds, UK). Pressure sensor 40PC-250G1A (40PC) from Honeywell (Illinois, USA) was selected based on its cost (£27 each), size, performance and operational conditions. The 40PC was a miniature (13×11×9.6mm) piezoresistive based pressure sensor that was fully signal conditioned and factory calibrated producing a linear voltage output over an operating pressure range of 0 to

250psi with a cited sensitivity of 16mV/psi and total accuracy of $\pm 0.2\%$ (%Span, between 0.5V to 4V). The sensor was a ‘plug-&-use’ device with only three wire connections: a standard +5V and Ground pin to provide power, and a Voltage Output pin. Five individual pressure sensors were used for each prototype and the same sensors were used in Prototype B after tests has been conducted on Prototype A. Each sensor was secured and electrically connected on a breadboard (Figure 52).

5.2.2.2 Hydraulic environment

The hydraulic environment was created using oil filled tubes connected to pressure sensors. Prototype A and B were constructed using different pressure tube materials.

Prototype A

As a preliminary test, silicone tubes were used in Prototype A as they were readily available in the laboratory. The silicone tube (unknown source) had a 1.5mm bore and 1mm wall thickness. Each tube was carefully filled with sunflower oil (Tesco, UK) to avoid inclusion of air bubbles in the system. The oil filled silicone tubes were temporary sealed at one end using clamps, while the other end was press fitted to the input port of the 40PC miniature pressure sensors.

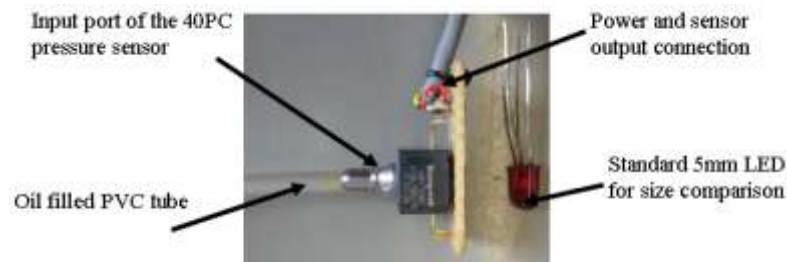


Figure 52 - Illustration of an oil filled tube fitted on the input port of the 40PC miniature pressure sensor.

Prototype B

A relatively stiffer ‘industrial-grade’ Polyvinylchloride (PVC) tubing with a 2mm bore and 1mm wall thickness (Altec Products Ltd, UK) was used in Prototype B. PVC was chosen for its cost (£8 per 30m) and the availability in different sizes. The bore size of the tube was chosen to allow snug press fit over the input port of the

pressure sensors. According to the chemical suitability chart from the manufacturer, corn oil, rather than sunflower oil, was chosen for chemical suitability with PVC. Each tube was carefully filled with corn oil (Tesco, UK) to avoid any inclusion of air bubbles. The oil filled PVC tubes were then permanently sealed at one end using cyanoacrylate adhesive (M-Bond-200, Vishay, USA), with the other end press fitted to the input port of the 40PC miniature pressure sensors (Figure 52).

5.2.2.3 Transducer structure

The same structural components were used in both Prototype A and B. The simple triaxial load transducer structure consisted of a sensing surface plate with an extended cylindrical end and accompanying transducer housing (Figure 54a and b). The two structural components were made of aluminium alloy. Technical drawings of the components have been included in Appendix B.

The transducer in the initial design concept, as illustrated in Figure 51, contained four pressure tubes arranged rectilinearly to detect the shear axis movement ($\pm X$ and $\pm Y$) of the sensing plate and an additional tube located on the underside of the extended cylindrical end of the sensing plate for detection of vertical (Z) deflection. The transducer housing contained 12 holes ($\text{Ø}3.5\text{mm}$) that allowed positioning of the pressure tubes. The four tubes positioned for detecting shear were suspended horizontally to the inner walls of the transducer housing by threading through the eight holes at the upper part of the housing. The two pairs of shear pressure tubes were in a two-tier arrangement, with the lower pair arranged for $\pm X$ shear and the upper pair for $\pm Y$ shear (Figure 51). The pressure tube for the vertical load was looped through the four holes located at the lower part of the housing creating an ‘U’ shape bend. The cylindrical end of the sensing surface plate was positioned on top of the vertical pressure tube, and was fitted snugly between the four shear tubes within the housing.

Unfortunately, such arrangement with the pressure tubes had caused the sensing surface plate to loss stability. The cylindrical end of the sensing plate would tilt and lever itself out from the housing when shear load was applied to the transducer.

Consequently, the initial design was modified such that the pressure tube for vertical load detection was wrapped around the cylindrical end of the sensing plate and sandwiched against the top of the transducer housing (Figure 53 and Figure 54). No modification was made to the transducer housing but the cylindrical end of the sensing plate was extended to 14mm instead of the original length of 12.5mm (Appendix B) so it was long enough to reach the lower tubes for shear (Y) detection.

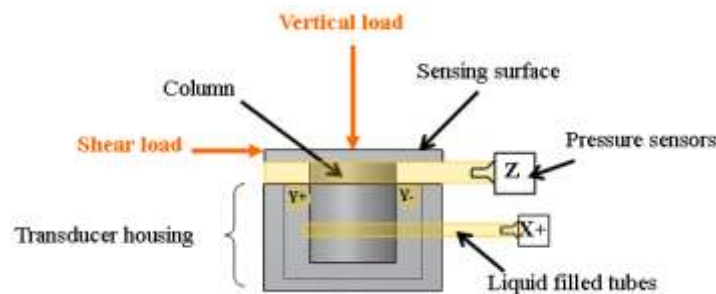


Figure 53 - The revised hydraulic based transducer design. The pressure tube for vertical load sensing was put between the sensing surface and the transducer housing.

All shear measurement tubes were 300mm long and the vertical tube was 400mm in length. The silicone tubes on Prototype A were not fixed to the transducer, whereas the vertical pressure tube on the prototype with PVC tubes was fixed between the sensing plate and the transducer housing using cyanoacrylate adhesive (M-Bond-200) to form a stiffer assembly. The complete Prototype A assembly with silicone pressure tubes measured 30×30×23.5mm. The silicone tubes were detached from the pressure sensors after calibration and were replaced with the PVC pressure tubes for constructing Prototype B. The same transducer structure was used for Prototype B but the holes on the sides of the transducer housing (Appendix B) were enlarged to 4mm allowing the PVC tubes to pass through. The PVC tubes were arranged such that they only extended out from one corner of the transducer (Figure 54b). The complete Prototype B with PVC pressure tubes measured 30×30×24mm.

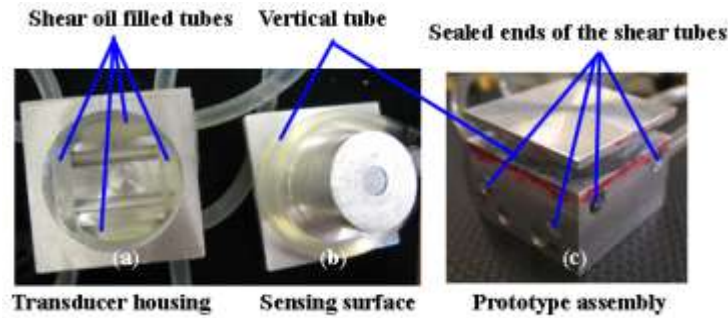


Figure 54 - The transducer housing with oil filled silicone tubes (a) and the vertical pressure tube around the loading plate (b). The same structures were used to assemble the prototype with PVC pressure tubes (c).

5.2.2.4 Circuit design

The miniature pressure sensors (40PC) were pre-amplified and preconditioned, therefore no other conditioning circuitry was required. All five pressure sensors (40PC) were powered via the same 5V supply outlet on the data acquisition system (DAQ) (USB-6225, National Instruments Corps, Ireland), which was also used to record their voltage outputs.

5.2.2.5 Prototype calibration

The two hydraulic based prototypes (A and B) were evaluated against a six-channel reference load cell (Nano25, ATI Industrial Automation, USA). Force outputs from the reference load cell and voltage outputs from the five pressure sensors were sampled simultaneously at 200Hz using the DAQ system (USB-6225). Data recording was controlled via a custom program written in LabView8.6 (National Instruments Corps, Ireland). All tests were conducted on the manually operated calibration rig described earlier (Section 4.5 and Figure 55). The prototypes were adhered, in turn, to the mounting platform of the calibration rig using double-sided tape. Each prototype was carefully aligned to the measurement axes of the reference load cell before bonding to the mounting platform. Following testing, each prototype was detached from the mounting platform.

Dynamic calibration tests for vertical and shear axes were conducted at 1Hz over the ranges of 0 to 40N and ± 40 N for 10 cycles, respectively. Because the loads were

applied manually, the actual load could be $\pm 15\%$ of the intended 40N. Vertical loads were applied manually with the steel rod ($\text{Ø}20\text{mm}$) on the calibration rig. The rod was put in series with a steel ball ($\text{Ø}23\text{mm}$) placed on top of the transducer (Figure 55a). The height of the prototypes, however, prevented the use of the calibration rig for pure shear tests. Consequently, shear loads were applied using the sharp end of a ball pen. In each instance, vertical load was applied to the centre of the sensing surface, while shear loads were applied to the mid-point of the corresponding surface of the plate.

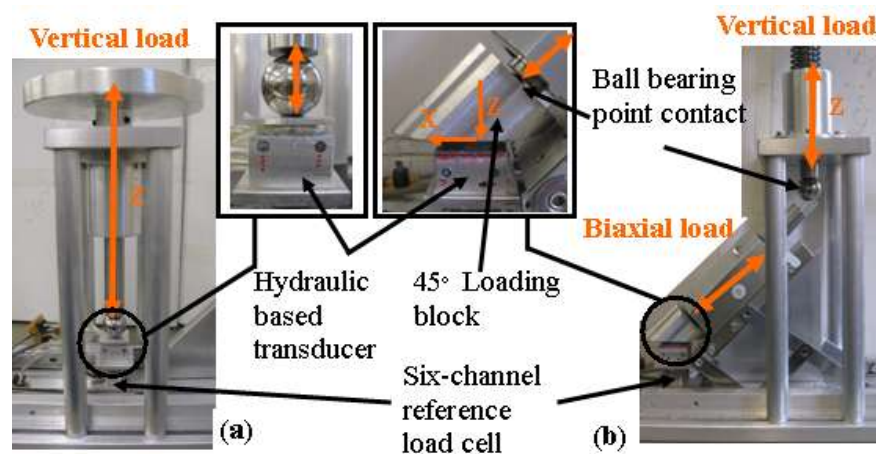


Figure 55 - Calibration rig setup for the application of pure vertical load (a) and biaxial (vertical and shear) load (b) to the hydraulic based triaxial load transducer prototype.

Because the silicone tubes and the two transducer structural components were not fixed together, the application of pure shear load on Prototype A caused the sensing surface plate to tilt and displace upward at the point of loading. A constant vertical load was required to hold down the sensing surface in position. Consequently, the shear axes of Prototype A were only evaluated by applying biaxial load to the transducer. A 45° angled loading block made of aluminium was secured on top of Prototype A to allow the application of biaxial load to the transducer via the calibration rig (Figure 55b). Prototype B did not have such a problem and pure shear loads were applied as described above, using the sharp end of a ball pen. In contrast to Prototype A, a complex triaxial load was applied manually to Prototype B for about 30s to assess its performance under combined vertical and shear loads.

5.2.2.6 Prototype calibration results

The mechanical properties of the silicone tubes used in Prototype A began to change after days in constant contact with the oil. The chemical reaction caused the oil to thicken and lumps of gel-like materials were found within the hydraulic environment. The pressure sensors had to be cleaned to ensure the lumps of materials would not affect the outputs before they were used again for constructing Prototype B. It was advised that the pressure sensors should be cleaned with isopropyl alcohol (IPA) or similar (Customer Response Centre, Honeywell.com, pers. comm.). Due to the compliance of the silicone tubes used in Prototype A, slight expansion of the silicone tubes external to the transducer housing were observed when load was applied to the tubes within the transducer. The same was not observed in Prototype B with the PVC pressure tubes. However, the disassembled Prototype B revealed that the PVC shear tubes had ‘permanently’ deformed to a Hertzian shape caused by the constant preloading condition due to the snug fit of the cylindrical column in the transducer. The PVC tubes returned close to their original shapes if no load was applied to the same location for a prolonged period (of the order of hours).

Table 6 - Assessment in the performance of the pressure sensors used in the prototypes.

<u>Pressure sensor 40PC-250G1A</u>		
	<ul style="list-style-type: none"> • Span = 4V – 0.5V = 3.5V • Total accuracy = ±0.2% (% Span) => ±0.007V error MAX • Sensitivity = 16.0mV/psi 	
Prototype	A	B
Output span (Vertical)*	0.79V => 49psi	0.05V => 3psi
Output span (Shear)*	0.32V => 20psi	0.03V => 2psi
Inherit sensor noise (peak-to-peak)*	±0.001V	±0.001V
Signal-to-noise ratio (Vertical)	395:1	25:1
Signal-to-noise ratio (Shear)	160:1	15:1
* information extracted from Figure 56, Figure 57 and Table 7		

In isolation, the pressure tubes were sufficiently sensitive to detect light finger touch. Although the selected pressure sensor was capable of withstand pressure of up to 250psi, the highest pressure detected was only 49psi from Prototype A (Table 6). The changes in pressure within the pressure tubes in Prototype B were considerably lower

than those in Prototype A (Table 6), hence the noise in the signal was more apparent in Prototype B (Figure 57).

The maximum load range of the pressure tubes were dependent on the stress at which the bore of the tube closed. Due to the compliance of the silicone material and the high Hertzian contact stress caused by the cylindrical column on the shear pressure tubes, the sensing surface of Prototype A displaced 1.5mm with an applied shear force just over 20N resulting in occlusion of the internal bore. Thus, Prototype A was limited to detecting shear loads less than 20N (Figure 56b). The pressure tube for sensing vertical load, in contrast, was spread over a larger contact area under the sensing surface plate, thus tolerated a load range of 0N-115N (Figure 56a).

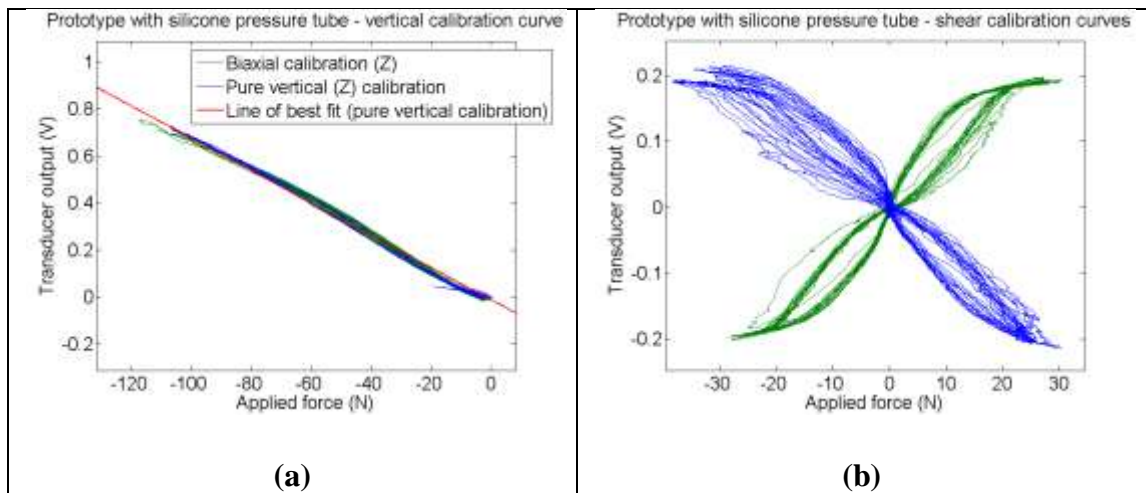


Figure 56 - Calibration curves for the silicone pressure tube prototype in vertical (a) and shear axes (b). The blue and green curves in (b) represent shear X and Y data during biaxial loading, respectively.

Figure 56 and Figure 57 illustrates typical calibration plots for each prototype in all three axes. Positive and negative shear data from their corresponding pressure tubes were put together in one graph (Figure 56b and Figure 57b). The results for each transducer axes have been summarised in Table 7. Non-linearity and hysteresis values were calculated based on the definition shown in Appendix A. The line of best fit ($y = mx+c$) for each calibration curve was obtained using the least-square method. Given that transducer outputs were biased to zero before each test, only the slopes of the best fit lines are shown. Transducer responses during the application of multi-

axial load were also plotted (Figure 56 and Figure 57) with the slopes of their best fit line summarised in Table 7.

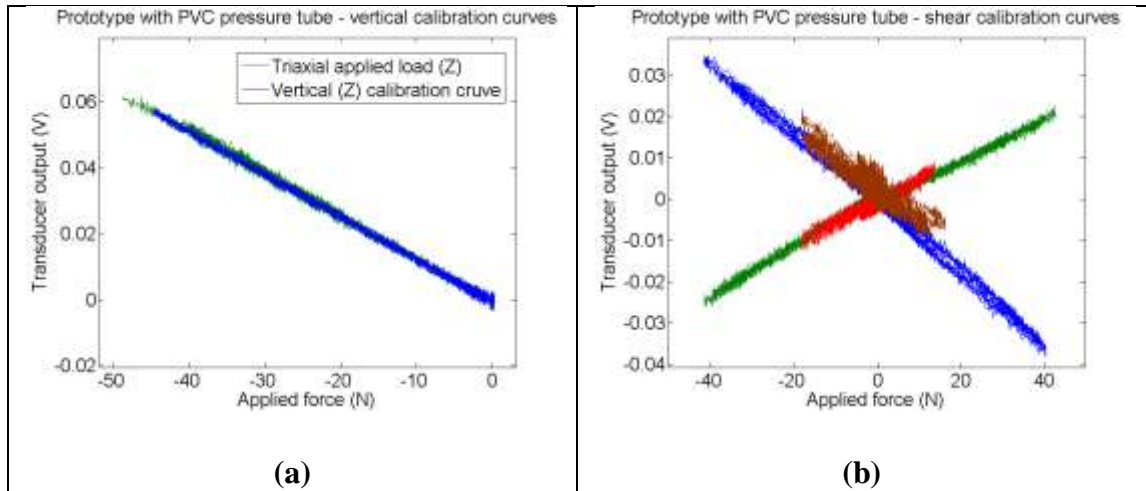


Figure 57 - Calibration curves for the PVC pressure tube prototype in vertical (a) and shear axes (b). The blue and green curves in (b) represent shear X and Y data during pure shear calibration, respectively. Brown and red curves represent the data during triaxial loading.

Table 7 - Calibration results of the hydraulic based prototypes. Typical results are shown. Non-linearity and hysteresis values were calculated based on the definition shown in Appendix A.

	Applied load	Slope of the best fit line ($y=mx+c$)	Goodness of fit	Non-linearity	Hysteresis
Prototype		m	R -Square	%	%
A (Silicone tube)	Bi-axial load (X)	0.00822	0.96	5.86	18.35
	Bi-axial load (Y)	0.00787	0.96	6.25	18.82
	Pure Z	0.00687	0.99	3.03	4.41
	Bi-axial load (Z)	0.00693	0.99		
B (PVC tube)	Pure X	0.00084	0.99	6.07	13.58
	Triaxial load (X)	0.00072	0.74		
	Pure Y	0.00054	0.98	5.17	12.01
	Triaxial load (Y)	0.00053	0.82		
	Pure Z	0.00127	0.99	2.05	4.86
	Triaxial load (Z)	0.00129	0.99		

5.2.3 Discussion

The transducer response in the vertical axis of Prototype A with the silicone tube was encouraging with both the hysteresis and non-linearity less than 5%. The slight deviation in the vertical calibration curves, during pure vertical loading and biaxial loading, were in a form of a sigmoid curve about the best-fit line (Figure 56a). This may have been caused by the initial collapsing of the silicone tube within the transducer followed by the expansion of the silicone tube external to the transducer observed during tests. The expansion of the silicone tubes may also have accounted for the relatively shallow slope in the vertical axis even though higher pressure was applied to the vertical tube than shear.

Partly due to the compliance of the silicone material, the shear tubes were unable to detect loads over 20N, hence the output from both shear axes (X and Y) in Prototype A saturated around $\pm 0.2V$. This maximum detectable load was also due to the small contact area on the column and the expansion along the length of the tubes external to the transducer housing due to increased pressure within the bore of the tube. This larger deformation in the silicone tubes resulted in a relatively higher output resolution compared to that in Prototype B in which PVC tubes were employed (Table 6). This can be seen also from the slopes of the best fit lines (Table 7), where the slope in Prototype A could be ten times higher than Prototype B (X-direction). The material of the tube and its containing liquid must be chemically compatible to avoid permanent change in the material characteristic and possible damage to the pressure sensors. Moreover, the tube material should be stiffer than the silicone used in the current study to maximise the detection range of the transducer. For these reasons, the PVC tubes should be chosen over the silicone tubes.

Using the stiffer PVC tubes in Prototype B allowed the transducer to measure loads of greater than 40N in all three axes. A linear output response can be seen in all three axes in Prototype B (Figure 57). The voltage outputs should be filtered to minimise error caused by the inherent noise from the pressure sensors. However, in order to increase the resolution of the transducer, the pressure sensors should be replaced with those with a measurement range of lower than 250psi. An alternative method for

loading on the shear pressure tubes would also increase the full-scale output span of the transducer and the maximum detectable load. To harness the full potential of the pressure tubes, the contact area between the column and the shear pressure tubes should be increased. The vertical tubes in both Prototype A and B were loaded with a relatively large contact area with the transducer and therefore had greater sensitivity, lower hysteresis & non-linearity (Table 7).

Theoretically, the location of the pressure tubes within the housing predicts zero crosstalk. This was reflected in the results, where negligible cross-talks were apparent in the vertical outputs when the two prototypes were loaded with biaxial or triaxial load (Figure 56a and Figure 57a). The cylindrical column used in the current design allowed axial rotation of the sensing surface plate without affecting the shear output. However, moments about the shear axes caused by off-centred or unevenly distributed load on the sensing surface would, in theory, have caused the column to tilt at an angle inducing mechanical crosstalk and thus unwanted shear responses. This was clearly demonstrated in both prototypes where the shear pressure tubes were in a two-tier configuration.

The slopes of the X-axes calibration curves were greater than those in Y-axes because the $\pm X$ shear tubes were positioned lower in the prototypes. This is because any shear load applied along the transducer surface would cause the column to tilt, therefore greater output was expected from the lower tubes. For the same reason, the Y-shear pressure tubes were relatively insensitive to the tilting of the column when multi-axial load was applied to the prototype (Figure 57), hence a better goodness of fit as shown in Table 7. Reductions in mechanical cross-talk could potentially be achieved by positioning the shear tubes in a single-tier format and locating them closer to the sensing surface.

The multiple-pressure tube based transducer was a simple design to extract triaxial load data. Off-the-shelf pre-amplified pressure sensors allowed an easy and quick way to construct the system. The size of the system has the capacity to be readily minimised by using smaller diameter tubes. Miniaturisation of the transducer for incorporation within an array, however, could be physically challenging. Smaller

diameter tubes could be used with the trade off of a smaller detectable load range due to smaller bore size. This is true if comparing with the same tube material, otherwise, a stiffer material would decrease the resolution of the system.

It was found that the shear tubes in Prototype B developed ‘permanent’ deformation when it was disassembled. This was possibly due to the high stress placed on the PVC tubes due to the tight fit between the column structure and the transducer housing. The permanent deformation may have been due to a viscoelastic effect within the material. High stress applied for long periods of time would cause the material to deform permanently. On the other hand, the loadings applied during shear testing were applied over much shorter time scales and therefore such an effect would have been less. Tests would be required to further examine the frequency response of the tubing within the hydraulic based triaxial load transducer.

In summary, results from the calibration tests were encouraging with both prototypes demonstrating the capability to detect triaxial load. A transducer incorporating an appropriate pressure tube material, such as PVC, has the potential to perform with minimal hysteresis and non-linearity. Good output resolution can be expected if the measurement range of the pressure sensors closely matches the expecting pressure changes within the pressure tubes. However, further tests are required to examine the frequency response of the transducer. Pressure tubes must be filled with fluid that is chemically compatible to avoid changes in the characteristic of the tube material and the performance of the pressure sensors. The production time and cost required for a discrete hydraulic triaxial load transducer was expected to be relative low if off-the-shelf pressure sensors and tubes materials were to be used. However, additional effort may be required to locate the pressure tubes in a single-tier configuration to minimise error induced by mechanical cross-talk and to minimise the overall dimensions of the transducer for an array. Moreover, miniaturisation of the transducer could be physically challenging and may never be suitable for in-shoe applications.

5.3 Development of an optoelectronic based triaxial load transducer

The use of optoelectronic technologies in load measurement has been discussed (Section 3.5). This section outlines the development of a triaxial load transducer using optoelectronic components. The prototypes were evaluated for their suitability in the design of a triaxial load distribution device.

5.3.1 Design concepts

The design concept for this optoelectronic triaxial load transducer was inspired by the work of several research groups (Hirose and Yoneda, 1990, Tada et al., 2002, Takahashi et al., 2003), in which four photo-sensing elements were used. Four-segmented photo sensors (often referred to as quadrant photodiode), can be regarded as an established technology and have been optimised for position sensing in various industrial applications, such as laser beam axis alignment. As discussed in Section 3.1, any displacement sensor can theoretically be calibrated as a load transducer. The component necessary to turn a displacement sensor to a load transducer would be an elastomeric holder to enclose the light-emitter and sensor units.

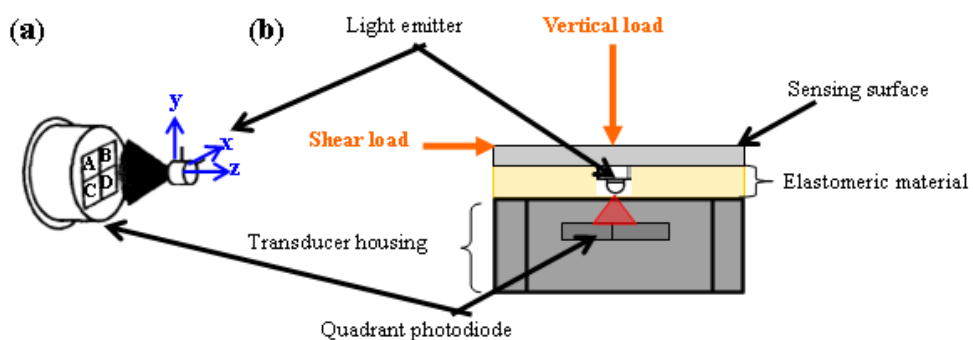
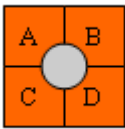
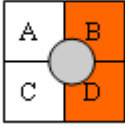
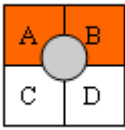


Figure 58 – The use of a quadrant photodiode to measure 3-axial minute displacements of a light source (a) and the basic concept of using such in a triaxial load transducer (b).

Figure 58a illustrates the use of a quadrant photodiode and a converging lens or pinhole set in front of the light source. This design enables the measurement of vertical (Z) movement as a change in the distance between the source and sensor influences the light intensity received at the photo sensor. It is also possible to

measure the horizontal (X and Y) movement by determining the ratios of the light intensity received by multiple photo sensors. Therefore, a triaxial load transducer could theoretically be achieved by enclosing such optical unit with an elastomeric holder, such as one illustrated in Figure 58b. In such a system, the compliant elastomeric material is positioned between the sensing surface which contains the light source and the sensor housing which holds the photodiode and would allow minute displacement in three cardinal directions in response to an applied triaxial load.

Table 8 – Formula for calculation of each load component from outputs of 4 photo sensor elements.

Applied load	Light spot movement relative to 4 sensors	Formula for quantifying the movement of the light spot, and therefore the applied load
Vertical (Z)		$Z = A + B + C + D$ (A, B, C and D are the photocurrents measured by each element.)
Shear (X)		$X = \frac{(B + D) - (A + C)}{Z}$
Shear (Y)		$Y = \frac{(A + B) - (C + D)}{Z}$

Consider the example shown in Table 8 where a small, uniform, circular beam of light falls on the centre of the active area of a quadrant photodiode. The vertical movement can be determined from the sum of the signals received from all four photodiodes. Shear loads can be determined from the position of the spot relative to the centre of the device, which in turn can be determined by comparing the signal received from each of the four separate photodiodes. The shear signals can be subsequently normalised to the total output from all four photo sensors, making them independent of the intensity of the light source as well as the vertical movement of the light source. Specifically, load in the X, Y and Z directions can be approximated by the formulas detailed in Table 8.

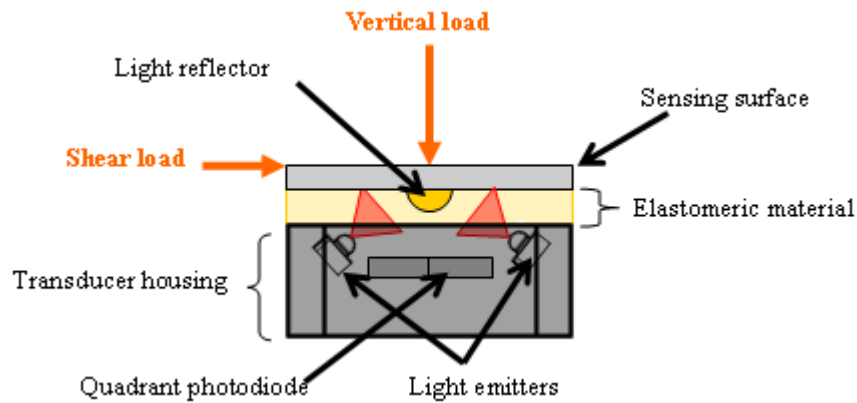


Figure 59 - The concept of using a quadrant photodiode to measure 3-axial minute movement of a light reflector hence the triaxial load applied to the transducer.

The conceptual transducer design illustrated in Figure 58b could be complex to manufacture, with wire connections required for the LED situated within the upper half of the transducer. An alternative would be to track the movement of a light reflector instead of the beam directly from the light source (Figure 59). Such an arrangement would require additional space within the sensor housing to accommodate the light emitter(s). However, the need for electrical connections within the upper half of the transducer would be mitigated, making the manufacturing process relatively faster and easier. While Figure 59 illustrates a discrete light reflector, it is noteworthy that an alternative arrangement in which a non-reflective area is positioned on a reflective background would act in a similar manner. In this case, the non-reflective surface would act as a light shielding mechanism blocking the light scattered within the sensor housing from reaching the photodiodes.

5.3.2 Proof of concept prototype

Prototypes with different light emitter-sensor arrangements and elastomeric materials were constructed to evaluate the feasibility of using four photo-sensing elements for triaxial load measurement.

5.3.2.1 Photo sensors

Different quadrant photodiodes were identified following extensive searches of product catalogues from hardware suppliers (RS Components Ltd, Northants, UK and Farnell UK Ltd, Leeds, UK) and photodiode manufacturers (Hamamatsu Photonics K.K., Higashi-ku, Japan; Silicon Sensor GmbH, Berlin, Germany; Honeywell Inc, Illinois, USA and Texas Instruments, Texas, USA). To minimise the total production costs, the use of two dual-element photodiodes as an alternative to quadrant photodiodes were also considered. For instance, two dual-element plastic package photodiodes (Hamamatsu S3096-02, £3 each) would cost five times less than a metal packaged quadrant photodiode (Hamamatsu S4349, £30). However, due to packaging limitations, dual-element photodiodes could not be physical aligned to ensure that there was consistent gap between individual photo elements, thus compromising the performance of the transducer as a whole.

Table 9 – Physical and electrical characteristics of the selected quadrant photodiodes.

Quadrant photodiodes	Hamamatsu S4349	Hamamatsu S5980
Active area	3×3mm	5×5mm
Element gap	0.1mm	0.03mm
Spectral response range	190 to 1000nm	320 to 1100nm
Peak sensitivity wavelength	720nm	960nm
Photo sensitivity	0.45A/W	0.72A/W
Dimensions	Ø9.2×4.1mm	10.6×8.8×1.26mm
Cost (£, each)	30.00	15.00

Consequently, two quadrant photodiodes from Hamamatsu (S4349 and S5980) were carefully selected based on their package size, the overall active area, the gap size between individual active areas, and cost. The S4349 contains a robust TO-5 metal package with a circular footprint of approximately Ø9.2mm, whereas the S5980 was a thin (1.26mm) ceramic surface mount sensor with a rectangular footprint of 10.6×8.8mm. Both photodiodes approximated the 10×10mm overall transducer surface area specified in the system requirements (Section 2.4.1). Other parameters of the photodiodes can be seen in Table 9.

5.3.2.2 Light emitters

There were several limitations that must be considered when using quadrant photodiode to detect movement. Firstly, the incident light beam must be smaller than the detector's total active area, but larger than the gap between individual active areas. A decrease in output signal strength can be seen if the light beam crosses the gap between the quadrants. This effect is more pronounced as the diameter of the light beam decreases, as a larger percentage of the beam power falls within the non-active gap. Therefore, the minimum light beam diameter should be at least one millimetre (Pacific Silicon Sensor Inc, 2009). Secondly, the total positional detection range is limited to the size of the incident beam area or the size of the detector's active area, whichever is smaller. Detection range increases with spot size, while positional resolution decreases because a given movement in a smaller spot creates a relatively larger differential signal than the same movement in a larger beam. The size of the incident light beam can be modified, regardless of the physical dimensions of the emitter itself, by using an optical lens and/or with a light-shielding structure with a hole of pre-determined size. Thirdly, the wavelength of the light source should ideally be matching the peak sensitivity wavelength of the photodiode for maximum performance. While it is recognised that optical filters, positioned between the light source and photodiode could be used to effectively limit the wavelengths that reached the photodiodes, it would result in an increase in cost and loss of intensity. Therefore, the chosen light source should have a dominant wavelength close to the peak sensitivity wavelength of the photodiode.

Table 10 - Technical characteristics of the light-emitting diode.

Light-emitting diode (LED)	Avago HLMP-Q105
Dominant wavelength	647nm
Viewing angle	28°
Luminous intensity	200mcd
Dimensions	2.08×2.08×2.92mm
Cost (£, each)	0.33

With the above in mind, a light-emitting diode (LEDs) from Avago Technologies (California, USA) was selected as the light source (Table 10). Compared to other incandescent light sources, LEDs are relatively cheap, typically have a lower energy consumption, longer lifetime, greater reliability and are available in miniature sizes. The dominant wavelength (647nm) of the LED was chosen to eliminate one source of variability between prototypes. Although the dominant wavelength (647nm) of the selected LED was lower than the peak sensitivity wavelengths (720nm and 960nm) of the two photodiodes described earlier (Table 9), it was sufficient to allow both photodiodes to deliver with the same sensitivity of about 0.42A/W, as specified in the manufacturers' datasheets. Therefore, both quadrant photodiodes could be regarded as having the same sensitivity. An LED with a small viewing angle (28°) was preferentially selected so that the incident beam would be concentrated without the need for additional lenses, thereby minimising the thickness and overall cost of the transducer.

5.3.2.3 Elastomeric material

A compliant elastomeric material sandwiched between the sensing surface and the base housing (Figure 60) was required to allow minute (sub-millimetres) triaxial displacement of the LED and provide a controlled restoring force during triaxial loading of the sensing surface. Thus, in addition to the arrangement of the LED and photodiodes, the mechanical characteristics of the elastomer would greatly influence the overall performance of the transducer. Time dependent non-linear behaviour would be expected when using elastomeric material.

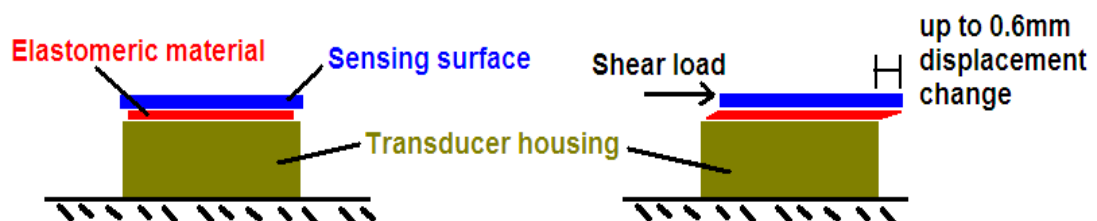


Figure 60 - Illustrating the deformation of the elastomeric material when shear load is applied to the transducer sensing surface.

To predict the required shear modulus of the elastomeric material, the system requirements (Section 2.4.1) and other physical assumptions were used to specify the following criteria of the material:

- Elastomer cross-sectional area = transducer's sensing surface area = 10×10mm.
- Elastomer thickness = 2mm, based on the ideal thickness of the overall transducer to be <5mm, the elastomer should be less than half the overall thickness. A thickness of 0.5mm at the lower spectrum was also considered to allow sufficient vertical movement for load sensing in the vertical axis.
- Transducer sensing surface allowable movement = 0.6mm. However, with a gap of 0.1mm between photodiode elements (Section 5.3.2.1), it was anticipated that a minimum 0.2mm movement in the transducer sensing surface at rated capacity load would be required for better sensitivity and resolution.
- Elastomer will be subjected to shear load of up to 300kPa, equivalent to 30N across the sensing surface area.

With the criteria above, it was anticipated the elastomeric material would have a shear modulus (G) between the ranges of 0.25MPa to 3MPa. The shear modulus was calculated based on the standard equation:

$$G = \frac{hF}{Ax},$$

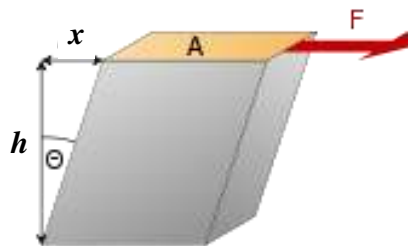
where

G = shear modulus

h = thickness of the elastomer

F = applied shear load

A = the area on which the shear load acts



The calculated material properties were fed into a software designed for material selection (CES EduPack 2009, Granta Design, UK), from which silicone rubber and natural rubber were predicted to have the potential to meet the criteria described above. Given that most material manufacturers only provide compressive or tensile

properties of their products, the compressive modulus (E) was subsequently estimated. The shear modulus (G) of a material is inherently related to its compressive modulus (E) based on the equation $E = 2G(1 + \nu)$, where E = compressive modulus, G = shear modulus, ν = Poisson's ratio of the material. Consequently, based on the Poisson's ratio of about 0.5 generic for silicone and rubber materials (Dechwayukul and Thongruang, 2008), the compressive modulus was predicted to be around 0.75MPa to 9MPa. With these figures in mind, elastomeric materials were subsequently obtained from 3 different sources:

1 - RS Components Ltd, Northants, UK

A flowable one-component acetoxy curing silicone rubber compound (RS692-542) was identified following extensive searches of hardware supply catalogues (RS Components Ltd). Limited material characteristics were specified by the manufacturer. However, with the specified tensile strength of 2MPa, suggested the silicone rubber may have a compressive modulus that meets the criteria above.

2 - Silicone Engineering Ltd, Lancashire, UK.

Silicone Engineering Ltd is a UK based company specialised in silicone since 1959. The company was approached with the estimated material properties discussed above, and they provided advice and samples of their products to be evaluated in this study. The samples were semi-transparent white-coloured silicone rubber sheets (Grade: KSIL-60, Thickness ~1.5mm) with typical tensile strength of 10.5MPa.

Silicone rubber is known to be difficult to adhere due to its inherent low surface tension. It was advised to alter the surface tension of the silicone sheets by chemical means to make the material more receptive to adhesion. LOCTITE®770™ primer and LOCTITE®406™ adhesive were suggested (B.Taylor, Silicone Engineering Ltd, pers.comm.). LOCTITE406 is a fast cured cyanoacrylate adhesive designed for the bonding of plastics and elastomeric materials, whereas LOCTITE770 is designed to work in conjunction with LOCTITE406 to make low energy surfaces suitable for bonding.

3 - The Tun Abdul Razak Research Centre (TARRC), UK

The Tun Abdul Razak Research Centre (TARRC) is the UK-based research and promotion centre of the Malaysian Rubber Board. The elastomeric material previously used in a shear force transducer (Williams et al., 1992) was also provided by the TARRC. TARRC was approached with the reference to the previous work and responded that the material was a rubber based on a standard conventional sulphur vulcanised recipe (M.Fernando, TARRC, pers. comm.). However, TARRC was not able to provide information regarding the characteristics of the material nor was it described in the literature (Williams et al., 1992). TARRC therefore agreed to manufacture a new batch of the same material in different thicknesses (0.5mm and 1mm) for the purpose of this study. The process of manufacturing the rubber material has been included in Appendix D. It was advised that cyanoacrylate adhesives can be used to bond the rubber to other materials, following careful cleaning and preparation of the rubber with agents such as toluene or acetone (JP. Gladwin, TARRC, pers. comm.).

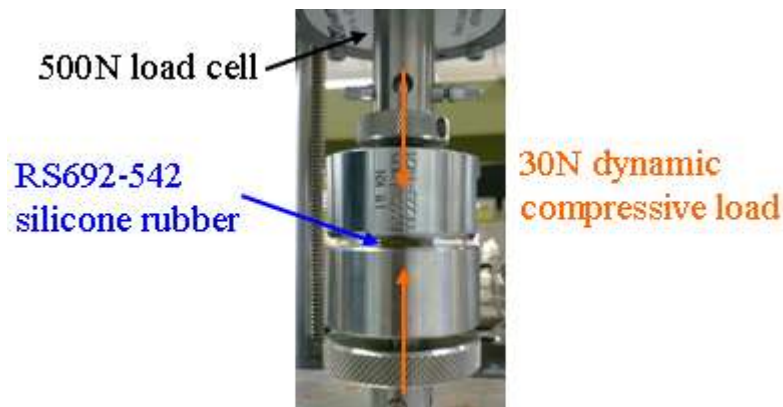


Figure 61 - Testing of the RS692-542 under dynamic compressive load using the Instron5848 material testing machine.

Given the inherent complexities associated with shear testing, the properties of each material were subsequently derived from dynamic compression testing for ease. Each of the sample materials was tested under dynamic compression tests via a material testing machine (Model 5848, Instron, USA) fitted with a 500N reference load cell (Figure 61). A 2N to 30N sinusoidal compressive load was applied to each material at a frequency of 1 Hz for 5 cycles. Each material had an estimated cross-sectional

area of 10×10mm. Figure 62 illustrates the stress-strain curves for each of the sample materials with estimated material properties summarised in Table 11.

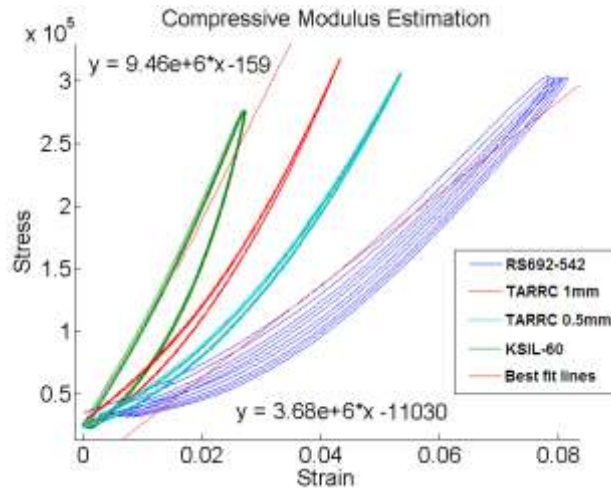


Figure 62 - Stress-Strain curves for different elastomeric material. The plot illustrates the estimated compressive modulus of the materials ranged from about 3.7MPa to 9.5MPa.

Compressive modulus and hysteresis were estimated from the stress-strain curves in Figure 62. Shear modulus (G) was estimated third of the compressive modulus (E), based on the relationship $G = E/2(1 + \nu)$ as discussed above. All the materials were found to match the predicted compressive modulus required for the development of multi-axial load transducer. The estimated hysteresis in the KSIL-60 was much higher than the others (Table 11) but it did not creep as much as the RS692-542 silicone compound with cyclic load (Figure 62). Consequently, all 4 materials were used and evaluated in the development of multi-axial load transducers.

Table 11 - Estimated material properties for the different elastomeric materials.

Material	Thickness	Estimated Hysteresis	Estimated Compressive Modulus	Estimated Shear Modulus
RS692-542	2mm	8.2%	3.7MPa	1.2MPa
KSIL-60	1.5mm	17.6%	9.5MPa	3.2MPa
TARRC 1mm	1mm	3.1%	6.9MPa	2.3MPa
TARRC 0.5mm	0.5mm	2.5%	5.4MPa	1.8MPa

5.3.2.4 Transducer structure

Each prototype consisted of three parts: 1) a sensing surface plate, 2) an elastomeric material, and 3) a transducer housing. Two distinct transducer housings, Structure A and B, were designed to facilitate the evaluation of different optical arrangements and elastomeric materials, respectively. To avoid physical damage and contamination of the photodiodes, both designs allowed the photodiode to be detached from the assembly while the transducers were prepared for different configurations.

Structure A

Transducer housing ‘Structure A’ was designed to house the S5980 quadrant photodiode for the evaluation of different optical arrangements. Prototype transducers were constructed only using KSIL60 silicone sheets. The KSIL60 was treated with LOCTITE®770™ before bonding to the sensing surface and Structure A using LOCTITE®406™ to complete one prototype transducer. Three different optical arrangements were constructed to direct light onto the quadrant photodiode: 1) an indirect light source from a reflective surface, 2) an indirect light source being blocked by a non-reflective surface, and 3) a direct light beam from a LED onto the photodiodes. Apology

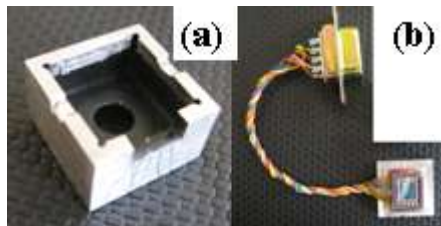


Figure 63 – Transducer housing ‘Structure A’ consisted of a base cap (a) and the S5980 photodiode on top of the base plate (b).

Structure A had a footprint of 17 x 17mm and consisted of two aluminium alloy parts, a base plate and a base cap (Figure 63). Technical drawings of the two parts have been included in Appendix B. The top inner surface of the base plate was first prepared with a thin non-conductive polyurethane coating (Gauge Coat-A, Vishay, USA) before the S5980 chip was soldered onto strain-gauge wires and secured onto

the top surface of the base plate (Figure 63b). The wires were padded to external cables connected to a RS-232 connector. The wire assembly was secured in place using lacquer. The inner surface of the base cap was sprayed with a black matt paint for a non-reflective finish (Figure 63a). The base cap fitted tightly onto the base plate and bonded together with cyanoacrylate adhesive (M-Bond-200, Vishay, USA) for extra security. A 2mm flat screwdriver was used to detach the cap from the base plate when necessary.

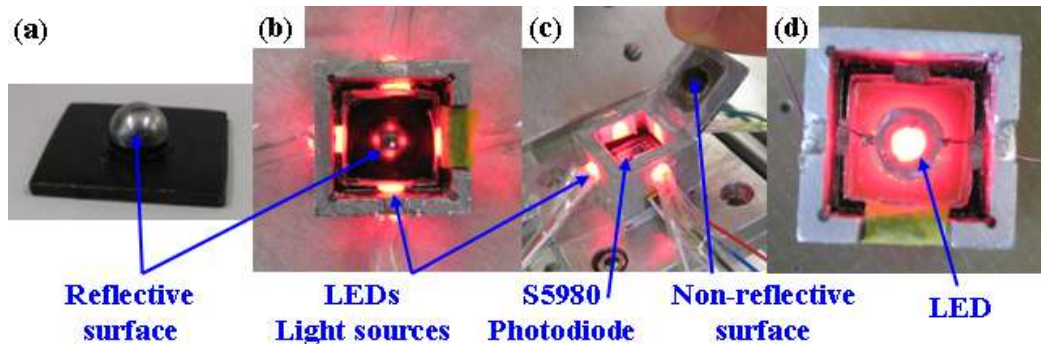


Figure 64 - Different optical arrangements: an indirect light source from a reflective surface (a,b), an indirect light source being blocked by a non-reflective surface (c), and a direct light beam from a LED onto the photodiodes (d).

Slight modifications were made on Structure A to facilitate the evaluation of the second design concept, in which the LED attached to the under surface of the sensing surface plate was replaced with a discrete reflective surface. The original circular opening ($\text{\O}5\text{mm}$) located at the top of the base cap was enlarged to a rectangular opening ($9\times 9\text{mm}$) for the insertion of the reflective surface. Holes located on each side of the base cap were also added to allow four LEDs to illuminate the inner space of the transducer (Figure 64b and c). Small pieces of white plastic were placed in front of the LEDs to diffuse the light.

The reflective surface consisted of a steel hemisphere ($\text{\O}5\text{mm}$) welded on a 2mm thick steel plate that had been sprayed with a non-reflective black paint (Figure 64a and b). To evaluate the ‘light-shielding’ design with a non-reflective surface, the paint was removed from the steel plate and the hemisphere was painted mat black (Figure 64c). Structure B was also evaluated with the LED attached to the underside of the sensing surface. The LED was attached onto a 2mm steel plate and powered

via strain gauge wires through the holes on the sides of the base cap. A miniature PVC hexagon screw nut with an inner diameter of about 3mm was placed over the LED with a small piece of white plastic on top to act as a diffuser (Figure 64d).

Structure B

Transducer housing ‘Structure B’ was used to evaluate the performance of prototypes using different elastomeric material under one optical configuration, where the direct light beam from a LED was pointed towards a quadrant photodiode. Three types of elastomeric materials (discussed previously in Section 5.3.2.3) were used; namely the 0.5mm and 1mm rubber sheets (TARRC) and a flowable silicone compound (RS692-542).



Figure 65 - Transducer housing ‘Structure B’ used in the evaluation of the optoelectronic based transducers. The bottom (a) and top (b) view of the structure with a S4349 photodiode inside. A technical drawing of the structure has been included in Appendix B.

Structure B was designed to house the S4349 quadrant photodiode thus had a smaller footprint (15×15mm) than Structure A. The simple structure was a 15mm cube made of aluminium alloy with a cylindrical hollowed centre and an alignment groove along the inside length of the hollow compartment. A technical drawing of the structure has been included in Appendix B. The alignment tip on the side of the photodiode package was slotted precisely in the alignment groove so the active photo elements were located at the centre of the transducer and aligned with the transducer axes (Figure 65a). The photodiode was secured in place with reusable putty adhesive. The five connection pins (Ground & 4 voltage output connections) on the S4349 chip were cabled through a 1mm hole at the side of the housing using strain-gauge wires. The wires were padded to external cables connected to a RS-232 connector.

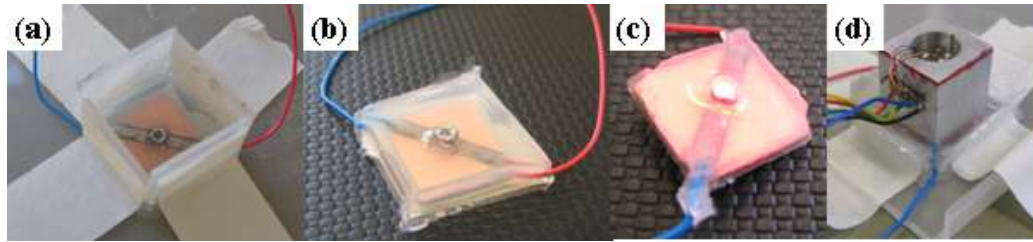


Figure 66 - The production steps for Prototype A: a) the PVA mould used to contain the silicone compound to be cured, b) the cured assembly, c) with the excess trimmed and d) the whole assembly bonded onto the transducer housing with another layer of silicone compound.

The TARRC rubber sheets were treated with LOCTITE®770™ before bonding to the sensing surface and Structure B using LOCTITE®406™. The flowable silicone compound (RS692-542) was first applied on the sensing surface together with the LED and wires attached. The whole assembly was then set within a mold (Figure 66a). Polyvinyl acetate (PVA) sheets were used to make the mould as the silicone compound did not adhere to it, thus allowing easy removal. The cured assembly was then trimmed before another uniform layer of silicone compound was applied for bonding on the transducer housing (Figure 66d). The silicone compound was carefully moulded and cured over 24 hours for an even thickness of 2mm. Any excess material was manually trimmed.

Structure B was used only in the evaluation of the initial design concept, with the LED attached to the underside of the sensing surface (Figure 58b). The sensing surface was a copper-clad laminate printed circuit board (PCB) of 15 x 15 x 1.5mm. The conducting copper layer of the PCB was first manually prepared with tracks for cable connections for the LED. The LED was secured onto the centre of the PCB using cyanoacrylate adhesive (M-Bond-200, Vishay, USA) before the pins were soldered on the tracks. Flexible power cables were attached to the edges of the tracks to minimise mechanical interference. Two triangular pieces of elastomer were used to allow for the LED and the connection cables to pass through. To further confine the light beam, a miniature hexagon steel screw nut with an inner diameter of 2mm was secured around the top of the LED using cyanoacrylate adhesive (Figure 66b). A small piece of frosted plastic sheet was put in front of the LED to act as a diffuser.

Completed prototypes

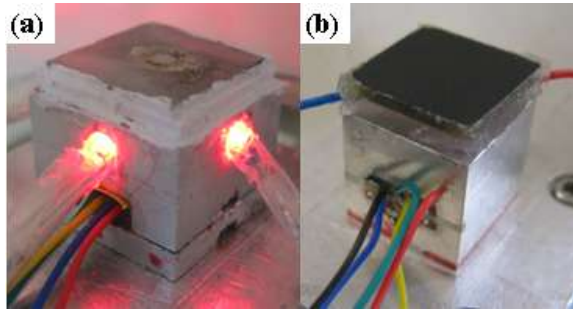


Figure 67 - Examples of the completed optoelectronic based prototypes. Prototype A with housing Structure A (a) and Prototype D with housing Structure B (b).

Table 12 - The configurations of six different optoelectronic based prototypes.

Prototype	A	B	C	D	E	F
Transducer housing	Structure A			Structure B		
Optical arrangement*	1	2	3			
LED(s)	Avago HLMP-Q105					
Photodiode	Hamamatsu S5980			Hamamatsu S4349		
Elastomeric material	KSIL60 1.5mm		RS692-542 2.0mm		TARRC 0.5mm	TARRC 1.0mm
Transducer Height	14.5mm		18.5mm		17mm	17.5mm
Sensing area	17×17mm			15×15mm		
* Optical Arrangements:						
1 – In-direct beam from a reflective hemisphere						
2 – In-direct beam from a non-reflective hemisphere						
3 – Direct beam from a single LED to the photodiode						

Figure 67 illustrates two completed prototypes, one with Structure A and one with Structure B. To minimise noise from other light sources, the edges of the semi-transparent KSIL-60 elastomer was coated with an opaque material (Figure 67a) and external light sources with-in the laboratory were extinguished during tests. Due to the smaller opening ($\varnothing 5\text{mm}$) at the top of the transducer housing in Structure B, external light sources had negligible effect on the photodiode outputs. Nonetheless, the top surface of the PCB was painted black to avoid potential light penetrate through the PCB (Figure 67a). A total of six prototypes were built with variation in optical arrangements and elastomeric materials as listed in Table 12. It should be

noted that the position of the photodiode chip in Prototype E and F was lowered about 1mm to avoid direct contact with the LED.

5.3.2.5 Circuit design

The single LED and the array of four LEDs used during the evaluation of the optoelectronic based transducer were powered via a 5V supply outlet on board of the data acquisition system (DAQ) (USB-6225, National Instruments Corps, Ireland). Figure 68 illustrates the circuits and the resistors used to limit the current in the LED(s).

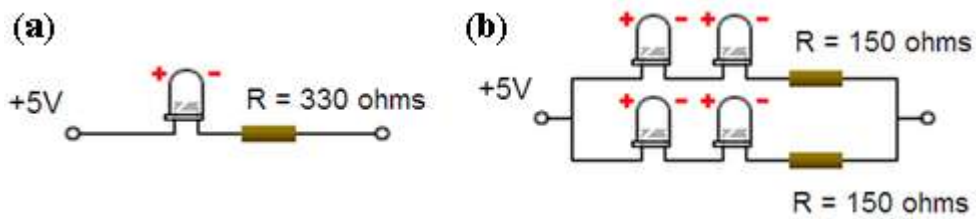


Figure 68 - Series (a) and parallel (b) circuits used to power a single LED and an array of four LEDs, respectively.

The signals from the quadrant photodiode were conditioned via a typical multi-element, common cathode circuit (Figure 69) constructed on a breadboard. The four output pins from the four individual photodiode elements were connected to a high performance quad operational amplifier (op-amp) (OPA404, Texas Instruments, USA) via a RS-232 connector on the breadboard circuit. The op-amp was specifically chosen for its operational speed and its capability to amplify all four outputs in one small package. The individual op-amps were powered by a bench top power supply and the same 15V connection was used as the reverse voltage for the photodiodes. The feedback resistance (R_F), and hence the gain of the op-amps, was adjusted depending on the overall intensity received by the photodiodes in each test. Resistance ranged from 82k Ω to 390k Ω during testing.

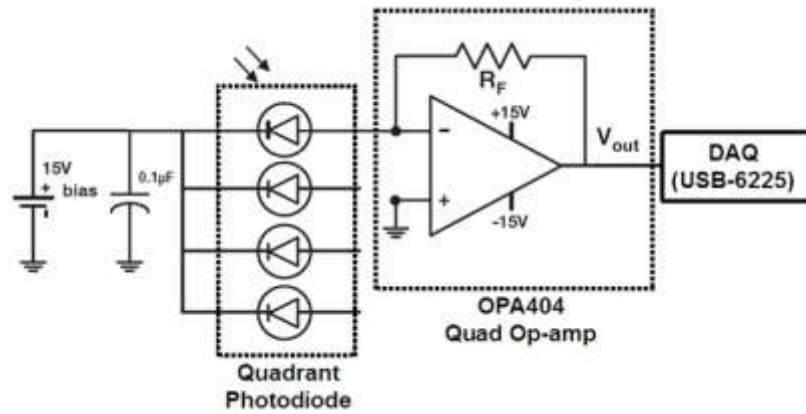


Figure 69 - A quadrant photodiode, its amplifiers and data recording device to measure 3-axial minute displacements of the optical arrangement. Diagram illustrates a simplified circuit with just one of the four op-amps.

The light intensity signals from the photodiodes were amplified by the op-amp circuit. It should be noted, that with the above circuit, the output voltage will be negative hence a decreased voltage with increased light intensity. The four amplified outputs from the op-amp were connected to the DAQ (USB-6225) for data recording. Data recording was controlled via a custom program written in LabView8.6 (National Instruments Corps, Ireland), which also calculated the movement of the optical arrangement in near real-time based on the equations listed in Table 8.

5.3.2.6 Prototype calibration

All prototypes were evaluated against a six-channel reference load cell (Nano25, ATI Industrial Automation, USA). Force outputs from the reference load cell and voltage outputs from the photodiode op-amp circuit were sampled simultaneously at 200Hz using the DAQ system (USB-6225). All tests were conducted on the manually operated calibration rig described earlier (Section 4.5). Prototypes were secured to the mounting platform of the calibration rig with a single drop of strain gauge-grade cyanoacrylate adhesive (M-Bond-200, Vishay, USA). Each prototype was carefully aligned to the measurement axes of the reference load cell before bonding to the mounting platform. Following testing, a 2mm flat screwdriver was used to detach each prototype from the mounting platform. Any glue residuals were gently removed prior mounting of another transducer.

Dynamic calibration tests for vertical and shear axes were conducted at 1Hz over the ranges of 0-40N and ± 40 N for 10 cycles, respectively. Because the loads were applied manually, the actual load could be $\pm 15\%$ of the intended 40N. Vertical loads were applied manually with the steel rod ($\text{\O}20\text{mm}$) on the calibration rig. The rod was put in series with a steel ball ($\text{\O}23\text{mm}$) onto a 2mm aluminium plate placed on top of the transducer. Shear loads were applied using the sharp end of a ball pen. In each instance, vertical load was applied to the centre of the sensing surface, while shear loads were applied to the mid-point of the corresponding surface of the plate.

As a preliminary assessment on the prototypes performance under combined vertical and shear loads, a complex triaxial load was applied manually to Prototype A, B and C for the duration of about 30s. A different loading regime was used for testing Prototype D, E and F: before one transducer was removed from the calibration rig, a controlled biaxial load was applied to the prototypes. The calibration rig was setup to apply a load at 45° towards and along one axis direction of the prototypes. The biaxial load was applied at 1Hz for 10 cycles and both vertical and shear force components were up to 40N ($\pm 15\%$).

5.3.2.7 Prototype calibration results

Due to the compliance of the silicone compound (RS692-542) used in Prototype D, the sensing surface was displaced 1.5mm with an applied shear force just over 10N, resulting in contact between LED and the transducer housing. Moreover, the power connection for the LED was damaged due to repetitive movement of the sensing surface during tests. Hence, Prototype D was not evaluated under biaxial load but was loaded up to 150N in the vertical direction and ± 10 N shear directions.

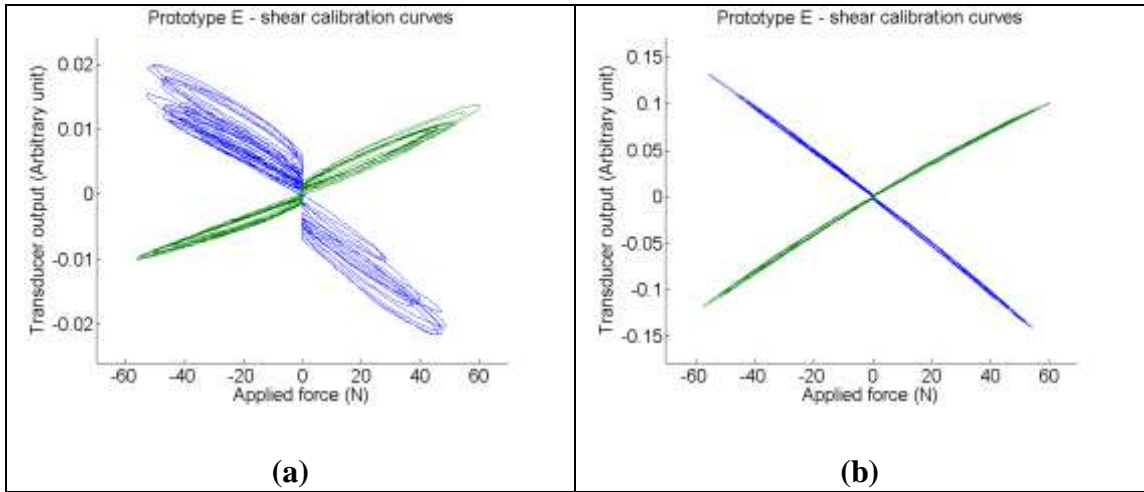


Figure 70- Calibration curves of Prototype E before (a) and after (b) securing the elastomeric material.

An audible noise was noticed during the testing of Prototype E. Thorough visual inspection of the disassembled transducer revealed that part of the elastomer was detached from the transducer housing. The effect, which was more apparent in the X-axis, resulted in an offset at zero load and large hysteresis loops in the response curve (Figure 70a). The problem was addressed by bonding a new piece of elastomer to the sensor housing. The calibration curve for Prototype E after securing the elastomer can be seen in Figure 70b (also in Appendix E).

For clarity, calibration plots for all prototypes have been included in Appendix E. Typical calibration results for each shear axis of the individual prototypes have been summarised in Table 13. However, the data in the vertical channels, both within and between prototypes, were obviously inconsistent (Appendix E). For that reason, data from all the vertical channels were excluded in Table 13. Non-linearity and hysteresis values were calculated based on the definition shown in Appendix A. The line of best fit ($y = mx+c$) for each calibration curve was obtained using the least-square method. Given that transducer outputs were biased to zero before each test, only the slopes of the best fit lines are shown. Transducer response in each axes during the application of multi-axial load were also plotted (Appendix E) with the slopes of their best fit line summarised in Table 13.

Table 13- Calibration results for each shear axes of the optoelectronic based prototypes. Typical results are shown. Non-linearity and hysteresis values were calculated based on the definition shown in Appendix A.

	Applied load	Slope of the best fit line (y=mx+c)	Goodness of fit	Non-linearity	Hysteresis
Prototype		<i>m</i>	<i>R-Square</i>	%	%
A	Pure X	0.00017	0.96	6.84	22.04
	Triaxial load (X)	0.00014	0.88		
	Pure Y	0.00024	0.97	5.54	22.41
	Triaxial load (Y)	0.00026	0.83		
B	Pure X	0.00019	0.96	8.11	24.93
	Triaxial load (X)	0.00007	0.48		
	Pure Y	0.00010	0.97	8.76	25.20
	Triaxial load (Y)	0.00003	0.29		
C	Pure X	0.00165	0.98	6.34	19.91
	Triaxial load (X)	0.00155	0.93		
	Pure Y	0.00146	0.96	9.27	23.71
	Triaxial load (Y)	0.00138	0.98		
D	Pure X	0.01070	0.99	3.75	6.56
	Pure Y	0.01352	0.99	2.55	5.25
E	Pure X	0.00246	0.99	2.73	4.88
	Bi-axial load (X)	0.00250	0.99		
	Pure Y	0.00185	0.99	2.37	4.89
F	Pure X	0.00369	0.99	7.02	7.48
	Bi-axial load (X)	0.00317	0.99		
	Pure Y	0.00508	0.99	5.44	8.09

5.3.3 Discussion

Before discussing the performance of each prototype, it should be noted again that the output voltages from the optoelectronic circuit described in Section 5.3.2.5 increased negatively with increased light intensity.

Transducer performance in the vertical axis was not consistent between prototypes and was discouraging. Initially, it was anticipated that, irrespective of transducer design, vertical loading would only result in an increase in overall light intensity at

the surface of the quadrant photodiode hence an increase in the negative voltage output from the op-amp circuits. However, irregular positive responses were observed in Prototype A (Appendix E) when biaxial load was applied. It was hypothesised that this phenomenon was likely caused by a combination of several factors. Firstly, it is possible that the reflective surface was not purely hemispherical. The effect of lack of uniformity would have been accentuated during off-axis loading where tilting of the sensing surface would have occurred leading to rotation of the hemisphere. Secondly, it is equally possible that the orientations of the four LEDs did not illuminate each side of the hemisphere with equal amounts of light. Imperfections in the hemispheric surface and/or lighting condition would cause the reflected light to scatter in an irregular fashion. Thirdly, the output in the vertical axis was affected by mechanical cross-talk when shear load was present. Other prototypes also appeared to have similar problems in that their responses in the vertical direction during multi-axial load were different from pure vertical loading (Appendix E). It was hypothesised that these unexpected responses were also caused by cross-talk from the shear axes.

The effect of cross-talk would be greater when the light beam was not aligned with the centre of the quadrant photodiode. The equations for the calculation of the triaxial load (Table 8) only hold true for a light beam in which a given movement of the beam results in the same change in incident power in all quadrants of the photodiode, over the entire dimensions of the beam. In fact, this occurs only with square or rectangular beams, and with quadrant photodiodes that have negligible gap space. However, uniformly round beam was used with the prototypes to minimise errors cause by the rotation of the sensing surface. Such a circular beam would limit the linear response range to the central portion of the spot (AP Technologies, 2011). A simplified example shown in Figure 71 illustrates how shear loads can affect the total intensity sensed by the photodiode, hence the vertical output. The total intensity could increase positively or negatively if shear load is present and the beam was not initially aligned to the centre of the quadrant photodiode (Figure 71). The same applies if the LED was fixed on the sensing plate at an angle to the photodiodes or if the sensing surface was tilted due to application of an off-axis load. The

misalignment of the LED in addition to the cross talk from the shear axes may also account for the mismatch between the vertical response slopes during pure vertical and multi-axial load in Prototype A and E (Appendix E). In particular, Prototype A demonstrated that the total intensity would increase positively or negatively due to cross-talk when shear load was present.

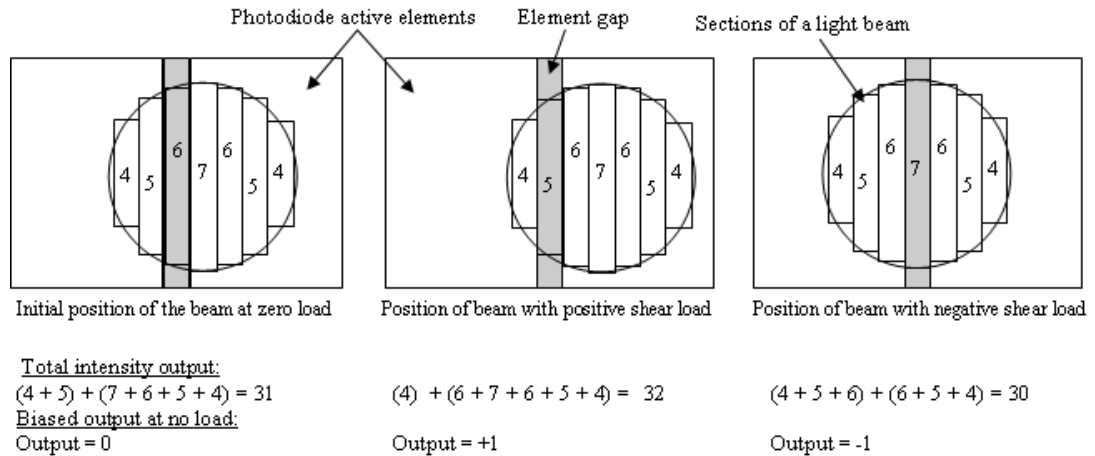


Figure 71 - A simplified example illustrating how the misalignment of the light beam could lead to cross-talk in the vertical output. The circular light beam has been simplified to rectangular sections with numbers representing the total intensity within each section. The intensity numbers are for illustration purpose and do not reflect the real values.

The vertical output is also apt to be affected by aging of the light source (light intensity decreases with age) as it measures the absolute values of the light intensity. Shear measurements would not be affected by the decrease in intensity with aging of the light source as only the ratios of the light intensities were measured. Based on the results generated and due to the points raised here, the current optical designs were regarded as not suitable for the measurement of vertical load.

All the prototypes showed promise for measuring shear loads but with one exception. The non-reflective hemisphere in Prototype B prevented light from reaching the photodiodes when vertical load was applied, hence the positive slope in the response curve (Appendix E). Although the vertical responses were relatively consistent (Appendix E), such an optical arrangement (with the non-reflective hemisphere on a reflective background) was to blame for the mismatch between the shear response slopes during pure shear and multi-axial load (Table 13 and Appendix E). The tilting

of the reflective background would scatter the light towards the photodiode in an irregular fashion, thus there was poor goodness of fit in the response curves when a complex load was applied to the prototype (Table 13).

Tilting of the sensing surface plate was caused by off-axis loading. One limitation of the calibration methodology employed was that ‘pure’ shear loads were not applied along the sensing surface of the transducer but were applied lower, on the mid-sides of the sensing plate. Although the prototype shear outputs were compared relative to the corresponding shear outputs from the multi-axial reference load cell, in theory, any off-axis load would have introduced a bending moment which in effect would have resulted in tilting of the sensing surface. However, despite this possible effect, most prototypes appeared to display negligible cross-talk in the shear axes, both from the vertical and from the other shear axis. This is best demonstrated by Prototype E, where the slopes of the best fit in the shear axes were practically identical during pure shear calibration and when the transducers were subjected to biaxial load. Prototype E was encouraging in that it displayed negligible cross-talk given that in theory off-axis shear loads would introduce bending moments.

Employing a reflective or non-reflective hemispherical surface, as used in Prototype A and B respectively, resulted in a similar response characteristic to the transducer in which a direct light beam from the LED was used (Prototype C, Appendix E). The manufacture of the ‘reflective’ design would be relatively simple, provided the sensing plate and hemisphere could be moulded as a single unit instead of being pieced together, as was done in the current study. However, the design also required the use of multiple LEDs within the transducer housing, compromising the overall size of the transducer and increasing the complexity of the accompanying electronics. This would be a major limitation in producing an array of transducers. The smallest optoelectronic based prototype constructed in the current study measured 15 x 15 x 17mm and was primarily limited by the size of the photodiodes. Although smaller LEDs are commercially available, custom made photodiode packages are required for further reductions in the dimensions of the transducer.

Prototypes A, B, and C were identical except for the optical arrangements. The range of linearity and hysteresis values were of the order of 4% and 5%, respectively. Whereas Prototypes D, E and F were identical except for the elastomer and the range of linearity and hysteresis values were of the order of 5% and 3%, respectively. One could conclude that the characteristics of the elastomer and the optical arrangement have a similar effect on the performance of the transducers. However, Prototypes D E & F used the same optical arrangement as Prototype C and differed only in the elastomeric material. The performance of Prototype C, with the KSIL-60 silicone sheet, in terms of non-linearity and hysteresis was approximately 3 to 4 times worse than transducers using the other elastomer. Such differences in hysteresis were anticipated from the compression testing of the materials conducted earlier (Section 5.3.2.3). However, the hysteresis values found during shear calibration (Section 5.3.2.7) were higher than those estimated from the compressive tests (Section 5.3.2.3), with the exception in Prototype D, because its shear calibration was conducted at relatively low load ($\pm 10\text{N}$). Higher hysteresis values found in the prototypes may have been caused by a combination of factors: 1) the materials were anisotropic, 2) the adhesive used for the bonding of the elastomer also affected the hysteresis value, and 3) the LED may not have travelled in the same path during loading and unloading conditions. The results have indicated that careful selection of the elastomer is paramount to sensor performance.

The performance of the transducers was largely dependent on the structural properties of the elastomeric material that separated the sensing plate from the transducer housing. The silicone compound (RS692-542) in Prototype D provided linear response with relatively low hysteresis, in both vertical and shear directions (Table 13). The thickness of the compound, however, would have to be decreased to avoid excessive deformation of the material which could lead to permanent damage to the LED or its power connections. The 0.5mm TARRC rubber medium used in Prototype E was one of the thinnest materials used in the construction of the transducers and appeared to provide the best linear response of the transducers with minimal hysteresis in the shear directions. In contrast with other materials, the

TARRC rubber was opaque and as such, the material would require no further modification to obstruct external light sources from reaching the photodiode.

In summary, the working prototypes demonstrated that various optical arrangements were not suitable for measuring triaxial load. However, a transducer incorporating a single LED and a quadrant photodiode with an appropriate elastomeric material, such as the 0.5mm TARRC rubber, has potential for measurement of shear loads. While additional construction modification would be required to strengthen the electronic connections, the sensing surface area of the transducer could be minimised if a single LED was mounted on the underside of the sensing surface plate. Nonetheless, the production cost for an optoelectronic based biaxial shear load transducer was expected to be relatively low in comparison with other technologies such as strain-gauge based transducers where labour intensive production is required.

5.4 Development of a magnetic based triaxial load transducer

The utilisation of magnetic sensing technologies in load measurement has been demonstrated previously and could potentially be used in the development of a triaxial load transducer (Section 3.6). This section outlines the development of a novel triaxial load transducer based on magnetic sensing technology. The prototypes were evaluated for their suitability in the design of a triaxial load distribution device.

5.4.1 Design concept

The design concept of this magnetic-based triaxial load transducer was based on the author's belief that any emitter-sensor type system based on one sensing technology could also be achieved the same way by using an emitter-sensor pair based on another sensing technology. In other words, the same idea used above in the optoelectronic based transducer (Section 5.3.1) could also be applied in a magnetic based design. A magnet would be the analogy for a light emitter, and a magnetic sensor would be the replacement for the photodiode sensor.

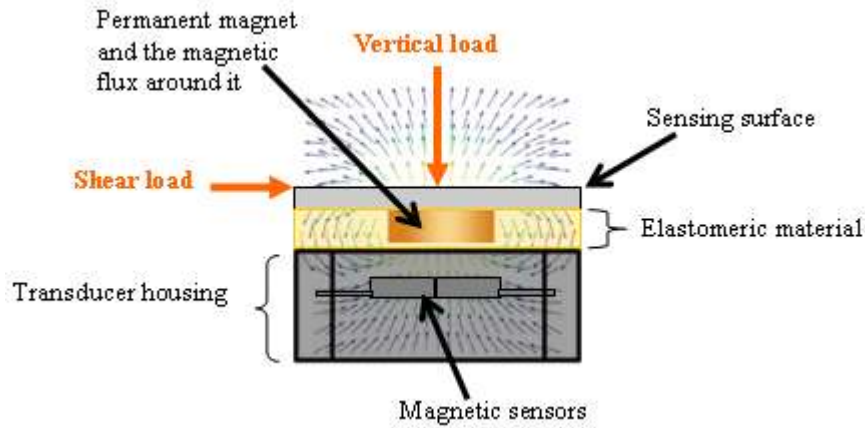
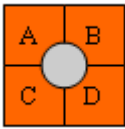
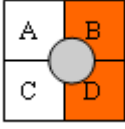
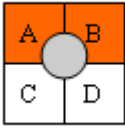


Figure 72 - The basic concept of a magnetic based triaxial load sensor.

Using the same load sensing concept as in the optoelectronic transducer (Section 5.3.1), triaxial load could, in theory, be detected with four magnetic sensors. A permanent magnet could be held in close proximity to the centre of four magnetic sensors located within a transducer housing (Figure 72). The unipolar head-on mode of operation and the unipolar slide-by arrangement between a magnet and magnetic sensor (Section 3.6) would be used for sensing vertical (Z -direction) and shear loads (X and Y directions), respectively. Such an arrangement would minimise the overall thickness of the transducer and reduce the number of magnets used in comparison to other methods discussed earlier (Figure 40, Section 3.6.3). The position of the magnet, and therefore the magnetic field around the sensors, will change when the sensing surface is subjected to external load. A compliant elastomeric material sandwiched between the sensing surface and the base housing would allow controlled minute movement of the magnet and provide a predictable restoring force. By comparing the signals received from each of the four separate sensors, the position of the magnet relative to its original centre location can then be determined. Table 14 illustrates how each load component could be obtained using the differential principle, where A, B, C and D are the signals generated from each of the magnetic sensors, as shown. The shear signals (X and Y) can be subsequently normalised to the total output from the four magnetic sensors to make them independent of the strength of the permanent magnet as well as the vertical movement (Z) of the magnet.

Table 14 – Formula for calculation of each load component from outputs of 4 magnetic sensors.

Applied load	Magnet movement relative to 4 sensors	Formula for quantifying the magnet movement, and therefore the applied load
Vertical (Z)		$Z = A + B + C + D$ (A, B, C and D are voltage outputs from each magnetic sensor.)
Shear (X)		$X = \frac{(B + D) - (A + C)}{Z}$
Shear (Y)		$Y = \frac{(A + B) - (C + D)}{Z}$

An experimental magnetic based transducer for the measurement of shear load has been developed previously (Tappin et al., 1980, Williams et al., 1992, Lord et al., 1992, Laing et al., 1992). In contrast to the current transducer design, their transducer had a ridge and groove feature which allowed only uniaxial movement of the magnet relative to the sensor. While the design allowed independent measurement of each shear axis, such a mechanical structure introduces friction between sensor components and, as such, is prone to mechanical wear. In contrast, the present design concept introduces a simple mechanical structure that avoids mechanical contact between components parts except, of course, for the deformation of the interposing elastomeric material. Commercially available hall-effect integrated circuits (ICs) microchips were selected for measurement of magnetic flux. The selected hall-effect sensor ICs incorporated signal amplification and signal conditioning circuits in one small package. These features provided a cost-effective design without the need for additional external circuitry between the sensor ICs and the read-out device, such as an oscilloscope or a personal computer.

5.4.2 Proof of concept prototypes

Different hall-effect sensor ICs, magnets and elastomeric material have been selected and assembled into prototypes to evaluate the concept of using these to measure

triaxial load. From the experience gained during the evaluation of the optoelectronic design (Section 5.3.3), it was anticipated that the reduction in sensitivity in the vertical axis would also be beneficial to minimise mechanical cross-talk on shear axes in the magnetic design. Although a transducer with minimal sensitivity to vertical load could only measure loads in the shear directions, such a biaxial shear load transducer would still satisfy the essential requirement of this study (Section 2.4.1). Nonetheless, prototypes were built to evaluate the feasibility of triaxial load sensing via four commercially available hall-effect sensor ICs. Some of the results outlined in the following sub-sections have been published previously (Lau et al., 2010a, Lau et al., 2010b) but will be discussed in more details below.

5.4.2.1 Hall-effect sensor ICs

Different hall-effect sensor ICs were identified following extensive searches of product catalogues from hardware suppliers (RS Components Ltd, Northants, UK and Farnell UK Ltd, Leeds, UK) and magnetic sensor manufacturers (Allegro MicroSystems Inc., MA, USA and Melexis Microelectronic Systems, Ieper, Belgium). Sensor ICs from Allegro (A1321EUA-T and A1301EUA-T) were carefully selected based on their size, performance and operational conditions. Both families of linear hall-effect sensor ICs provided a continuous-time voltage output that was linear and proportional to the applied magnetic flux density. Hall-effect elements respond to physical stress by modifying their output response (Section 3.6), but the A1321 family sensor ICs have integrated circuitry that is factory optimised for temperature stability and immunity to mechanical stress with sensitivity of 5mV/G. In contrast, the A1301 family sensor ICs do not include build-in compensation circuits but are optimised for low-noise voltage output with sensitivity of 2.5mV/G.

Table 15 - Physical and electrical characteristics of the hall-effect sensor ICs.

Hall-effect sensor	Allegro A1321EUA-T	Allegro A1301EUA-T
Sensitivity	5mV/G	2.5mV/G
Dimensions	4×3×1.5mm	
Cost (£, each)	1.30	1.09

Both sensor ICs could be operated by a voltage supply of 5V, had a typical output voltage of between 0.2 to 4.7V, and had a quiescent output voltage that was 50% of the supply voltage. The presence of a south-polarity magnetic flux line perpendicular to the branded face of the sensor IC would increase the output voltage above the quiescent voltage. Conversely, the application of a north-polarity magnetic field would decrease the output voltage from its quiescent value. Both sensor ICs were available in a 3-Pin SIP package or 3-Pin SOT23W (3×3×1mm footprint including the 3-pins) surface mount package. The 3-Pin SIP package (4×3×1.5mm excluding the 3-pins) was chosen for ease of manual handling and cabling during the prototyping stage. To keep the final dimensions of the transducer to a minimum, the four sensor ICs were arranged side by side together in a rectilinear grid arrangement (Figure 73).

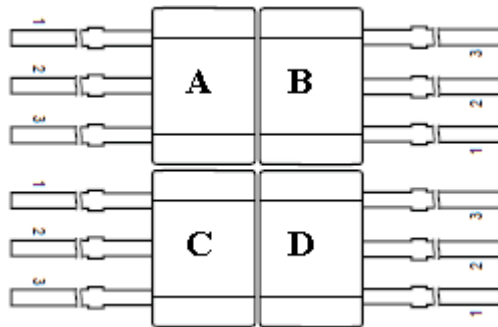


Figure 73 - Four hall-effect sensor ICs in a rectilinear grid arrangement.

5.4.2.2 Permanent magnets

Selection of the appropriate dimensions and strength of the permanent disc magnet was critical for accurate determination of its movement relative to the sensors. The size and position of the magnet from the sensor ICs would define the change in density of the magnetic field with relative movement of the magnet. For small relative movements of sub-millimetres, it is advisable to use a disc magnet that is small in diameter and closely positioned near the sensor ICs (J.C.Deporter and P.Bundy, Melexis Microelectronic Systems, Ieper, Belgium, pers. comm.). The length of a disc magnet can be relatively larger than its diameter but a magnet of a given pole face area will exhibit increasing field strength with length (Honeywell-

Inc., 2011a). External magnetic fields may disturb and have a relatively large influence on the existing field around the sensor IC particularly if a smaller magnet was used. On the other hand, the stray fields from a weaker magnet would have a smaller influence on other neighbouring transducers, which is crucial if multiple transducers are to be incorporated in an array. With the above in mind, the size of the permanent magnet should be smaller than the total size of the four hall-effect sensor ICs: about '8×6mm' and '6×6mm' if SIP and SOT23W sensor packages were used, respectively. To minimise the height of the final product, the ideal length of the disc magnet would be less than 2mm.

In accordance with the specified system requirements (Section 2.4.1), the sensing surface area of each transducer within an array was required to be 10×10mm and with maximum spacing of 1.5mm between neighbouring transducers. Therefore, the strength of the magnet should not introduce cross-talk to other transducers placed within a 10.75mm radius. To minimise the height of the final product, the ideal air-gap between the magnet and the sensor ICs would be less than 2mm. Although the application of a strong magnetic field does not damage the sensor ICs, it does force their output to a point of saturation. As mentioned above, with a 5V power supply, the output voltage range would be between 2.5V to 0.2V for a north-polarity magnetic field. As a rough estimate, the magnet should have surface field strength within the range of 500Gauss to 1000Gauss to avoid voltage saturation in the sensor ICs at sensor sensitivities between 2.5mV/G to 5mV/G. However, given the magnet was not centrally positioned relative to the centre-axis of the active hall-element within each sensor IC during operation, the strength of the magnet could be moderately higher than that estimated for a centric design. Two permanent magnets which satisfied the above requirements were selected (Table 16).

Table 16 - Technical information of the permanent magnets from Assemtech Europe Ltd. (Essex, UK).

Magnet	Assemtech M1219-1	Assemtech M1219-4
Type	Neodymium Iron Boron (NdFeB)	
Dimensions	3mm dia. × 1mm	6mm dia. × 2mm
Strength	1000 Gauss at 0.5mm	1000 Gauss at 2mm
Cost (£, each)	0.40	0.48

Evaluation of permanent magnets

Several magnets of type M1219-1 and M1219-4 were purchased from the suppliers (RS Components Ltd, Northants, UK and Farnell UK Ltd, Leeds, UK). One magnet from each batch was tested against a 3-Pin SIP package A1301 hall-effect sensor IC. The purposes of these tests were to:

1. Define the distances of the magnet relative to the active hall-element at which sensor voltage saturation would occur.
2. Determine whether the selected magnet field strength could introduce cross-talk to sensor ICs placed within a 10.75mm radius, and
3. To identify the optimal location of the magnet relative to the sensor ICs package.

Initially, the two magnets were compared during unipolar slide-by mode in which the permanent magnet was moved parallel to the face of the sensor IC package. The results were evaluated against the following requirements:

1. The magnet would not introduce significant cross-talk to hall-effect sensors placed within a 10.75mm radius.
2. The magnet would allow the air-gap of 2mm or less between the magnet and the sensor ICs.

The magnet that satisfied the above requirements was then identified and evaluated in the head-on mode of operation, in which the magnet moves orthogonally towards the face of the sensor IC. It should be noted, that the Total effective air gap (TEAG) is represented by the sum of the active area depth (AAD) and the air gap (AG) as discussed in Section 3.6. The AAD distance was 0.5mm for the 3-Pin SIP package sensor (Figure 75). Because of its obvious mechanical importance, the AG distance rather than TEAG is specified hereafter unless specifically stated otherwise.

Setup for the unipolar slide-by mode of operation

During the evaluation in the unipolar slide-by mode operation, each magnet was secured, in turn, to a precision (0.002mm resolution, ± 0.005 mm repeatability)

miniature linear actuator KUMINA-20-24 (KSS Co Ltd, Japan) using double-sided adhesive. The linear actuator moved the magnet parallel to the face of the sensor IC package at a speed of 2mm/s over its full 20mm length. The relative position of the magnet was then maintained for 5 seconds before it was returned to the zero position at the same speed. The linear actuator was fixed on the table top, whereas the sensor IC was secured half way along the 20mm length of the actuator, using double-sided adhesive on a manoeuvrable wooden platform (Figure 74a). Aluminium plates of different thickness (0.89mm, 1.49mm and 2.08mm) were used to set the air-gap between the magnet and the face of the sensor IC package. The spacer plates were also used to make sure the face (north-pole) of each magnet was set parallel to the face of the sensor IC package. The spacer was removed before the start of each test. Vertical and horizontal lines in $\pm 1\text{mm}$ steps were marked on the wooden platform to allow the repositioning of the sensor IC. The sensor IC was also re-orientated at 90 degrees about its central axis in order for the magnet to travel along the sensor IC from North to South and from West to East (Figure 74b).

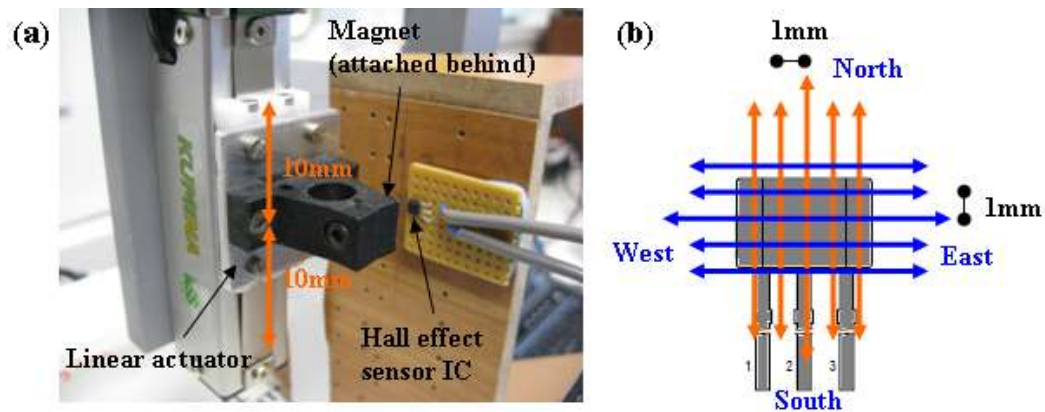


Figure 74 – Experimental setup for the evaluation of magnets in the unipolar slide-by mode of operation (a); and illustration of the paths of the moving magnet relative to the centre lines of the sensor IC.

Setup for the head-on mode of operation

The selected magnet from the slide-by evaluation was again secured onto the linear actuator (Figure 75a) to be evaluated in the head-on mode of operation. Nine different positions were evaluated by repositioning the sensor IC: with the magnet centred at the corners, mid-edges and the centre of the sensor (Figure 75b). The

magnet was progressed from a distance 20mm orthogonal to the face of the sensor package at a rate of 2mm/s to a final air gap distance of 0.89mm from the sensor surface. The air gap was set using an aluminium plate when the actuator maintained its position at the end of its 20mm length. The spacer plate was taken away before the start of each test. During tests, the air gap distance was maintained for a period of 5 seconds before the actuator brought the magnet back to its baseline position.

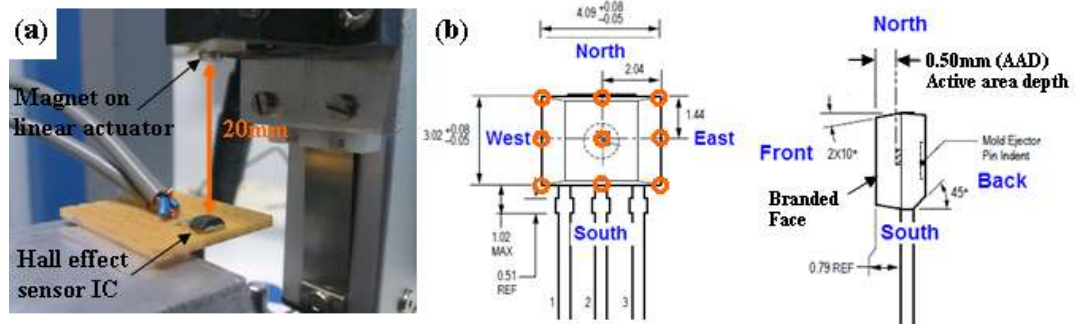


Figure 75 - Experimental setup for the evaluation of magnets in the unipolar head-on mode of operation (a); and illustration of the 9 magnet locations (orange circles) relative to the sensor IC during tests (b).

Electrical setup for evaluation of the permanent magnets

The hall-effect sensor IC was powered via the 5V supply outlet of the data acquisition system (DAQ) (USB-6225, National Instruments Corps, Ireland). The voltage output from the sensor IC was connected to the same DAQ for data recording via a custom program (LabVIEW 8.6, National Instruments Corps, Ireland). Movement of the linear actuator was controlled via another custom program (MATLAB, MathWorks Inc, MA, USA). Both MATLAB and LabVIEW software were operated on the same personal computer. There was no feedback signal from the actuator to identify its position within space over time. Nonetheless, assuming the magnet acts as a point source with greatest magnetic field strength at its centre, the mid-point of the magnet relative to the centre location of the hall-sensing element within the IC could be determined from the sensor voltage output and the speed of the moving magnet.

Results & Discussions

Initial tests were conducted and confirmed that movement of the linear actuator itself did not influence the magnetic field around the sensor IC. In addition, the quiescent voltage output of the sensor IC was found to be about 2.52V and would saturate at about 0.10V (Figure 76) with a north-polarity magnetic field.

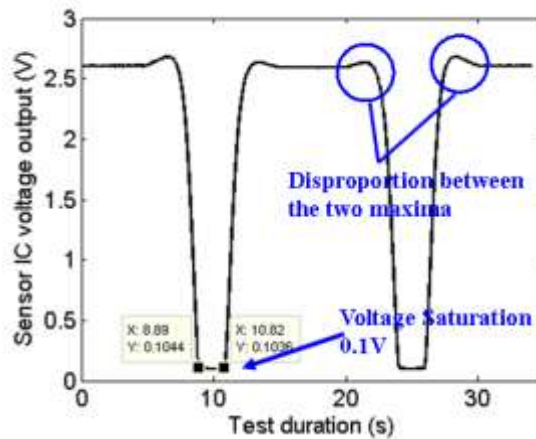


Figure 76 – Typical voltage output waveform from the hall-effect sensor IC when a magnet (M1219-4) travelled across with 1.49mm air-gap in the slide-by mode of operation.

Figure 76 illustrates a typical voltage output waveform from the sensor IC for the duration of one complete test cycle in the slide-by mode of operation. The waveform has two minima which are mirrored because the magnet travelled towards, passed the sensor and then returned back along the same path. In the example illustrated in Figure 76, the two minima were flat because the sensor output was saturated by the magnet strength at those conditions. Even though the north-polarity of the magnet was facing towards the sensor, voltage higher than the quiescent output (2.52V) was apparent due to the presence of magnetic flux lines in the opposite directions (south) surrounding the magnet as illustrated in Figure 77. This natural magnetic phenomenon is undesirable in the current design and, if not accounted for, would introduce substantial error when quantifying the magnet movement using the calculating formula as stated in Table 14. It would also influence the output of neighbouring transducers. It was concluded, therefore, that sensor ICs should not be located: 1) near the area of the magnet where an opposite magnetic polarity is present and, 2) too close to a magnet where the sensor would saturate. So the active

movement range of the magnet should only result in sensor output voltages between 0.10V to 2.52V. The disproportion between the two maxima of the waveform (Figure 76) could be caused by one or the combination of two factors: 1) the face of the magnet was not aligned accurately parallel to the face of the sensor package during tests, and/or 2) the north-south polar axis of the magnet was not perpendicular to the opposing face of the magnet. While the latter source of error was dependent on the precision of the manufacturing process of the magnet, the former source of error was minimised by ensuring the faces of both the magnet and the sensor IC were in complete contact with the aluminium spacer plates.

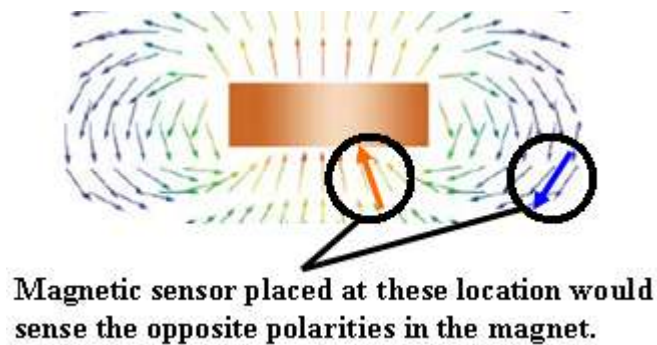


Figure 77 - The lines of flux, illustrated by arrows, originating at the north pole of a disc magnet and terminating at its south pole. Illustrating the presences of flux lines in opposite directions near the disc magnet.

Knowing the speed of the moving magnet, the output waveform in Figure 76 can be reproduced to reflect the relationship between sensor voltage output and distance between the magnet and the centre-line of the sensor, as shown in Figure 78. For optimal sensitivity, the sensor ICs should ideally be positioned where the greatest rate of change in magnetic flux density occurs. For that, the gradients along the sensor output waveform was calculated. The gradient plot for the M1219-4 magnet with 1.49mm air-gap in the slide-by mode test can be found within Figure 78. Voltage-versus-distance plots and gradient plots for other tests conducted have been included in Appendix F. The ideal location of the magnet relative to the centre of the sensor IC can be determined by estimating the locality of the four points described in Table 17, where an example has also been given referring to Figure 78. Based on the data from all tests and for each ‘magnet and air-gap’ configuration, the relative locations of the magnet at which an optimal sensor response can be expected were

mapped. Figure 79a is a map drawn to scale by hand for tests conducted with the M1219-1 magnet with 0.89mm air-gap. The locations where the greatest change in magnetic flux occurred were marked by an 'x', whereas the distances beyond the point where magnetic flux lines were in the opposite directions was considered as a 'dead-zone' and was shaded black. The drawn map was later digitised and enhanced for ease of interpretation. As expected from a point-source magnet, a circular pattern can be seen on the map (Figure 79a) because the sensor would produce a constant voltage output if an ideal point-source magnet was situated around the sensor at a fixed radius. Therefore, the sensor output curves from tests conducted along the centre line of the sensor IC (Appendix F) can be used as the representative data set and their results have been summarised in Table 18.

Table 17 – The 4 key locations for mapping the magnetic field around a hall-effect sensor IC*.

Location	Description	Example (Figure 78)
A	Greatest rate of change in magnetic flux density	2.74mm
B	Magnetic flux lines in the opposite directions	4.83mm
C	No change in magnetic field strength	>10mm
D	Saturated sensor output (0.1V)	1.85mm

*All distances (mm) are expressed relative to the centre of the sensor IC.

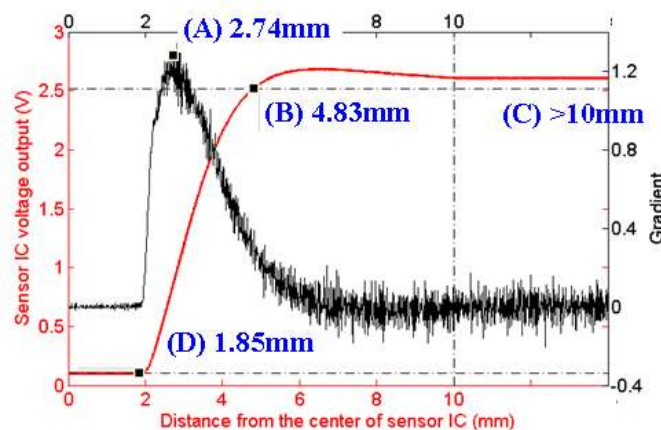


Figure 78 - Sensor voltage output versus the distance (Red axes) between the magnet (M1219-4) and the centre-line of the sensor with air-gap of 1.49mm. The gradient curve axis (Black axes) is offset for ease of interpretation. Dotted lines indicate the sensor saturation voltage (0.1V), quiescent voltage (2.52V) and the effective length of the linear actuator (10mm). Results beyond the 10mm point illustrates sensor output

during the 5s hold of the magnet and when the magnet was at its zero position. Please refer to Table 17 for description for locations A,B,C and D.

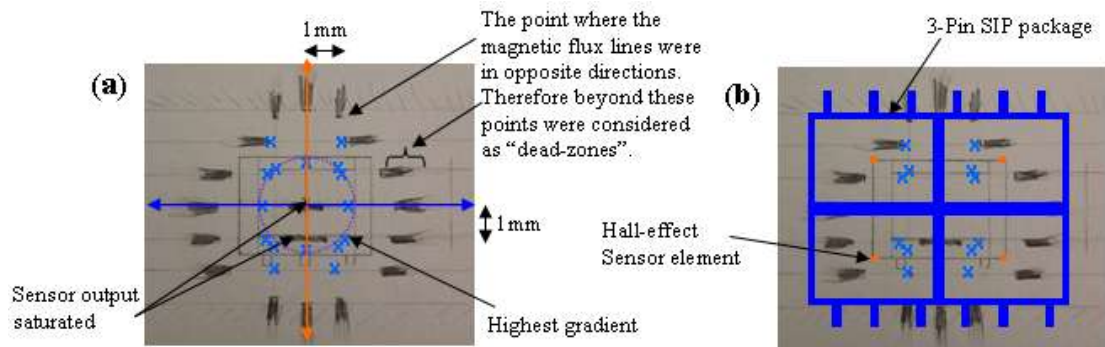


Figure 79 – A map drawn to scale by hand illustrating the presence of magnetic flux lines in the opposite direction (black shaded area) and the locations where the greatest change in magnetic flux occurred (marked X) when the M1219-1 magnet was bought near a A1301 hall-effect sensor IC at an air-gap of 0.89mm (a). The hand drawn map was digitally enhanced for ease of interpretation with the centre-line of the sensor (a) and the position of the four sensor ICs mapped onto the image (b).

Table 18 – Summary of the results for each magnet and air-gap arrangement.

Magnet	M1219-1 (3mm dia. x 1mm)			M1219-4 (6mm dia. x 2mm)		
Air-gap (mm)	0.89	1.49	2.08	0.89	1.49	2.08
Greatest change in magnetic flux density (mm)	1.25	1.21	1.8	2.8	2.74	2.64
Magnetic flux lines in the opposite directions (mm)	2.95	4.34	5.57	4.51	4.83	5.77
No change in magnetic field strength (mm)	9.22	9.67	9.62	>10	>10	>10
Saturated sensor output (mm)	N/A	N/A	N/A	2.56	1.85	N/A
All distances (mm) are expressed relative to the centre of the sensor IC.						

As expected from the manufacturer’s specifications of the magnets (Table 16) and the sensor IC (sensitivity of 2.5mV/G), the 3mm magnet did not saturate the sensor output during tests and the 6mm magnet saturated the sensor when the air gap was under 2mm (Table 18). Due to the arrangement of the four sensor ICs and their sensor package size, each of the four active hall-effect element within the sensors would have been $\sqrt{2.04^2 + 1.44^2} = 2.50\text{mm}$ away from the centre of the magnet (Figure 79b). At that distance, a near maximum rate of change in magnetic flux

density with the 6mm diameter magnet (M1219-4) would have been well utilised. However, the air-gap would have had to be greater than 0.89mm to avoid sensor saturation. Sensor ICs of smaller package should be used to allow further miniaturisation of the transducer sensing surface area and therefore the four active hall-effect elements would be less than 2.5mm from the centre of the magnet. As a result, a further increase in the air-gap would be necessary to avoid sensor saturation. The increase in the overall transducer thickness was regarded as a disadvantage. The strength of the 6mm magnet was also found to influence other sensors positioned over 10mm with a opposite flux line direction (Table 18). Thus, the 6mm diameter magnet (M1219-4) was deemed not suitable for purpose and rejected.

The 3mm diameter magnet (M1219-1) did not appear to be strong enough to influence the outputs produced by neighbouring transducers. However, with the active hall-effect element 2.5mm away from the magnet, the air gap would have to be kept as low as possible in order to obtain an optimal location for highest rate of change in magnetic flux density. The hall-effect elements would be <2.5mm away from the magnet if the SOT23W package sensors were used, therefore it was anticipated that the 3mm diameter magnet would give better performance if coupled with the smaller surface mount sensors. This would have also allowed the reduction in air-gap giving greater sensitivity and further miniaturisation of the transducer. Although the selection of the magnet-sensor pair was a compromise, the properties of the 3mm magnet were deemed sufficient to be incorporated in a proof of concept prototype.

The 3mm magnet (M1219-1) was selected and assessed in the unipolar head-on mode of operation. The results of the tests have been included in Appendix F. As expected, the data obtained from the unipolar head-on test closely matched the corresponding results from the unipolar slide-by arrangement (Appendix F). Unfortunately, because the magnet would be at the corners of the four sensor ICs (Figure 79b), the gradient curves (Figure 80, and reproduced in Appendix F) predicted that the sensors would be $(0.34/1.98 \times 100)$ 17% less sensitive to vertical movement of the magnet than if the magnet was at the centre of the sensor. Moreover, the sensitivity would worsen with increased air-gap distance. The vertical

movement of the magnet would need to be increased to compensate for the lost of sensitivity, otherwise the sensor ICs would detect negligible change in magnetic flux density, hence being unable to detect vertical load.

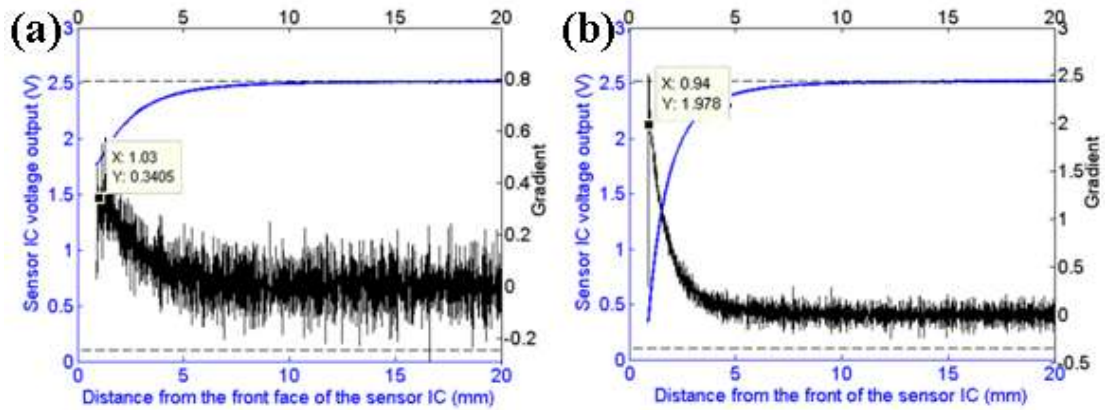


Figure 80 –Sensor IC voltage output as a function of air-gap distance between magnet (M1219-1) and sensor face (A1301) (Blue axes), and the rate of change of voltage (Black axes). Illustrated is the effect of air-gap distance (x-axis) on the gradient of the output waveform (y-axis) when the magnet was at the corner (a) and centre (b) of the sensor IC. Figures are reproduced in Appendix F.

5.4.2.3 Transducer structure

The structure of the transducer prototype was designed to aid the swapping of components for the evaluation of different ‘sensor ICs + magnet + elastomeric material’ configuration. The three types of elastomeric material discussed previously (Section 5.3.2.3) were evaluated; namely a pre-formed 1.5mm silicone sheet (KSIL60), 0.5mm and 1mm rubber sheets (TARRC) and a flowable silicone compound (RS692-542). The KSIL60 and TARRC rubber sheets were treated with LOCTITE®770™ before bonding between the sensing surface and the transducer housing using LOCTITE®406™. A uniform layer of RS692-542 was applied between the sensing surface and the transducer housing and left over 24 hours for the bonding to cure. The RS692-542 silicone cured with a thickness of 0.17mm and the excess was manually trimmed.

The transducer housing had a long rectangular opening that penetrated through the left and right sides of the transducer (Figure 81). The four sensor ICs could be slotted in place, two from each side, with their pins located at the sides of the transducer for cable connections. The transducer housing was made of aluminium alloy for its non-

magnetic property. The sensing surface, in contrast, was made from steel plate (1.7mm) so that permanent magnets could be attached and swapped with ease as necessary. The midpoint of the sensing surface was marked on the underside to ensure consistent positioning of the magnet. There was also a circular opening ($\text{\O}7\text{mm}$) that penetrated through the centre of the upper and lower surfaces of the housing allowing manual positioning of the magnets using tweezers. The hole also allowed the trimming of the elastomeric material for the magnet to attach directly onto the steel plate. A technical drawing of the transducer housing has been included in Appendix B. Due to limitations in the availability of manufacturing facilities, the transducer housing was manufactured as two halves and assembled using fixing screws (Figure 81).

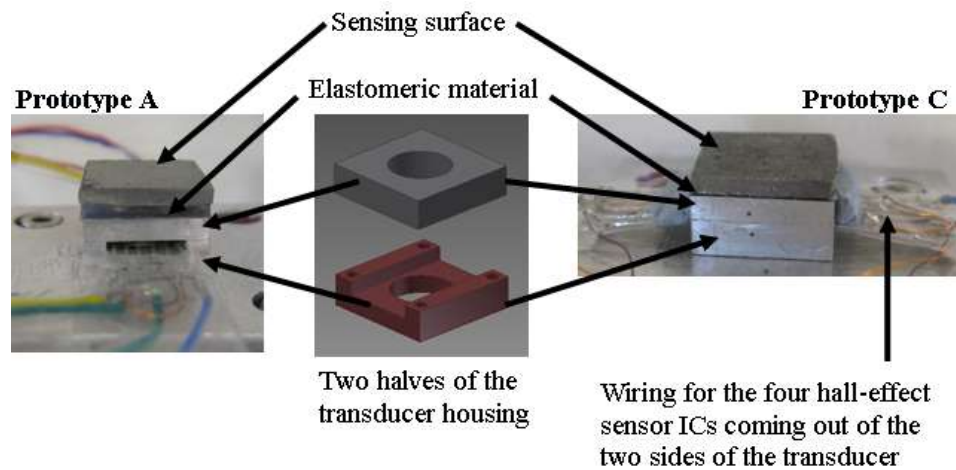


Figure 81 - The completed magnetic load transducer Prototypes A and C. The sensing surface was made of steel plate and the two halves of the transducer housing were made of aluminium and were secured with fixing screws.

Five prototype configurations were evaluated (Table 19). Figure 81 illustrates two of the completed prototypes, A and C. Two magnets were stacked together for Prototype E in order to boost the magnet strength to compensate for the increased air-gap in comparison to Prototype D, which was identical except for the thickness of the elastomeric material.

Table 19 – The configurations of five different magnetic based prototypes.

Prototype	A	B	C	D	E
Magnet	Assemtech M1219-1				2 x M1219-1
Hall-effect ICs	A1321EUA-T	A1301EUA-T			
Elastomeric material	KSIL 60 1.5mm		RS692-542 0.17mm	TARRC 0.5mm	TARRC 1.0mm
Air-gap	2.5mm		1.17mm	1.5mm	2.0mm
Transducer Height	9.20mm		7.87mm	8.20mm	8.70mm
Sensing area	13×13mm				

5.4.2.4 Circuit design

Each hall-effect sensor IC was powered via the same 5V supply outlet on board of the data acquisition system (DAQ) (USB-6225, National Instruments Corps, Ireland). The four voltage outputs from the ICs were connected to the same DAQ for data recording. Data recording was controlled via a custom program written in LabView8.6 (National Instruments Corps, Ireland). The software was programmed to calculate the movement of the magnet in real-time using equations from Table 14.

5.4.2.5 Prototype calibration

The prototypes were calibrated using a six-channel reference load cell (Nano25, ATI Industrial Automation, USA). Force outputs from the reference load cell and voltage outputs from the magnetic sensor ICs were sampled simultaneously at 200Hz using the same DAQ system (USB-6225, National Instruments Corps, Ireland). Calibration tests were conducted on the manually operated calibration rig described earlier (Section 4.5). Vertical loads were applied manually with the steel rod (Ø20mm) on the calibration rig, which was put in series with a steel ball (Ø23mm). Shear loads were applied using the sharp end of a ball pen. In each instance, vertical load was applied to the centre of the sensing surface, while shear loads were applied to the mid-point of the corresponding surface of the plate. Dynamic calibration tests for vertical and shear axes were conducted at 1Hz over the ranges of -40N and ±40N for 10 cycles, respectively. Because the loads were applied manually, the actual load could be ±15% of the intended 40N. As a preliminary assessment on the transducer

performance under combined vertical and shear loads, a complex triaxial load was applied manually to each prototype for the duration of about 30s.

Each prototype was in turn secured to the mounting platform of the calibration rig with a single drop of strain gauge-grade cyanoacrylate adhesive (M-Bond-200, Vishay, USA). Prototypes were carefully aligned to the measurement axes of the reference load cell before bonding to the mounting platform. A 2mm flat screwdriver was used to detach each prototype from the mounting platform. Any glue residuals were gently removed prior mounting of another transducer.

5.4.2.6 Prototype calibration results

Calibration tests were conducted in the order from Prototype A to E. Changes in the voltage outputs that were not compatible with correct operation of the four sensor ICs were observed during testing of Prototype C. The unwanted changes in the voltage output were caused by the magnetised steel rod on the calibration rig that was used for applying vertical load to the transducer. This was confirmed from the raw voltage data obtained from Prototype B, in which the voltage output from each of the four sensor ICs were 0.4V higher than the expected voltage of 2.3V with an air-gap of 2.5mm (Figure 80a). The use of the ball pen did not influence the shear axes. Subsequently, from Prototype C onwards, the tower and tilting platform were removed from the calibration rig assembly. Therefore, calibration forces were applied manually and, without the support from linear bearings, aligned along the test axes as accurate as possible. Both vertical and shear forces were applied using a plastic rod in series with a 3/16" (\varnothing 4.763mm) acrylic ball (The Precision Plastic Ball Company Limited, Ilkley, UK).

Loosening of the fixing screws occurred during testing of Prototype D, resulting in unwanted slipping between the top and bottom halves of the transducer housing. The effect which was apparent in only one direction of the Y-axis, resulted in a larger hysteresis loop in the response curve (Figure 82a). The problem was addressed by bonding the two halves of the sensor housing with cyanoacrylate adhesive (M-Bond-

200, Vishay, USA). The calibration curve for Prototype D after securing the transducer housing can be seen in Figure 82b (also in Appendix G).

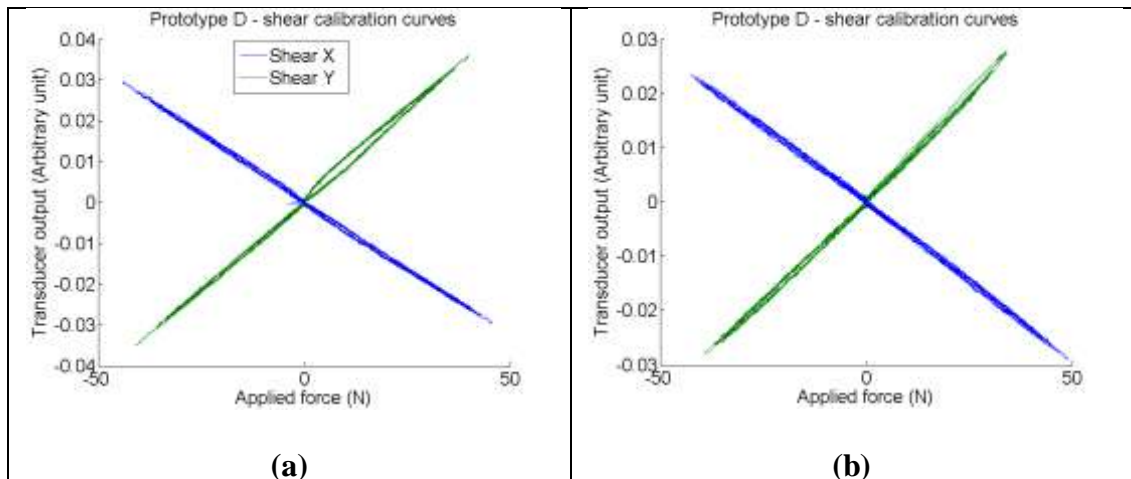


Figure 82 – Calibration curves of Prototype D before (a) and after (b) securing the transducer assembly.

For clarity, calibration plots for all prototypes have been included in Appendix G. Typical calibration results for each shear axis of the individual prototypes have been summarised in Table 20. However, the data in the vertical channels, both within and between prototypes, were obviously inconsistent (Appendix G). For that reason, data from all the vertical channels were excluded in Table 20. Non-linearity and hysteresis values were calculated based on the definition shown in Appendix A. The line of best fit ($y = mx+c$) for each calibration curve was obtained using the least-square method. Given that the transducer outputs were biased to zero before each test, only the slopes of the best fit lines were analysed and presented (Table 20). The transducers' responses in each axis during the application of randomly directed force are plotted (Appendix G) with the slopes of their best fit line summarised in Table 20. There was similarity in the results from Prototype C and D, Figure 83 is presented to allow further exploration of the calibration residuals in these two cases.

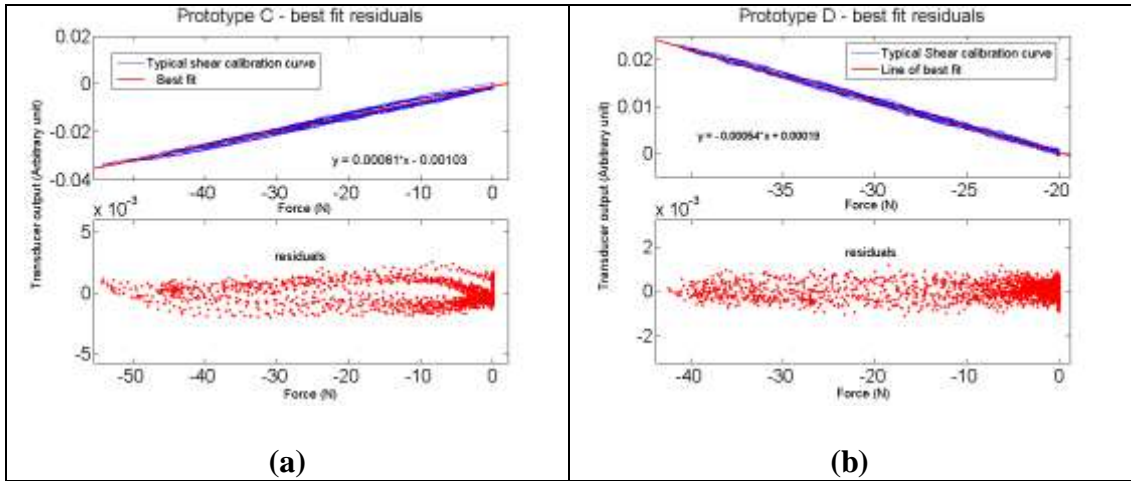


Figure 83 –Best fit line and residuals plots for Prototype C (a) and D (b). Typical outputs from the negative shear axes are presented.

The inherit peak-to-peak voltage noise from an A1321 sensor ($\pm 0.005V$) were more than twice that of an A1301 sensor ($\pm 0.002V$). These levels of noise were reflected in the vertical output response in Prototype A and B (Appendix G), where the peak-to-peak transducer outputs at zero loads were approximately four times the values stated above because they were the sum of four sensors. The rated output span in the vertical calibration curves (Appendix G) estimated the signal-to-noise ratio of 1:1 and 2:1 for Prototype A and B respectively.

Table 20- Calibration results for each shear axes of the magnetic based prototypes. Typical results are shown. Non-linearity and hysteresis values were calculated based on the definition shown in Appendix A.

	Applied load	Slope of the best fit line (y=mx+c)	Goodness of fit	Non-linearity	Hysteresis
Prototype		<i>m</i>	<i>R-Square</i>	%	%
A	Pure X	0.00096	0.95	12.41	25.37
	Triaxial load (X)	0.00096	0.92		
	Pure Y	0.00065	0.91	15.11	28.81
	Triaxial load (Y)	0.00066	0.87		
B	Pure X	0.00063	0.98	7.41	21.05
	Triaxial load (X)	0.00060	0.97		
	Pure Y	0.00044	0.98	7.42	19.24
	Triaxial load (Y)	0.00046	0.96		
C	Pure X	0.00062	0.98	6.84	12.20
	Triaxial load (X)	0.00050	0.98		
	Pure Y	0.00050	0.99	6.47	9.31
	Triaxial load (Y)	0.00044	0.97		
D	Pure X	0.00077	0.99	4.19	6.89
	Triaxial load (X)	0.00072	0.99		
	Pure Y	0.00055	0.99	3.27	6.10
	Triaxial load (Y)	0.00055	0.99		
E	Pure X	0.00562	0.99	7.70	17.66
	Triaxial load (X)	0.00419	0.97		
	Pure Y	0.00386	0.99	6.54	18.75
	Triaxial load (Y)	0.00306	0.95		

5.4.3 Discussion

The five prototypes were capable of withstanding vertical loads of 40N. The slopes of the vertical (Z) calibration curves for Prototype A and B closely matched those during the application of a complex multi-axis load (Appendix G). Such response may give the impression that the transducers were sensitive to vertical load but it is equally possible that the magnetic field was enhanced by the steel rod used to apply the load. Nonetheless, the estimated signal-to-noise ratio of no better than 2:1 meant that the vertical output were unusable. The A1301 family of hall-effect sensor ICs

appeared to have lower error caused by the inherit noise from the sensor ICs than did the A1321 family and would, therefore, be more appropriate for use within a transducer.

The response in the vertical channel with Prototype E during triaxial loading did not match the response during the application of pure vertical load (Appendix G). This possibly reflects the structural properties of the elastomeric material. The response of the transducers was dependent, in large part, on the material properties and thickness of the elastomer. Prototype E was constructed using a relatively thick (1mm) rubber material. The lower effective stiffness of the material allowed greater movement and tilting of the sensing surface, which was most evident during the application of unevenly distributed load or edge loading. The opposite effect could be seen in Prototype C where its 0.17mm thin elastomeric material allowed negligible vertical and tilting movement in the sensing surface hence a flat response curve (Appendix G).

A major limitation of the calibration methodology employed was that prototypes were manually loaded and, as such, pure uniaxial loads were not applied. Although the prototype shear outputs were compared relative to the corresponding shear outputs from the multi-axial reference load cell, the ‘pure’ shear loads were not applied along the sensing surface of the transducer but were applied lower, on the mid-sides of the sensing plate. In theory, any off-axis load would introduce a bending moment which in effect would result in tilting of the sensing surface. In Prototype C and E there was a considerable discrepancy in the slope of best fit line recorded during the application of pure shear compared to the application of complex triaxial loads. While this phenomenon probably reflects the effect of tilting or off-axis loading of the transducer, it is also possible that the shear modulus of the elastomeric material of the transducer differs with the application of combined vertical and shear load. Other prototypes, in contrast, appeared to display negligible cross-talk between outputs from the three axes. This is best demonstrated by Prototype D, where the slopes of the best fit in the shear axes were practically identical during pure shear calibration and when the transducers were subjected to triaxial loads. Such

performance is most favourable in a multi-axial load transducer where errors caused by edge effects and cross-talks between axes should be kept to a minimum.

Hysteresis and non-linearity values of Prototype A and B which used the KSIL-60 elastomer were found to be similar to those from the optoelectronic-based prototype transducers that also used KSIL-60 (Section 5.3.2.7). The hysteresis value of Prototype C with the RS692-542 elastomer was larger in the magnetic prototype because shear calibration was conducted at $\pm 40\text{N}$ compare to $\pm 10\text{N}$ in the optoelectronic-based prototype. However, the hysteresis values from the magnetic-based prototypes D and E which used the TARRC elastomer were higher in comparison to the optoelectronic-based prototypes. This was believed to be due to the loosening of the fixing screws in the transducer housing and the subsequent application of cyanoacrylate adhesive to fix the housing would be to blame for the increase in hysteresis and non-linearity.

The working prototypes demonstrated the feasibility of the magnetic based transducer design for measurement of biaxial but not triaxial load and that small dimensions of transducer could be readily achieved. The thinnest prototype was 7.87mm and could have been further miniaturised, for example, by using surface mount sensor ICs (-0.5mm) or by reducing the thickness of the sensing surface (-1mm) or the base of the transducer housing (-1 to -2mm). The use of surface mount sensor ICs would have allowed the surface area of the transducer to be reduced, where 10x10mm would be possible. The results indicated that the performance of the transducers was dependent on the mechanical properties of the elastomeric material that separated the sensing plate from the transducer housing. The 0.5mm rubber medium (Prototype D) was one of the thinnest materials used in the construction of the transducer and appeared to provide the best linear response of the transducers with minimal hysteresis. As a result of the rectangular shape of the sensor ICs, the slope of the best fit lines of the Y-axis shear were systematically smaller than those of the X-axis shear (Table 20). The use of the smaller surface mount sensor package, again, would have allowed the four hall-elements to be located at equal distances from the centre of the magnet.

The design of the magnetic transducer used in the current study was simple, easy to fabricate and provided a rigid base for housing the sensor ICs. It could have been improved by manufacturing the housing as one piece with the capacity to withstand vertical load 2500kPa and shear loads 300kPa specified earlier (Section 2.4.1) to ensure a sufficient safety margin for the clinical evaluation of biaxial loads during human gait. The use of fixing screws within the prototypes allowed relative movement between components and, therefore, should be avoided in miniature transducers. Cabling within and external to the transducer was minimal as a result of using integrated circuits with built-in amplifier and signal conditioning circuits.

In summary, the use of a permanent magnet in combination with four hall-effect sensors ICs fixed in a unipolar head-on arrangement was not suitable for the detection of vertical loads. However, good performance was achieved from the shear outputs of the transducer, when a carefully selected elastomeric material was used. In comparison with other technologies such as the optoelectronic based transducer described earlier (Section 5.3), it would be expected that the production cost for a magnetic based biaxial shear load transducer would be relatively low.

5.5 Conclusion

The development and preliminary evaluation of various multi-axial load transducers has been discussed. The piezoelectric based prototype transducer from 'Kent' and various novel hydraulic, optoelectronic and magnetic-based prototypes were evaluated for their capability in measuring triaxial load. Each prototype transducer had its strengths and weaknesses, but they all satisfied the minimum system requirement, the ability to measure biaxial shear load. Although piezoelectric and hydraulic-based prototypes also displayed the potential of achieving the ultimate requirement of measuring triaxial load, they had several major limitations that prevent their application for routine clinical use.

Although the piezoelectric based transducer had the potential for detecting triaxial load in a relatively small package (13×13×2.7mm), it was extremely sensitive to bending. The bending of the transducer resulted in unacceptable crosstalk and

erroneous reading. A more robust transducer housing would be necessary to minimise such mechanically induced error. This however, would likely increase the overall dimensions of the transducer potentially larger than the magnetic based prototype (13×13×7.87mm), and would render it unsuitable for in-shoe application. Moreover, the transducer and its connections to the charge amplifier circuits were extremely sensitive to electromagnetic noise or any static charge brought near by the subject. High precision and quality control are paramount in the manufacturing of a piezoelectric based transducer, hence it would be time consuming and costly even in mass production. An enclosed transducer design would also be necessary to avoid permanent failure of the bonding of the piezoelectric material on the transducer housing which may otherwise cause injury during use. Furthermore, relatively expensive low-noise cabling and electronics are essential for quasi-static load measurement. Therefore, piezoelectric based transducers are not currently economically viable especially in a load distribution measurement system that requires large numbers of discrete transducers. As such, piezoelectric-based transducer design was not considered further in the current study.

The hydraulic-based prototype transducers were capable of measuring triaxial load. Hardware and manufacturing costs were considerably lower than the piezoelectric-based design through the use of off-the-shelf components. A hydraulic-based transducer incorporating an appropriate pressure tube material (PVC) and a chemically compatible fluid (corn oil) has the potential to perform with minimal hysteresis and non-linearity. The hydraulic based transducer was the only design suitable for use in harsh electromagnetic noisy environments such as in a MRI laboratory. However, the hydraulic based prototypes were the largest (30×30×24mm) and miniaturisation of such for incorporation within an array could be physically challenging. Management of the large amount of oil-filled tubes in a large transducer array would be difficult or impractical. The hydraulic based designs seemed impossible for the development of a high spatial resolution load distribution measurement device, let alone for in-shoe applications. Therefore, the hydraulic based designs were not worthy of further investigation in the development of a load distribution measurement device.

In contrast to the piezoelectric and hydraulic-based transducers discussed above, the optoelectronic based transducers were only suitable for measuring biaxial shear load. The smallest optoelectronic based prototype measured 15×15×17mm but were only limited by the size of the photodiodes, which could be further miniaturised. Although not suitable for the measurement of vertical load, high performance in shear measurement with minimal hysteresis and non-linearity were achievable with the optimal selection of optoelectronic components and elastomer material. The prototypes also displayed negligible cross-talk between shear channels during multi-axial load. While additional construction consideration may be necessary to strengthen the electronic connections for the single LED at the upper half of the transducer, it is possible to construct a biaxial shear load distribution measurement device using these relatively low-cost optoelectronic based transducers.

Similarly to the optoelectronic-based transducers, the magnetic-based transducers were also suitable for the measurement of biaxial shear load. In contrast to the optoelectronic based design where further signal optimisation would be possible with a custom designed amplifier circuit, the magnetic based transducers utilised off-the-shelf pre-conditioned ICs which cannot be customised for the purpose of shear measurement. As a result, the selection of permanent magnet and its position within the transducer was of paramount importance. Magnetic based transducers must be constructed and operated with care to ensure any external ferrous materials or the magnets within each transducer would not influence the output of other neighbouring transducers. On the other hand, the overall dimensions of the transducers were the smallest in the magnetic based design with the use of these miniature ICs. Moreover, further external signal conditioning circuits were not required. Therefore, it is possible to construct a relatively low-cost biaxial shear load distribution measurement device using an array of magnetic based transducers.

In summary, both the optoelectronic and magnetic based prototype transducers should be evaluated further for their suitability in the development of a biaxial shear distribution system. Transducers of the same dimensions should be built in order to facilitate a direct comparison between the two designs.

Chapter 6

Further improvement of two different biaxial shear transducers

From the experience and results obtained during previous testing (Section 5.3.3 and 5.4.3), both the optoelectronic and magnetic based transducer designs have been selected to be evaluated further for their suitability in the development of a biaxial shear load distribution measurement system. Two improved transducers are built to the same dimensions in order to facilitate a direct comparison between the two designs.

6.1 Transducer designs

Two improved transducer designs were constructed using the same optoelectronic (Section 5.3.1) and magnetic (Section 5.4.1) based load sensing technologies described earlier. The following sections describe the two new transducer designs selected for array development.

6.1.1 Optoelectronic based biaxial shear transducer

A new optoelectronic based biaxial shear transducer was constructed based on the optimal light emitter-photodiode arrangement and elastomeric material identified earlier (Section 5.3.3). Brief descriptions of the components used in the construction of the transducer have been included in Table 21.

Table 21 - Components used in the construction of the new optoelectronic based biaxial shear transducer.

Components	Descriptions
Quadrant photodiodes	Model: Hamamatsu S4349 Dimensions: $\text{Ø}9.2 \times 4.1 \text{mm}$ Cost: £30.00
LED	Model: Avago HLMP-Q105 Dimensions: $2.08 \times 2.08 \times 2.92 \text{mm}$ Cost: £0.33
Elastomeric material	TARRC 0.5mm rubber Dimensions: $15 \times 15 \times 0.5 \text{mm}$ Estimated cost: £0.21
External amplifier	Model: Texas Instruments OPA404 Cost: £20.52
Transducer structure/housing	Aluminium Estimated cost: £15.00
Cables	Standard 5 core ribbon cable Estimated cost: £1.80

The biaxial shear transducer was based on the same design and arrangement of components as Prototype B (Section 5.3.2.4), but with two exceptions: (1) The sensing surface was constructed from aluminium ($15 \times 15 \times 3 \text{mm}$) as opposed to copper-clad laminate PCB for a more robust design to avoid bending of the PCB during loading; and (2) The LED was set flush within a $\text{Ø}2.5 \times 2 \text{mm}$ deep cavity located at the centre of the aluminium sensing surface plate to avoid direct contact with the LED. The completed transducer measured $18.5 \times 15 \times 15 \text{mm}$ (Figure 84).

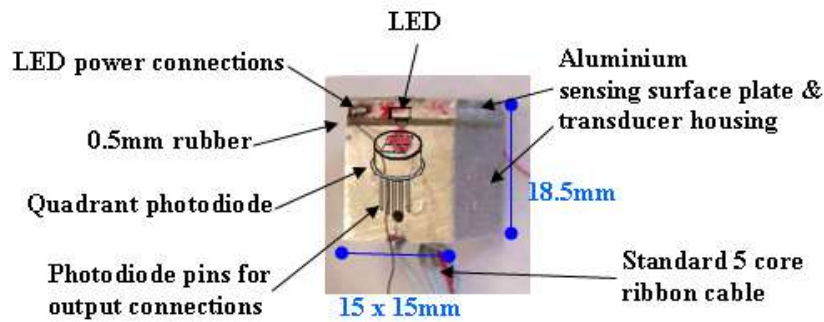


Figure 84 - Illustration of the components used in the assembly of the optoelectronic based biaxial shear transducer.

The LED was secured in place using cyanoacrylate adhesive (M-bond 200, Vishay, USA). The assembly was then treated with a non-conductive polyurethane coating (Gauge Coat-A) before the two pins of the LED were cut and soldered onto strain gauge wires. The two strain gauge wires channelled through two shallow grooves located on the under-surface of the sensing plate and terminated at opposite corners of the plate. The terminals were padded on both sides of the sensing surface (Figure 84), and were connected to the 5V power supply on the DAQ system using two longer strain gauge wires.

In comparison to earlier prototypes (Section 5.3.3) where two triangular sheets of rubber sheet were used, a single rectangular sheet of TARRC 0.5mm rubber was used in the new transducer to separate the sensing surface plate and transducer housing. The rubber sheet had a hole ($\text{\O}3\text{mm}$) in the centre to accommodate the LED (Avago HLMP-Q105) and was treated with LOCTITE®770™ before bonding between the sensing surface and the transducer housings using LOCTITE®406™. Visual checks were performed to ensure the rubber was fully bonded and that the assembly was aligned with the transducer axes.

The electronic circuits were the same as discussed in Section 5.3.2.5. Briefly, the single LED was powered via the 5V supply on board of the DAQ system (USB-6225, National Instruments Corps, Ireland) in series with a 330Ω current limiting resistor. Standard 5 core ribbon cable was used to feed the outputs from the photodiode chip to the op-amp circuit (Figure 84). The feedback resistors (R_F) for each of the quad op-amps (OPA440) were $390\text{k}\Omega$. The op-amp chip was powered via

a $\pm 15V$ bench top power supply. The four voltage outputs from the op-amps were connected via another 5 core ribbon cable to the DAQ system for data recording.

6.1.2 Magnetic based biaxial shear transducer

The optimal ‘magnet, elastomeric material and Hall-effect sensor ICs’ arrangement for assembling a biaxial shear transducer had been identified (Section 5.4.3). Brief descriptions of the components used in the construction of the transducer have been included in Table 22.

Table 22 - Components used in the construction of the new magnetic based biaxial shear transducer.

Components	Descriptions
4 Hall-effect sensor ICs	Model: Allegro A1301 (3-Pin SIP) Dimensions: 4×3×1.5mm Cost: £1.09, each
Permanent magnet	Model: Assemtech M1219-1 Dimensions: Ø3.0×1.0mm Cost: £0.40
Elastomeric material	TARRC 0.5mm rubber Dimensions: 15×15×0.5mm Estimated cost: £0.21
Transducer structure/housing	Aluminium Estimated cost: £15.00
Cables	Standard 6 core ribbon cable Estimated cost: £1.80

The construction of a new biaxial shear transducer was the same as Prototype D (Section 5.4.2.3) except its overall dimensions and housing material. Since the dimensions of the optoelectronic based transducer described above (Section 6.1.1) was restricted by the size of the photodiode, thus the height and the sensing surface area of this magnetic based transducer were enlarged to match those dimensions of the optoelectronics based transducer in order to facilitate a direct comparison between the two designs. The transducer housing and the sensing surface plate, in contrast to Prototype D, were both made of aluminium. The thickness of the sensing surface plate was 2mm and a new transducer housing design was introduced. The technical drawing of the transducer housing has been included in Appendix B. The completed transducer measured 17.5×15×15mm (Figure 85).

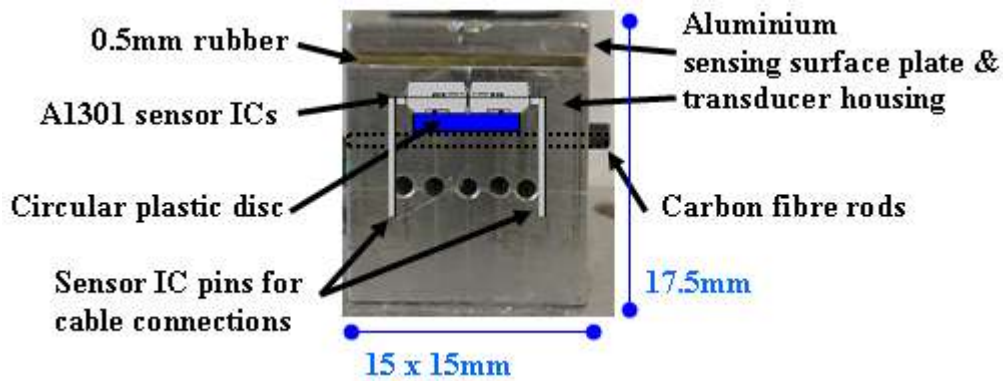


Figure 85 – The components used in the assembly of the magnetic based biaxial shear transducer.

Four 3-Pin SIP packaged A1301 hall-effect sensor ICs were secured onto a circular plastic disc ($\text{Ø}11 \times 2\text{mm}$) using strain gauge adhesive (M-bond 200, Vishay, USA). The circular disc was trimmed to allow the 12 pins from the four sensor ICs to be bent at 90 degrees for wire connections via the bottom of the transducer (Figure 85). The circular disc with the sensor ICs attached was then inserted into the hollow compartment of the transducer housing. Carbon fibre rods ($\text{Ø}1.2 \times 13\text{mm}$) were slotted through the hollow compartment to support and secure the circular disc assembly into place. The whole assembly was carefully adjusted to align with the transducer axes before being fixed permanently using strain gauge adhesive (M-bond 200, Vishay, USA). The same adhesive was also used to secure the 3mm diameter magnet (M1219-1) onto the base of the aluminium sensing plate before the rubber was bonded onto the same surface and assembled onto the transducer housing using LOCTITE®406™.

All four hall-effect sensor ICs were powered via the same 5V supply outlet on board of the DAQ system (USB-6225, National Instruments Corps, Ireland). The four voltage outputs from the ICs were connected to the same DAQ for data recording during calibration. A standard 6 core ribbon cable was used to provide those connections described above.

6.2 Calibration method

This section describes the calibration and analytical procedures for the evaluation of the optoelectronic and magnetic-based biaxial shear transducers.

6.2.1 Experimental setup

The availability of a new mechanical testing instrument (ElectroForce3200, Bose Corp., USA) allowed the biaxial shear transducers to be evaluated in a more controlled manner compare to the manually controlled calibration rig used previously (Section 4.5). The uniaxial testing system was fitted with a 450N reference load cell. The load cell was based on strain gauge technology with a 12000Hz natural frequency and accuracy of 0.25% full scale (equivalent of $\sim 1\text{N}$). The system was capable of performing static and dynamic tests up to 200Hz and simultaneously provided displacement data to $\pm 0.0325\text{mm}$ accuracy.

A 40mm aluminium extension rod fitted at one end with a 3/16" ($\text{\O} 4.763\text{mm}$) acrylic ball (The Precision Plastic Ball Company Limited, Ilkley, UK) was rigidly secured in series with the actuator of the uniaxial mechanical testing machine. Aluminium and acrylic were specifically chosen for their non-magnetic properties, and the assembly allowed for point loading of the transducers during static and dynamic tests.

Two aluminium mounting adapters were specifically designed for mounting the biaxial shear transducers to the reference load cell in the ElectroForce3200 system: one for mounting the transducer in an up-right position to assess crosstalk during vertical loading (Figure 86a); another for mounting the transducer on its sides allowing shear loading of the transducer (Figure 86b). Each of the mounting adaptors were mounted in two orthogonal adaptor rails which allowed for precise positioning of the biaxial shear transducers in the plane orthogonal to the applied load (Figure 86). The adaptor rails were screw mounted to the reference load cell, whereas the mounting adaptors were secured in place in the rail using two screw nuts (Figure 86). The combination of adaptor rails and mounting adaptors allowed the biaxial shear transducer to be repositioned with respect to the linear actuator. Therefore, the

application of on-axis or off-axis load, vertical or shear load was possible by repositioning the transducer between tests (Figure 86).

Vertical loading - Both biaxial shear transducer were tested under vertical load (Figure 86a). The mounting adaptor had a groove to allow wires to pass through the bottom of each transducer during vertical tests (Appendix B). Once the transducer was aligned to the loading axis, two screws were used to lock the transducer in place in the mounting adaptors (Figure 86).

Shear loading - To apply shear load to the transducer, an aluminium cap bracket was secured to the sensing surface of the transducer using adhesive (M-bond 200) before mounting the transducer in a sideways position (Figure 86b). The point load was applied to the side of the bracket and parallel to the sensing surface of the transducer (Figure 86). Following testing in one shear direction, a 2mm flat screwdriver was used to detach the cap from the transducer. Any glue residuals were gently removed prior to re-adhering the cap for evaluation of the other shear axis direction. Technical drawings of the two mounting adaptors, the two adaptor rails and the cap bracket are included in Appendix B.

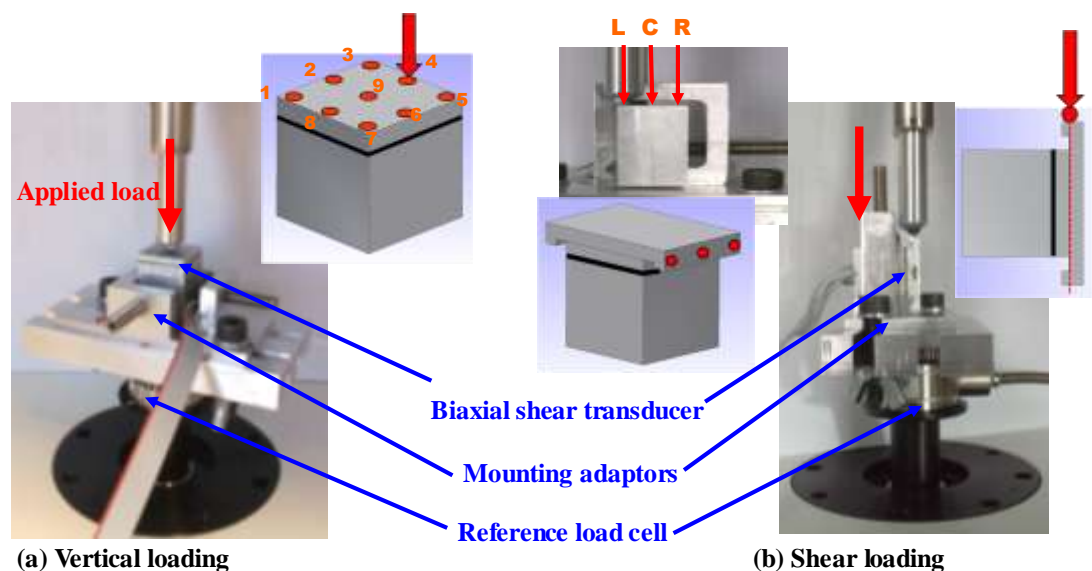


Figure 86 - Calibration setup on the BOSE ElectroForce 3200 material testing machine for vertical testing (a) and shear calibration (b). Red dots and numbers indicate the positions of the applied load during on-axis and off-axis tests. L, C and R means Left, Centre and Right side of the transducer.

6.2.2 Loading protocols

Each biaxial shear transducer was calibrated under dynamic conditions in the shear axes. The mechanical testing machine was set to apply a 1Hz cyclic shear load over a range of $\pm 50\text{N}$ for 15 cycles (Figure 87a). This corresponded to a shear stress of 220kPa over the sensing surface area of $15 \times 15\text{mm}$ of the biaxial shear transducer. More in-depth testing was then carried out after each transducer was calibrated:

Vertical loading

1. A cyclic vertical load over a range of 2N to 350N at 1Hz for 15 cycles was applied through point loading at 9 different locations - at the centre of the transducer and at each corner and edge at separate times (Figure 86a). The crosstalk present on the shear channels was measured.

Shear loading

1. A shear load ranging from 5N to 50N at 1Hz for 15 cycles (Figure 87a) was applied along the centre line of the transducer. The same loading sequence was repeated for each direction of each shear axis. The crosstalk present on the other shear axis was measured. Accuracy and repeatability of the transducer output between those 15 cycles was examined.
2. A shear load ranging from 5N to 50N at 1Hz for 15 cycles (Figure 87a) was applied along the outer edges of the transducer. The error in the corresponding shear axis and crosstalk present on the other shear channel were measured.
3. Shear loads of different frequencies were applied to the transducer using the dynamic mechanical analysis (DMA) frequency sweep function on the ElectroForce3200 machine. The loading sequence (Figure 87b) began with a 30N ramp with 8 seconds hold, for determination of transducer creep, before applying cyclic load of 10 different frequencies to the transducer: 0.5Hz, 1Hz, 20Hz, 40Hz, 70Hz, 90Hz, 110Hz, 140Hz, 180Hz and 200Hz. A 30N load hold (8 seconds) and a single pre-conditioning cycle was applied to the transducer between each frequency (Figure 87b). A 5N load hold was maintained for 8 seconds following the completion of the frequency sweep, allowing an estimate

of creep-recovery. The same loading sequence was subsequently applied to each shear axis of the transducer.

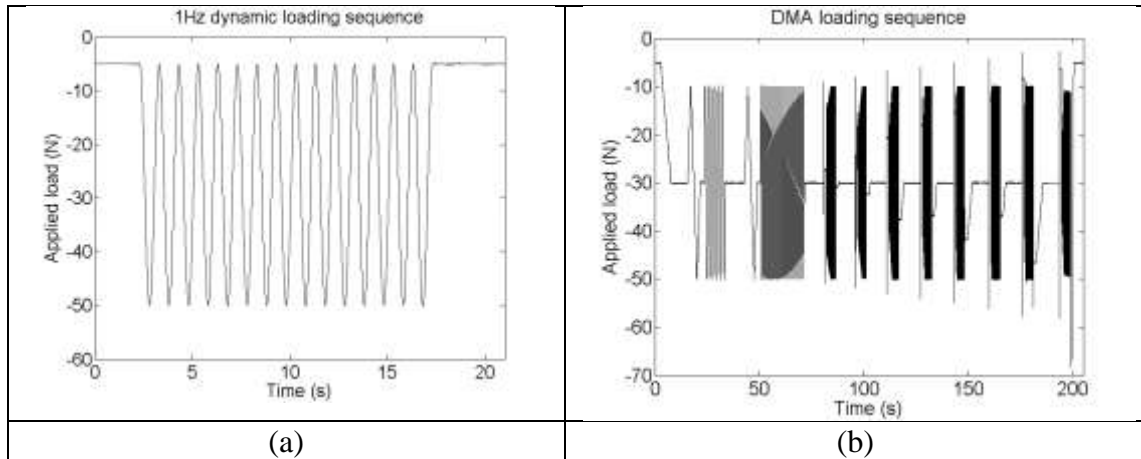


Figure 87 – A typical cyclic loading sequence ranging from 5N to 50N at 1Hz for 15 cycles (a), and a typical dynamic mechanical analysis (DMA) frequency sweep sequence (b) used in loading the biaxial shear transducers at 10 different frequencies, from 0.5Hz to 200Hz.

6.2.3 Data Reduction

Displacement and force data from the ElectroForce3200 testing machine were output as two voltage sources, which were connected to a DAQ (USB-6225) controlled via a custom program written in LabVIEW8.6 (National Instruments Corps, Ireland). Consequently the four signals from the biaxial shear transducer and two signals from the ElectroForce3200 were simultaneously recorded. Data were sampled simultaneously at 5000Hz during frequency sweep tests to allow optimum Fourier Transform frequency response analysis. The sampling frequency of the DAQ was set at 200Hz for all other tests. Data were subsequently post-processed in MATLAB (MathWorks Inc, MA, USA).

Transducer characteristics such as frequency response, hysteresis, non-linearity and cross-talk were examined based on the definitions and methods of calculation shown in Appendix A. Accuracy and repeatability of the transducer shear outputs were assessed during shear Protocol 1 - when pure shear load was applied along the centre line of the transducers at 1Hz for 15 cycles in each shear direction. In terms of accuracy, the maximum absolute difference of the read versus applied load and the root mean squared error (RMSE) were examined. The RMSE error was also

expressed as a percentage of the rated capacity. In terms of repeatability, the average peak-to-peak outputs from the reference load cell and the transducers during the 15 cycles of shear load were examined. Standard deviation of those 15 peak-to-peak outputs were compared as the indication of the repeatability of the transducers outputs.

6.3 Results & Discussion

The results from calibration and testing of the optoelectronic and magnetic-based transducers are presented under four categories corresponding to the requirements (#1 to #28) set out earlier in Section 2.4.1.

6.3.1 Transducer performance

#1 Rated Capacity, #2 Resolution

The two transducers were calibrated up to 50N shear (rated capacity) and were fully tested to withstand vertical load of up to 350N. Both transducers were analogue devices with continuous resolution. Therefore, in practical terms, the resolution of the transducer systems was limited by the quality of the analogue-to-digital electronics within the DAQ instrument (USB-6225) which converted the four voltage outputs from each transducer to digital data recorded by the computer. The average peak-to-peak voltage changes in the four outputs from each transducer when loaded at the rated capacity (50N) have been summarised in Table 23. Although the changes were of the order of millivolts, baseline voltage ranged from -1V to -2V in the optoelectronic based transducer and +2.3V to +2.4V in the magnetic based transducer. Consequently, the DAQ system was set to measure input voltage ranges between 0V to -2.5V and 0V to +2.5V for the optoelectronic based transducer and the magnetic based transducer, respectively.

The analogue-to-digital convertor within the DAQ system had a 16-bit resolution meaning it could resolve 38 μ V steps with the 2.5V voltage range mentioned above. The manufacturer of the DAQ system specified the absolute accuracy was 360 μ V (at full scale -1V to 1V) and 1620 μ V (at full scale -5V to 5V), hence, it is fair to

assume the absolute accuracy at full scale range of 0V to +/- 2.5V would be around $(360 \div 2V \times 2.5V) = 450\mu V$. Based on these figures, the optoelectronic based and magnetic based transducer system had an estimated load resolution of about $(50N \div [99000/450 \mu V])$ 0.23N and $(50N \div [47000/450 \mu V])$ 0.48N, respectively (Table 23).

Table 23 - Average peak-to-peak voltage change from the four sensing elements within the transducers when loaded at the rated capacity (50N) and the load resolution of the transducer systems.

Transducer	Average peak-to-peak voltage (V)	(SD)	System resolution	Sensitivity
Optoelectronic	0.099	0.057	0.23N	1.98mV/N
Magnetic	0.047	0.010	0.48N	0.94mV/N

#3 – Accuracy

Table 24 lists the absolute error for each shear axis of the two prototypes. The maximum difference between the transducer output and applied shear load was found to be <6N in the optoelectronic based transducer during cyclic loading. The absolute error found of the magnetic based transducer during shear loading (<3N) was half that of the optoelectronic transducer. The RMSE data for both transducers was approximately 1N in reading compared to the output from the reference load cell during dynamic load (Table 24). It should be noted that the overall accuracy of the transducers was not only dependent on the performance of the active element of each transducer design but also dependent on contributions from other sources of error such as frequency response (#4), hysteresis (#5), non-linearity (#6), signal noise (#8), and cross-talk (#9) which will be discussed below.

Table 24 - Accuracy of the transducer load outputs with applied shear load at 1Hz. Maximum error (N) and root mean squared error (RMSE) in Newtons and % rated capacity (50N) are presented.

Transducer	Shear axis	Maximum absolute error (N)	RMSE (N)	RMSE (%RC)
Optoelectronic	Negative X	5.91	1.24	2.48
	Positive X	3.72	1.11	2.22
	Negative Y	4.74	1.30	2.60
	Positive Y	4.30	1.15	2.29
Magnetic	Negative X	2.13	0.63	1.26
	Positive X	2.15	0.80	1.59
	Negative Y	2.67	0.90	1.81
	Positive Y	2.83	0.87	1.74

#4 – Frequency response

Figure 88 illustrates the performance of the biaxial shear transducers at various loading frequencies - ranging from 0.5Hz to 200Hz. The calibrated outputs from the optoelectronic based transducer and magnetic based transducer were found to be 90.1% and 89.4% of the applied load at 200Hz, respectively (Figure 88). It was expected that both transducers would possess a similar frequency response because both transducers were constructed with the same elastomeric material.

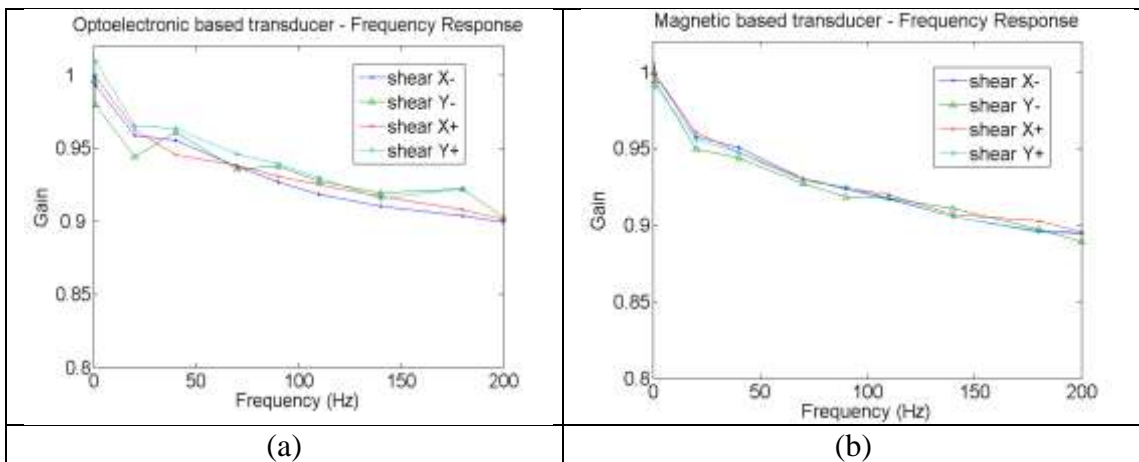


Figure 88 - Frequency response plots of the optoelectronic (a) and magnetic based biaxial shear transducers (b) across frequencies from 0.5Hz to 200Hz.

#5 – Hysteresis, #6 – Non-linearity, #7 – Combined error

Figure 89 illustrates the calibration curves for each shear axes of each transducer. The line of best fit ($y = mx+c$) for each calibration curve was obtained using the least-squares method. Given that the transducer outputs were biased to zero before each test, only the slopes of the best fit lines were analysed and presented (Table 25).

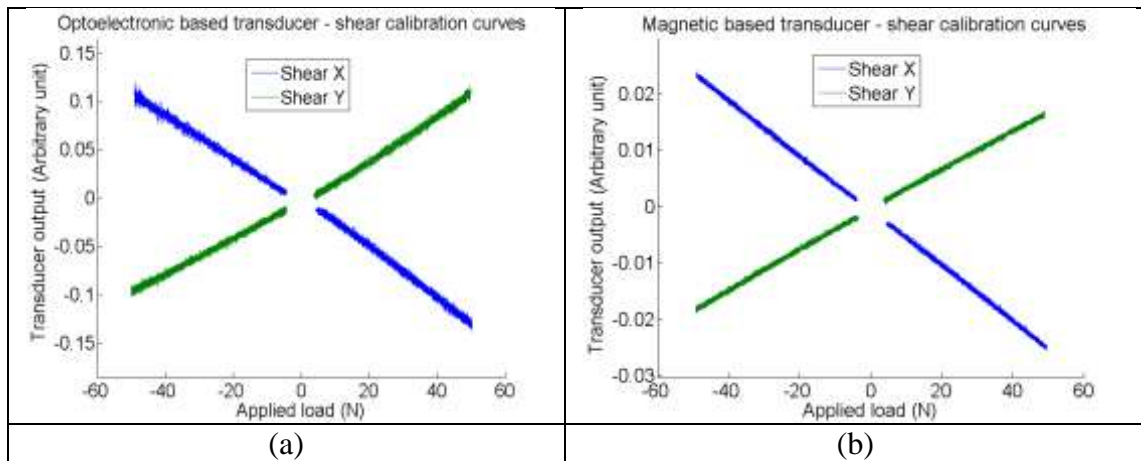


Figure 89- Calibration curves of the optoelectronic (a) and magnetic (b) based biaxial shear transducer. Calibration was conducted with shear load ranging from 5N to 50N.

Non-linearity and hysteresis values were calculated (Table 25) based on the definition shown in Appendix A. Non-linearity % was on average approximately half that of hysteresis %, thus the non-linearity data can also be seen as the combined error based on the definition in Appendix A. Both transducers had similar characteristics in terms of non-linearity and hysteresis. Non-linearity and hysteresis values were practically identical to those found previously from Prototype E (Section 5.3.2.7) in which the same elastomeric material was used. Both transducers displayed linear response to load with high goodness of fit (Table 25).

As expected from the results obtained from the prototypes earlier (Section 5.4.2.6), the slope of the best fit lines of the Y-axis shear of the magnetic-based transducer were systematically smaller than those of the X-axis shear (Table 25). This was due to the fact that the four active hall-effect sensing elements in the magnetic-based transducer were not in a rectilinear grid arrangement relative to the centre of the magnet. As a result, the output span in the Y-axis was relatively lower than the X-

axis. Assuming the signal noise level was constant, the reduced output range may also account for the greater absolute error found in the Y-axis (see #3 Accuracy). Results from the optoelectronic-based transducer were less consistent than for the magnetic-based transducer, in particular in the negative Y-axis (Table 25). This was possibly caused by error due to poor placement of the LED relative to the photodiode.

Table 25 - Shear axes calibration results.

	Shear axis	Slope of the best fit line (y=mx+c)	Goodness of fit	Non-linearity	Hysteresis
Transducer		<i>m</i>	<i>R-Square</i>	%	%
Optoelectronic	Negative X	-0.00230	0.99	2.75	5.53
	Positive X	-0.00265	0.99	2.93	5.50
	Negative Y	0.00189	0.99	2.41	6.24
	Positive Y	0.00232	0.99	2.70	5.74
Magnetic	Negative X	-0.00049	0.99	2.59	5.88
	Positive X	-0.00049	0.99	2.63	4.48
	Negative Y	0.00036	0.99	3.36	6.61
	Positive Y	0.00034	0.99	2.49	5.08

#8 Signal noise

Noise in each shear axis of the optoelectronic based transducer was found to be inconsistent between tests. As illustrated in Figure 92a and Figure 93a below, signal noise found in the same shear axes varied between ± 0.001 or ± 0.005 (arbitrary transducer output units) resulting in a signal-to-noise ratio of about 57:1 or 11:1 which equated to an error of about $\pm 0.5N$ or $\pm 2.5N$, respectively. Fluctuation in the applied load via the ElectroForce3200 testing machine was also found to be inconsistent between tests. Figure 90a illustrates typical waveforms showing the 5N load hold at the end of the 1Hz cyclic loading sequence, when the load fluctuated $\pm 0.05N$ or $\pm 0.1N$ in some cases. No obvious pattern was found for the differences in output noise and applied load between tests, which occurred regardless of whether it was on-axis or off-axis loading. However, the increased signal noise corresponded to increased fluctuation in the applied load. Such a phenomena was not apparent in the

magnetic based transducer, which suggested the construction of the optoelectronic based transducer with its LED and power cables may have influenced the response of the transducer (see also #23 Transducer sensing surface allowable movement).

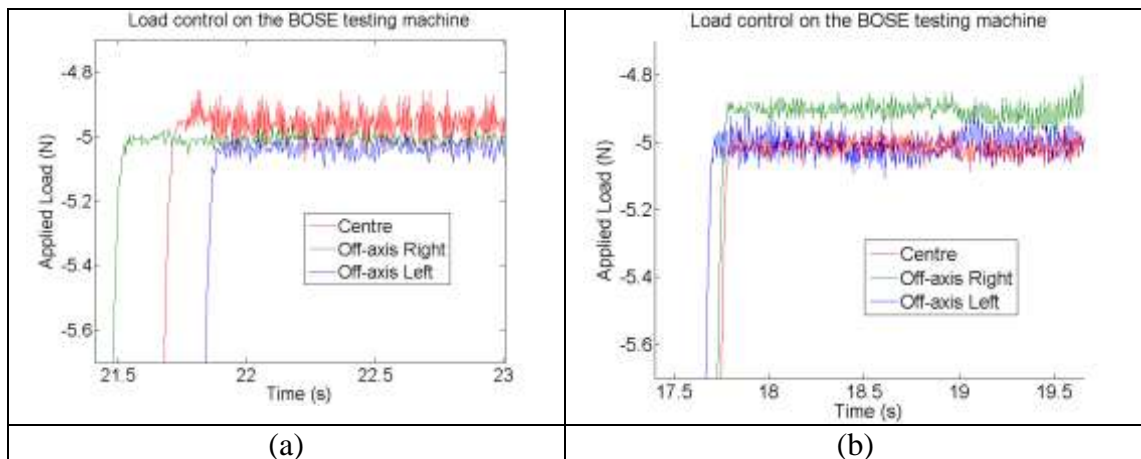


Figure 90 - Waveforms illustrating the load applied to the optoelectronic (a) and magnetic (b) based biaxial shear transducer by the BOSE testing machine under load control. In (a), the variation in the load during ‘centre’ loading was significantly greater than during ‘off-axis’ loading.

Noise found in the magnetic based transducer (Figure 92b and Figure 93b,) was consistent between shear channels at ± 0.0005 (arbitrary transducer output units) resulting in a signal-to-noise ratio of 25:1 and 18:1, which equated to an error of about $\pm 1\text{N}$ and $\pm 1.4\text{N}$ in the shear X and Y axes, respectively. The fluctuation in the applied load during tests on the magnetic based transducer was found to be relatively consistent. Figure 90b illustrates typical waveforms showing the 5N load hold fluctuated no greater than $\pm 0.06\text{N}$ during tests on the magnetic based transducer.

#9 – Cross-talk, #10 – Error due to off-axis loading

Crosstalks in the shear axes due to vertical loading at the centre of the optoelectronic based and magnetic based transducers are illustrated in Figure 91. Crosstalk with vertical loading at the centre of both transducers was found to be relatively low and generally less than the signal noise level discussed above. Consequently, to examine the true effect of crosstalk without the influence of noise within the signal outputs, the line of best fit ($y = mx+c$) for each crosstalk output curve was obtained using the least-squares method. Given that the transducer outputs were biased to zero before each test, only the slopes of the best fit lines were analysed and presented (Table 26).

Crosstalk caused by any magnitude of vertical load could then be obtained by multiplying the slope of the best fit line with the vertical load, which has been completed for 50N and 350N (Table 26). The results are also expressed as a percentage of the rated capacity (%RC) of the shear axes (50N). Both transducers only had about 1N (2%RC) crosstalk in the shear axes when 350N vertical load was applied to the centre of the transducers (Figure 91, Table 26). Such crosstalk of ~1N was within the accuracy (RMSE) of the transducers discussed earlier (#1 Accuracy). It should be noted that it was also possible that the vertical load was not perfectly aligned to the centre of the transducers and the crosstalk data was a reflection of true shear loads caused by off-axis loading. Anyhow, both transducers were capable of withstanding the equivalent of about half of body weight and when this load was evenly distributed there was negligible effect on the shear outputs.

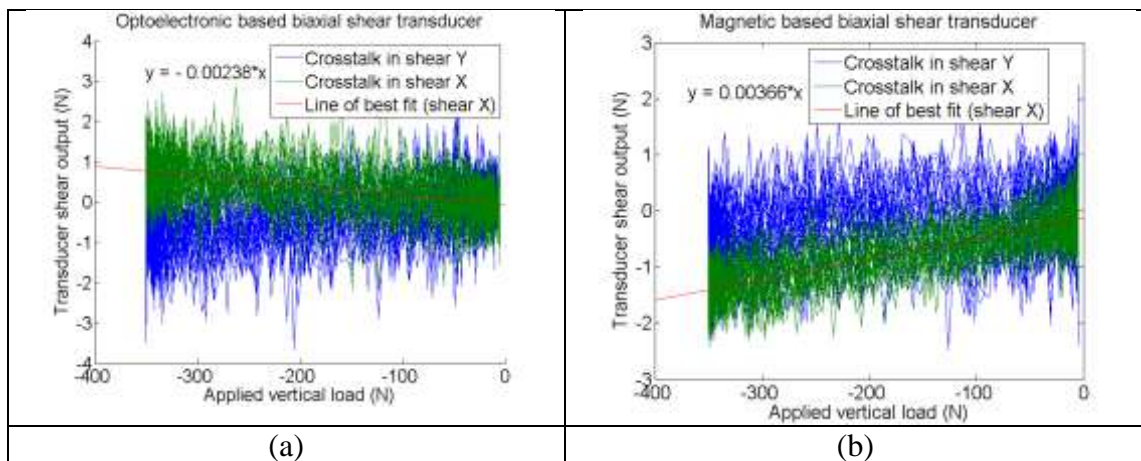


Figure 91 – Crosstalk in the shear axes due to vertical load at the centre of the optoelectronic (a) and magnetic (b) based biaxial shear transducer. As an example, lines of best fit to the shear X outputs are shown which correspond to those summarised in Table 26.

When off-axis vertical loading was applied to the transducers, crosstalk in the shear axes was increased (Table 26). The worst crosstalk was 12.2N (24.4% RC) in the optoelectronic based transducer and 5.4N (10.8%RC) for the magnetic based transducer when 350N vertical load was applied to the corners of the transducers. Figure 92 illustrates the typical effect of off-axis shear load in the transducers' calibration curves. The line of best fit for each off-axis response curve was obtained and compared to the calibration curve (also in Table 25) of the corresponding shear axis (Table 27). The error in shear load output could then be calculated by comparing

these slopes of best fit lines (Table 27). The application of 50N off-axis shear load resulted in an error of <4.5N (9.1%RC) in the optoelectronic based transducer and <3.5N (6.9%RC) in the magnetic based transducer in the same shear axis (Table 27). Given that both transducers were similar in design and had the same elastomeric material, the results (Table 27) have clearly shown that the magnetic-based transducer was much less sensitive to off-axis vertical loading, i.e. the mechanical tilting of the sensing surface plate. This was due to the fact that any slight tilting of the LED light source was detectable by the photodiodes; whereas the tilting of the magnet had less influence in the magnetic field around the sensors ICs.

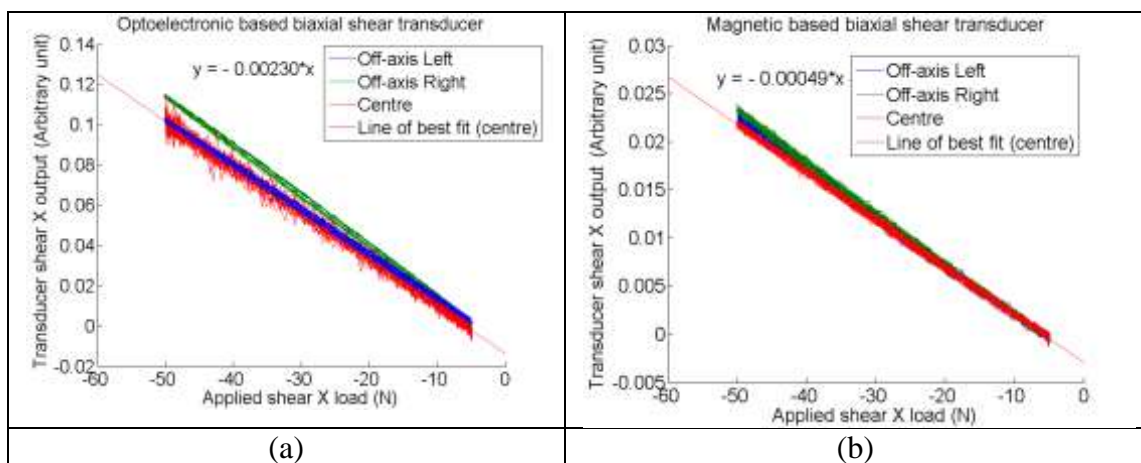


Figure 92 – Deviation from the calibration curve due to off-axis shear loading to the optoelectronic (a) and magnetic (b) based biaxial shear transducer. The plots illustrate typical responses in the negative shear axis and with other directions summarised in Table 27.

Figure 93 illustrates crosstalk in the shear axis due to on-axis and off-axis shear load applied to the other shear axis. The error due to crosstalk can be calculated by comparing the slope of the crosstalk response curve to the calibration curve of the corresponding shear axis (Table 27). Minimal crosstalk was found during 50N on-axis shear loading, which resulted in an error of <1N (2%RC) in the orthogonal shear axis of both transducers (Table 27). However, this was not true for all axes. For instance, crosstalk for the Y-axis of the magnetic-based transducer was as high as 4.3N (8.7%RC). This error was likely to have been caused by the non-rectilinear grid arrangement of the active hall-effect sensor elements, which resulted in a lower output span of the Y-axis (see #3 Hysteresis) hence crosstalk had a relatively higher effect in the Y-axis. Crosstalk could be minimised to <1N had the hall-effect sensors

been located equidistant from the centre of the magnet. This could be achieved for future manufacture if the surface mount version of the hall-effect sensor IC were to be used instead. Again, it should be noted that it was also possible that the pure shear load was not perfectly aligned along the centre-line of the transducers and the crosstalk data was a reflection of true shear loads in the orthogonal shear axis caused by off-axis loading.

While pure shear load in one shear axis resulted in minimal crosstalk in the orthogonal shear axis, off-axis shear loading resulted in significantly greater crosstalk in the orthogonal shear axis. 50N off-axis shear load applied to one shear axis resulted in a maximum error of <8.2N (16.3%RC) in the optoelectronic based transducer and <10.1N (20.2%RC) in the magnetic based transducer in the orthogonal shear axis (Table 27).

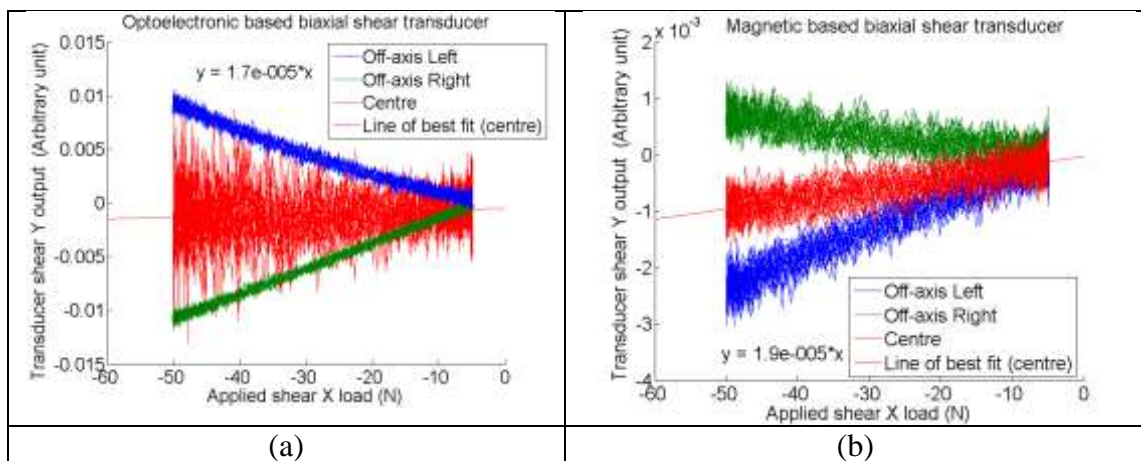


Figure 93 - Crosstalk in the shear axes of the optoelectronic (a) and magnetic (b) based biaxial shear transducers due to off-axis and on-axis shear load applied in the other shear axis. The plots illustrate typical responses in the shear Y axis when shear load was applied in the negative X shear direction.

Table 26 - Crosstalk in the shear axes due to on-axis and off-axis vertical loading. Please refer to Figure 86 for the locations of the applied load.

Transducer	Location of the applied vertical load	Slope of the best fit line		Error (with 350N vertical load)				Error (with 50N vertical load)			
		Shear X	Shear Y	Shear X (N)	Shear Y (N)	Shear X (% RC)	Shear Y (% RC)	Shear X (N)	Shear Y (N)	Shear X (% RC)	Shear Y (% RC)
Optoelectronic	Corner 1	0.02622	0.02193	9.18	7.68	18.35	15.35	1.31	1.10	2.62	2.19
	Corner 3	0.03489	0.01766	12.21	6.18	24.42	12.36	1.74	0.88	3.49	1.77
	Corner 5	0.02450	0.01960	8.57	6.86	17.15	13.72	1.22	0.98	2.45	1.96
	Corner 7	0.02479	0.02030	8.68	7.10	17.35	14.21	1.24	1.01	2.48	2.03
	Edge 2	0.03382	0.00507	11.84	1.77	23.68	3.55	1.69	0.25	3.38	0.51
	Edge 4	0.01316	0.02277	4.61	7.97	9.21	15.94	0.66	1.14	1.32	2.28
	Edge 6	0.02213	0.00622	7.74	2.18	15.49	4.35	1.11	0.31	2.21	0.62
	Edge 8	0.00590	0.02146	2.07	7.51	4.13	15.02	0.30	1.07	0.59	2.15
	Centre	0.00238	0.00263	0.83	0.92	1.67	1.84	0.12	0.13	0.24	0.26
Magetic	Corner 1	0.01391	0.01014	4.87	3.55	9.74	7.10	0.70	0.51	1.39	1.01
	Corner 3	0.01417	0.01393	4.96	4.88	9.92	9.75	0.71	0.70	1.42	1.39
	Corner 5	0.01511	0.01341	5.29	4.69	10.58	9.39	0.76	0.67	1.51	1.34
	Corner 7	0.01545	0.01456	5.41	5.09	10.82	10.19	0.77	0.73	1.55	1.46
	Edge 2	0.00119	0.00519	0.42	1.82	0.84	3.63	0.06	0.26	0.12	0.52
	Edge 4	0.00127	0.00628	0.44	2.20	0.89	4.39	0.06	0.31	0.13	0.63
	Edge 6	0.00123	0.00487	0.43	1.71	0.86	3.41	0.06	0.24	0.12	0.49
	Edge 8	0.00418	0.00798	1.46	2.79	2.93	5.59	0.21	0.40	0.42	0.80
	Centre	0.00366	0.00131	1.28	0.46	2.57	0.92	0.18	0.07	0.37	0.13

Table 27 - Crosstalk in shear axes due to on-axis and off-axis shear loading.

Transducer	Shear axis	Location of the applied shear load	Slope of the best fit line		Error (with 50N shear load)			
			Shear X	Shear Y	Shear X (N)	Shear Y (N)	Shear X (% RC)	Shear Y (% RC)
Optoelectronic	Negative X	Left	-0.00223	-0.00019	1.47	4.98	2.95	9.96
		Centre	-0.00230	0.00002	0.00	0.36	0.00	0.71
		Right	-0.00251	0.00023	-4.48	5.05	-8.97	10.11
	Positive X	Left	0.00289	0.00010	-4.55	2.16	-9.09	4.33
		Centre	0.00265	0.00003	0.00	0.56	0.00	1.13
		Right	0.00260	0.00016	0.95	3.41	1.89	6.81
	Negative Y	Left	0.00027	-0.00197	5.03	-2.22	10.07	-4.43
		Centre	0.00005	-0.00189	0.98	0.00	1.96	0.00
		Right	-0.00038	-0.00184	8.15	1.25	16.30	2.49
	Positive Y	Left	0.00009	0.00241	1.62	-2.09	3.25	-4.17
		Centre	0.00010	0.00231	1.89	0.00	3.78	0.00
		Right	0.00011	0.00230	2.07	0.36	4.14	0.71
Magnetic	Negative X	Left	-0.00051	0.00005	-1.61	6.84	-3.23	13.68
		Centre	-0.00049	0.00002	0.00	2.55	0.00	5.10
		Right	-0.00053	-0.00001	-3.38	2.09	-6.76	4.18
	Positive X	Left	0.00053	-0.00007	-3.32	10.10	-6.64	20.19
		Centre	0.00049	-0.00003	0.00	4.33	0.00	8.66
		Right	0.00051	0.00001	-1.63	0.98	-3.26	1.95
	Negative Y	Left	0.00006	0.00038	6.17	-2.43	12.34	-4.87
		Centre	0.00001	0.00036	0.71	0.00	1.42	0.00
		Right	0.00005	0.00038	4.82	-2.99	9.63	-5.99
	Positive Y	Left	-0.00005	-0.00035	4.69	-1.90	9.37	-3.80
		Centre	0.00000	-0.00034	0.29	0.00	0.58	0.00
		Right	0.00003	-0.00037	3.47	-3.48	6.93	-6.95

#11 Repeatability

Repeatability of the applied cyclic load and the repeatability of the corresponding transducer outputs is summarised in Table 28. There was greater variation in the applied load during tests on the optoelectronic-based transducer than on the magnetic-based transducer. Variation in the output of the magnetic-based transducer was consistent across all axes. Variation in the output of the optoelectronic-based transducer output (Negative X), however, was not consistent across shear channels. The average peak-to-peak transducer outputs were generally greater than the applied load due to signal noise and transducer accuracy discussed earlier.

Table 28 - Repeatability of the two biaxial shear transducers.

Transducer	Shear axis	Average peak-to-peak applied load (N)	(SD)	Average peak-to-peak transducer output (N)	(SD)
Optoelectronic	Negative X	44.96	0.05	48.83	1.25
	Positive X	45.02	0.08	47.66	0.48
	Negative Y	44.95	0.07	47.82	0.58
	Positive Y	45.01	0.07	48.09	0.54
Magnetic	Negative X	44.98	0.05	45.97	0.34
	Positive X	44.93	0.04	45.83	0.31
	Negative Y	44.97	0.04	46.51	0.51
	Positive Y	44.98	0.04	46.59	0.45

#12 Creep

The creep in output signal from the two transducers was determined by the slope of the fitted straight line during 30N load hold at the initial stage of the DMA testing sequence (Figure 87b), whereas creep recovery was determined during load hold of 5N at the end stage of the DMA testing sequence (Figure 90). Typical transducer outputs during load hold of 30N can be seen in Figure 94. The fitted slope of the creep signal was multiplied by 10 to indicate the variation of load reading after 10s static loading on the transducers. Results are also expressed as a percentage (%RC) of the rated capacity (50N) of the shear axes (Table 29). Average data has been presented with standard deviations showing the similarities between the four axes of the transducers (Table 29).

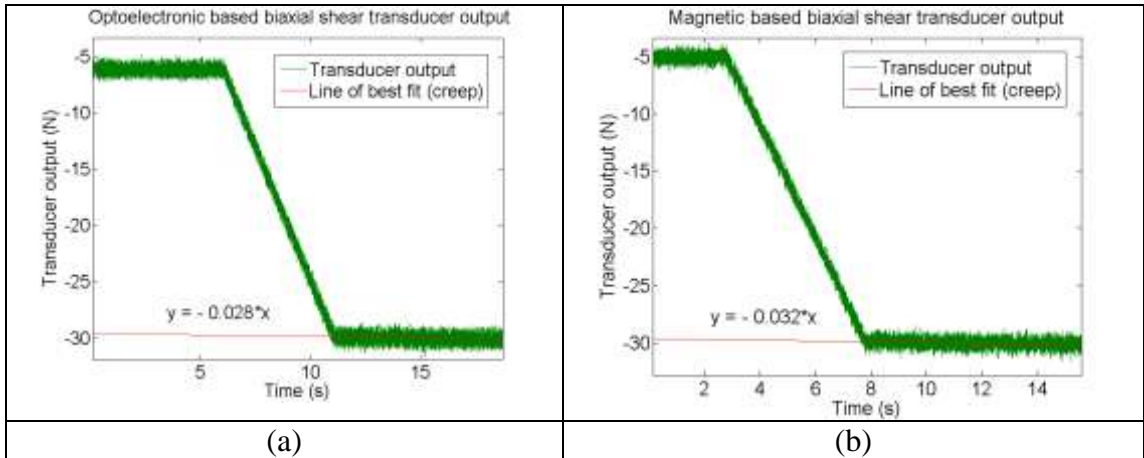


Figure 94 – Typical creep found in the transducer output signals during load hold of 50N.

Table 29 – Average creep and creep recovery with 30N load hold. Average data for the four axes in each transducer are presented.

Transducer	Average Creep (N)			Average Creep Recovery (N)		
	after 10seconds	(SD)	Error (%RC)	after 10seconds	(SD)	Error (%RC)
Optoelectronic	0.28	0.04	0.55	-0.38	0.05	-0.77
Magnetic	0.33	0.01	0.67	-0.34	0.07	-0.69

#13 Temperature sensitivity

Both transducers were tested at room temperature, because it was anticipated that with the current designs, the transducers would only be used as a force platform. Sensitivity to variation in temperature would be important and further testing would be necessary if the transducers were to be miniaturised for in-shoe applications.

6.3.2 Hardware

#14 Sampling frequency

The output bandwidth of the A1301 hall-effect ICs used in the magnetic based transducer was 20kHz, whereas the OPA404 op-amp used in the optoelectronic based transducer had a bandwidth of 6.4MHz. The data acquisition system (USB-6225) had a sampling rate of 250kS/s (samples per seconds), which equates to a maximum sampling frequency of 62kHz (250k samples ÷ 4 shear channels) if one transducer was connected. Therefore, the sampling frequency should not exceed 20kHz for the magnetic-based transducer and 62kHz for the optoelectronic-based

transducer. That said, sampling rate of up to 5000Hz was used during the evaluation of the transducers, which was adequate, since the frequency content of the applied load was no higher than 200Hz.

#15 Power consumption, #16 Multiplexing capability, #17 Computational requirements

Power consumption of each biaxial shear transducer was estimated (Table 30). Power needed for the operation of the data acquisition system (i.e. the analogue-to-digital convertor) and the computer necessary for processing and storing of the data was not included, but was assumed to be the same for both transducers.

Table 30 - Power consumptions for each individual biaxial shear transducer.

Transducers	Sensing components	Others	Total Power Dissipation
Optoelectronic	OPA404 op-amp Input voltage = $\pm 15V$ Input current = 10.5mA (Max) Power, Quiescent = 315mW (Manufacturer specified maximum power dissipation = 1000mW)	LED light emitter circuit 330 Ω resistor = 33mW LED diode = 18mW	366 to 1051mW
Magnetic	A1301 Hall-effect ICs Input voltage = 5V Input current = 11mA (Max) Power = 55mW \times 4	N/A	220mW

The computational requirements for both transducers were the same because the same equations were used to determine shear outputs from four input voltages. Instead of the software approach employed in the current study, it is possible to implement the computational stage electronically within each transducer. The electronic approach would decrease the four transducer outputs of the current design to just two voltage outputs that are directly related to shear load. However, the additional electronics would require an increase in the overall dimensions of the transducers, if they were to be incorporated within the transducer.

#18 Hardware costs

Component costs for the construction of each transducer are summarised in Table 31. Costs shown are based on the construction of a one-off transducer excluding the necessary labour for assembly of the transducer. The data acquisition system (USB-6225) used in the current study had a specification greater than required for the connection of just one transducer and as such the cost of the system (£1260.00) was not taken into account. At about £22 per transducer, the magnetic based transducer was estimated to be approximately 3 times less expensive than the optoelectronic based transducer (Table 31).

Table 31 - Hardware costs for constructing an optoelectronic based transducer or a magnetic based transducer.

Transducer	Optoelectronic	Magnetic
Sensing elements	Hamamatsu S4349 photodiode £30.00	Allegro A1301 × 4 £4.36
External amplifier circuit	Texas Instruments OPA404 £20.52	£0.00
Other components	LED £0.33	Magnet £0.40
Transducer structure	£15.00	
Cables	£1.80	
Elastomeric material	£0.21	
Total	£67.86	£21.77

6.3.3 Physical requirements

#19 Transducer sensing surface area, #20 Transducer thickness

The optoelectronic based transducer could be decreased from its current thickness of 18.5mm to about 10.5mm. However, the sensing surface area (15×15mm) of the transducer would be limited by the dimensions of the S4349 photodiode chip (Ø9.2×4.1mm), leaving just under 3mm surrounding the chip for a robust transducer housing. Alternative surface mount package or even a custom ordered photodiode chip would be necessary to further minimise the overall size of the optoelectronic based transducer. Whereas the dimensions of the current magnetic-based transducer

design were enlarged only for the purpose of this evaluation. If the surface mount A1301 (3×3×1mm, Section 5.4.2.1) chips were to be incorporated in the magnetic based transducer, it would have the potential to be further miniaturised to a sensing surface of 10×10mm and a thickness of just 6.5mm (2mm sensing surface + 0.5mm elastomeric medium + 1mm A1301 chip + 3mm circuit board and transducer housing).

#21 Suitability for in-shoe applications, #22 Easy to mount/wear

Neither transducer is currently suitable for in-shoe applications. However, both could be incorporated into an array to produce a load distribution measurement platform. A mechanism for mounting transducers into an array was not developed in the current study, but could be easily incorporated into the design and would permit swapping of transducers in the array if necessary. As discussed above (#20 Transducer thickness), the magnetic-based transducer has a greater potential to be miniaturised for in-shoe application. However, mounting inside a shoe could be physically challenging, but it may be possible to join adjacent transducers with silicone rubber or similar for a semi-flexible insole device.

#23 Transducer sensing surface allowable movement, #24 Spatial resolution

Under 50N load, the average transducer sensing surface displacement was <0.28mm, which was nearly 3 times less than the requirement of 0.75mm (Section 2.4.1). Therefore, with a 0.6mm gap between adjacent transducers to allow the movement of the sensing surfaces, a spatial resolution of 15.6mm would be possible in an array of transducers each with a sensing surface area of 15×15mm.

The movement in the optoelectronic based transducer was found to be lower (0.24mm) than the magnetic based transducer (0.28mm) (Table 32), even though both transducers were very similar in design. It is possible that differences between transducers in the amount of cyanoacrylate adhesive used to bond the elastomer to the housing had increased the overall stiffness of the optoelectronic-based transducer. However, the differences in movement between designs was negligible, given the spatial resolution of the mechanical testing machine was ±0.03mm.

Using the displacement change found in both transducers, the shear modulus of the transducers was estimated to be about 0.6MPa. Such a value was 3 times less than the shear modulus estimated earlier (1.8MPa) during testing of the elastomeric material alone (Section 5.3.2.3). This phenomenon could have been a result of combination of factors: 1) The adhesive used in bonding the elastomer to the housing would have affected the shear modulus of the overall assembly; 2) the elastomer was anisotropic, therefore the shear modulus in Section 5.3.2.3 may have been overestimated; 3) lubricant was not used during compressive testing of the elastomer (Section 5.3.2.3) therefore the friction between the elastomer and the material testing machine would have caused changes in its compressive behaviour (Koh and Kelly, 1989, Pinarbasi et al., 2006, Tsai, 2005). The estimated compressive modulus could be at least 2.6 times higher than the real value for the tested sample material of the size 10×10mm (Dechwayukul and Thongruang, 2008).

Table 32 - Transducer sensing surface displacement changes from 0N to 50N. Data presented is based on average displacement change during cyclic loading.

Transducer	Shear axis	Average sensing surface displacement at 50N (mm)	(SD)
Optoelectronic	Negative X	0.238	0.0023
	Positive X	0.240	0.0041
	Negative Y	0.242	0.0030
	Positive Y	0.244	0.0039
Magnetic	Negative X	0.283	0.0006
	Positive X	0.284	0.0008
	Negative Y	0.281	0.0013
	Positive Y	0.278	0.0006

#25 Reusability and life span

Both transducers were designed to be reusable. There are two key factors that are likely to have an effect on the life expectancy of the devices: 1) Degradation in the performance of the electronics over time; 2) the aging of the elastomeric material. The light source in the optoelectronic-based transducer would have an expected lifetime of 50,000 hours (Lingard, 2009), equating to 5.7 years with fulltime (24/7) operation. The only electronic component that could fail in the magnetic based

transducer was the hall-effect sensor ICs. Longevity is a typical feature of hall-effect sensing devices, for example a hall-effect switch could handle 30 billion continuous operations (Honeywell-Inc., 2011a). Long term reliability and the service life of the elastomeric material have not been tested. However, remarkable longevity of natural rubber has been noted in the literature, with negligible changes noted in the material properties of natural rubber with 2 years of aging at ambient temperatures (Mott and Roland, 2001).

6.3.4 Manufacturing requirements

#26 Batch production

Batch production of the optoelectronic based transducer would be more complex and time consuming than the magnetic based transducer due to the power connections required for the LED in the upper part of the transducer. The assembly of the magnetic based transducer was relatively simple with the electronics residing only in the lower part of the transducer. Batch production of the transducer structures, however, would be relatively simple. Both the housing and the sensing surface plate could be manufactured using a 3D printer or by injection moulding if strong plastic could be used instead of aluminium.

#27 Matrix arrangement capability, #28 Cabling

The location of the power connections for the LED of the optoelectronic-based transducer would complicate their incorporation into a large array. The current design would have to be modified to ensure the power connections would be sufficiently robust to withstand continuous movement of the sensing surface and avoid damage from adjacent transducers. The optoelectronic-based design would also require additional room for external amplifiers, whereas the magnetic based transducers would require minimum cabling arrangement beneath the transducers in a matrix arrangement.

6.4 Conclusion

Two individual biaxial shear transducers based on two separate load sensing technologies, optoelectronic and magnetic, were evaluated. Both shear transducers were capable of withstanding high vertical load (350N) with minimal cross-talk (<2.5%) to the shear axes. Dynamic performance of both transducers relative to a strain-gauge based reference load cell, revealed average differences of ~1N at physiological load rates (frequencies <75Hz, Section 2.3.1) increasing to about 10% error at a frequency of 200Hz.

The transducers had similar performance in terms of hysteresis (~6%RC), non-linearity (~3%RC) and creep (~0.7%RC). Despite the resolution of the optoelectronic-based transducer being twice that of the magnetic-based transducer, the magnetic-based transducer was less affected by crosstalk, had better repeatability and a greater signal to noise ratio. The magnetic-based transducer had a better overall accuracy. Although high frequency and/or off-axis loading may result in errors greater than 10% (Reading), transducer performance should be acceptable for most clinical measurements and gait applications.

In terms of the physical dimensions of the transducers, the magnetic based transducer has the potential to be readily miniaturised to a thickness of 6.5mm. The magnetic based transducer could be assembled easily using off-the-shelf sensor ICs and a transducer sensing surface area of 10×10mm could be achieved with currently-available low-cost miniature surface mount components. The magnetic-based transducer, therefore, had the greater capacity to form arrays of various sizes with better spatial resolution than the optoelectronic-based design.

In terms of hardware, the magnetic-based transducer required less power to operate, which is important in the development of a large array of transducers for load distribution measurement. Moreover, the magnetic based transducer was less complex and 3 times cheaper to manufacture. Although both transducers required a mounting mechanism for construction of an array, cable management would be less complex with the magnetic-based design.

In summary, the magnetic-based transducer had greater overall accuracy and was easier and cheaper to manufacture than the optoelectronic-based transducer. The magnetic-based design also had greater potential for miniaturisation, making it an ideal candidate for incorporation within an array of suitable spatial resolution for the clinical measurement of shear distribution beneath the human foot.

Chapter 7

Development of a biaxial shear distribution measurement system

In the previous chapter (Chapter 6) an evaluation of the performance of discrete biaxial shear transducers has been presented. This evaluation determined that the magnetic-based transducer design possessed the necessary performance, hardware and physical characteristics for integration into an array. This chapter demonstrates the potential of using this technology for practical measurement of shear force distribution under the foot – suitable for clinical use. The development of a small (56×44.5mm) modular load sensing platform consisting 20 transducers (each 22.7×11.5×11.5mm) capable of biaxial shear distribution measurement is described.

7.1 System design and construction

While it was recognised that many approaches would be suitable for the production of an array from the current transducer design, a modular approach was employed in the current study for demonstration purposes. A modular approach has the advantage that any faulty transducers could be swapped with ease and the transducers could be arranged in different configurations - in several or in a single cluster. Moreover, the electronics and software implementation could be modified or upgraded if necessary in the future. The complete system consisted of the following components:

1. 20 discrete magnetic-based biaxial shear transducers.
2. A mounting platform for fixing the transducers in a matrix arrangement.
3. Electronic circuits for the acquisition of the data.
4. Computer software for processing, interpreting and recording shear data.

Each of these modules will be discussed in details in the following sub-sections.

7.1.1 Transducer design

To maximise the spatial resolution of the array, the 3-Pin SOT23W miniature surface mount version of the A1301 hall-effect sensor IC was incorporated into the new design of each transducer. The four surface mount sensor ICs were positioned as close as possible within a rectilinear pattern (Figure 95b), ensuring each active element was closer to the centre of the magnet and thereby maximising their sensitivity to changes in magnetic flux density associated with movement of the magnet (Section 5.4.2.2). In comparison to the prototypes constructed earlier (Section 5.4.2.3), the active elements inside each IC in the new design would be 2.08mm from the centre of the magnet (Figure 95). Moreover, each of the active elements would be equidistant from the centre of the magnet. The air gap (AG) between the permanent magnet and the sensor ICs was also decreased to 0.5mm. The active area depth (AAD) of the SOT23W package was 0.28mm, thus the total effective air gap (TEAG) between the magnet and sensor ICs was 0.78mm under no load conditions. Initial tests were conducted to ensure the outputs from the sensor ICs did not saturate with the configuration described above.

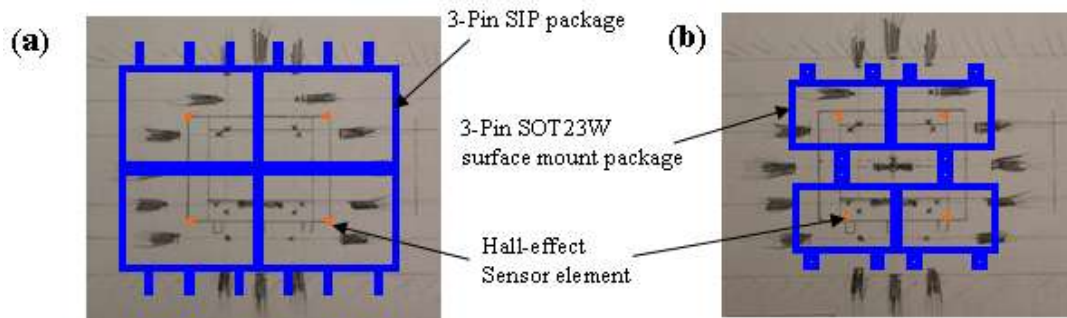


Figure 95 – Comparing the positions of the active elements within the SIP packaged sensor ICs previously used in the prototypes (Section 5.4.2.3) (a) and the SOT23W surface mount sensor ICs (b) with the magnetic flux around a magnet. Please refer to Figure 79 for a more detailed description of the diagram.

The method of measuring biaxial shear load with four magnetic sensors was the same using the differential principle as described earlier (Section 5.4.1). The set of four A1301 sensor ICs for each discrete transducer were manually soldered onto printed circuit boards (PCB) of 1mm thickness. Each PCB had tracks ($\text{Ø}8.32\text{mm}$) for cabling and mounting of the ICs (Figure 96a). Each PCB was trimmed to size (Figure 96c) and wires were organised to exit from its underside (Figure 96d) before it was inserted into the transducer housing. Low-noise cables (Habia Cable Ltd, UK) of the same type used in the ‘Kent’ system (Section 5.1.1) were used in the assembly of the PCBs because they were small in diameter and were generously provided by the research group at the University of Kent. However, it should be noted that other less expensive cables could have been used, such as the standard 6 core ribbon cable used earlier (Section 6.1.2). Three 2-way crimp sockets (M20-1060200, Harwin Inc, USA) were connected to the ends of the wires, one for the power connection and two for the 4 signal outputs from the transducer.



Figure 96 - The design of the circuit board for each transducer (a) and an array of such prepared on a printed circuit board (PCB) (b). Each circuit was cut to size (c) and the four sensor ICs were then soldered and wired manually (d).

The dimensions of the transducer housing was $11.50 \times 11.50 \times 20$ mm, but the sensing surface plate was only $10 \times 10 \times 2$ mm (Figure 97), allowing a gap of 1.5mm between sensing surfaces of adjacent transducers. Smaller transducer housings ($11.50 \times 11.50 \times 6$ mm) were also manufactured to demonstrate the potential of the same transducer design to be miniaturised. Technical drawings of these parts have been included in Appendix B. The underside of the sensing surface plate had a circular indentation (0.1mm deep) in the centre to allow precise attachment of the permanent magnet (Figure 97). The transducer housing contained four holes ($\text{Ø}2.4$ mm), one on each of the vertical sides of the transducer (Figure 97). The design allowed placement of a steel rod through several adjacent housings for precise alignment of the transducers in an array. The next section discusses how these parts were manufactured and assembled together.

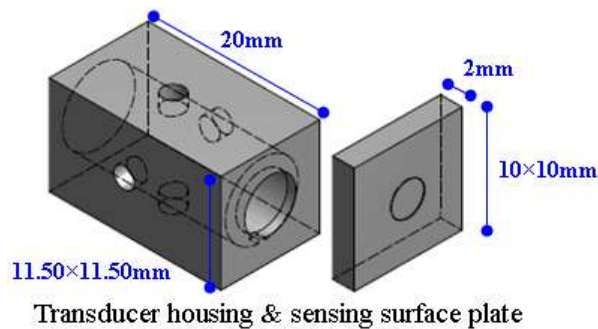


Figure 97 - Overall dimensions of the transducer housing and the sensing surface plate.

7.1.2 Batch production of discrete transducers

To demonstrate the feasibility and potential for a fast and low-cost production for the transducer design, transducer housings were manufactured from plastic rather than metal. The transducer housings and sensing surface plates were manufactured using a 3D printer (Eden350, Objet Geometries Inc, USA). The material used in the printing was an acrylic polymer (Fullcure-840VeroBlue, Objet Geometries Inc, USA) with a compressive strength of 79.3MPa (805kg/cm²). Thus, each transducer would be more than capable of supporting a person's weight (~80kg) and withstand the heel strike forces (up to 3 times body weight) recorded during running (Section 2.3.2) without breaking.

Each biaxial shear transducer, both the smaller miniaturised version and the bigger design for the platform system, consisted of 6 components as follows:

1. Transducer housing.
2. Transducer sensing surface plate.
3. Four hall-effect sensor ICs (Allegro A1301KLHLT-T) on a PCB circuit.
4. Permanent magnet (M1219-1, $\text{\O}3\text{mm}\times 1\text{mm}$).
5. Elastomeric material (TARRC 0.5mm, $10\times 10\text{mm}$).
6. Sensor IC spacer (0.4mm paper card).

An assembly drawing of the transducer can be seen at the end of Appendix B. The sensor IC spacer was a circular disc that had a small cut out on one side to align itself precisely in the transducer housing. Each spacer also had two rectangular cut-outs to allow precise alignment and orientation of the sensor ICs in the transducer (Figure 98e). A technical drawing of the spacer can be found in Appendix B. The spacers were laser cut (VersaLASER VLS platform, Universal Laser Systems Inc., USA) to size from paper card of 0.4mm thickness.

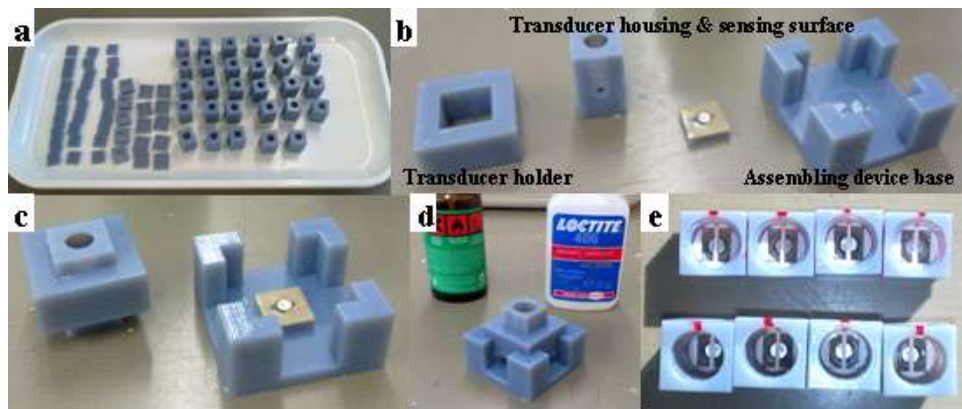


Figure 98 – Steps in the batch production of the biaxial shear transducers. Transducer housings and sensing surface plates from the 3D printer (a). The magnet and elastomeric material bonded to the sensing surface plate (b) before placement in the assembling device (c) for bonding the transducer housing to the surface plate (d). The sensor IC spacers were then placed inside the transducer housings before the hall-effect sensor ICs circuit boards were installed (e).

A transducer assembling device was designed and built to facilitate a fast but accurate production process for assembling the transducers. The assembling device was manufactured using the same 3D printer and material as described above for

precision. The assembling device consisted of two parts: 1) a transducer holder, and 2) a base holder (Figure 98b). Technical drawings of the assembling device parts can be found in Appendix C.

Figure 98 illustrates the steps in constructing each transducer. Firstly, the permanent magnet was bonded (LOCTITE®406™ cyanoacrylate adhesive) onto the circular indentation on the underside of the sensing surface plate. A small sheet (~13×13mm) of TARRC 0.5mm rubber was then treated with LOCTITE®770™ before bonding to the surface plate using LOCTITE®406™. The rubber sheet had a circular hole in the centre for the magnet and excess rubber along the edge of the plate was manually trimmed (Figure 98b). The magnet-sensing surface plate assembly was then placed onto the square extrusion slot on the base holder of the assembling device, and the transducer housing slotted into the transducer holder of the assembling device (Figure 98c). The unbounded side of the rubber was then treated with LOCTITE®770™ and LOCTITE®406™ was applied to one end of the transducer housing before the transducer holder was then slotted into the base holder of the assembling device. The holder was advanced until the transducer housing contacted the rubber for an instant bonding.

Visual checks were performed to ensure the rubber was fully bonded between the transducer structures (housing and sensing surface plate). In comparison to the aluminium prototype transducer constructed earlier (Section 6.1.2), the bonding between the rubber and the plastic transducer structure was more secure. Sensor IC spacers were positioned within the transducer housing (Figure 98e) before the hall-effect sensor IC circuit board assembly (Figure 96d) was placed inside to form a complete biaxial shear transducer. Figure 99 illustrates 20 biaxial shear transducers assembled into a 4×5 array and two miniaturised versions. Overall dimensions of each platform type transducers were 22.7×11.5×11.5mm, and 8.5×11.5×11.5mm for the in-shoe type transducers. The overall surface area of the transducer array was 56×44.5mm.



Figure 99 - 20 biaxial shear transducers in a 4×5 array, and 2 transducers in a miniaturised package.

7.1.3 Hardware and Electrical implementation

A robust platform was constructed using aluminium to hold the 20 biaxial shear transducers in a 4×5 array (Figure 100). The platform consisted of the following parts:

1. **A mounting platform base** – The base consisted of an aluminium base plate containing a series of Ø5mm rectilinear holes which allowed passage of crimp sockets from each transducer and ensuring the transducers sat flush on the base. The same holes also allowed screws to pass through to secure the walls and legs of the platform.
2. **Four mounting platform walls** – Each wall contained three threaded holes for attachment to the platform base. Each wall also contained five horizontally positioned holes (Ø2.4mm), 11.5mm apart, which allowed adjacent transducers to be braced to a fixed position by a steel rod.
3. **Two mounting platform legs** – Each leg consisted of a rectangle aluminium block with two threaded holes for fixation beneath the platform base. The legs provided adequate dead space for managing cables from all 20 transducers.



Figure 100 - The completed biaxial shear distribution measurement platform containing 20 biaxial shear transducers in a 4x5 matrix arrangement (a) and the managed cables on the underside of the platform (b).

Technical drawings of the parts of the platform have been included in Appendix B and the completed biaxial shear distribution measurement platform is shown in Figure 100a. The cables from all 20 individual transducers were organised via three junction pads: one pad contained 20 pairs of crimp terminals and was wired to the 5V supply from the DAQ board (USB-6225) to provide power to all 20 transducers; the other two pads, each contained 40 crimp terminals, that relayed the transducer output to the DAQ via a 40-way ribbon cable (3659-Series, 3M, USA). The cable was especially chosen for its round construction which permitted easier routing. No other electronics were required between the transducer and the DAQ.

7.1.4 Software implementation

Data recording via the DAQ system (USB-6225) was controlled by a custom LabVIEW8.6 program. Three separate custom programs were written:

1. A program that simultaneously recorded the four signals from any one biaxial shear transducer and the applied force and displacement data from the ElectroForce3200. Sampling rate was set at 200Hz, except during DMA testing which sampled at 5000Hz.
2. A program that recorded the outputs from all 20 transducers and calculated, in real-time, the directions and vector magnitudes of the shear load from each transducer, as well as the total X-axis and Y-axis shear load measured by all 20 transducers. Sampling rate was set at 200Hz.
3. The program in (2) above was modified to connect with a USB camera that provided real-time video streams of the area around the platform. This program also provided real-time visual information of the direction and magnitude of the shear load from each transducer, as well as the total X-axis and Y-axis shear load measured by all 20 transducers. However, it did not have the data recording capability as in (2) but data acquisition was conducted at 200Hz. Screenshots of the program has been included in Appendix H.

7.2 System calibration

Each of the 20 biaxial shear transducers was individually calibrated under dynamic conditions using previously described mechanical testing equipment (ElectroForce3200) and methods (Section 6.2). The shear load was applied to the transducer using the mechanical testing instrument (ElectroForce3200) described earlier (Section 6.2). Briefly, the ElectroForce3200 system had a single linear actuator for the application of uniaxial load, statically or dynamically at up to 200Hz. The system also provided displacement feedback of its linear actuator. Both the applied load and the displacement data were output from the system as two voltage sources, which were connected to the DAQ (USB-6225) for data recording. Data recording was controlled via a LabVIEW program (program #1, Section 7.1.4) and the raw data were post-processed in MATLAB.

Pure shear load over a range of 2N to 30N at 1Hz for 15 cycles was applied to each shear direction of the transducer at separate times. Load was applied to the transducer via a 3/16" (\varnothing 4.763mm) acrylic ball attached to the end of the actuator. Two different adjustable mounting adapters were used to fix the transducer in an upright position for axial tests or in a side-way position for shear calibration (Figure 101). Because the new transducers were smaller than those tested earlier (Chapter 6), a square adaptor was fitted to the outside of the new transducers for mounting. The spacer was 3D printed using the same acrylic polymer used in the construction of the transducer housing (Section 7.1.2). A technical drawing of the adaptor has been included in Appendix B.

In place of the metal bracket used during transducer development (Section 6.2), a plastic cap was secured to the sensing surface of the transducer to transmit shear load to the transducer surface during testing. The point load from the actuator was aligned to the sensing surface of the transducer and was applied to the side of the cap during shear loading (Figure 101). The plastic cap was again 3D printed for a precise press fit to the sensing surface plate without the need for adhesive. The dimensions of the plastic cap can be seen in the technical drawing shown in Appendix B.

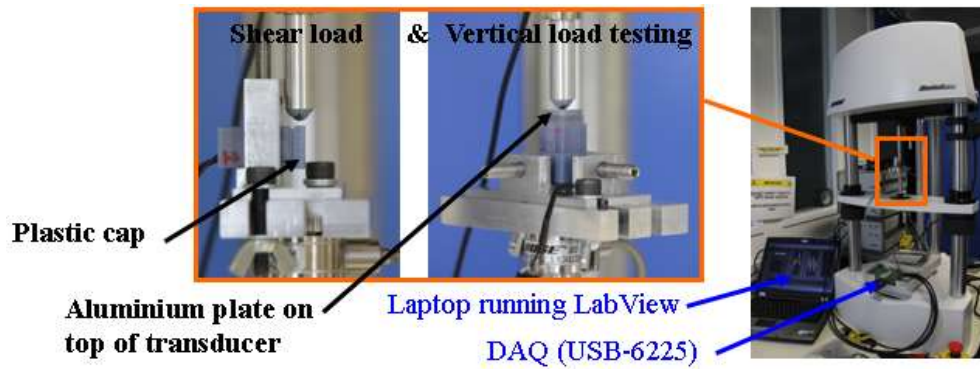


Figure 101 - Setup in the ElectroForce3200 during shear load calibration and vertical load testing of the biaxial shear transducers.

Loading protocol

In addition to transducer calibration described above, the following tests were conducted on one representative transducer:

1. A series (9 tests) of cyclic vertical loads, over a range of 2N to 30N at 1Hz for 10 cycles were applied through point loading at the centre of the transducer and subsequently at each corner and along the edges of the transducer. A vertical load range of 2N to 350N at 1Hz for 5 cycles was subsequently applied but only to the centre of the transducer. To avoid fracture of the acrylic transducer sensing surface structure under high point loads, a 2mm aluminium plate was positioned on top of the transducer during vertical tests (Figure 101). The crosstalk present on the shear channels was measured in each test.
2. Shear loads ranging from 2N to 30N were applied for 15 cycles (1Hz) along the center line of the transducer. The loading sequence was repeated for each shear direction. The crosstalk present on the other shear channel was measured. Accuracy and repeatability of the transducer output between the 15 load and unloading cycles was examined.
3. Off-axis shear loading. Shear loads ranging from 2N to 30N were applied for 15 cycles (1Hz) to the extreme left and right edges of the transducer. The error in the corresponding shear axis and crosstalk on the other shear channel were measured.
4. The DMA frequency sweep function on the ElectroForce3200 was used to apply shear load at 10 different frequencies to the transducer: 0.5Hz, 1Hz, 20Hz, 40Hz,

70Hz, 90Hz, 110Hz, 140Hz, 180Hz and 200Hz. The test was conducted only on the $-X$ shear axis assuming consistent frequency response in the $+X$ and $\pm Y$ axis as demonstrated earlier (Figure 88b).

5. In contrast to the creep analysis conducted earlier (Section 6.3.1) with a relatively slow increasing ramp to a short constant load, a square wave with prolonged constant load was used here instead. A square wave of 2 cycles which ramped between 2N and 30N with holds of 16 seconds between ramps was applied to the $-X$ shear axis. A loading sequence which ramped between 2N to 15N was also used. Any creep and creep recovery in the signal were measured.
6. Tests were conducted to examine the performance of the transducer housing at different temperatures (25°C, 30°C, 35°C and 40°C). A hollow transducer structure, without electronics, was positioned within a temperature controlled saline bath (Figure 102). The saline bath was filled with distilled water and the water temperature was controlled via the ElectroForce3200 system. Shear load ranging from 5N to 30N at 1Hz for 10 cycles was applied along the centre line of the transducer. Changes in the displacement of the transducer sensing surface during loading at different temperatures were measured.

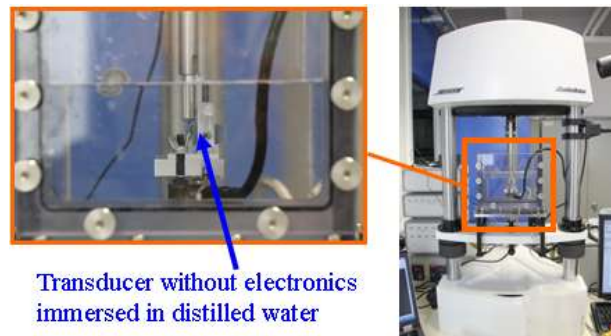


Figure 102 - The setup in the ElectroForce3200 with a temperature controlled saline bath filled with distilled water.

7.2.1 Results and discussion

The slopes of the calibration curves obtained from the calibration of the 20 biaxial shear transducers have been summarised in Table 34. Theoretically, the response from each transducer should be the same. However, despite the precision in the transducer construction process, the standard deviation of the slopes revealed that a

single calibration factor could not be shared among all transducers (Table 34). The reason for the difference in response between transducers is unclear, but may have arisen from several sources, including:

1. The unique magnetic flux pattern of each permanent magnet.
2. Alignment errors in manual fixation of the hall-effect sensor ICs.
3. Minor variations in the thickness of the elastomeric material.
4. Application of load not perfectly aligned with the centre line of the transducer.

Nonetheless, the variability in the calibration curves between opposite directions in the same axis was found to be small (Table 34). Consequently, the calibration factor used for each shear axis was calculated as the average slope over its negative and positive directions. The maximum error in using the mean slope was ~1N, on average, when 30N (rated capacity) was applied to the transducers (Table 34). In comparison to the traditional approach of using a multi-dimensional square matrix in calculating the force output from a multi-channel load cell (Hirose and Yoneda, 1990), this approach simplified the computation required to calculate the shear load outputs from all 20 transducers. The shear load from the transducer array was simply calculated by multiplying one calibration factor by the corresponding shear axis output (Table 33).

Table 33 - Equations for converting the four voltage outputs from the hall-effect sensors ICs to shear load output.

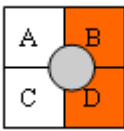
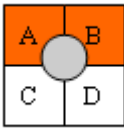
Transducer output (N)	Magnet movement relative to 4 sensors	Formula for quantifying the magnet movement, and therefore the applied load
Shear (X)		$X = \left[\frac{[(B + D) - (A + C)] \div Z}{Xaxis \text{ Calibration Factor}} \right]$ <p style="text-align: center;">where, $Z = A+B+C+D$</p>
Shear (Y)		$Y = \left[\frac{[(A + B) - (C + D)] \div Z}{Yaxis \text{ Calibration Factor}} \right]$

Table 34 - Variability in the calibration curves for the 20 biaxial shear transducers.

Transducer #	Calibration slopes		Average slope (X-axis)	The maximum error in using the average slope (N)		Transducer #	Calibration slopes		Average slope (Y-axis)	The maximum error in using the average slope (N)	
	Negative X	Positive X		Negative X	Positive X		Negative Y	Positive Y		Negative Y	Positive Y
1	0.00204	0.00186	0.00195	1.33	1.46		0.00217	0.00254	0.00236	2.56	2.19
2	0.00333	0.00299	0.00316	1.53	1.70		0.00326	0.00317	0.00322	0.37	0.38
3	0.00268	0.00272	0.00270	0.23	0.23		0.00290	0.00292	0.00291	0.12	0.12
4	0.00152	0.00147	0.00150	0.47	0.48		0.00184	0.00181	0.00182	0.27	0.27
5	0.00333	0.00319	0.00326	0.63	0.66		0.00330	0.00366	0.00348	1.62	1.47
6	0.00294	0.00323	0.00308	1.51	1.38		0.00349	0.00322	0.00336	1.17	1.27
7	0.00241	0.00272	0.00257	1.94	1.71		0.00247	0.00269	0.00258	1.32	1.22
8	0.00266	0.00268	0.00267	0.12	0.12		0.00265	0.00280	0.00273	0.86	0.81
9	0.00281	0.00297	0.00289	0.85	0.81		0.00284	0.00286	0.00285	0.09	0.09
10	0.00252	0.00226	0.00239	1.59	1.78		0.00289	0.00264	0.00276	1.32	1.45
11	0.00285	0.00272	0.00278	0.68	0.72		0.00269	0.00285	0.00277	0.94	0.88
12	0.00284	0.00301	0.00292	0.90	0.85		0.00288	0.00292	0.00290	0.20	0.20
13	0.00256	0.00265	0.00261	0.52	0.50		0.00240	0.00274	0.00257	2.12	1.86
14	0.00237	0.00209	0.00223	1.77	2.01		0.00280	0.00271	0.00275	0.49	0.51
15	0.00225	0.00247	0.00236	1.44	1.31		0.00289	0.00263	0.00276	1.37	1.51
16	0.00307	0.00356	0.00332	2.38	2.05		0.00343	0.00386	0.00365	1.84	1.64
17	0.00218	0.00270	0.00244	3.56	2.88		0.00313	0.00246	0.00279	3.20	4.07
18	0.00306	0.00297	0.00302	0.41	0.42		0.00097	0.00103	0.00100	0.85	0.80
19	0.00406	0.00438	0.00422	1.18	1.09		0.00404	0.00415	0.00409	0.40	0.39
20	0.00244	0.00232	0.00238	0.75	0.79		0.00218	0.00248	0.00233	2.09	1.84
Average	0.00272			1.17			0.00278			1.15	
SD	0.00057			0.76			0.00065			0.89	

The following sub-sections present the results from the calibration and testing of the representative transducer as well as the measurement system as a whole. Transducer #9 from the array was randomly selected as the representative transducer (Table 34). Results are broken down and presented under four categories corresponding to the requirements (#1 to #28) set out earlier in Section 2.4.1.

7.2.1.1 Transducer performance

#1 – Rated capacity, #2 – Resolution,

All 20 transducers in the shear distribution measurement system were calibrated to 30N shear (rated capacity) and the representative transducer was fully tested to withstand vertical loads up to 350N.

Table 35 - Average peak-to-peak voltage change from the four hall-effect chips within the representative transducer when loaded at the rated capacity (30N), and the calculated load resolution of the transducer.

Average peak-to-peak voltage (V)	(SD)	System resolution	Sensitivity
0.180	0.050	0.075N	6mV/N

As discussed earlier (Section 6.3.1), the resolution of the transducer was limited by the quality of the analogue-to-digital electronics within the DAQ instrument (USB-6225) which converted the voltage outputs from each hall-effect sensor IC to digital data recorded by the computer. The accuracy of the DAQ system was estimated to be around 450 μ V (Section 6.3.1). The average peak-to-peak voltage changes in the four sensor IC outputs from the representative transducer when loaded at the rated capacity (30N) are summarised in Table 35. Based on these figures, the representative transducer had an estimated load resolution of about 0.075N ($30\text{N} \div [180000/450\mu\text{V}]$) (Table 35).

#3 – Accuracy

The maximum difference between the output from the representative transducer and the applied load was found to be <1.6N during cyclic loading (Loading protocol 2) and an average error of <0.8N could be expected when measuring dynamic load (1Hz) up to 30N (Table 36). In comparison to the earlier prototype transducer which

used larger hall-effect sensor ICs (Section 6.3.1), the surface mount sensor ICs used in the current design ensured that each hall-effect active element were equidistant from the centre of the magnet. Hence, the accuracy was relatively consistent across shear axes (Table 36). However, it should be noted that the overall accuracy of the transducer also reflects other sources of error such as hysteresis, non-linearity, signal noise and frequency response, which will be discussed below.

Table 36 - Accuracy of the representative transducer compared with the applied shear load at 1Hz. Maximum error (N) and root mean squared error (RMSE) in Newtons and % rated capacity (30N) are presented.

Shear axis	Maximum absolute error (N)	RMSE (N)	RMSE (%RC)
Negative X	1.34	0.50	1.66
Positive X	1.59	0.79	2.62
Negative Y	0.97	0.40	1.33
Positive Y	1.40	0.57	1.91

#4 – Frequency response

Figure 103 illustrates the response of the representative transducer at loading frequencies, ranging from 0.5Hz to 200Hz. Consistent with the previous results (Section 6.3.1), the calibrated output from the transducer was found to be about 90% of the applied load at 200Hz. At a loading rate of 1Hz, approximately 97% of the applied load was registered by the transducer (Figure 103), which was expected because $\sim 0.8\text{N}$ error ($29.2 \div 30 \times 100 = 97\%$) was predicted in the X-axis output (Transducer #9, Table 34).

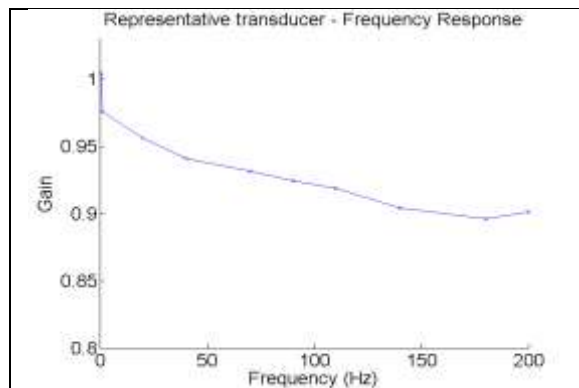


Figure 103- Frequency response plot of the representation transducer across frequencies from 0.5Hz to 200Hz.

#5 – Hysteresis, #6 – Non-linearity, #7 – Combined error

Figure 104 illustrates the calibration curves for each shear axis of the representative transducer. The line of best fit ($y = mx+c$) for each calibration curve was obtained using the least-squares method. Given that the transducer outputs were biased to zero before each test, only the slopes of the best fit lines were analysed and presented (Table 37). Non-linearity and hysteresis values were calculated (Table 37) based on the definition shown in Appendix A. Percentage non-linearity was approximately half of the hysteresis, thus the non-linearity data can also be seen as the combined error based on the definition in Appendix A. The response of the transducer was linear over the 30N range, with a consistent hysteresis of <4% across all shear axes (Table 37).

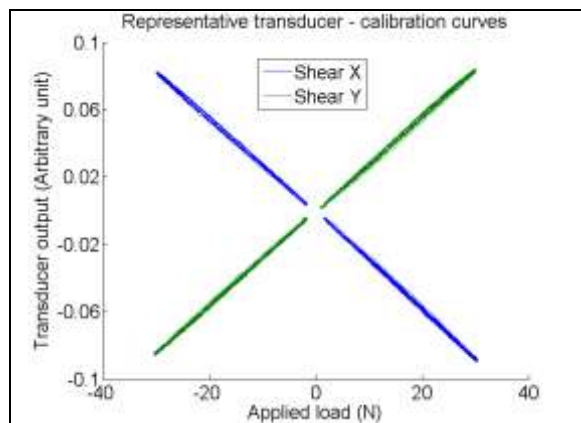


Figure 104 - Calibration curves of the representative transducer.

Table 37 – Hysteresis and non-linearity of the representative transducer.

Shear axis	Slope of the best fit line ($y=mx+c$)	Goodness of fit	Non-linearity	Hysteresis
	m	R -Square	%	%
Negative X	0.00281	0.99	1.47	3.55
Positive X	0.00297	0.99	1.42	3.48
Negative Y	0.00284	0.99	1.86	3.64
Positive Y	0.00286	0.99	1.92	3.80

#8 – Signal noise

Signal noise was measured as the peak-to-peak transducer output with no load applied. Noise was consistent across shear channels at ± 0.0005 (arbitrary transducer

output unit). Given the output span of the transducer (Figure 104), the signal-to-noise ratio was about 86:1, equating to an error of about $\pm 0.2N$. The signal-to-noise ratio was greater than that found in the early transducer design (Section 6.3.1) because the new transducer had a greater displacement change in the sensing surface plate, resulting in a greater output span (see #23 Transducer sensing surface allowable movement).

#9 – Cross-talk, #10 – Error due to off-axis loading

Crosstalk in the shear axes due to vertical loading of 350N applied at the centre of the representative transducer can be seen in Figure 105. To examine the true effect of crosstalk without the influence of noise within the signal outputs, the line of best fit ($y = mx+c$) for each crosstalk output curve was obtained using the least-square method. Given that the transducer outputs were biased to zero before each test, only the slopes of the best fit lines were analysed and presented (Table 38). Results are also expressed as a percentage (%RC) of the rated capacity (30N) of the shear axes.

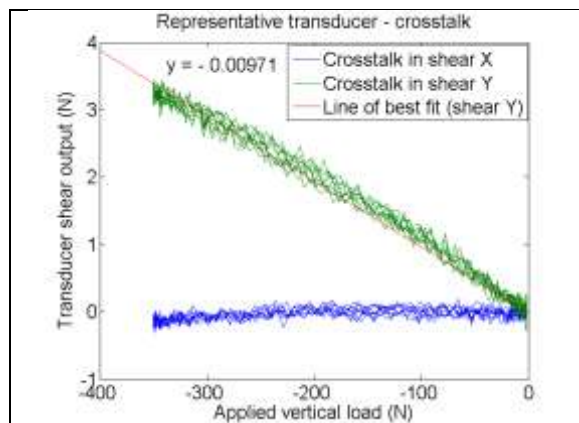


Figure 105 – Crosstalk in the shear axes due to vertical load applied at the centre of the representative transducer. As an example, the line of best fit to the shear Y output is shown and also summarised in Table 38.

The greatest crosstalk was 4.1N (13.7% RC) and occurred on the shear X-axis when 30N vertical load was applied to the corner of the transducer. As expected, vertical load applied to the corners of the transducer affected both X and Y axis equally (Table 38). However, vertical load applied to the edge of the transducer would result in asymmetric crosstalk. For instance, Edge2 and Edge4 were the edges along the

shear X-axis therefore they were affected by crosstalk more than the Y-axis when vertical load was applied to Edge2 and Edge4 (Table 38).

The 3.4N error observed in the Y-axis with a vertical load of 350N was not anticipated (Table 38). The results from vertical loading at the transducer corners suggest that both shear axes would be affected equally by crosstalk. The relatively high error found in the Y-axis may reflect slight misalignment of the point load with the introduction of the 2mm aluminium plate (Section 7.2 and Figure 101). An off-axis load would cause the aluminium plate to tilt and therefore a true shear load would be transmitted to the transducer. Nonetheless, the response from the X-axis (Table 38) suggests the transducer was capable of withstanding high vertical loads and that an evenly distributed load, or point load, at the centre of the sensing surface would have negligible effect on shear output.

Table 38 – Crosstalk in the shear axes due to on-axis and off-axis vertical load.

Location of the applied vertical load	Slope of the best fit line		Error (at 30N vertical load)			
	Shear X	Shear Y	Shear X (N)	Shear Y (N)	Shear X (% RC)	Shear Y (% RC)
Corner 1	0.12263	0.10718	3.68	3.22	12.26	10.72
Corner 3	0.07541	0.10711	2.26	3.21	7.54	10.71
Corner 5	0.13766	0.12945	4.13	3.88	13.77	12.95
Corner 7	0.07807	0.04675	2.34	1.40	7.81	4.67
Edge 2	0.08873	0.00997	2.66	0.30	8.87	1.00
Edge 4	0.00230	0.10273	0.07	3.08	0.23	10.27
Edge 6	0.08021	0.03031	2.41	0.91	8.02	3.03
Edge 8	0.00266	0.08428	0.08	2.53	0.27	8.43
Centre	0.00254	0.02386	0.08	0.72	0.25	2.39
			Error (at 350N vertical load)			
Centre	0.00024	0.00972	0.08	3.40	0.27	11.34

Figure 106a illustrates the typical effect of off-axis shear load on the calibration curve. The line of best fit for each off-axis response curve was obtained and compared to the calibration curve of the corresponding shear axis (Table 39). The error in shear load output at the rated capacity (30N) could then be calculated by comparing these slopes of best fit lines (Table 39). The maximum error of 5.5N (18.4%RC) due to the application of 30N off-axis shear load was found in the +X-

axis of the representative transducer, which was relatively higher than the average error of around 3N found in other shear directions (Table 39).

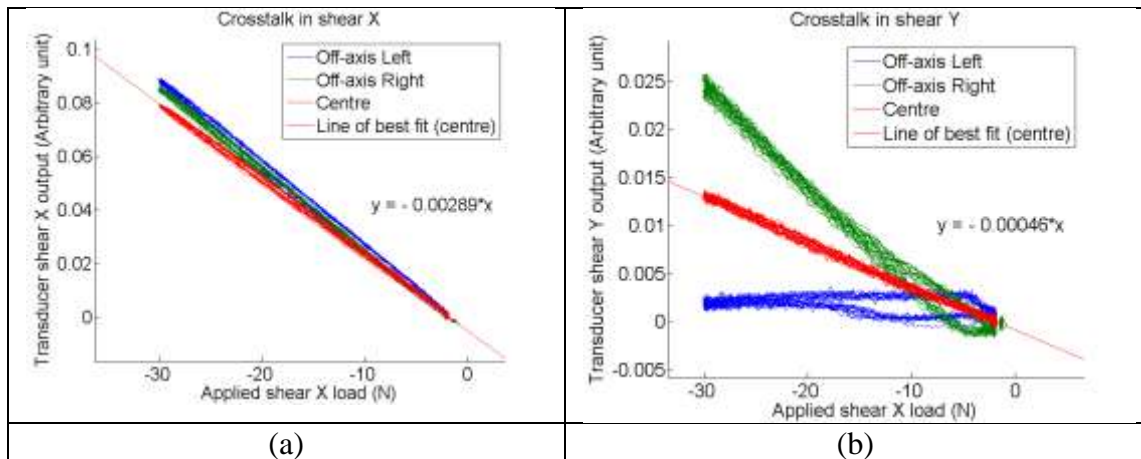


Figure 106- Deviation from the calibration curve due to off-axis shear X loading (a) and crosstalk in the shear Y-axis due to on-axis and off-axis shear load applied in the X-axis. The plots illustrate a typical response from the representative transducer when shear load was applied in the negative X direction.

Figure 106b illustrates crosstalk in the shear axis due to on-axis and off-axis shear load applied to the orthogonal shear axis. The error due to crosstalk can be calculated by comparing the slope of the crosstalk response curve to the calibration curve of the corresponding shear axis (Table 39). 30N off-axis shear load applied to one shear axis resulted in a maximum error of 9.47N (31.56%RC) on the orthogonal shear axis (Table 39). Crosstalk was found to be less during 30N on-axis shear loading, which resulted in an error of <4.87N (16.23%RC) in the orthogonal shear axis (Table 39).

Table 39- Crosstalk in the shear axes due to on-axis and off-axis shear loading.

Shear axis	Location of the applied shear load	Slope of the best fit line		Error (at 30N shear load)			
		Shear X	Shear Y	Shear X (N)	Shear Y (N)	Shear X (% RC)	Shear Y (% RC)
Negative X	Left	-0.00313	-0.00007	-2.46	-0.72	-8.22	-2.39
	Centre	-0.00289	-0.00046	0.00	-4.87	0.00	-16.23
	Right	-0.00303	-0.00086	-1.41	-9.03	-4.71	-30.09
Positive X	Left	-0.00303	-0.00028	-1.42	-2.93	-4.73	-9.76
	Centre	-0.00289	-0.00026	0.00	-2.78	0.00	-9.27
	Right	-0.00342	0.00084	-5.53	8.83	-18.44	29.45
Negative Y	Left	0.00084	0.00318	-8.68	-3.42	-28.93	-11.39
	Centre	0.00042	0.00285	-4.34	0.00	-14.47	0.00
	Right	0.00004	0.00318	-0.44	-3.41	-1.46	-11.37
Positive Y	Left	-0.00091	0.00310	9.47	-2.63	31.56	-8.77
	Centre	-0.00039	0.00285	4.04	0.00	13.46	0.00
	Right	0.00024	0.00312	-2.53	-2.79	-8.42	-9.31

Crosstalk in the shear axis due to off-axis shear load along the same axis was consistent whether it was off-axis towards the left or right side of the transducer (Table 39). However, crosstalk found in the orthogonal shear axis was not the same when off-axis shear load was applied towards the left and right (Table 39). Although this response was unexpected, the pattern of the response suggests that off-axis shear load applied to two diagonal corners (corners 2 and 4) resulted in higher crosstalk in the orthogonal shear axis than the other two diagonal corners (Figure 107). The reason for this effect and also the hysteresis loop pattern found in the response curve (Figure 106b) is unknown. Speculatively, the hysteresis loop may be due to simultaneous rotation and translation of the sensing surface plate which may have a different path during the loading and unloading phases. However, this does not explain why the response to loading on the left side of the transducer differed from loading on the right side. A more thorough test is required to investigate the response from the hall-effect sensor ICs in relation to its distance from the magnet.

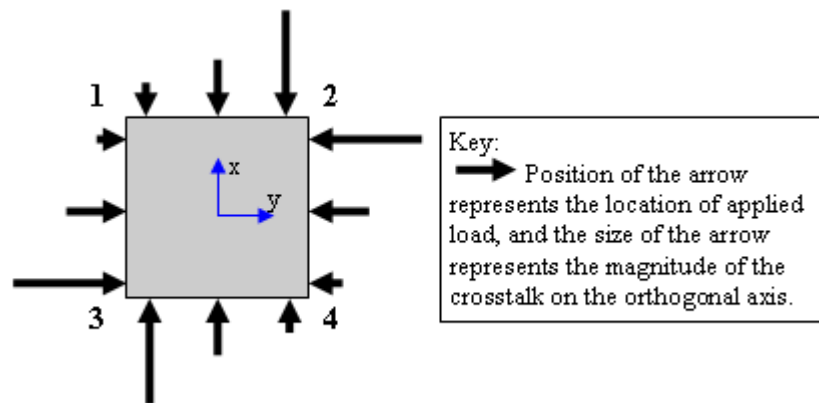


Figure 107 - Schematic illustration of the crosstalk magnitude in the orthogonal shear axis at the locations where shear load was applied.

#11 – Repeatability

Repeatability of the applied 1Hz cyclic load and the repeatability of the corresponding outputs from the representative transducer are summarised in Table 40. The average peak-to-peak output of the transducer was ~97% of the applied load, which agrees with the results found in the frequency responses analysis (#2 Frequency responses). The variation (SD) in transducer output (Table 40) was comparable to that of the applied load.

Table 40 - Repeatability of the representative transducer.

Shear axis	Average peak-to-peak applied load (N)	(SD)	Average peak-to-peak transducer output (N)	(SD)
Negative X	28.06	0.08	27.67	0.09
Positive X	28.14	0.07	27.80	0.11
Negative Y	28.15	0.07	27.81	0.08
Positive Y	28.10	0.12	27.67	0.16

#12 – Creep

Figure 108 illustrates the transducer output when a square wave loading sequence was applied to the transducer. It was apparent that the transducer output under constant loading approximates an exponential function (Figure 90), which reflects the properties of the elastomeric material used in the construction of the transducer and is likely to be temperature dependent (#13 Temperature sensitivity). Creep was calculated relative to the load applied (Figure 109). As the creep followed the typical form of an exponential function, an average value of 2.6% (of the applied load) could be assumed to be a good approximation of the creep maximum for the transducers (Figure 109). Therefore, creep was likely to result in an error of less than 1N.

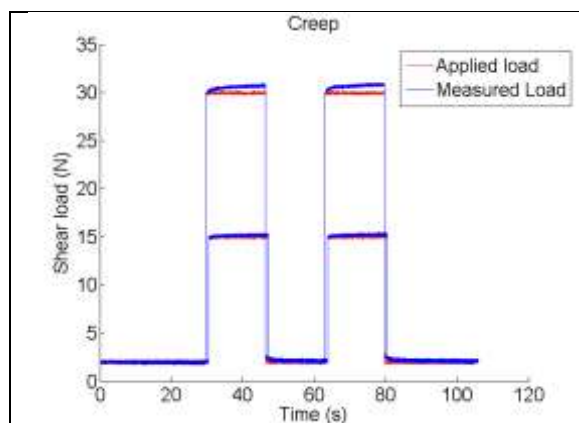


Figure 108 - A plot showing the applied load and the load measured by the representative transducer.

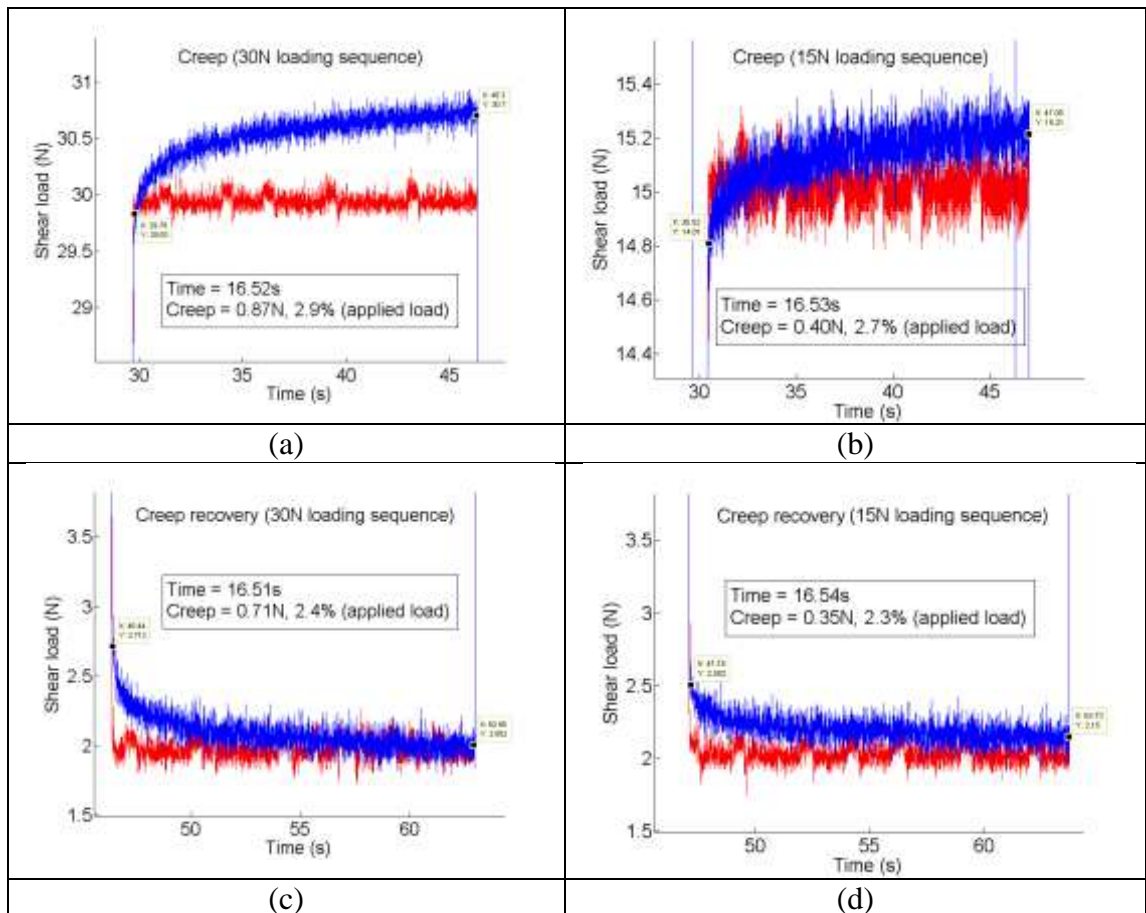


Figure 109 - Creep (a, b) and creep recovery (c, d) of the representative transducer. The plots were extracted from the waveform in Figure 108.

#13 – Temperature sensitivity

A dry temperature testing chamber was not available for the dynamic evaluation of the transducer with the material testing machine. Consequently, a temperature controlled water bath was used to test the structural components of the transducer at different temperatures. The slopes of the curves in Figure 110 illustrate increased transducer sensitivity with increased temperature. It should be noted that the baseline of each curve in Figure 110 were off-set for illustration purposes. As expected, the elastomer was more compliant with increased temperature. Therefore, at higher temperature, a shear load of equal magnitude would result in greater displacement of the magnet relative to the sensor ICs leading to an increase in the span of the transducer output.

Minimal transducer output error was predicted at temperatures below 35°C (Table 41). However, relatively large errors (up to 14% of the applied load) and an increase in hysteresis were apparent above 35°C if the room temperature calibration curves were to be used. During testing at 40°C, shear loading resulted in a creep of 0.068mm over the 3 test cycles (Figure 110). Consequently, the transducer and subsequent array should operate at temperatures below 35°C to avoid errors associated with material creep.

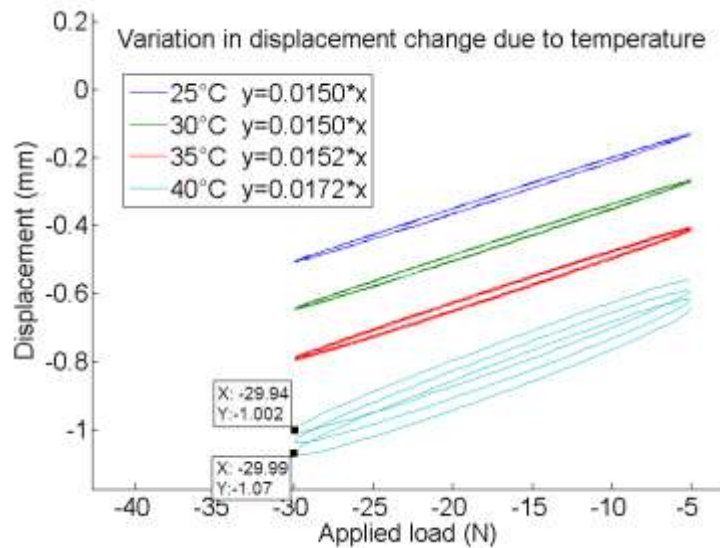


Figure 110 - Variation in displacement change of the transducer sensing surface plate under cyclic loading due to change in temperature. Only three cycles of data per testing condition are shown and the baseline of each curve was off-set for illustration purposes, therefore relative displacement values should be used for interpretation.

Table 41 – Transducer output error due to change in temperature. Error was calculated based on the slope of the curves in Figure 110 and assuming 1) displacement changed linearly with load, and 2) the transducer was calibrated at 25°C.

Temperature	Slope	Displacement at 30N	Transducer output error (N)	Error (% of applied load)
25°C	0.01504	0.45	0.00	0.00
30°C	0.01507	0.45	0.07	0.25
35°C	0.01529	0.46	0.51	1.69
40°C	0.01720	0.52	4.32	14.41

7.2.1.2 Hardware

#14 – Sampling frequency

The output bandwidth of the A1301 hall-effect ICs was 20kHz, whereas the DAQ system (USB-6225) had a sampling rate of 250kS/s (samples per seconds). In the case here when 20 biaxial shear transducers were connected to the DAQ, there were a total of 80 analogue voltage channels to be sampled. As a result, the maximum sampling frequency the DAQ could run at was 3kHz (250000 samples ÷ 80 shear channels). That said, sampling rates of up to 5kHz were used during the evaluation of the representative transducer because only that particular transducer was connected to the DAQ during testing. A sampling rate of 200Hz was used during the evaluation of the transducer array as a whole to avoid overloading the computer to maintain a near real-time visual feedback on the monitor of the directions and magnitudes of each of the transducer outputs.

#15 – Power consumption, #16 – Multiplexing capability, #17 – Computational requirements

The power consumption of the SOT23W surface mount A1301 hall-effect IC was the same as the SIP packaged ICs specified earlier (Section 6.3.2) at 220mW each. Therefore the total power dissipation by the 20 transducers in the measurement system was 4.4W. Power requirements of the DAQ system was <1.4W. Power needed for the operation of the DAQ system (i.e. the multiplexor circuit and analogue-to-digital convertor) and the computer necessary for processing and storing of the data were not critical in a platform system such as in the current design. However, a data acquisition device that is smaller in size would be required if the transducers were to be used in in-shoe experiments, unless the subject would be carrying the electronics in a backpack.

Multiplexing and recording of the many signals from the transducer array has been demonstrated with the DAQ system used in the current study. Within the DAQ system (USB-6225) was a multiplexing circuit capable of handling 80 analogue channels. However, the computational power of the computer required for processing

the data from all 20 transducers, hence the 80 voltage signals with the current design, could be considerable, depending on the sampling rate of the DAQ. The laptop (Intel 2GHz Duo Core processor and 1GB RAM) used in the current study was running LabVIEW8.6 software, but was not able to provide data visually in real-time with simultaneous data recording to the computer disc at 200Hz.

Further optimisation in the software program and a faster CPU and computer disc would be needed to simultaneously record data and provide real-time visual feedback during subject trials. Another solution would be to implement the computational stage electronically within each transducer. In that case, the 20 transducers would only have a total of 40 signal outputs. Moreover, the computer would only need to perform one multiplication per axis signal to compute the shear load output. However, such an approach would only work for a platform system. The extra electronics would mean an increase in the overall dimensions of the transducers or that they would need to be located externally. This would mean that they were not suitable for in-shoe applications. Nonetheless, a bigger multiplexing circuit or a different multiplexing strategy would be required if more transducers were to be used in the implementation of a large array system.

#18 – Hardware costs

It was estimated the hardware costs for the construction of one transducer in the batch production described above (Section 7.1.2) was £6.23 (Table 42), excluding labour costs. The time required to assemble one transducer was estimated to be around 15 minutes, provided the PCB circuits were ready made. Such low-cost and quick transducer construction would not be possible with other load sensing technologies such as strain gauged based designs.

Manufacture of the aluminium transducer mounting platform was estimated to cost £10, excluding labour costs. The 40-way cables (3659-Series, 3M, USA) used to connect between the transducer array and the DAQ were £10.46 per metre. The DAQ system (USB-6225) used in this study cost £1260, and was a multi-purpose DAQ system designed for quick prototype testing and evaluation. However, a relatively

simple multiplexing analogue-to-digital convertor circuit alone would be suitable for mass production and may be considerably cheaper.

Table 42 - Hardware costs for constructing one magnetic based biaxial shear transducer in a batch production.

Items	Info	Cost
Hall-effect sensors	Allegro A1301KLHLT-T x 4	£2.00
Printed circuit board	Standard 1mm PCB	£0.20
Magnet	Assemtech M1219-1	£0.37
Transducer structure	3D printing	£1.20
Cables	cost estimate based on 5-way ribbon cable	£1.80
Crimp Sockets	Harwin Inc. M20-1060200	£0.56
Elastomeric material	TARRC 0.5mm	£0.10
Total		£6.23

7.2.1.3 Physical requirements

#19 – Transducer sensing surface area, #20 – Transducer thickness

The current study has shown that a transducer sensing surface of 10×10mm was possible using surface mount A1301 hall-effect sensor ICs. Each transducer in the array was 22.7mm tall but this could have been further decreased for a thinner and more portable platform system. The miniaturised version of the transducer was only 8.5mm thick, and could have been further miniaturised by: 1) replacing the 1mm PCB with thin <0.2mm polyester flexible printed circuits, thereby allowing the thickness of the transducer housing to reduce by ~1.5mm, and 2) reducing the thickness of the sensing surface plate from 2mm to 1mm. Therefore, a transducer thickness of 6mm would be feasible provided a stronger material than acrylic were used in the construction of the transducer structure.

#21 – Suitability for in-shoe applications, #22 – Easy to mount/wear

An ideal in-shoe transducer would be as thin as possible. However, the current design with a thickness of 8.5mm would be suitable for in-shoe applications. Although mounting of the transducer could be physically challenging, others have used transducers of similar thickness (10mm) inside female high-heel shoes (Cong et

al., 2011). The transducers for the platform system had a simple, but effective, mounting mechanism involving a rigid rod to secure and link adjacent transducers. The design allowed quick and easy construction of the transducer array, and the replacement of faulty transducers could have been done with ease if necessary.

#23 – Transducer sensing surface allowable movement, #24 – Spatial resolution

The displacement of the sensing surface plate in the representative transducer with the application of 30N shear load was about 0.37mm (Table 43). This displacement was found to be consistent between axes. Based on the displacement change in the sensing surface plate during calibration, the shear modulus of the transducer was estimated to be about 0.6MPa, which was consistent with that found for the earlier prototype (Section 6.3.3).

The gap of 1.5mm between the sensing surface plate of adjacent transducers used in the current array would have allowed adequate space for their movement and was also sufficient to avoid contact even in overloaded conditions (>60N). However, if overloading conditions could be avoided altogether, then the gap between adjacent transducers could be reduced to 0.8mm, resulting in a spatial resolution better than the current 11.5mm for the platform system.

Table 43 - Sensing surface displacement change from 0N to 30N in the representative transducer. Data presented is based on average displacement change during 1Hz cyclic loading.

Shear axis	Average sensing surface displacement at 30N (mm)	(SD)
Negative X	0.371	0.0021
Positive X	0.385	0.0023
Negative Y	0.376	0.0021
Positive Y	0.364	0.0019

#25 – Reusability and life expectancy

As discussed earlier (Section 6.3.3), longevity is a typical feature of hall-effect sensing devices. Although the long term reliability and the service life of the elastomeric material used in the current design have not been tested, it has been reported that 2 years of ambient temperature aging does not cause substantial

changes in properties of the material (Mott and Roland, 2001). Although the transducer has been tested at different temperatures in water, whether the properties of the acrylic material may change due to temperature and sweat inside the shoe is still unclear. It is recommended that a different material, such as aluminium or stronger plastic is used in the construction of the in-shoe type transducers.

7.2.1.4 Manufacturing requirements

#26 – Batch production

Batch production of the transducers, both the platform types and the in-shoe type, was simple and required minimal labour. Precision and quick transducer construction was made possible with a simple assembling device. If the construction of the electronic circuits were out-sourced, the assembling of the transducers could be done in-house quickly at <15mins per transducer.

#27 – Matrix arrangement capability, #28 – Cabling

The current platform design allowed flexibility in the arrangement of the transducers. The platform was setup as a 4×5 array but could be easily rearranged, or even have the transducers scattered across the platform at different locations. For example, it is possible to have two array clusters instead, one for measuring the forefoot area and one for the hindfoot. However, additional walls for the mounting platform would be needed. The large number of cables from the 20 transducers was carefully managed (Figure 100) and they were easily accessible. Space for the connectors was not an issue. The detachment or reconnection of any transducer could be easily achieved.

7.3 Preliminary subject trial

7.3.1 Method

Data were collected on the left foot of an individual (age 28, height 169cm, weight 60kg) with no history of lower limb complications. The completed biaxial shear distribution measurement platform (Figure 100a) was secured on the centre of a

Kistler force plate and the array of transducers was set flush in a 200cm × 80cm wooden walkway (Figure 111). The raised wooden platform was level with the sensing surface of the transducer array and was neither in contact with the Kistler force plate nor the transducer array. The subject was tested barefoot in three experiments: 1) The subject was asked to balance on their heel on the transducer array, 2) walking was initiated from one end of the walkway and the individual was asked to step onto the array of transducers with their forefoot, and 3) with their hindfoot. One trial was conducted in each experiment.

The purpose of these trials was not to make comparison between forefoot and hindfoot data but to demonstrate the utility of the system and to allow comparison between the Kistler force plate as a secondary check of the quality of the total shear output from the biaxial shear distribution measurement system under real-life dynamic conditions. To synchronise the Kistler system with the transducer array, a sharp shear load was applied manually to one of the transducers in the array and the measured peaks from the two systems were subsequently correlated. Both systems had the same sampling frequency of 200Hz.

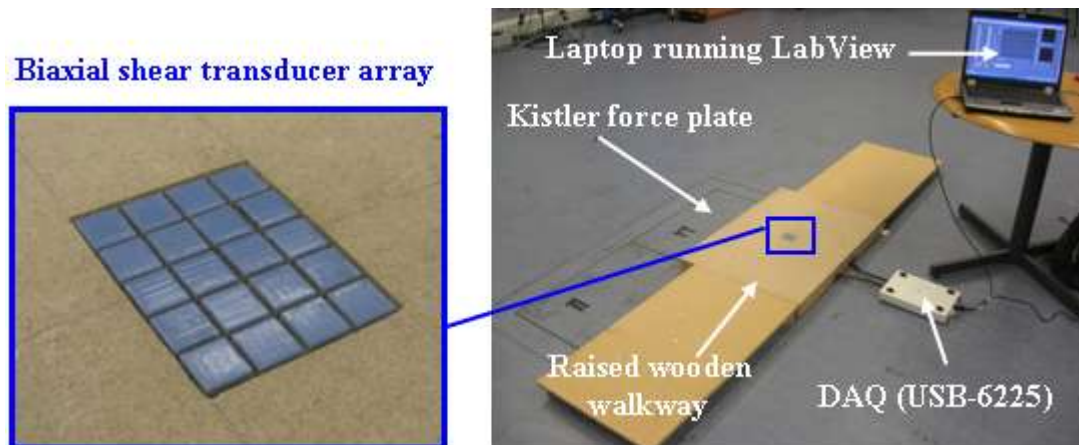


Figure 111 - Experimental setup for preliminary subject trials on the biaxial shear distribution measurement system. The system was secured on a Kistler force plate and the data from the two systems were compared.

The total X-axis (anterior-posterior) and Y-axis (medial-lateral) shear loads measured by the biaxial shear distribution measurement system were calculated by summing the outputs from all 20 individual transducers. The results from each of the

3 experiments were compared with the corresponding X and Y axis shear load measured from the Kistler force plate.

7.3.2 Results and discussion

Measured shear outputs from each of the transducers are graphically illustrated in Appendix H along with an accompanying picture of the subject's foot in contact with the transducer array. The turning motion of the subject's feet was observed during heel contact on the transducer array, with the shear vectors from the transducers showing a spiral pattern (Appendix H).

Figure 112, Figure 113 and Figure 114 below illustrates the summed outputs from the transducer array compared with the corresponding X and Y axis shear load measured from the Kistler force plate during each of the 3 experiments. The measured load from the biaxial shear distribution measurement system matched closely with the output from the Kistler force plate, with root mean squared error of less than 2N. The maximum resultant shear load measured by one of the transducers in the array during forefoot and hindfoot stepping was 14.8N and 13.4N, respectively. One transducer measured a maximum resultant shear load of 10.7N when the subject was balancing on the heel. An evenly distributed load on the transducer array would be unlikely when the subject was balancing on the heel, however the maximum error found between the Kistler force plate and the summed outputs from the array were no more than 4.64N (Figure 114). Therefore, high accuracy and reliable data can be expected from the biaxial shear distribution measurement system in real-life testing.

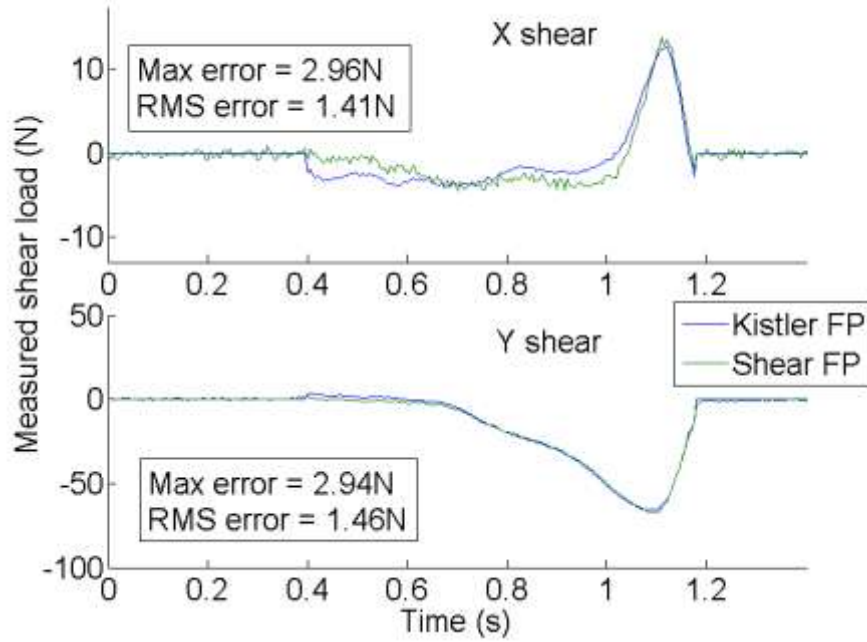


Figure 112 – Total shear force (X and Y axis) measured by the Kistler force plate and the biaxial shear distribution measurement system during ‘forefoot’ subject trail.

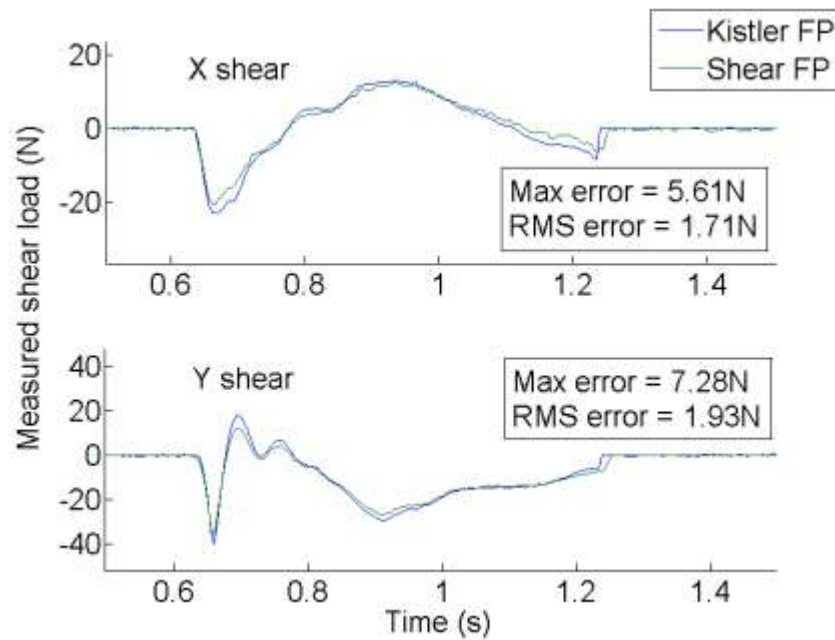


Figure 113 - Total shear force (X and Y axis) measured by the Kistler force plate and the biaxial shear distribution measurement system during ‘hindfoot’ subject trail.

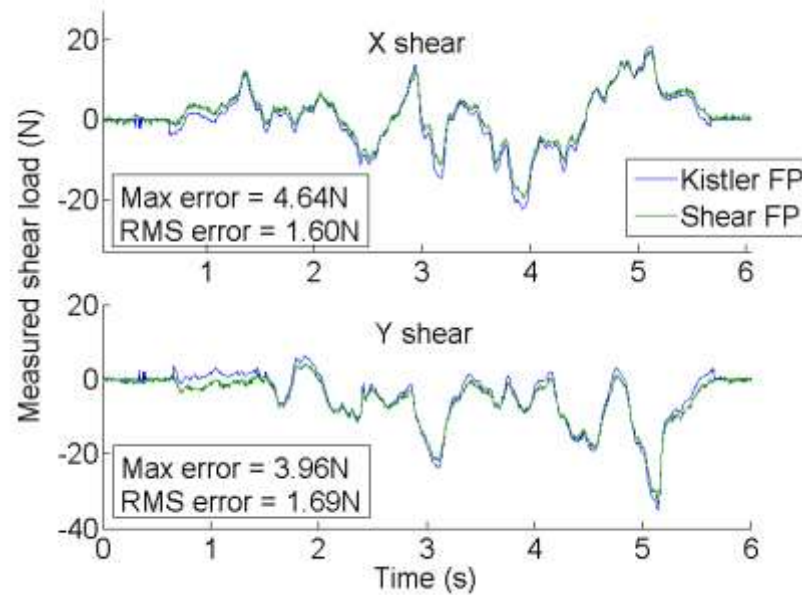


Figure 114 - Total shear force (X and Y axis) measured by the Kistler force plate and the biaxial shear distribution measurement system when the subject was balancing on the heel.

7.4 Conclusion

A low-cost high spatial resolution biaxial shear distribution measurement system has been designed, constructed and evaluated. The modular system consisted of 20 transducers in a 4×5 array arrangement covering an area of 56×44.5mm and a spatial resolution of 11.5mm. The modular platform design could provide flexibility in the arrangement of the individual transducers and could be easily adapted to accommodate more transducers for a larger array system. Each transducer within the array employed magnetic-based hall-effect sensors to detect shear load. With such a method, miniature transducers (8.5×11.5×11.5mm) were constructed and they had the potential to be further miniaturised to a thickness of 6mm. Moreover, off-the-shelf sensor ICs were readily available at low-cost, which is a critical element allowing the implementation of a big array system.

The system as a whole was very simple to use. The software package allowed real-time monitoring, however, simultaneous data recording would have required greater computing power. Further optimisation in the software may be required if a greater

number of transducers were to be used in a large array system. Computational work within software could, potentially, also be reduced by performing pre-calculations electronically within each transducer. A different multiplexing strategy, that was as efficient as the current design, but deliverable at a lower cost on a larger scale, would be required for the implementation of a low-cost large array system.

Although the transducer array could not measure triaxial load, results collected from preliminarily subject trials have shown that the transducer array could deliver accurate shear measurement data during gait when compared with a ‘gold standard’ force platform system. The system also performed well in situations where an evenly distributed load over the transducer surfaces cannot be guaranteed.

Chapter 8

Conclusions and future work

The overall aim of the current study was to develop a multi-axial load distribution measurement device that could be used continuously. Although each of the separate chapters of this thesis have been discussed individually throughout, this chapter will discuss the steps taken in achieving the aim of the study, making direct reference to the objectives set in Section 2.4. Finally, recommendations for future research studies are provided. Possible clinical and industrial applications of the device developed in this current study are also suggested.

8.1 Overall project discussion

The clinical need for a multi-axial load distribution measurement device and hence the motivation of the current study has been presented (Section 2.1). The overall aim of this study was to develop a low-cost device that could measure multi-axial load distribution on the foot during gait. Several objectives were identified at the outset and they were undertaken to achieve the ultimate goal:

Objective 1: To identify essential and desirable system design requirements for the development of a multi-axial load distribution measurement device.

The findings of the literature review (Sections 2.2 and 2.3) on prior work conducted in the field of biomechanics in both normal and diabetic populations provided sufficient information for preparing the list of system design requirements (Section 2.4.1). Many of the requirements were determined based on the characteristics of commercially available pressure distribution systems and other experimental devices capable of multi-axial load measurement (Table 1, Section 2.2.3), so that the performance of the device developed in the current study would be comparable if not better than other existing devices. Performance of existing devices helped identify transducer performance requirements such as measurement accuracy, hysteresis, non-linearity and crosstalk. The working temperature range requirement, transducer dimensions and spatial resolution were also determined from the review of existing devices.

The review on different transducer configurations employed by currently available commercial devices (Section 2.2.4) also helped identify the desired area of the transducer sensing surface. The findings also provided inspiring design ideas to aid the decision in building the final load distribution measurement system using multiple discrete transducers. The advantage of such a design is that each transducer could be detached from the assembly individually for calibration or repair when necessary.

The frequency response and sampling rate requirements were based on reported frequency content in plantar load measurements measured by other researchers (Section 2.3.1). The magnitude of loads that the transducer would need to be able to measure was also considered (Sections 2.3.2 and 2.3.3). The findings helped to set the rated capacity requirement for vertical and shear measurement. Possible mechanical abuse was considered and a safety factor of >2 was used to avoid overloading and potential damage of the transducer.

Objective 2: To identify load sensing technologies with the greatest potential to meet the requirements outlined in Objective 1

It was beyond the scope of this current study to explore all possible means of load sensing or to invent novel technologies for load sensing. However, 7 different electronic-based load sensing technologies were identified and explored (Chapter 3), namely: resistive, piezoelectric, capacitive, optoelectronic, magnetic, pneumatic and hydraulic-based technologies. Non-electronic systems or cumulative-based load measurement methods were not considered in the current study because they do not allow the recording of temporal loading information. Hence they do not meet the system design requirement of the current study (Section 2.4.1).

The basic operation, possible signal conditioning and electronic circuit requirements, and the potential ways of constructing a transducer using each of the technologies were studied. The literature review on the current state-of-the-art also helped to predict the transducer characteristics achievable with each of the 7 load sensing technologies. Advantages and limitations of each technology were then critically reviewed and compared against the system design requirements identified at the outset. A scoring system was used to compare each technology to identify those worth investigating for their suitability for the development of a low-cost multi-axial load distributional measurement device (Section 3.9). From this, it was concluded (Section 3.10) that magnetic-based and optoelectronic-based techniques displayed the highest potential in meeting the system design requirements. The hydraulic-based method was also chosen to be investigated further because hydraulic systems can be very simple in design and it was believed that it may hold many opportunities for

achieving the aim of the current study. Piezoelectric-based systems scored relatively low, but were also considered because the current study benefitted from the availability of a pre-existing piezoelectric triaxial force transducer prototype from the University of Kent. Consequently, 4 different load sensing technologies were evaluated further, namely piezoelectric, hydraulic, optoelectronic and magnetic-based technologies.

Objective 3: To establish an efficient and effective method of calibrating multi-axial load transducers.

The many standard practices and procedures currently used in the calibration of uniaxial load transducers were explored (Chapter 4). Other methods detailed in the literature for the calibration of triaxial load transducers were also examined (Section 4.4). Findings from these reviews provided guidance in designing a calibration rig suitable for the current study. Based on the method of using a secondary force calibration standard, the calibration rig was custom designed to allow static and dynamic calibration of the many prototype transducers to be developed in the current study, in both the vertical and shear directions (Section 4.5). Transducers were mounted on a multi-channel reference load cell which recorded the applied calibration loads. The calibration rig also allowed the simultaneous application of vertical and shear load to assess the response of the transducer prototypes. While the manually operated calibration rig was suitable for evaluating a number of initial prototypes for each sensing technology, the magnitude and rate of loading was not sufficiently controlled or efficient for evaluating the final prototypes or the numerous transducers in the array. Consequently, a material testing machine was employed to undertake controlled static and dynamic vertical and shear loading protocols (Section 6.2). The material testing machines, with customer designed adaptors for the mounting of different transducer prototypes, allowed a relatively quick and reliable procedure for the calibration and evaluation of the transducers.

Objective 4: To identify the optimal transducer design to be incorporated in a multi-axial load distribution measurement device against the design requirements in Objective 1.

Four different load sensing technologies were identified in Objective 2 to have the highest potential to meet the system design requirements of the current study. Consequently, various multi-axial load prototype transducers based on these four different technologies were designed and evaluated (Chapter 5). The piezoelectric-based prototype transducers from the University of Kent were also evaluated for comparative purposes (Section 5.1). The approach of using piezoelectric-based material as the means for triaxial load measurement did not meet the system design requirements, primarily due to cost and manufacturing complications. On evaluation, the piezoelement was found to be extremely sensitive to bending, off-axis loading and signal drift. While such limitations may be overcome with the use of stiffer housing materials and better charge amplifier circuits, such requirements render the technique cost ineffective.

A novel hydraulic-based prototype transducer was constructed and evaluated (Section 5.2). The hydraulic system utilised off-the-shelf pressure sensors and the simplicity of the design allowed easy and low-cost manufacturing of the transducer. Theoretically, the location of the pressure tubes within the transducer housing predicted zero crosstalk, and the transducer had the potential to perform with minimal hysteresis and non-linearity if an appropriate pressure tube material was used. The hydraulic based transducer was the only transducer prototype suitable for triaxial load measurement. However, the transducer was large in size and was not suitable for incorporation within a matrix arrangement for load distribution measurement.

Preliminary evaluation of the optoelectronic-based prototype revealed that the transducer was capable of biaxial shear measurement with minimal hysteresis and non-linearity with optimal selection of transducer components (Section 5.3). Although the overall dimensions of the prototype were limited by the size of the chosen photodiode, the design concept could potentially be miniaturised. Similarly, a novel magnetic-based transducer prototype was also found to be capable of biaxial shear measurement and performed as well as the optoelectronic-based design in terms of non-linearity, hysteresis and crosstalk (Section 5.4). The different dimensions of the optoelectronic-based and magnetic-based prototypes, however, did not allow a fair a

fair comparison between the two transducer designs. Consequently, beta versions of the two prototypes were constructed with the same dimensions with further design modifications.

New and improved optoelectronic-based and magnetic-based prototype transducers were then calibrated and comprehensively evaluated against the system design requirements (Chapter 6). In terms of transducer performance, both designs had similar characteristics such as hysteresis (~6%RC), non-linearity (~3%RC), creep (~0.7%RC) and frequency response (10% error at <200Hz) that met the system design requirements of the current study. The magnetic-based prototype displayed better measurement accuracy and was less affected by crosstalk. In terms of physical requirements, the magnetic-based system had the potential to be miniaturised easily using off-the-shelf sensor components. In comparison to the optoelectronic-based design, the sensor components used in the magnetic-based device would require fewer wire connections, and less power to operate, and was estimated to be 3 times cheaper to manufacture. Consequently, the magnetic-based prototype was identified to be the optimal transducer design for incorporation in a biaxial shear distribution measurement device.

Objective 5: To design, manufacture and evaluate a multi-axial load distribution measurement device against the design requirements in Objective 1.

Although the magnetic-based shear transducer design was not suitable for triaxial load measurement, the device satisfied the essential requirement of being capable of measuring biaxial shear load. A small transducer array was subsequently built to demonstrate the clinical potential of the magnetic-based design for biaxial shear distribution measurement (Section 7.3). To demonstrate the potential for low-cost manufacturing of the device, a 3D printing fabrication techniques were used in the construction of the transducer housing structure. Electronic circuits were manually prepared, requiring only short assembly times as each transducer required minimal electrical connection. This also allowed easy cable management when incorporating all 20 individual transducer into a matrix arrangement for biaxial shear distribution measurement.

A representative transducer in the array was tested and evaluated thoroughly against the system design requirements (Section 7.2). The performance and characteristics of the transducer have met all the system design requirements except in two cases: 1) in the extreme cases error of up to 14%RC were present when a point load was applied to a corner of the transducer, and 2) an error of around 14% was present when the transducer was used above 35°C, which nearly met the requirement of <10% below 40°C. The device was linear over the rated capacity of 30N and accurate to ~2%RC. The transducers incorporated within the array were too large for in-shoe application. However, a transducer thickness of 6mm would be feasible using the same magnetic-based load sensing principle. A miniature transducer with thickness of 8.5mm was demonstrated in the current study.

The transducers in the array were 22.7×11.5×11.5mm in size, and contained mechanical features to allow easy mounting in a matrix arrangement. A preliminary subject trial was conducted to assess the overall performance of the biaxial shear distribution measurement device (Section 7.3). Load distribution data was multiplexed to a laptop and results were compared to a Kistler force measurement platform. High accuracies (RMSE <2N) were found even in situations when unevenly distributed load was applied to the device, for instance, when the subject was balancing on their heel on the transducer array.

Further work is required to expand the current design to measure load distribution over the whole plantar surface of the foot. Other recommendations for future work are discussed further below (Section 8.2). Nonetheless, the overall aim of the current study was achieved successfully, with the design, manufacture and initial evaluation of a magnetic-based biaxial shear distribution measurement device that consists of 20 transducer elements. The device was fit for purpose to allow data collection during gait, thus potentially providing valuable biomechanical data for identifying feet that may be at risk of diabetic neuropathic ulceration.

8.2 Recommendations for future Work

8.2.1 Further evaluation of the magnetic-based transducer

Shear forces during gait are influenced, in part, by the frictional properties of the surface interface. Therefore, there is a need to establish the optimal surface finish for the transducer. Friction coefficient of the transducer is dependent on the material used in the construction of the transducer sensing surface, which would influence the shear load to be measured. Acrylic polymer was used in the current study for the transducer array. Further tests would be required to verify that acrylic was sufficient to provide sensing surface properties that are similar to a typical hard floor surface.

Further investigation of the effect of temperature and humidity effects are also necessary. Although a representative transducer from the array was tested at various temperatures (25°C to 40°C), the test was conducted under water without electronics. Although it was predicted from the manufacturer's datasheet that the electronics would have <1% differences in sensitivity over the operating range of 10 to 40°C, no information was found regarding how the 3D printed transducer housing material may response under water. Therefore, to examine the true effect of temperature and humidity on transducer output, the completed transducer with electronics should be evaluated in a dry temperature and humidity-controlled chamber.

Tests conducted previously (Section 5.4.2.2) have shown that the magnetic-based shear transducers were not sensitive to the changing magnetic field from adjacent transducers. Further tests should be carried out to verify that any metallic material brought near to the array would not influence the measured output. The use of the system would be limited if it were sensitive to strong external field changes. For example, a user wearing any prosthesis or orthosis that may contain metallic or magnetic parts might not be able to use the device for accurate load measurement. The device should also be tested for its suitability to be used in conjunction with other magnetic based motion analysis systems, such as those from Ascension Technology Corp. (USA) or Polhemus (USA).

8.2.2 Batch production of the transducers

There were minor issues with the production of the magnetic-based biaxial shear transducers in the current study. Acrylic polymer was used in the final transducer design and the bonding of which to the elastomeric material was relatively easy using cyanoacrylate adhesives. However, if the transducer were to be manufactured in a different material other than plastics, for example in the earlier prototypes where aluminium was used, it would be more difficult to bond the materials together using adhesives. Therefore, future transducers should have the rubber material bonded to the metal structure during the curing stage of the rubber. The metal surface should be prepared by sandblasting, painting on a primer coat and then painting on a top bonding coat prior to the curing stage. The whole assembly should then be put into a hot press and the rubber would bond firmly onto the metal as it cures (JP. Gladwin, TARRC, pers. comm.).

The design of the transducer array in the current study was constructed using numerous discrete biaxial shear transducers. The assembly of which could be time consuming if a larger array were to be constructed. Wire management could also be challenging as the number of transducers increases. One solution would be to manufacture the transducer array as one device. This could be done, for example, by building the array in two parts: 1) the upper part consisting of a large piece of the elastomeric material and an array of sensing surface plates bonded next to each other with gaps in between, and 2) the lower part would contain all the Hall-effect sensor ICs, perhaps all soldered onto one big circuit board and multiplexed for minimum output wires. With such a design, the upper part with different elastomeric materials designed for different measurement range could be swapped with ease.

8.2.3 Clinical trials

Although with some limitations, the magnetic-based biaxial shear distribution measurement system developed in this thesis could now be used in clinical trials without major modifications. It would be necessary to locate the position of the foot on the transducer array during gait in order to allow comparison between its outputs and shear values currently available in the literature. There are two possible solutions: 1) incorporate more transducer elements in the current design to cover the

whole plantar surface of the foot, or 2) incorporate a tracking system to track the foot location when it is in contact with the transducer array. The latter could be readily achieved in most gait laboratories that have motion capture systems. Another method would be to mount a camera towards the underside of the transducer array with the subject walking on a glass walkway (Chen et al., 2010). However, this would be restricted to a transducer array of small size no larger than the current system otherwise the mounting platform would obstruct the viewing of the camera. Alternatively, a gait initiation rather than mid-gait data collection protocol could be used. As previously demonstrated on a small triaxial load distribution measurement platform (Davis et al., 1998), the subject could be tested with their foot strategically located on the transducers. The subject would subsequently initiate walking and the load under the specific region of the foot during the initiation phase of walking would be recorded.

With any of the experimental setups described above, the ultimate goal would be to validate the amount of shear load the foot experiences during gait. The clinical validity of plantar shear parameters, and more specifically the shear-time integral, needs further study to clarify whether it is the peak, the average, or the exposure time of plantar shear load that is important in diabetic foot ulceration. In future studies, techniques to quantify in-shoe shear load should also be considered.

8.2.4 Elastomeric material testing

A compliant elastomeric material sandwiched between the sensing surface plate and the housing of the transducer was required in the current biaxial shear transducer design. The overall performance of the transducers was largely dependent of the mechanical characteristics of the elastomer. These materials typically demonstrate non-linear viscoelastic properties, including creep and hysteresis, which are often influenced by temperature and loading frequency. As such, transducer characteristics are expected to be influenced by both of these factors. As demonstrated in Section 7.2.1.1, the output of the final magnetic-based transducer was relatively robust, with minimal loss of signal up to loading frequencies of 200Hz when compared to a reference load cell. However, the mechanical properties of both the acrylic material

used in the construction of the transducer housing and the elastomer separating the housing from the sensing surface plate were shown to be temperature sensitive, resulting in substantial errors (14%) at temperatures above 35C. Consequently, it is recommended that the current transducer array is not operated at temperatures above 35C.

More extensive mechanical testing of the current and alternative elastomeric materials over a range of different temperatures and frequencies would be necessary to further improve the overall accuracy of the transducers. Alternative signal processing methods to compensate the creep in the transducer should also be tested, where a study has demonstrated that the error in an elastomer-based magnetoresistive accelerometer could be reduced from 3% to 0.08% (Kim Le, 2008).

8.2.5 Construction of triaxial load transducer

The ultimate goal of the current study was to develop a triaxial load distribution measurement device. However, none of the low-cost prototype transducers investigated in this study was suitable for triaxial distribution measurement. Nonetheless, the magnetic-based biaxial shear transducers that was developed had desirable performance characteristics such as good accuracy (~2%), low hysteresis (<4%) and non-linearity (<2%). The transducers were not able to measure vertical load. The change in magnetic field due to the relatively small vertical movement of the magnet was not large enough for the Hall-effect sensor ICs to detect. Further work is recommended to investigate whether the use of a flux concentrator or an additional magnetoresistive-based sensor IC in the transducer would be sufficient to measure vertical load. Magnetoresistive-based sensors are typically more sensitive than Hall-effect devices but they responds to parallel fields (Section 3.6.1). As such, the additional ICs would need to be mounted in an upright position and would increase the overall thickness of the transducer.



Figure 115 – The construction of a triaxial load transducer by combining a shear transducer with a transducer capable of measuring vertical load. The magnetic-based shear transducer was Prototype C described earlier (Section 5.4.2.3).

Alternatively, the biaxial shear transducers developed in this study could potentially be combined with existing uniaxial load transducers to form a triaxial load transducer. An attempt was made at bonding Kent's piezoelectric transducer to the base of the magnetic-based shear prototype transducer (Figure 115). The Kent's transducer was used to provide the additional vertical load measurement. However, the application of shear load during calibration testing resulted in delamination of the 'Kent' transducer, a common failure mode of the device (Thornton, 2009). As a result, the concept was not evaluated further. However, other vertical load or pressure transducers could potentially be used instead. For instance, the elastomeric material used in the construction of the magnetic-based transducer could potentially be replaced with commercially available capacitance-based or a resistive-based pressure transducer, such as those manufactured by Novel GmbH (Germany) and RSscan International (Belgium).

8.2.6 Potential of an hydraulic-based triaxial load transducer

The hydraulic-based triaxial transducer designed in this study was not investigated further, primarily because its dimensions rendered it unsuitable for incorporation within an array of suitable spatial resolution for load distribution measurement beneath the foot. However, the transducer has potential to be used in a broad spectrum of applications other than gait analysis. For example, the transducer would be compatible in magnetic resonance imaging (MRI) and may be useful for applications in which simultaneous measurement of force and soft-tissue deformation are required (Liu et al., 2000, Petre et al., 2008).

In a preliminary investigation, the hydraulic-based transducer was used to record triaxial load beneath the hallux during uni-pedal stance (Lau et al., 2009). The

transducer was secured on a 6-channel reference load cell (Nano25, ATI Industrial Automation, USA) during testing. Dynamic performance of the transducer revealed average differences of <3.5N between the transducer and the reference load cell, which is comparable to the more expensive strain-gauge-based tri-axial device developed by the Davis group (Davis et al., 1998). Therefore, with minimum modification, the current design of the hydraulic-based triaxial load transducer would be readily deployable for other applications and could deliver reliable results.

8.2.7 Potential of the optoelectronic-based biaxial transducer

The optoelectronic-based biaxial transducer designed in this study was not investigated further because it was more expensive and more complex to manufacture than the magnetic-based transducer. However, the concept of load sensing using optoelectronic components should not be overlooked. Such a technique has an advantage over the magnetic-based design in that the optical approach would not be affected by external magnetic fields. Thus it would possibly be suitable for use within MRI machines and in conjunction with magnetic based motion analysis systems.

In regard to manufacturing costs, the photodiodes may be replaced with LEDs. LEDs are relatively cheap and given they can also be used as both an emitter and receiver at the same time (Dietz et al., 2003) makes them an attractive alternative. Multiplexing such a system would seem feasible, as demonstrated in the patented multi-touch display (US20060086896) from New York University, and therefore construction of a low-cost, large transducer array would be possible. However, LEDs are not specifically designed for sensing and, as such, would require further investigation.

It should also be noted that the advancement in stretchable substrates for optoelectronics (Kim et al., 2010), may make optical-based in-shoe transducer possible in the future. The researchers have embedded miniature inorganic LEDs and photo-detectors in waterproof substrates, which allow them to be flexed and stretched, making them suitable for in-shoe applications.

8.2.8 Methods for the calibration of a large transducer array

A calibration rig capable of simultaneous application of vertical and shear load was designed in the current study. The apparatus was suitable for the calibration of individual multi-axial load transducers under both static and dynamic loading conditions. However, using the manually operated rig required adjustment of the setup between tests and manual application of load which was labour intensive. A more automated technique in which a mechanical testing machine was used for calibration of individual multi-axial load transducers was also established. Although both of these calibration techniques were effective for the purpose of testing and evaluating discrete transducers, they would not be optimal for calibration of a large number of transducers. A more time-effective and work-efficient calibration method would therefore be necessary for the calibration of a load distribution measurement device, which may contain more than 600 transducers thereby ensuring coverage of the whole plantar surface of the foot.

The traditional least-squares calibration method was employed throughout the study, which required precise application of a wide set of known load to the individual transducers via those calibration machines described above. Alternative calibration methods, such as the 'shape-from-motion' technique (Voyles et al., 1997) or its modified version (Oddo et al., 2007), have been suggested to be comparable to traditional least-squares methods but without the need for precise application of known loads to the transducer. Briefly, a mass attached to the transducer sensing surface is randomly moved through the sensing space of the transducer while its outputs are continuously recorded. Singular value decomposition is then used to calculate the calibration matrix of the transducer. While, such a method has the ability to economically and rapidly calibrate transducers and has been used on different multi-axial transducers including miniature sensors (Keekyoung et al., 2007, Voyles and Khosla, 1997, Yu et al., 2006), it is not suitable for transducers that demonstrate a non-linear response to load (Voyles and Khosla, 1997). Further research as to the potential of the technique for calibration of a large array of transducers therefore is warranted.

8.3 Using the devices in other applications

The use of load transducers can be found not only in bioengineering research but in nearly all disciplines. Although there may be a need to modify the current designs, such as increasing the rated capacity of the transducer for sport analysis, there is a broad spectrum of applications which could potentially benefit from the devices developed from this study:

Medical

- Monitor the rapid changing of foot shape and gait pattern in children could enable the recognition of possible pathology to allow early interventions (Bertsch et al., 2004, D. Stephensen, 2009, Bosch et al., 2007). The same applies in the hand, where the grasping actions and forces in children could give insights into the neuro-motor development and any pathological dysfunctions (Del Maestro et al., 2011).
- Biomechanical analysis of lower limb prosthetic systems (Magnissalis et al., 1992) and amputee gait (Berme et al., 1976) would help relate pressure and shear forces to prosthesis comfort and fitting to reduce skin damage (Beccai et al., 2005). Locomotion studies can also be conducted on animals (Elissa Krakauer, 2002).

Sports

- Studies have suggested plantar load measurement would help in injury prevention (Gabriel et al., 2008). Load measurement devices may be used to detect the effects of fatigue (Bisiaux and Moretto, 2008) and multi-axial impact loads during jumps (Elvin et al., 2007).
- Load transducers can be applied through pedals to compare cycling biomechanics. Such methods may assist individuals to cycle more successfully and more vigorously, enough to reach a heart rate necessary for improving fitness and strength training (Johnston et al., 2008). Strength/power training in other

sports such as soccer and the evaluation of jumping skill in volleyball were also evaluated previously (Wong et al., 2007, Stephens et al., 2007).

Industrial

- Robotic fingers must have the ability of multi-dimensional tactile sensing in order to perform grasping and manipulating tasks (Chi and Shida, 2004, Chu et al., 1996). Robots used in search and rescue missions could greatly benefit from multi-axial load transducer to help the robot to sufficiently grasp items, whether to deliver aid to victims or bring back objects for analysis (Lowe et al., 2007). Other than industrial robots, functionality of prosthetic hands can be improved by incorporating transducers to measure grip force to detect the onset of object slip from the hand (Cranny et al., 2005).
- The gripping performance of car tyres or even those on an aeroplane can be evaluated with a biaxial shear distribution measurement device, hence the patented transducer system by the car tyre company (Triaxial force pin sensor array, US6536292 B1, 2003).

Consumer products

- Multi-axial load distribution measurement devices have the potential to be used in the development of custom-made footwear. The footwear could be for diabetic patients (Long et al., 2007, Bus et al., 2006, Chiu and Shiang, 2007, Hennig and Milani, 1995) or even for military (Birrell et al., 2007) and safety purposes (Cooper et al., 2008). They also can be used to investigate the effectiveness of shear-reduction and impact absorption of insoles (Chen et al., 2003, Chen et al., 2007, Lavery et al., 2005, Bus et al., 2006) or orthotic inserts (Lott et al., 2007, Burns J, 2007, Guldemond et al., 2007b).
- Load transducers would also help to test whether contact pressure or shear data are factors that can determine comfort and discomfort (Buckle and Fernandes, 1998). The results would help in the design of biomechanically sound seats and beds (Goossens et al., 1993) that may prevent pressure sores (Clark and Rowland,

1989). The products would also protect wheelchair users from ulcers (Gefen, 2007, Akins et al., 2011, Apatsidis, 1999).

- Video game and computer manufacturers keep pushing the envelope to make their products more life-like (Lowe et al., 2007). To do this, force sensing and feedback devices are required for a more interactive human-machine interface (Adams et al., 1999). The video game controllers, the Wii Balance Board, is a good example, which can also be used as a clinical tool (Clark et al., 2010). Miniature force transducers can also be used in advanced computer pen input devices (Clijnen et al., 2003b). Load transducers are also used to aid in optimising computer key design that could possibly reduce subject discomfort and fatigue (Bufton et al., 2006).
- Force transducers could be worn inside the shoe with a feedback system that could inform the subject when local pressure or shear exceeds a pre-determined threshold. Such a warning systems could potentially prevent injuries or ulceration by altering the subject to change their walking pattern (Descatoire et al., 2009). Dynamically sensing wheelchair push-rim propulsion forces would allow further understanding of how forces generated by the individual are being directed to help optimising efficiency and performance of the wheelchair as well as help indentifying causes of injuries (Asato et al., 1993). However, this would require further testing of the long-term performance of the transducer (Hurkmans et al., 2006).

References

Abbott, A.C., Carrington, L.A., Ashe, H., Bath, S., Every, C.L., Griffiths, J., Hann, W.A., Hussein, A., Jackson, N., Johnson, E.K., Ryder, H.C., Torkington, R., Ross, V.E.E.R., Whalley, M.A., Widdows, P., Williamson, Boulton & M.A.J. (2002) The North-West Diabetes Foot Care Study: incidence of, and risk factors for, new diabetic foot ulceration in a community-based patient cohort, Oxford, ROYAUME-UNI, Blackwell.

Adams, R., Moreyra, M. & Hannaford, B. (1999) Excalibur - a three axis force display. in Proceedings ASME.

AIHW (2008) Diabetes Australian Facts. Australian Institute of Health and Welfare: Canberra. [Online]. [Accessed 12th January 2013]. Available from: www.aihw.gov.au/publication-detail/?id=6442468075

Akhlaghi, F. (1995) An in-shoe biaxial shear force transducer utilizing piezoelectric copolymer film and the clinical assessment of in-shoe forces. Ph.D. thesis, University of Kent.

Akhlaghi, F. & Pepper, M. (1996) In-shoe biaxial shear force measurement: The Kent shear system. *Medical and Biological Engineering and Computing*, 34, 315-317.

Akins, J. S., Karg, P. E. & Brienza, D. M. (2011) Interface shear and pressure characteristics of wheelchair seat cushions. *J Rehabil Res Dev*, 48, 225-34.

Allegro Micro Systems Inc. (2011) Application Information: Hall-effect IC applications guide. Allegro MicroSystems Inc. [Online]. [Accessed 12th January 2013]. Available from: <http://www.allegromicro.com/en/Design-Center/Technical-Documents/Hall-Effect-Sensor-IC-Publications.aspx>

Anichini, R., Zecchini, F., Cerretini, I., Meucci, G., Fusilli, D., Alviggi, L., Seghieri, G. & De Bellis, A. (2007) Improvement of diabetic foot care after the Implementation of the International Consensus on the Diabetic Foot (ICDF): Results of a 5-year prospective study. *Diabetes Research and Clinical Practice*, 75, 153-158.

Antonsson, E. K. & Mann, R. W. (1985) The frequency content of gait. *Journal of Biomechanics*, 18, 39-47.

Apatsidis, D. P. (1999) Study of the effect of various materials on the distribution of seating interface pressure in severely disabled wheelchair users. MSc thesis, Bioengineering Unit. University of Strathclyde.

AP Technologies (2011) Position sensing photodiodes. [Online]. [Accessed 12th January 2013]. Available from: <http://www.aptechnologies.co.uk/support/photodiodes/bi-cell-a-quadrant-photodiodes>

Armstrong, D. G., Peters, E. J. G., Athanasiou, K. A. & Lavery, L. A. (1998) Is there a critical level of plantar foot pressure to identify patients at risk for neuropathic foot ulceration? *The Journal of Foot and Ankle Surgery*, 37, 303-307.

Arnau, A. (2008) *Piezoelectric transducers and applications*, 2nd Edition. Springer.

Asato, K. T., Cooper, R. A., Robertson, R. N. & Ster, J. F. (1993) SMART Wheels: development and testing of a system for measuring manual wheelchair propulsion dynamics. *Biomedical Engineering, IEEE Transactions on*, 40, 1320-1324.

Bacarin, T. A., Sacco, I. C. N. & Hennig, E. M. (2009) Plantar pressure distribution patterns during gait in diabetic neuropathy patients with a history of foot ulcers. *Clinics*, 64, 113-120.

Bader, D. L., Bouten, C. V. C., Colin, D. & Oomens, C. W. J. (2005) *Pressure Ulcer Research: Current and Future Perspectives*, Springer. p.276.

Barron, A. (2009) *Piezoelectric Materials Synthesis*. Connexions Web site. <http://cnx.org/content/m25441/1.2/>. [Accessed 12th January 2013]

Beccai, L., Roccella, S., Arena, A., Valvo, F., Valdastrì, P., Menciassi, A., Carrozza, M. C. & Dario, P. (2005) Design and fabrication of a hybrid silicon three-axial force sensor for biomechanical applications. *Sensors and Actuators A: Physical*, 120, 370-382.

Bennett, L., Kavner, D., Lee, B. K. & Trainor, F. A. (1979) Shear vs pressure as causative factors in skin blood flow occlusion. *Arch Phys Med Rehabil*, 60, 309-14.

Berme, N., Lawes, P., Solomonidis, S. & Paul, J. P. (1976) A shorter pylon transducer for measurement of prosthetic forces and moments during amputee gait. *Engineering in Medicine*, 4, 6-8.

Bertsch, C., Unger, H., Winkelmann, W. & Rosenbaum, D. (2004) Evaluation of early walking patterns from plantar pressure distribution measurements. First year results of 42 children. *Gait & Posture*, 19, 235-242.

Bhatt, T. & Pai, Y. C. (2009) Generalization of Gait Adaptation for Fall Prevention: From Moveable Platform to Slippery Floor. *J Neurophysiol*, 101, 948-957.

Birrell, S. A., Hooper, R. H. & Haslam, R. A. (2007) The effect of military load carriage on ground reaction forces. *Gait & Posture*, 26, 611-614.

Bisiaux, M. & Moretto, P. (2008) The effects of fatigue on plantar pressure distribution in walking. *Gait & Posture*, 28, 693-698.

Black, J., Baharestani, M., Cuddigan, J., Dorner, B., Edsberg, L., Langemo, D., Posthauer, M. E., Ratliff, C., Taler, G. & National Pressure Ulcer Advisory, P.

(2007) National Pressure Ulcer Advisory Panel's updated pressure ulcer staging system. *Urol Nurs*, 27, 144-50, 156.

Boffeli, T. J., Bean, J. K. & Natwick, J. R. (2002) Biomechanical abnormalities and ulcers of the great toe in patients with diabetes. *The Journal of Foot and Ankle Surgery*, 41, 359-364.

Bosch, K., Gerss, J. & Rosenbaum, D. (2007) Preliminary normative values for foot loading parameters of the developing child. *Gait & Posture*, 26, 238-247.

Boulton, A. J. M. (2006) The diabetic foot. *Medicine*, 34, 87-90.

Boulton, A. J. M., Vileikyte, L., Ragnarson-Tennvall, G. & Apelqvist, J. (2005) The global burden of diabetic foot disease. *The Lancet*, 366, 1719-1724.

Brand, P. (1991) The insensitve foot (including leprosy). In: Jahss MH, editor. *Disorders of the foot and ankle: Medical and surgical management*. 2nd Edition. Philadelphia. WB saunders, p2170-86.

Brown, W. T. (2001) *In the beginning : compelling evidence for creation and the flood*, Phoenix, Ariz., Center for Scientific Creation.

Buckle, P. & Fernandes, A. (1998) Mattress evaluation--assessment of contact pressure, comfort and discomfort. *Applied Ergonomics*, 29, 35-39.

Buften, M. J., Marklin, R. W., Nagurka, M. L. & Simoneau, G. G. (2006) Effect of keyswitch design of desktop and notebook keyboards related to key stiffness and typing force. *Ergonomics*, 49, 996 - 1012.

Bullimore, S. R. & Burn, J. F. (2007) Ability of the planar spring-mass model to predict mechanical parameters in running humans. *Journal of Theoretical Biology*, 248, 686-695.

Burns J, L. K., Ryan Mm, Crosbie J, Ouvrier RA (2007) Interventions for the prevention and treatment of pes cavus. *Cochrane Database of Systematic Reviews: Reviews 2007*.

Bus, S., Haspels, R., Van Schie, C. & Mooren, P. (2006) Biomechanical optimization of orthopedic footwear for diabetic patients using in-shoe plantar pressure measurement. *Gait & Posture*, 24, S84-S85.

Bus, S. A. & Lange, A. D. (2005) A comparison of the 1-step, 2-step, and 3-step protocols for obtaining barefoot plantar pressure data in the diabetic neuropathic foot. *Clinical biomechanics (Bristol, Avon)*, 20, 892-899.

Bus, S. A., Maas, M., De Lange, A., Michels, R. P. J. & Levi, M. (2005) Elevated plantar pressures in neuropathic diabetic patients with claw/hammer toe deformity. *Journal of Biomechanics*, 38, 1918-1925.

Bus, S. A., Van Deursen, R. W. M., Kanade, R. V., Wissink, M., Manning, E. A., Van Baal, J. G. & Harding, K. G. (2009) Plantar pressure relief in the diabetic foot using forefoot offloading shoes. *Gait & Posture*, 29, 618-622.

Calvert, P., Patra, P., Lo, T.-C., Chen, C. H., Sawhney, A. & Agrawal, A. (2007) Piezoresistive sensors for smart textiles. IN YOSEPH, B.-C. (Ed.). SPIE.

Campbell, T. E., Munro, B. J., Wallace, G. G. & Steele, J. R. (2007) Can fabric sensors monitor breast motion? *Journal of Biomechanics*, 40, 3056-3059.

Catalfamo, P., Moser, D., Ghoussayni, S. & Ewins, D. (2008) Detection of gait events using an F-Scan in-shoe pressure measurement system. *Gait & Posture*, 28, 420-426.

Cavanagh, P. R., Hewitt Jr, F. G. & Perry, J. E. (1992) In-shoe plantar pressure measurement: a review. *The Foot*, 2, 185-194.

Cavanagh, P. R., Ulbrecht, J. S. & Caputo, G. M. (2000) New developments in the biomechanics of the diabetic foot. *Diabetes/Metabolism Research and Reviews*, 16, S6-S10.

Ceyssens, F., Driesen, M., Wouters, K., Puers, R. & Leuven, K. U. (2008) A low-cost and highly integrated fiber optical pressure sensor system. *Sensors and Actuators A: Physical*, 145-146, 81-86.

Chang, W. L. & Seigreg, A. A. (1999) Prediction of ulcer formation on the skin. *Medical Hypotheses*, 53, 141-144.

Cheer, K., Shearman, C. & Jude, E. B. (2009) Managing complications of the diabetic foot. *BMJ*, 339.

Chen, L. R., Chen, K. H. & Yang, S. W. (2007) The Biomechanical Effects of Insole for Pes Cavus. *Journal of Biomechanics*, 40, S709.

Chen, W.-M., Vee-Sin Lee, P., Park, S.-B., Lee, S.-J., Phyu Wui Shim, V. & Lee, T. (2010) A novel gait platform to measure isolated plantar metatarsal forces during walking. *Journal of Biomechanics*.

Chen, W.-P., Ju, C.-W. & Tang, F.-T. (2003) Effects of total contact insoles on the plantar stress redistribution: a finite element analysis. *Clinical Biomechanics*, 18, S17-S24.

-
- Chesnin, K. J., Selby-Silverstein, L. & Besser, M. P. (2000) Comparison of an in-shoe pressure measurement device to a force plate: concurrent validity of center of pressure measurements. *Gait & Posture*, 12, 128-133.
- Chevalier, T. L., Hodgins, H. & Chockalingam, N. (2010) Plantar pressure measurements using an in-shoe system and a pressure platform: A comparison. *Gait & Posture*, 31, 397-399.
- Chi, Z. & Shida, K. (2004) A new multifunctional tactile sensor for three-dimensional force measurement. *Sensors and Actuators A: Physical*, 111, 172-179.
- Chiou, J. A., Chen, S. & Jiao, J. (2003) Humidity-Induced Voltage Shift on MEMS Pressure Sensors. *Journal of Electronic Packaging*, 125, 470-474.
- Chiu, H.-T. & Shiang, T.-Y. (2007) Effects of Insoles and Additional Shock Absorption Foam on the Cushioning Properties of Sport Shoes. *Journal of Applied Biomechanics*, 23, 119-127.
- Christ, P., Gender, M. & Seitz, P. (1998) A 3-D pressure distribution measuring platform with 8x8 sensors for simultaneous measurement of vertical and horizontal forces. VI EMED Scientific Meeting. Brisbane.
- Chu, Z., Sarro, P. M. & Middelhoek, S. (1996) Silicon three-axial tactile sensor. *Sensors and Actuators A: Physical*, 54, 505-510.
- Clark, M. & Rowland, L. B. (1989) Comparison of contact pressures measured at the sacrum of young and elderly subjects. *Journal of Biomedical Engineering*, 11, 197-199.
- Clark, R. A., Bryant, A. L., Pua, Y., Mccrory, P., Bennell, K. & Hunt, M. (2010) Validity and reliability of the Nintendo Wii Balance Board for assessment of standing balance. *Gait & Posture*, 31, 307-310.
- Clayton, W. & Elasy, T. A. (2009) A Review of the Pathophysiology, Classification, and Treatment of Foot Ulcers in Diabetic Patients. *Clinical Diabetes*, 27, 52-58.
- Clijnen, J., Reynaerts, D. & Van Brussel, H. (2003a) Design of an optical tri-axial force sensor. IN BAR-COHEN, Y. (Ed.) SPIE Conference.
- Clijnen, J., Reynaerts, D. & Van Brussel, H. (2003b) Development of a miniature optical tri-axial force sensor. Euroensors XVII, the European Conference on Solid-State Transducers. Guimaraes, Portugal
- Cobb, J. & Claremont, D. (1995) Transducers for foot pressure measurement: survey of recent developments. *Medical and Biological Engineering and Computing*, 33, 525-532.

Colin E. Thomson, J. N. A. G. (2002) 50 foot challenges: assessment and management, Elsevier Health Sciences, 2002.

Cong, Y., Tak-Man Cheung, J., Leung, A. K. L. & Zhang, M. (2011) Effect of heel height on in-shoe localized triaxial stresses. *Journal of Biomechanics*, 44, 2267-2272.

Cooper, R. C., Prebeau-Menezes, L. M., Butcher, M. T. & Bertram, J. E. A. (2008) Step length and required friction in walking. *Gait & Posture*, 27, 547-551.

Cranny, A., Cotton, D. P. J., Chappell, P. H., Beeby, S. P. & White, N. M. (2005) Thick-film force and slip sensors for a prosthetic hand. *Sensors and Actuators A: Physical*, 123-124, 162-171.

Crosbie, J. & Burns, J. (2008) Are in-shoe pressure characteristics in symptomatic idiopathic pes cavus related to the location of foot pain? *Gait & Posture*, 27, 16-22.

Cruickshank, A., Urry, S. & Smeathers, J. (2007) The effect of running on in-shoe temperature and humidity. *Journal of Science and Medicine in Sport*, 10, Supplement 1, 44.

D. Stephensen, W. D., M. Winter, O. Scott, (2009) Comparison of biomechanical gait parameters of young children with haemophilia and those of age-matched peers. *Haemophilia*, 15, 509-518.

Dai, X.-Q., Li, Y., Zhang, M. & Cheung, J. T.-M. (2006) Effect of sock on biomechanical responses of foot during walking. *Clinical Biomechanics*, 21, 314-321.

Davis, B. L. (2010) A Device for Simultaneous Measurement of Pressure and Shear Force Distribution on the Plantar Surface of the Foot. [Accessed 28th Feb 2010] www.lerner.ccf.org/bme/davis/lab/simultaneous_measurement_device.php

Davis, B. L., Cothren, R. M., Quesada, P., Hanson, S. B. & Perry, J. E. (1996) Frequency content of normal and diabetic plantar pressure profiles: Implications for the selection of transducer sizes. *Journal of Biomechanics*, 29, 979-983.

Davis, B. L., Perry, J. E., Neth, D. C. & Waters, K. C. (1998) A Device for Simultaneous Measurement of Pressure and Shear Force Distribution on the Plantar Surface of the Foot. *Journal of Applied Biomechanics*, 14, 93-104.

Davis, W., Norman, P., Bruce, D. & Davis, T. (2006) Predictors, consequences and costs of diabetes-related lower extremity amputation complicating type 2 diabetes: The Fremantle Diabetes Study. *Diabetologia*, 49, 2634-2641.

DCCT (1993) Diabetes Control and Complications Trial Research Group. The Effect of Intensive Treatment of Diabetes on the Development and Progression of Long-

Term Complications in Insulin-Dependent Diabetes Mellitus. *New England Journal of Medicine*, 329, 977-986.

Dechwayukul, C. & Thongruang, W. (2008) Compressive modulus of adhesive bonded rubber block. *Songklanakarin Journal of Science and Technology*, 30, 221-225.

Del Maestro, M., Cecchi, F., Serio, S. M., Laschi, C. & Dario, P. (2011) Sensing device for measuring infants' grasping actions. *Sensors and Actuators A: Physical*, 165, 155-163.

Dietz, P., Yerazunis, W. & Leigh, D. (2003) Very Low-Cost Sensing and Communication Using Bidirectional LEDs. *UbiComp 2003: Ubiquitous Computing*.

Dillingham, T. R., Pezzin, L. E. & Shore, A. D. (2005) Reamputation, mortality, and health care costs among persons with dysvascular lower-limb amputations. *Archives of Physical Medicine and Rehabilitation*, 86, 480-486.

Drerup, B., Szczepaniak, A. & Wetz, H. H. (2008) Plantar pressure reduction in step-to gait: A biomechanical investigation and clinical feasibility study. *Clinical Biomechanics*, 23, 1073-1079.

Dytran.com (2011) Piezoelectric Measurement System Comparison: Charge Mode vs. Low Impedance Voltage Mode (LIVM). Dytran Instruments Inc. [Accessed 20th January 2013]. Available at <http://www.dytran.com/go.cfm/en-us/content/tech-education>.

Eils, E., Nolte, S., Tewes, M., Thorwesten, L., Volker, K. & Rosenbaum, D. (2002) Modified pressure distribution patterns in walking following reduction of plantar sensation. *Journal of Biomechanics*, 35, 1307-1313.

Elissa Krakauer, P. L., Daniel Schmitt, (2002) Hand and body position during locomotor behavior in the aye-aye (*Daubentonia madagascariensis*). *American Journal of Primatology*, 57, 105-118.

Elvin, N. G., Elvin, A. A. & Arnoczky, S. P. (2007) Correlation Between Ground Reaction Force and Tibial Acceleration in Vertical Jumping. *Journal of Applied Biomechanics*, 23, 180-189.

Faber, G. S., Kingma, I., Martin Schepers, H., Veltink, P. H. & Van Dieën, J. H. (2010) Determination of joint moments with instrumented force shoes in a variety of tasks. *Journal of Biomechanics*, 43, 2848-2854.

Fernandes, C. P., Glantz, P.-O. J., Svensson, S. A. & Bergmark, A. (2003) A novel sensor for bite force determinations. *Dental Materials*, 19, 118-126.

Fong, D. T.-P., Chan, Y.-Y., Hong, Y., Yung, P. S.-H., Fung, K.-Y. & Chan, K.-M. (2008) Estimating the complete ground reaction forces with pressure insoles in walking. *Journal of Biomechanics*, 41, 2597-2601.

Frykberg, R. G. (1998) Diabetic foot ulcers: Current concepts. *The Journal of Foot and Ankle Surgery*, 37, 440-446.

Frykberg, R. G., Lavery, L. A., Pham, H., Harvey, C., Harkless, L. & Veves, A. (1998) Role of neuropathy and high foot pressures in diabetic foot ulceration. *Diabetes Care*, 21, 1714-1719.

Frykberg, R. G., Zgonis, T., Armstrong, D. G., Driver, V. R., Giurini, J. M., Kravitz, S. R., Landsman, A. S., Lavery, L. A., Moore, J. C., Schuberth, J. M., Wukich, D. K., Andersen, C. & Vanore, J. V. (2006) Diabetic Foot Disorders: A Clinical Practice Guideline (2006 Revision). *The Journal of Foot and Ankle Surgery*, 45, S1-S66.

Gabriel, R., Monteiro, M., Moreira, H. & Maia, M. (2008) Contribution of plantar pressure to the prevention and quantification of the muscle-skeletal injury risk in hiking trails - a pilot study. *Acta Bioeng Biomech*, 10, 51-4.

Garshelis, I. J. & Tollens, S. P. L. (2010) A magnetoelastic force transducer based on bending a circumferentially magnetized tube. *Journal of Applied Physics*, 107, 09E719.

Gary William Richards, S. K. C., Aurel Vincent Stan (2003) Triaxial force pin sensor array. United States, The Goodyear Tire & Rubber Company. US Patent US006536292B1.

Gautschi, G. (2002) Piezoelectric sensorics: force, strain, pressure, acceleration and acoustic emission sensors, materials and amplifiers, Springer.

Gefen, A. (2007) Pressure-Sensing Devices for Assessment of Soft Tissue Loading Under Bony Prominences: Technological Concepts and Clinical Utilization. *Wounds*, 19, 350-362.

Gefen, A., Megido-Ravid, M., Itzchak, Y. & Arcan, M. (2000) Biomechanical Analysis of the Three-Dimensional Foot Structure During Gait: A Basic Tool for Clinical Applications. *Journal of Biomechanical Engineering*, 122, 630-639.

Giacomozzi, C. (2010) Appropriateness of plantar pressure measurement devices: A comparative technical assessment. *Gait & Posture*, 32, 141-144.

Giacomozzi, C. & Macellari, V. (1997) Piezo-dynamometric platform for a more complete analysis of foot-to-floor interaction. *Rehabilitation Engineering, IEEE Transactions on*, 5, 322-330.

Giacomozzi, C., Macellari, V., Leardini, A. & Benedetti, M. (2000) Integrated pressure-force-kinematics measuring system for the characterisation of plantar foot loading during locomotion. *Medical and Biological Engineering and Computing*, 38, 156-163.

Giacomozzi, C., Sawacha, Z., Uccioli, L., D'ambrogi, E., Avogaro, A. & Cobelli, C. (2008) The role of shear stress in the aetiology of diabetic neuropathic foot ulcers. *Journal of Foot and Ankle Research*, 1, O3.

Goldstein, B. & Sanders, J. (1998) Skin response to repetitive mechanical stress: A new experimental model in pig. *Archives of Physical Medicine and Rehabilitation*, 79, 265-272.

Goossens, R. H. M., Snijders, C. J., Hoek Van Dijke, G. A. & Den Ouden, A. H. (1993) A new instrument for the measurement of forces on beds and seats. *Journal of Biomedical Engineering*, 15, 409-412.

Goossens, R. H. M., Zegers, R., Van Dijke, G. A. H. & Snijders, C. J. (1994) Influence of shear on skin oxygen tension. *Clinical Physiology*, 14, 111-118.

Gordois, A., Scuffham, P., Shearer, A., Oglesby, A. & Tobian, J. A. (2003) The Health Care Costs of Diabetic Peripheral Neuropathy in the UK. *Diabetes Care*, 26, 1790-1795.

Graeme, J. G. (1995) Photodiode amplifiers: op amp solutions. 1st Edition.

Guinta, S. (1996) Capacitance and capacitors (Ask the applications engineer - 21). 30.

Guldmond, N. A., Leffers, P., Sanders, A. P., Schaper, N. C., Nieman, F. & Walenkamp, G. H. I. M. (2007a) Daily-life activities and in-shoe forefoot plantar pressure in patients with diabetes. *Diabetes Research and Clinical Practice*, 77, 203-209.

Guldmond, N. A., Leffers, P., Schaper, N. C., Sanders, A. P., Nieman, F., Willems, P. & Walenkamp, G. H. I. M. (2007b) The effects of insole configurations on forefoot plantar pressure and walking convenience in diabetic patients with neuropathic feet. *Clinical Biomechanics*, 22, 81-87.

Gurney, J. K., Kersting, U. G. & Rosenbaum, D. (2008) Between-day reliability of repeated plantar pressure distribution measurements in a normal population. *Gait & Posture*, 27, 706-709.

Guyton, G. P. & Saltzman, C. L. (2001) The Diabetic Foot : Basic Mechanisms of Disease. *J Bone Joint Surg Am*, 83, 1083-1096.

Hachisuka, K., Takahashi, M., Ogata, H., Ohmine, S., Shitama, H. & Shinkoda, K. (1998) Properties of the flexible pressure sensor under laboratory conditions simulating the internal environment of the total surface bearing socket. *Prosthetics and Orthotics International*, 22, 186-192.

Hall, M. G., Fleming, H. E., Dolan, M. J., Millbank, S. F. D. & Paul, J. P. (1996) Static in situ calibration of force plates. *Journal of Biomechanics*, 29, 659-665.

Hall, R. S., Desmoulin, G. T. & Milner, T. E. (2008) A technique for conditioning and calibrating force-sensing resistors for repeatable and reliable measurement of compressive force. *Journal of Biomechanics*, 41, 3492-3495.

Harris, G. F., Acharya, K. R. & Bachschmidt, R. A. (1996) Investigation of spectral content from discrete plantar areas during adult gait: an expansion of rehabilitation technology. *Rehabilitation Engineering, IEEE Transactions on*, 4, 360-374.

Hayes, A. & Seitz, P. (1997) The average pressure distribution of the diabetic foot: Can it be used as a clinical diagnostic aid? *Clinical Biomechanics*, 12, S3-S4.

HBM (2010) Piezoelectric force transducer: 5 rules for installation and mounting. HBM, Darmstadt, Germany. [Accessed 20th January 2013]. Available at <http://www.hbm.com/en/menu/tips-tricks/force-measurement/piezoelectric-force-transducer-5-rules-for-installation-and-mounting/>

Hennig, E. M. & Milani, T. L. (1995) In-shoe pressure distribution for running in various types of footwear. *Journal of Applied Biomechanics*, 11, 299-310.

Heo, J.-S., Chung, J.-H. & Lee, J.-J. (2006) Tactile sensor arrays using fiber Bragg grating sensors. *Sensors and Actuators A: Physical*, 126, 312-327.

Heywood, E. J., Jeutter, D. C. & Harris, G. F. (2004) Tri-axial plantar pressure sensor: design, calibration and characterization. *Engineering in Medicine and Biology Society, 2004. IEMBS '04. 26th Annual International Conference of the IEEE*.

Hirose, S. & Yoneda, K. (1990) Development of optical six-axial force sensor and its signal calibration considering nonlinear interference. *Robotics and Automation, 1990. Proceedings., 1990 IEEE International Conference on*.

Hoiting, G. J. (2005) Measuring MRI noise. (Chapter 8: Considerations in laser Doppler interferometry of MR scanner bore vibrations). University of Groningen.

Honeywell-Inc. (2011a) Hall effect sensing and application. Honeywell Sensing and Control, MN 55422. [Accessed 20th January 2013]. Available at: sensing.honeywell.com/index.php?ci_id=47847

Honeywell-Inc. (2011b) Magnetoresistive Sensors Industry: Position and solid state sensing., Honeywell Sensing and Control. [Accessed 20th January 2013]. Available at: sensing.honeywell.com/index.php?ci_id=50272

Hosein, R. & Lord, M. (2000) A study of in-shoe plantar shear in normals. *Clinical Biomechanics*, 15, 46-53.

Hsiao, H., Guan, J. & Weatherly, M. (2002) Accuracy and precision of two in-shoe pressure measurement systems. *Ergonomics*, 45, 537-555.

Huang, C.-T., Shen, C.-L., Tang, C.-F. & Chang, S.-H. (2008a) A wearable yarn-based piezo-resistive sensor. *Sensors and Actuators A: Physical*, 141, 396-403.

Huang, C.-T., Tang, C.-F., Lee, M.-C. & Chang, S.-H. (2008b) Parametric design of yarn-based piezoresistive sensors for smart textiles. *Sensors and Actuators A: Physical*, 148, 10-15.

Huang, Y.-M., Tsai, N.-C. & Lai, J.-Y. (2010) Development of tactile sensors for simultaneous, detection of normal and shear stresses. *Sensors and Actuators A: Physical*, 159, 189-195.

Hughes, R., Rowlands, H. & Mcmeekin, S. (2000) A laser plantar pressure sensor for the diabetic foot. *Medical Engineering & Physics*, 22, 149-154.

Hurkmans, H. L. P., Bussmann, J. B. J., Benda, E., Verhaar, J. A. N. & Stam, H. J. (2006) Accuracy and repeatability of the Pedar Mobile system in long-term vertical force measurements. *Gait & Posture*, 23, 118-125.

Jeffcoate, W. J. & Harding, K. G. (2003) Diabetic foot ulcers. *The Lancet*, 361, 1545-1551.

Jin, W. L. & Mote, J. C. D. (1998) Development and calibration of a sub-millimeter three-component force sensor. *Sensors and Actuators A: Physical*, 65, 89-94.

Johnston, T. E., Prosser, L. A. & Lee, S. C. K. (2008) Differences in pedal forces during recumbent cycling in adolescents with and without cerebral palsy. *Clinical Biomechanics*, 23, 248-251.

Kanda, Y. & Yasukawa, A. (1981) Hall-effect devices as strain and pressure sensors. *Sensors and Actuators*, 2, 283-296.

Karki, J. (2000) Signal conditioning piezoelectric sensors. Texas Instruments: Application Report SLOA033A - September 2000. [Accessed 20th January 2013]. <http://www.ti.com/lit/an/sloa033a/sloa033a.pdf>

Kärki, S., Lekkala, J., Kuokkanen, H. & Halttunen, J. (2009) Development of a piezoelectric polymer film sensor for plantar normal and shear stress measurements. *Sensors and Actuators A: Physical*, 154, 57-64.

Katragadda, R. B. & Xu, Y. (2008) A novel intelligent textile technology based on silicon flexible skins. *Sensors and Actuators A: Physical*, 143, 169-174.

Keekyoung, K., Yu, S., Richard, M. V. & Bradley, J. N. (2007) Calibration of Multi-Axis MEMS Force Sensors Using the Shape-From-Motion Method. *Sensors Journal, IEEE*, 7, 344-351.

Keller, T. S., Weisberger, A. M., Ray, J. L., Hasan, S. S., Shiavi, R. G. & Spengler, D. M. (1996) Relationship between vertical ground reaction force and speed during walking, slow jogging, and running. *Clinical Biomechanics*, 11, 253-259.

Kengne, A. P., Djouogo, C. F. T., Dehayem, M. Y., Fezeu, L., Sobngwi, E., Lekoubou, A. & Mbanya, J.-C. (2009) Admission Trends Over 8 Years for Diabetic Foot Ulceration in a Specialized Diabetes Unit in Cameroon. *The International Journal of Lower Extremity Wounds*, 8, 180-186.

Kim, G.S. (2007a) Design of a six-axis wrist force/moment sensor using FEM and its fabrication for an intelligent robot. *Sensors and Actuators A: Physical*, 133, 27-34.

Kim, G.S. (2007b) Development of a three-axis gripper force sensor and the intelligent gripper using it. *Sensors and Actuators A: Physical*, 137, 213-222.

Kim, G.S., Kang, D.I. & Rhee, S.H. (1999) Design and fabrication of a six-component force/moment sensor. *Sensors and Actuators A: Physical*, 77, 209-220.

Kim, G.S., Shin, H. J. & Yoon, J. (2008) Development of 6-axis force/moment sensor for a humanoid robot's intelligent foot. *Sensors and Actuators A: Physical*, 141, 276-281.

Kim Le, P. (2008) Methods to correct for creep in elastomer-based sensors. *Sensors*, 2008 IEEE 26-29 Oct. 2008.

Kim, R.-H., Kim, D.-H., Xiao, J., Kim, B. H., Park, S.-I., Panilaitis, B., Ghaffari, R., Yao, J., Li, M., Liu, Z., Malyarchuk, V., Kim, D. G., Le, A.-P., Nuzzo, R. G., Kaplan, D. L., Omenetto, F. G., Huang, Y., Kang, Z. & Rogers, J. A. (2010) Waterproof AlInGaP optoelectronics on stretchable substrates with applications in biomedicine and robotics. *Nat Mater*, 9, 929-937.

Kirtley, C. (2005) Resolution of Forces, Friction, and the ground reaction vector. [Online]. [Accessed on 11 August 2011] Available from: <http://www.clinicalgaitanalysis.com/teach-in/friction.html>.

Kistler.com (2010) The Piezoelectric Effect. Kistler Holding AG. [Online]. [Accessed 17 March 2011] Available from: http://www.kistler.com/gb_en-gb/Technology_Piezoelectric/The-Piezoelectric-Effect.html.

Koh, C. G. & Kelly, J. M. (1989) Compression stiffness of bonded square layers of nearly incompressible material. *Engineering Structures*, 11, 9-15.

Kong, P. W. & De Heer, H. (2009) Wearing the F-Scan mobile in-shoe pressure measurement system alters gait characteristics during running. *Gait & Posture*, 29, 143-145.

Kram, R., Griffin, T. M., Donelan, J. M. & Chang, Y. H. (1998) Force treadmill for measuring vertical and horizontal ground reaction forces. *J Appl Physiol*, 85, 764-769.

Kreuzer, M. (2007) Strain measurement with fiber bragg grating sensors. (White Paper). HBM, Darmstadt, Germany.

Kuphaldt, T. R. (2002) Practical AC Circuits. [Accessed 20th January 2013] Available from: <http://openbookproject.net/electricCircuits/>.

Laing, P., Deogan, H., Cogley, D., Crerand, S., Hammond, P. & Klenerman, L. (1992) The development of the low profile Liverpool shear transducer. *Clinical Physics and Physiological Measurement*, 13, 115-124.

Lau, H. C., Stansfield, B., Solomonidis, S., Wearing, S. & Pepper, M. (2008) Time dependent characteristics of the "Kent" triaxial force transducer system for in-shoe load distribution measurement. XI EMED Scientific Meeting ESM. Dundee, Scotland.

Lau, H. C., Stansfield, B., Wearing, S., Solomonidis, S. & Spence, W. (2009) A low-cost tri-axial load sensor system: design, characteristics and its potentials. XXII Congress of the International Society of Biomechanics (ISB2009). Cape Town.

Lau, H. C., Stansfield, B., Wearing, S., Solomonidis, S. & Spence, W. (2010a) Low-cost shear stress distribution measurement: is it possible? 6th World Congress on Biomechanics (WCB2010). Singapore.

Lau, H. C., Wearing, S., Stansfield, B., Solomonidis, S. & Spence, W. (2010b) Low-cost bi-axial shear stress transducer: a step closer to shear distribution measurement. 2nd congress of the International Foot and Ankle Biomechanics Community (i-FAB 2010). Seattle, USA.

Lavery, L. A., Armstrong, D. G., Wunderlich, R. P., Tredwell, J. & Boulton, A. J. M. (2003) Predictive Value of Foot Pressure Assessment as Part of a Population-Based Diabetes Disease Management Program. *Diabetes Care*, 26, 1069-1073.

Lavery, L. A., Lanctot, D. R., Constantinides, G., Zamorano, R. G., Athanasiou, K. A. & Agrawal, C. M. (2005) Wear and Biomechanical Characteristics of a Novel Shear-Reducing Insole with Implications for High-Risk Persons with Diabetes. *Diabetes Technology & Therapeutics*, 7, 638-646.

Lebar, A. M., Harris, G. F., Wertsch, J. J. & Hongsheng, Z. (1996) An optoelectric plantar "shear" sensing transducer: design, validation, and preliminary subject tests. *Rehabilitation Engineering, IEEE Transactions on*, 4, 310-319.

Lee, M. (2006) Design Article: The art of capacitive touch sensing. Cypress Semiconductor Corp. [Online]. [Accessed 20th January 2013] Available from: http://www.planetanalog.com/document.asp?doc_id=527410.

Levy, M. J. & Valabhji, J. (2004) The diabetic foot. *Surgery (Oxford)*, 22, 338-341.

Levy, M. J. & Valabhji, J. (2008) The diabetic foot. *Surgery (Oxford)*, 26, 25-28.

Leymarie, F., Richard, J. L. & Malgrange, D. (2005) Factors associated with diabetic patients at high risk for foot ulceration. *Diabetes & Metabolism*, 31, 603-605.

Li, Y.J., Sun, B.Y., Zhang, J., Qian, M. & Jia, Z.Y. (2009a) A novel parallel piezoelectric six-axis heavy force/torque sensor. *Measurement*, 42, 730-736.

Li, Y.J., Zhang, J., Jia, Z.Y. & Qian, M. (2009b) A novel piezoelectric 6-component heavy force/moment sensor for huge heavy-load manipulator's gripper. *Mechanical Systems and Signal Processing*, 23, 1644-1651.

Li, Y.J., Zhang, J., Jia, Z.Y., Qian, M. & Li, H. (2009c) Research on force-sensing element's spatial arrangement of piezoelectric six-component force/torque sensor. *Mechanical Systems and Signal Processing*, 23, 2687-2698.

Li, Y., Cheng, X. Y., Leung, M. Y., Tsang, J., Tao, X. M. & Yuen, M. C. W. (2005) A flexible strain sensor from polypyrrole-coated fabrics. *Synthetic Metals*, 155, 89-94.

Liedtke, C., Fokkenrood, S. A. W., Menger, J.T., Van Der Kooij, H. & Veltink, P.H. (2007) Evaluation of instrumented shoes for ambulatory assessment of ground reaction forces. *Gait & Posture*, 26, 39-47.

Lin, W. & Beebe, D. J. (2002) Characterization of a silicon-based shear-force sensor on human subjects. *Biomedical Engineering, IEEE Transactions on*, 49, 1340-1347.

Lingard, R. (2009) Lifetime of white LEDs (Building Technologies Program). U.S. Department of Energy. [Accessed 20th January 2013] Available from http://apps1.eere.energy.gov/buildings/publications/pdfs/ssl/lifetime_white_leds.pdf

-
- Liu, J. Z., Dai, T. H., Elster, T. H., Sahgal, V., Brown, R. W. & Yue, G. H. (2000) Simultaneous measurement of human joint force, surface electromyograms, and functional MRI-measured brain activation. *Journal of Neuroscience Methods*, 101, 49-57.
- Long, J. T., Klein, J. P., Sirota, N. M., Wertsch, J. J., Janisse, D. & Harris, G. F. (2007) Biomechanics of the double rocker sole shoe: Gait kinematics and kinetics. *Journal of Biomechanics*, 40, 2882-2890.
- Lord, M. (1997) Spatial resolution in plantar pressure measurement. *Medical Engineering & Physics*, 19, 140-144.
- Lord, M. & Hosein, R. (2000) A study of in-shoe plantar shear in patients with diabetic neuropathy. *Clinical Biomechanics*, 15, 278-283.
- Lord, M., Hosein, R. & Williams, R. B. (1992) Method for in-shoe shear stress measurement. *Journal of Biomedical Engineering*, 14, 181-186.
- Lord, M. & Smith, D. M. (1983) Static response of a simple piezoelectric load cell. *Journal of Biomedical Engineering*, 5, 162-164.
- Lott, D. J., Hastings, M. K., Commean, P. K., Smith, K. E. & Mueller, M. J. (2007) Effect of footwear and orthotic devices on stress reduction and soft tissue strain of the neuropathic foot. *Clinical Biomechanics*, 22, 352-359.
- Lott, D. J., Zou, D. & Mueller, M. J. (2008) Pressure gradient and subsurface shear stress on the neuropathic forefoot. *Clinical Biomechanics*, 23, 342-348.
- Low, D. C. & Dixon, S. J. (2010) Footscan pressure insoles: Accuracy and reliability of force and pressure measurements in running. *Gait & Posture*, 32, 664-666.
- Lowe, M., Hood, E. & Ozog, M. (2007) Thin-film force sensors: opening doors in automated systems. *Sensor Review*, 27, 99-102.
- Lu, T.-F., Lin, G. C. I. & He, J. R. (1997) Neural-network-based 3D force/torque sensor calibration for robot applications. *Engineering Applications of Artificial Intelligence*, 10, 87-97.
- Macellari, V. & Giacomozzi, C. (1996) Multistep pressure platform as a stand-alone system for gait assessment. *Medical and Biological Engineering and Computing*, 34, 299-304.
- Mack, O. (2007) Investigations of piezoelectric force measuring devices for use in legal weighing metrology. *Measurement*, 40, 746-753.
- Mackenzie, I. C. (1974) The effects of frictional stimulation on mouse ear epidermis. *J Investig Dermatol*, 63, 194-198.

Mackey, J. R. & Davis, B. L. (2006) Simultaneous shear and pressure sensor array for assessing pressure and shear at foot/ground interface. *Journal of Biomechanics*, 39, 2893-2897.

Maetzler, M., Bochdansky, T. & Abboud, R. J. (2010) Normal pressure values and repeatability of the Emed® ST2 system. *Gait & Posture*, 32, 391-394.

Magnissalis, E. A., Karagiannopoulos, L. E., Solomonidis, S. E., Spence, W. D. & Paul, J. P. (1992) Biomechanical analysis of lower limb prosthetic systems. *Experimental Mechanics*, 377-387.

Maluf, K. S. & Mueller, M. J. (2003) Comparison of physical activity and cumulative plantar tissue stress among subjects with and without diabetes mellitus and a history of recurrent plantar ulcers. *Clinical Biomechanics*, 18, 567-575.

Martínez-Nova, A., Cuevas-García, J. C., Pascual-Huerta, J. & Sánchez-Rodríguez, R. (2007) BioFoot® in-shoe system: Normal values and assessment of the reliability and repeatability. *The Foot*, 17, 190-196.

Martínez-Nova, A., Sánchez-Rodríguez, R., Pérez-Soriano, P., Llana-Belloch, S., Leal-Muro, A. & Pedrera-Zamorano, J. D. (2010) Plantar pressures determinants in mild Hallux Valgus. *Gait & Posture*, 32, 425-427.

Mcalpine, R. R., Morris, A. D., Emslie-Smith, A., James, P. & Evans, J. M. M. (2005) The annual incidence of diabetic complications in a population of patients with Type 1 and Type 2 diabetes. *Diabetic Medicine*, 22, 348-352.

Ming, Z. & Roberts, V. C. (1993) The effect of shear forces externally applied to skin surface on underlying tissues. *Journal of Biomedical Engineering*, 15, 451-456.

Mott, P. H. & Roland, C. M. (2001) Aging of Natural Rubber in Air and Seawater, RUBDIV. [Accessed 20th January 2013] Available from http://www.polymerphysics.net/pdf/RubberChemTech_74_79_01.pdf

Moulik, P. K., Mtonga, R. & Gill, G. V. (2003) Amputation and Mortality in New-Onset Diabetic Foot Ulcers Stratified by Etiology. *Diabetes Care*, 26, 491-494.

Nanoident Technologies AG (2006) Austrian ultra-thin organic fingerprint sensor launches. *Biometric Technology Today*, 14, 4-5.

National Physical Laboratory (2010) How many different types of force transducer are there? (FAQ - Force). [Accessed 20th January 2013] Available from [http://www.npl.co.uk/reference/faqs/how-many-different-types-of-force-transducer-are-there-\(faq-force\)](http://www.npl.co.uk/reference/faqs/how-many-different-types-of-force-transducer-are-there-(faq-force))

Nevill, A., Pepper, M. & Whiting, M. (1995) In-shoe foot pressure measurement system utilising piezoelectric film transducers. *Medical and Biological Engineering and Computing*, 33, 76-81.

NHMRC (2005) National Evidence Based Guidelines for the Management of Type 2 Diabetes Mellitus (2001): Part 6 Detection and Prevention of Foot Problems in Type 2 Diabetes (last updated 2005). National Health and Medical Research Council, Australian Government.

NHS (2011) Scottish Diabetes Survey 2011. Scottish Diabetes Survey Monitoring Group. NHS Scotland. [Accessed 20th January 2013] Available from <http://www.diabetesinscotland.org.uk/Publications/SDS%202011.pdf>

Nicolopoulos, C. S., Anderson, E. G., Solomonidis, S. E. & Giannoudis, P. V. (2000) Evaluation of the gait analysis FSCAN pressure system: clinical tool or toy? *The Foot*, 10, 124-130.

Nilsson, J. & Thorstensson, A. (1989) Ground reaction forces at different speeds of human walking and running. *Acta Physiologica Scandinavica*, 136, 217-227.

Noda, K., Hoshino, K., Matsumoto, K. & Shimoyama, I. (2006) A shear stress sensor for tactile sensing with the piezoresistive cantilever standing in elastic material. *Sensors and Actuators A: Physical*, 127, 295-301.

Oddo, C. M., Valdastrri, P., Beccai, L., Roccella, S., Carrozza, M. C. & Dario, P. (2007) Investigation on calibration methods for multi-axis, linear and redundant force sensors. *Measurement Science and Technology*, 623.

Orlin, M. N. & Mcpoil, T. G. (2000) Plantar Pressure Assessment. *PHYS THER*, 80, 399-409.

OSI Optoelectronics Inc. (2010) Position sensing detectors and photodiodes, general discussion. OSI Optoelectronics Inc. - Application Notes. [Accessed 20th January 2013] Available from <http://www.osioptoelectronics.com/application-notes/AN-Position-Sensing-Photodiodes.pdf>

Owings, T. M., Apelqvist, J., Stenström, A., Becker, M., Bus, S. A., Kalpen, A., Ulbrecht, J. S. & Cavanagh, P. R. (2009) Plantar pressures in diabetic patients with foot ulcers which have remained healed. *Diabetic Medicine*, 26, 1141-1146.

Pacific Silicon Sensor Inc. (2009) Pacific Silicone Sensor Q Series Data Sheet, High Voltage Quad Sum and Differences Amplifier (Part Description QP45-Q-HVSD).

Palmer, J. D., Burke, G. E., O'leary, J. P., Freed, M. & Krusen, F. H. (1968) Ulcer formation: role of pressure and shear. 5th International Congress of Physical Medicine. Montreal.

Parish, L. C., Lowthian, P. & Witkowski, J. A. (2007) The decubitus ulcer: many questions but few definitive answers. *Clinics in Dermatology*, 25, 101-108.

Park, Y.-K., Kumme, R. & Kang, D.-I. (2002) Dynamic investigation of a three-component force-moment sensor. *Measurement Science and Technology*, 654.

Parvataneni, K., Ploeg, L., Olney, S. J. & Brouwer, B. (2009) Kinematic, kinetic and metabolic parameters of treadmill versus overground walking in healthy older adults. *Clinical Biomechanics*, 24, 95-100.

Pataky, T. C. (2012) Spatial resolution in plantar pressure measurement revisited. *Journal of Biomechanics*, 45, 2116-2124.

Pataky, Z., Assal, J.-P., Conne, P., Vuagnat, H. & Golay, A. (2005) Plantar pressure distribution in Type2 diabetic patients without peripheral neuropathy and peripheral vascular disease. *Diabetic Medicine*, 22, 762-767.

PCB Piezotronics (2010) Signal conditioning basics for ICP & charge output sensors. [Accessed 20th January 2013] Available from http://www.pcb.com/TechSupport/tech_signal

Perry, J. E., Hall, J. O. & Davis, B. L. (2002) Simultaneous measurement of plantar pressure and shear forces in diabetic individuals. *Gait & Posture*, 15, 101-107.

Petre, M., Erdemir, A. & Cavanagh, P. R. (2008) An MRI-compatible foot-loading device for assessment of internal tissue deformation. *Journal of Biomechanics*, 41, 470-474.

Pinarbasi, S., Akyuz, U. & Mengi, Y. (2006) A new formulation for the analysis of elastic layers bonded to rigid surfaces. *International Journal of Solids and Structures*, 43, 4271-4296.

Pinzur, M. S. (2004) Diabetic Foot. *eMedicine*. [Accessed 20th January 2013] Available from <http://emedicine.medscape.com/article/237378-overview>

Prosser, L. A., Stanley, C. J., Norman, T. L., Park, H. S. & Damiano, D. L. (2011) Comparison of elliptical training, stationary cycling, treadmill walking and overground walking. Electromyographic patterns. *Gait & Posture*, 33, 244-250.

Razian, M. A. (2000) A miniature piezoelectric tri-axial force transducer and a novel charge multiplexing technique for biomedical applications (gait analysis). Department of Eletronics. Canterbury, University of Kent.

Razian, M. A. & Pepper, M. G. (1998) A novel tri-axial force transducer for in-shoe and other biomechanical applications. *Journal of Biomechanics*, 31, 133.

Razian, M. A. & Pepper, M. G. (2003) Design, development, and characteristics of an in-shoe triaxial pressure measurement transducer utilizing a single element of piezoelectric copolymer film. *IEEE Transactions on Neural Systems and Rehabilitation Engineering*, 11, 288-293.

Reiber, G. E. & Ledoux, W. R. (2003) *Epidemiology of Diabetic Foot Ulcers and Amputations: Evidence for Prevention. The Evidence Base for Diabetes Care*. John Wiley & Sons, Ltd.

Riley, P. O., Dicharry, J., Franz, J., Croce, U. D., Wilder, R. P. & Kerrigan, D. C. (2008) A Kinematics and Kinetic Comparison of Overground and Treadmill Running. *Medicine & Science in Sports & Exercise*, 40, 1093-1100
10.1249/MSS.0b013e3181677530.

Riley, P. O., Paolini, G., Della Croce, U., Paylo, K. W. & Kerrigan, D. C. (2007) A kinematic and kinetic comparison of overground and treadmill walking in healthy subjects. *Gait & Posture*, 26, 17-24.

Rosenbaum, D., Hautmann, S., Gold, M. & Claes, L. (1994) Effects of walking speed on plantar pressure patterns and hindfoot angular motion. *Gait & Posture*, 2, 191-197.

Rosenblatt, N. J. & Grabiner, M. D. (2010) Measures of frontal plane stability during treadmill and overground walking. *Gait & Posture*, 31, 380-384.

Sanders, J. (1995) Interface mechanics in external prosthetics: review of interface stress measurement techniques. *Medical and Biological Engineering and Computing*, 33, 509-516.

Schepers, H. M., Koopman, B. F. J. M., Asseldonk Van, E. H. F., Buurke, J. H. & Veltink, P. H. (2008) The Forceshoe: What has been achieved? - Ambulatory estimation of ankle and foot dynamics and center of mass movement. 10th International Symposium on 3D Analysis of Human Movement. Santpoort/Amsterdam, The Netherlands, RRD.

Schepers, H. M., Van Asseldonk, E., Buurke, J. H. & Veltink, P. H. (2009) Ambulatory Estimation of Center of Mass Displacement During Walking. *Biomedical Engineering, IEEE Transactions on*, 56, 1189-1195.

Shaw, J. E., Van Schie, C. H., Carrington, A. L., Abbott, C. A. & Boulton, A. J. (1998) An analysis of dynamic forces transmitted through the foot in diabetic neuropathy. *Diabetes Care*, 21, 1955-1959.

Singh, N., Armstrong, D. G. & Lipsky, B. A. (2005) Preventing Foot Ulcers in Patients With Diabetes. *JAMA*, 293, 217-228.

Sirohi, J. & Chopra, I. (2000) Fundamental Understanding of Piezoelectric Strain Sensors. *Journal of Intelligent Material Systems and Structures*, 11, 246-257.

Stephens, T. M., Lawson, B. R., Devoe, D. E. & Reiser, R. F. (2007) Gender and Bilateral Differences in Single-Leg Countermovement Jump Performance with Comparison to a Double-Leg Jump. *Journal of Applied Biomechanics*, 23, 190-202.

Stokes, I. A. F., Faris, I. B. & Hutton, W. C. (1975) The Neuropathic Ulcer and Loads on the Foot in Diabetic Patients. *Acta Orthopaedica Scandinavica*, 46, 839 - 847.

Stucke, S., Mcfarland, D., Goss, L., Fonov, S., Mcmillan, G. R., Tucker, A., Berme, N., Cenk Guler, H., Bigelow, C. & Davis, B. L. (2012) Spatial relationships between shearing stresses and pressure on the plantar skin surface during gait. *Journal of Biomechanics*, 45, 619-622.

Sumiya, T., Suzuki, Y., Kasahara, T. & Ogata, H. (1998) Sensing stability and dynamic response of the F-Scan in-shoe sensing system: A technical note, Baltimore, MD, ETATS-UNIS, Rehabilitation Research and Development Service.

Suresh, R., Tjin, S. C. & Ngo, N. Q. (2004) Shear force sensing by strain transformation using non-rectilinearly embedded fiber Bragg grating. *Sensors and Actuators A: Physical*, 116, 107-118.

Tada, M., Sasaki, S. & Ogasawara, T. (2002) Development of an optical 2-axis force sensor usable in MRI environments. *Sensors*, 2002. Proceedings of IEEE.

Takahashi, N., Tada, M., Ueda, J., Matsumoto, Y. & Ogasawara, T. (2003) An optical 6-axis force sensor for brain function analysis using fMRI. *Sensors*, 2003. Proceedings of IEEE.

Tappin, J. W., Pollard, J. & Beckett, E. A. (1980) Method of measuring 'shearing' forces on the sole of the foot. *Clinical Physics and Physiological Measurement*, 83.

Thornton, B. (2009) Evaluation of the characteristics of an in-shoe tri-axial piezoelectric pressure transducer. MSc thesis, Bioengineering Unit. Glasgow, University of Strathclyde.

Tiwana, M. I., Shashank, A., Redmond, S. J. & Lovell, N. H. (2011) Characterization of a capacitive tactile shear sensor for application in robotic and upper limb prostheses. *Sensors and Actuators A: Physical*, 165, 164-172.

Tsai, H.C. (2005) Compression analysis of rectangular elastic layers bonded between rigid plates. *International Journal of Solids and Structures*, 42, 3395-3410.

Tsai, Y. C., Chang, S. L., Yang, S. W. & Lai, S. M. (2007) Effect of Insole and Sock Materials on Walking Plantar Pressure in Diabetic Patients. *Journal of Biomechanics*, 40, S448.

Uccioli, L., Caselli, A., Giacomozzi, C., Macellari, V., Giurato, L., Lardieri, L. & Menzinger, G. (2001) Pattern of abnormal tangential forces in the diabetic neuropathic foot. *Clinical Biomechanics*, 16, 446-454.

Urry, S. (1999) Plantar pressure-measurement sensors. *Measurement Science and Technology*, 10, R16-R32.

Veltink, P. H., Liedtke, C. & Droog, E. (2004) Ambulatory measurement of ground reaction forces. *Systems, Man and Cybernetics, 2004 IEEE International Conference on*.

Veltink, P. H., Liedtke, C., Droog, E. & Van Der Kooij, H. (2005) Ambulatory measurement of ground reaction forces. *Neural Systems and Rehabilitation Engineering, IEEE Transactions on*, 13, 423-427.

Veves, A., Murray, H. J., Young, M. J. & Boulton, A. J. M. (1992) The risk of foot ulceration in diabetic patients with high foot pressure: a prospective study. *Diabetologia*, 35, 660-663.

Voyles, M., R., Morrow, D., J., Khosla & K., P. (1997) The shape from motion approach to rapid and precise force/torque sensor calibration, New York, NY, ETATS-UNIS, American Society of Mechanical Engineers.

Voyles, R. & Khosla, P. (1997) Collaborative Calibration: Extending Shape from Motion Calibration. *IEEE International Conference on Robotics and Automation*.

Wang, L. & Beebe, D. J. (2000) A silicon-based shear force sensor: development and characterization. *Sensors and Actuators A: Physical*, 84, 33-44.

Wang, W. C., Ledoux, W. R., Sangeorzan, B. J. & Reinhall, P. G. (2005) A shear and plantar pressure sensor based on fiber-optic bend loss. *Journal of Rehabilitation Research and Development*, 42, 315-325.

Wank, V., Frick, U. & Schmidtbleicher, D. (1998) Kinematics and Electromyography of Lower Limb Muscles in Overground and Treadmill Running. *Int J Sports Med*, 19, 455,461.

Warabi, T., Kato, M., Kiriyama, K., Yoshida, T. & Kobayashi, N. (2005) Treadmill walking and overground walking of human subjects compared by recording sole-floor reaction force. *Neuroscience Research*, 53, 343-348.

Watkins, P. J. (2003) The diabetic foot. *BMJ*, 326, 977-9.

Wearing, S. C., Urry, S. R. & Smeathers, J. E. (2000) The effect of visual targeting on ground reaction force and temporospatial parameters of gait. *Clinical Biomechanics*, 15, 583-591.

Wharton, A. (2006) Piezoelectric Materials. [Accessed 20th January 2013] Available from: <http://mimp.mems.cmu.edu/hst/aaron/Introduction.htm>.

Williams, R. & Airey, M. (2002) *The Size of the Problem: Epidemiological and Economic Aspects of Foot Problems in Diabetes*. The Foot in Diabetes. John Wiley & Sons, Ltd.

Williams, R., Porter, D., Roberts, V. & Regan, J. (1992) Triaxial force transducer for investigating stresses at the stump/socket interface. *Medical and Biological Engineering and Computing*, 30, 89-96.

Witt, G. R. (1974) The electromechanical properties of thin films and the thin film strain gauge. *Thin Solid Films*, 22, 133-156.

Wong, P.-L., Chamari, K., Chaouachi, A., Mao, D. W., Wislã, Ff, U. & Hong, Y. (2007) Difference in plantar pressure between the preferred and non-preferred feet in four soccer-related movements. *British Journal of Sports Medicine*, 41, 84-92.

Wounds International (2010) International review. Pressure ulcer prevention: pressure, shear, friction and microclimate in context. A consensus document. Wounds International, London.

Yamada, M., Takebayashi, T., Notoyama, S. & Watanabe, K. (1992) A switched-capacitor interface for capacitive pressure sensors. *Instrumentation and Measurement, IEEE Transactions on*, 41, 81-86.

Yavuz, M., Botek, G. & Davis, B. L. (2007a) Plantar shear stress distributions: Comparing actual and predicted frictional forces at the foot-ground interface. *Journal of Biomechanics*, 40, 3045-3049.

Yavuz, M., Erdemir, A., Botek, G., Hirschman, G. B., Bardsley, L. & Davis, B. L. (2007b) Peak Plantar Pressure and Shear Locations. *Diabetes Care*, 30, 2643-2645.

Yavuz, M., Tajaddini, A., Botek, G. & Davis, B. L. (2008) Temporal characteristics of plantar shear distribution: Relevance to diabetic patients. *Journal of Biomechanics*, 41, 556-559.

Young, M. J., Veves, A. & Boulton, A. J. M. (1993) The diabetic foot: Aetiopathogenesis and management. *Diabetes/Metabolism Reviews*, 9, 109-127.

Yu, S., Keekyoung, K., Voyles, R. M. & Nelson, B. J. (2006) Calibration of multi-axis MEMS force sensors using the shape from motion method. *Robotics and Automation, 2006. ICRA 2006. Proceedings 2006 IEEE International Conference on*.

Yung-Hui, L. & Wei-Hsien, H. (2005) Effects of shoe inserts and heel height on foot pressure, impact force, and perceived comfort during walking. *Applied Ergonomics*, 36, 355-362.

Zhu, F. & Spronck, J. W. (1992) A capacitive tactile sensor for shear and normal force measurements. *Sensors and Actuators A: Physical*, 31, 115-120.

Zhu, F., Spronck, J. W. & Heerens, W. C. (1991) A simple capacitive displacement sensor. *Sensors and Actuators A: Physical*, 26, 265-269.

Zou, D., Mueller, M. J. & Lott, D. J. (2007) Effect of peak pressure and pressure gradient on subsurface shear stresses in the neuropathic foot. *Journal of Biomechanics*, 40, 883-890.

Appendix A - Terminology

This appendix describes some of the load transducer terminologies and engineering terms used throughout this study. Brief descriptions of how they were calculated and presented throughout this thesis are shown below:

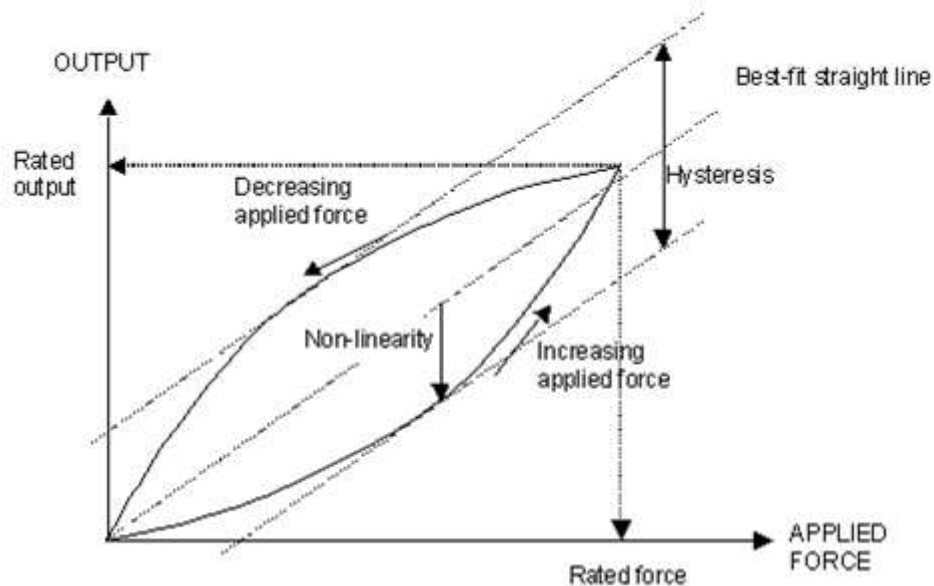


Figure 116 - Typical output characteristics of a force measurement system. (Modified image from The National Physical Laboratory (NPL) <http://www.npl.co.uk>, UK)

Rated capacity: The maximum force that the transducer is designed to measure.

Rated output (span or full-scale output): The output at the rated capacity minus the output at zero applied load.

Sensitivity: Full-scale output divided by the rated capacity of a given transducer.

Non-linearity: The maximum deviation of the calibration curve from the best-fit least-squares line; expressed as a percentage of the rated output and measured on increasing load only.

Hysteresis: The maximum difference of readings between the increasing and decreasing forces at any given force; expressed as a percentage of the rated output.

Combined error (non-linearity and hysteresis): The maximum deviation of the calibration curve from the best-fit least-squares line; expressed as a percentage of the rated output and measured on both increasing and decreasing load.

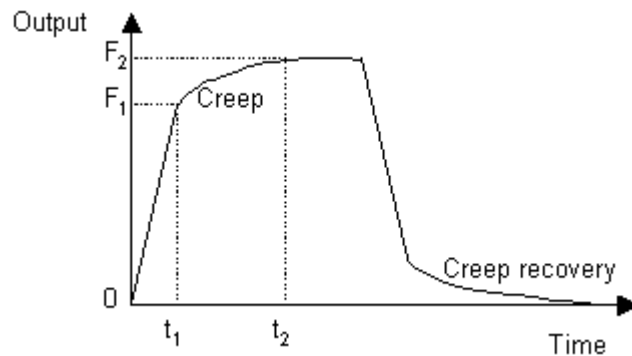


Figure 117 - Creep curve of a typical force transducer. (Image from The National Physical Laboratory (NPL) <http://www.npl.co.uk>, UK)

Creep: The change in transducer output that occurs with time when a constant load is applied with environmental and other variables remaining constant. Creep is specified over a fixed time period, t_1 to t_2 .

Creep recovery: The change in no-load output occurring with time, after removal of a load, which has been applied for a specific period of time.

Cross-talk: Multi-axis load measurement devices may suffer from mechanical coupling between the mutually perpendicular sensing axes. For example, if vertical axis Z is loaded, a small effect can be witnessed on both the outputs of shear X and Y axes. This effect is called cross-talk and is expressed as a percentage of the rated capacity for the axis. With one component loaded to capacity, and the other unloaded, the output of the unloaded component will not exceed the percentage specified of its rated capacity.

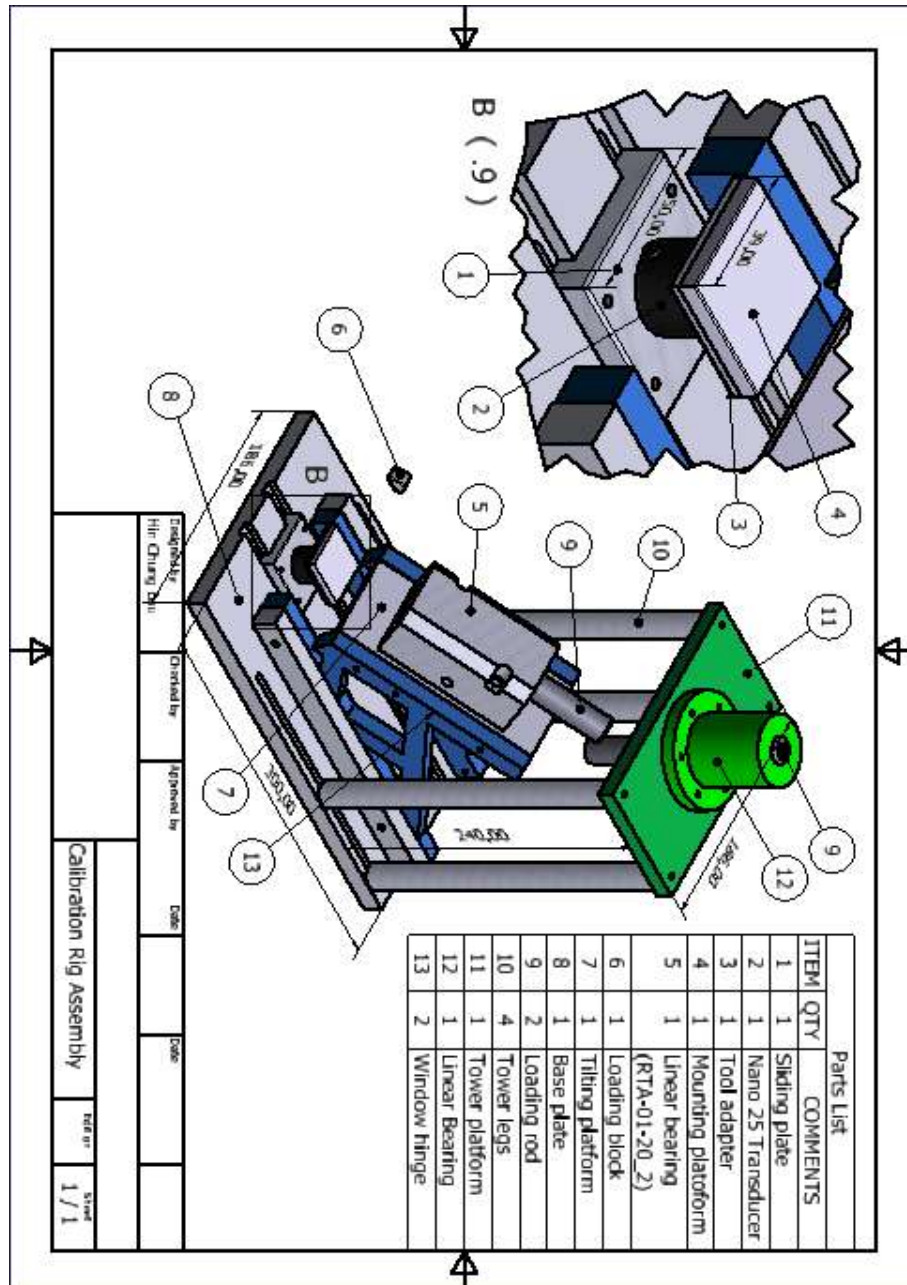
Signal-to-noise ratio (SNR): SNR is a measure used to compare the level of a desired signal to the level of background noise. It was defined in this study as the ratio of signal amplitude to the noise amplitude, expressed as $A_{signal} : A_{noise}$.

Frequency response: The frequency response describes how a measurement device would respond given an input across the frequency spectrum. It is affected by the nature of the mechanical structure, both within the transducer and of its mounting. A transducer on a rigid foundation will have a natural frequency of oscillation and large dynamic errors occur when the frequency of the vibration approaches the natural frequency of oscillations of the system.

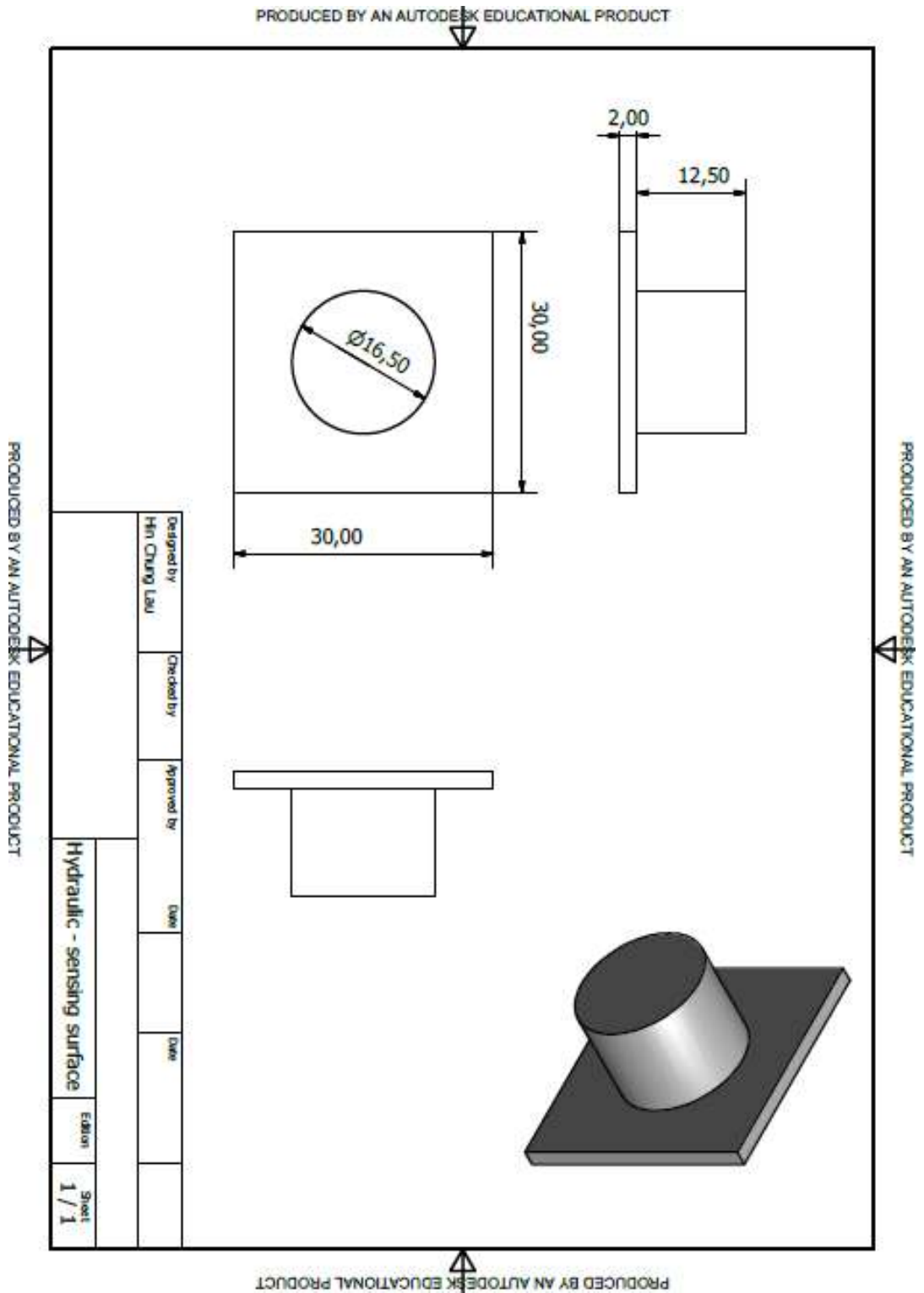
Discrete Fourier transform of the signal from the reference load cell and the multi-axial transducers from the current study were found by taking the fast Fourier transform (FFT). Single-sided amplitude spectrum of each signal was obtained using the `fft()` function in MATLAB. The amplitude ratios for a range of loading frequencies were calculated by dividing the peaks from the amplitude spectrum of the multi-axial transducer to the amplitude spectrum of the reference load cell. A bode diagram, or an amplitude ratio (gain) plot, was then plotted against frequency.

Appendix B - Technical drawings of equipment components

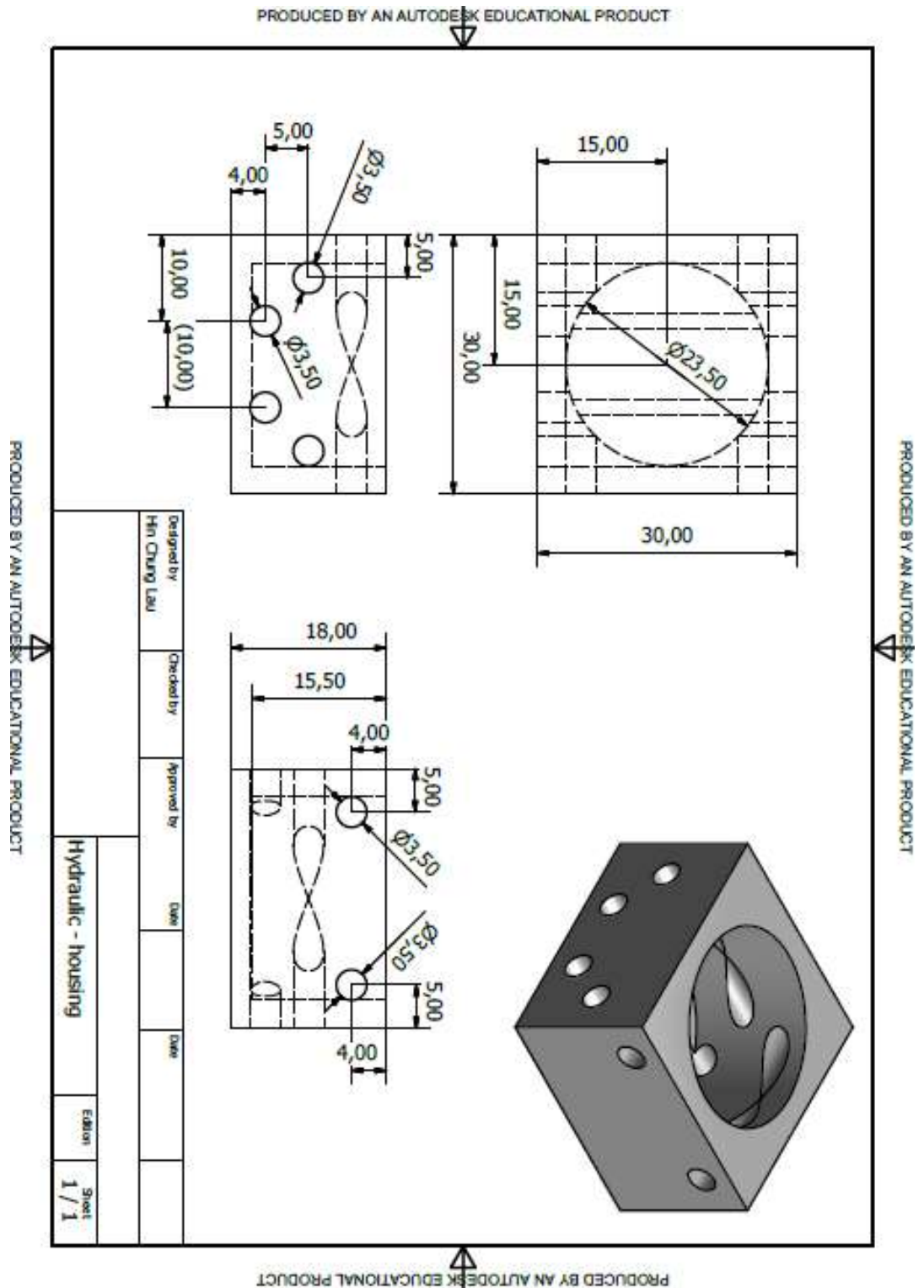
1. Calibration rig assembly: Number of parts listed with brief dimensions shown in millimetres.



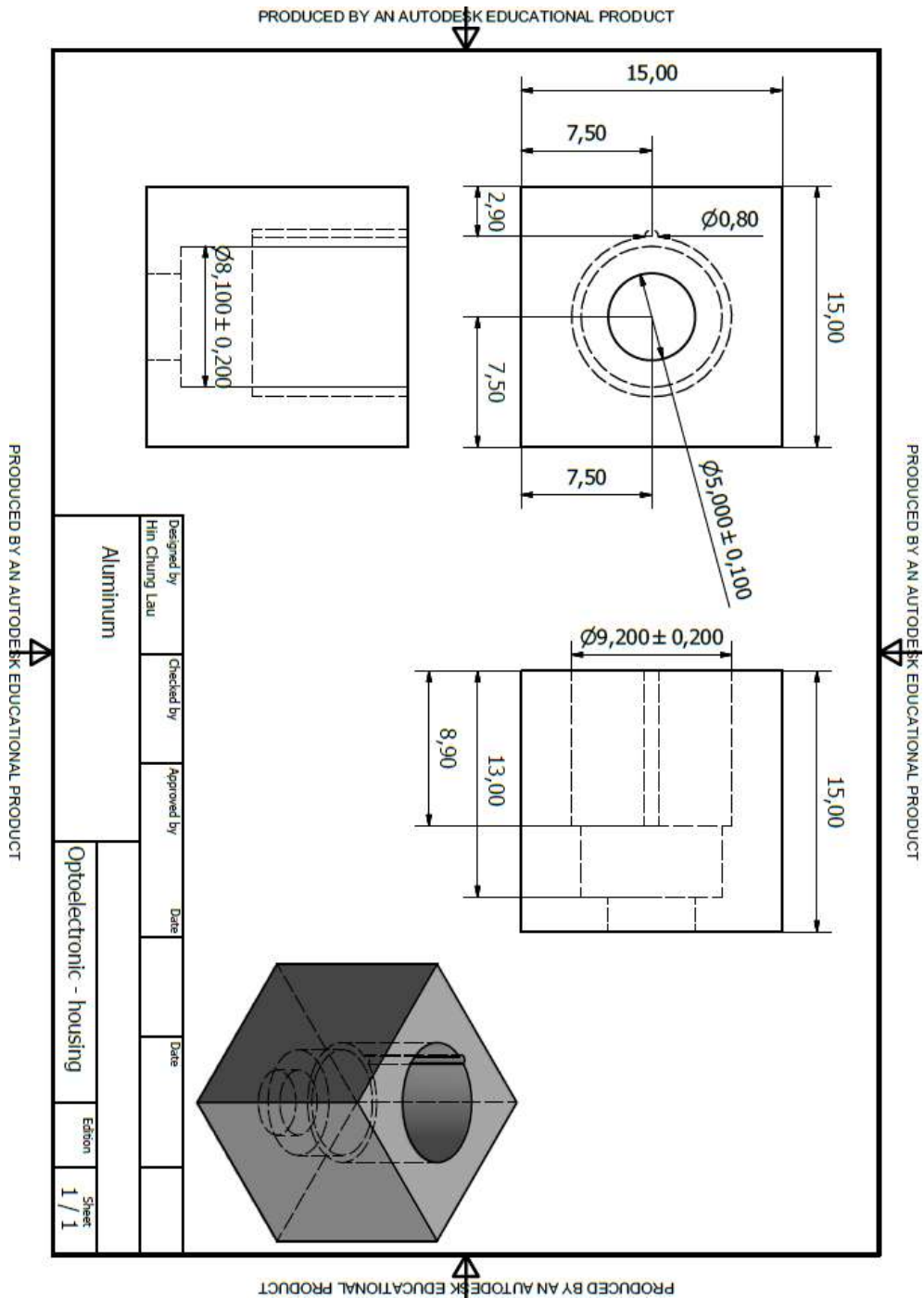
2. Technical drawing of the sensing surface plate for the hydraulic based load transducer prototype.



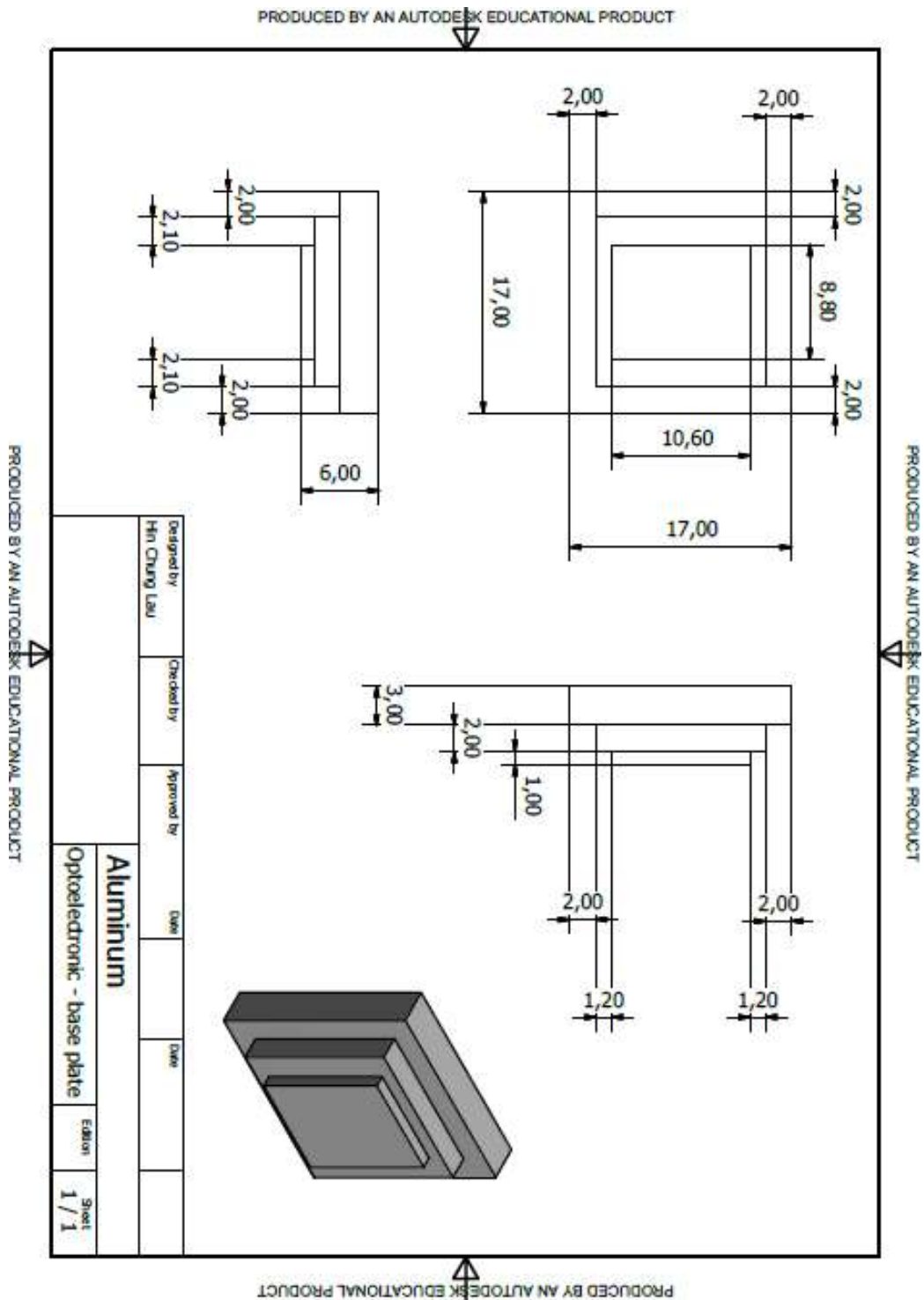
3. Technical drawing of the transducer housing for the hydraulic based load transducer prototype.



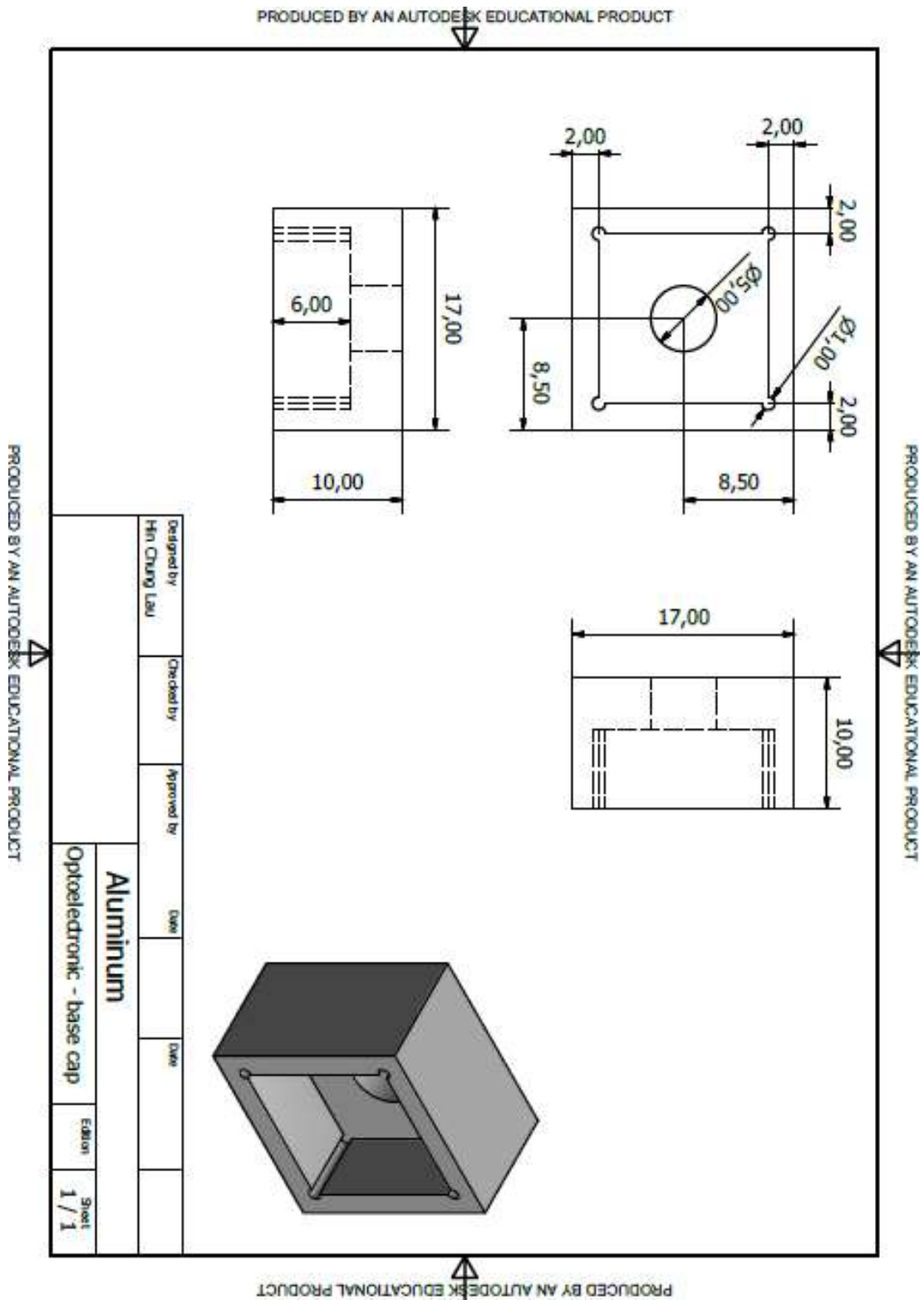
4. Technical drawing of the transducer housing for the optoelectronic based load transducer prototypes.



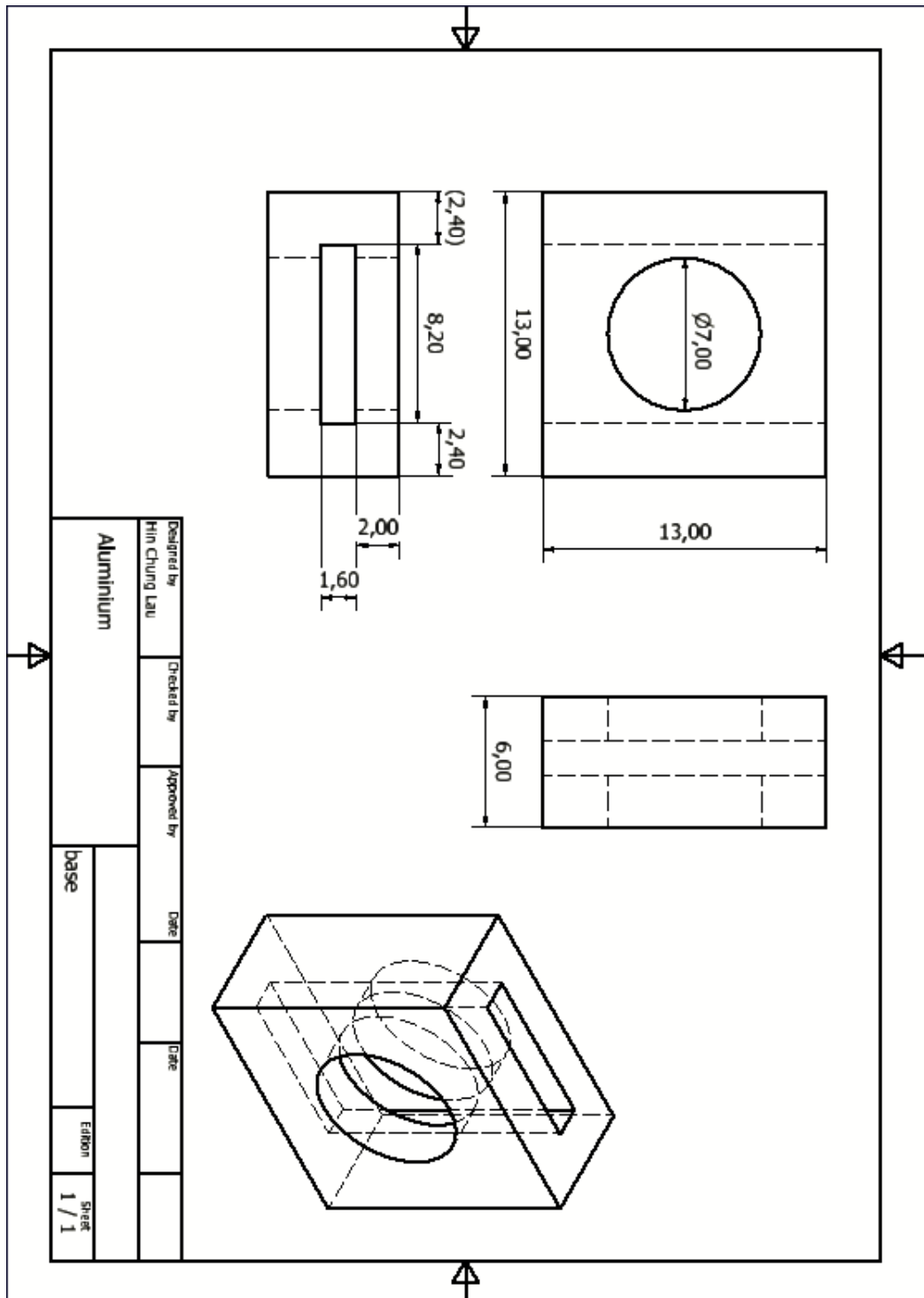
5. Technical drawing of the base plate used in the optoelectronic based prototypes.



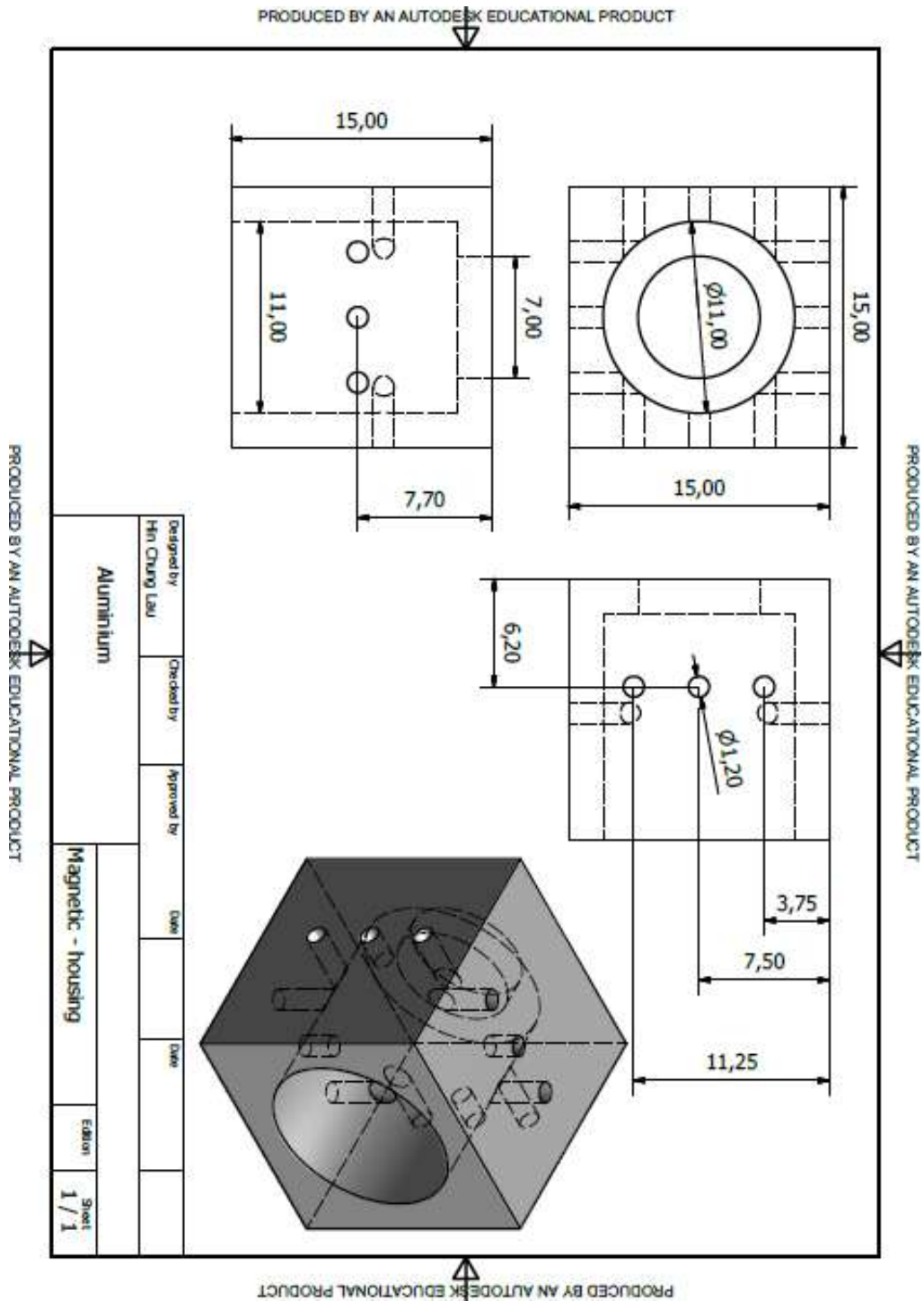
6. Technical drawing of the base cap used in the optoelectronic based prototypes.



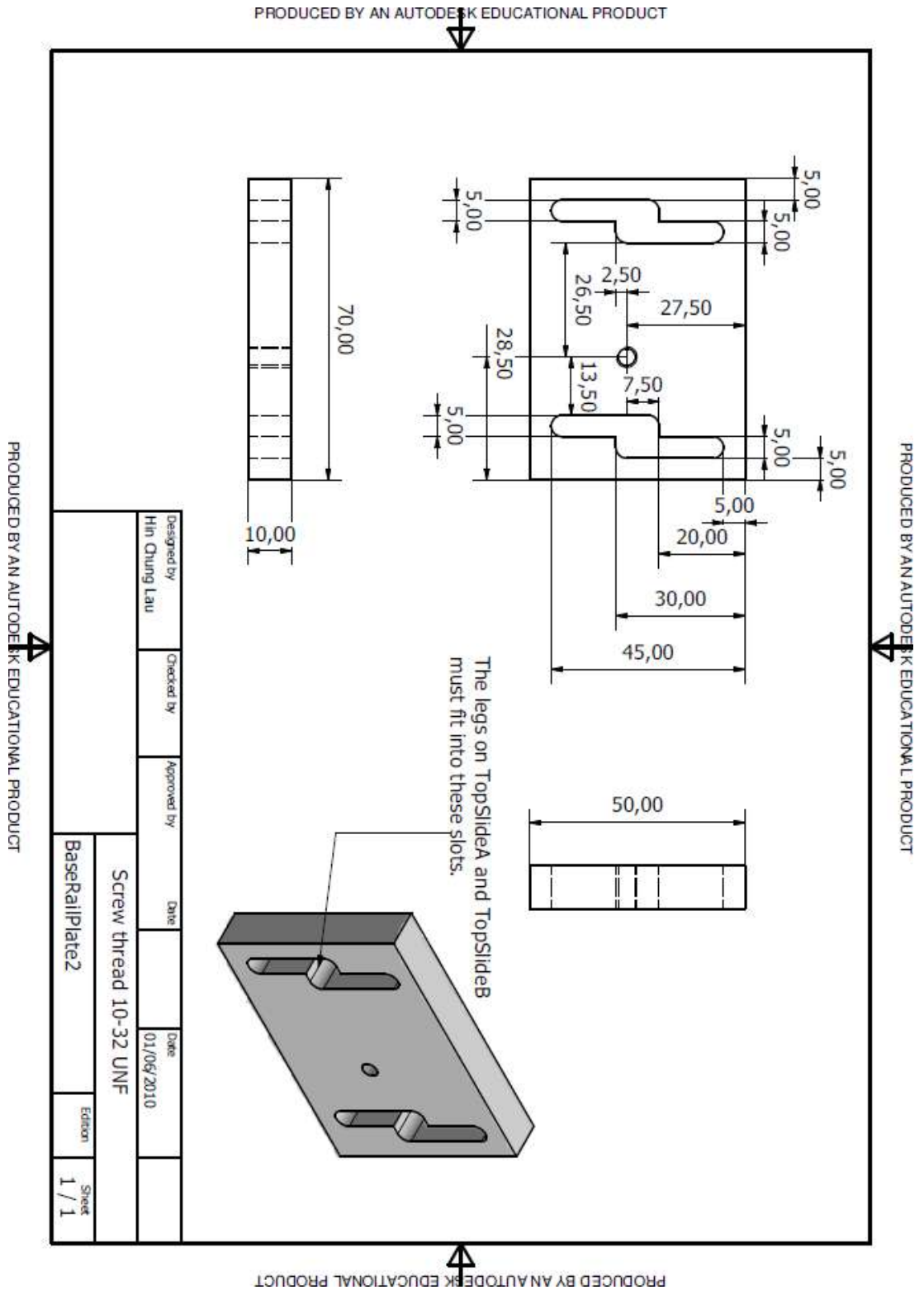
7. Technical drawing of the transducer housing for the magnetic based load transducer prototypes.



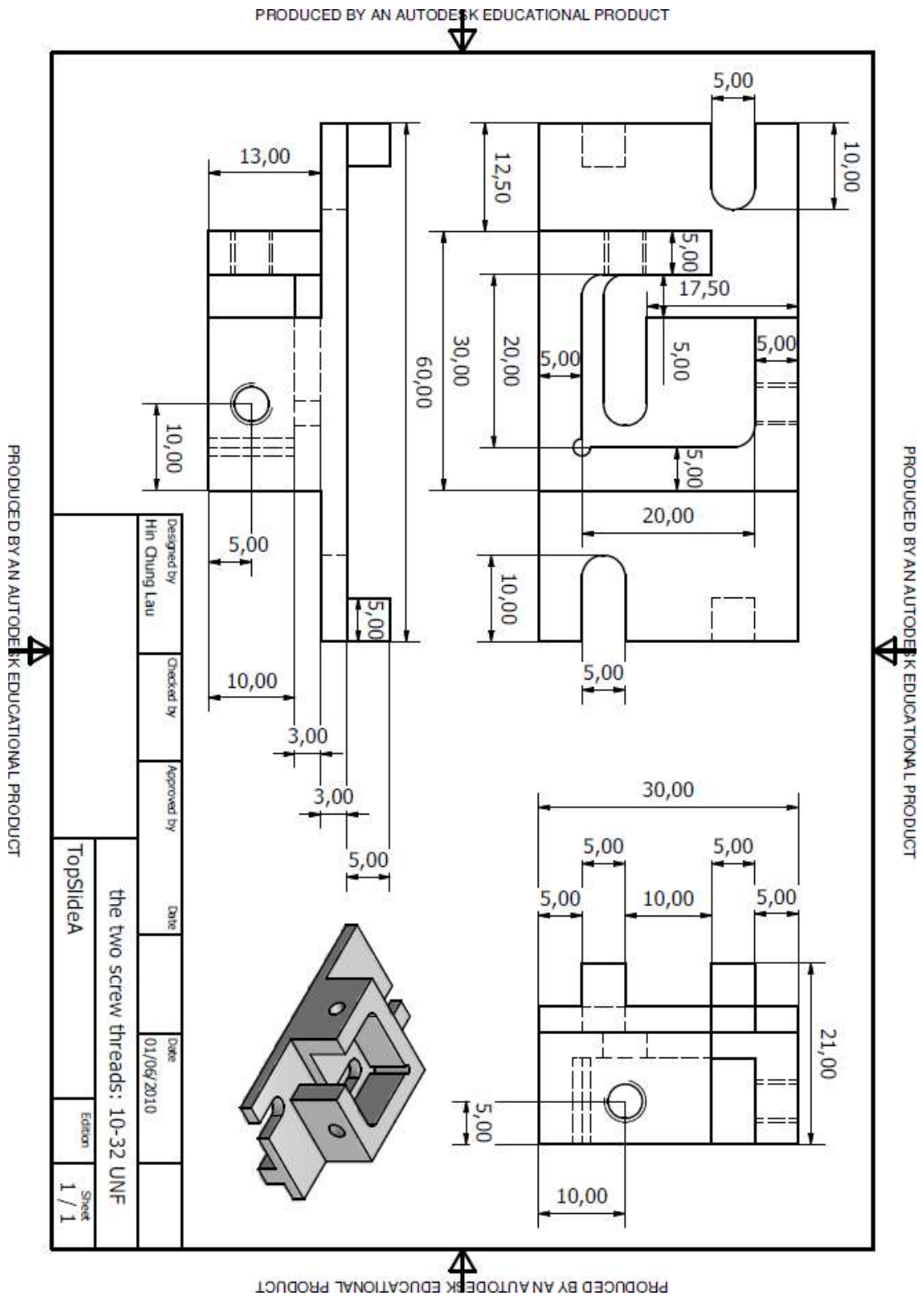
8. Technical drawing of the transducer housing for the magnetic based bi-axial shear stress transducer.



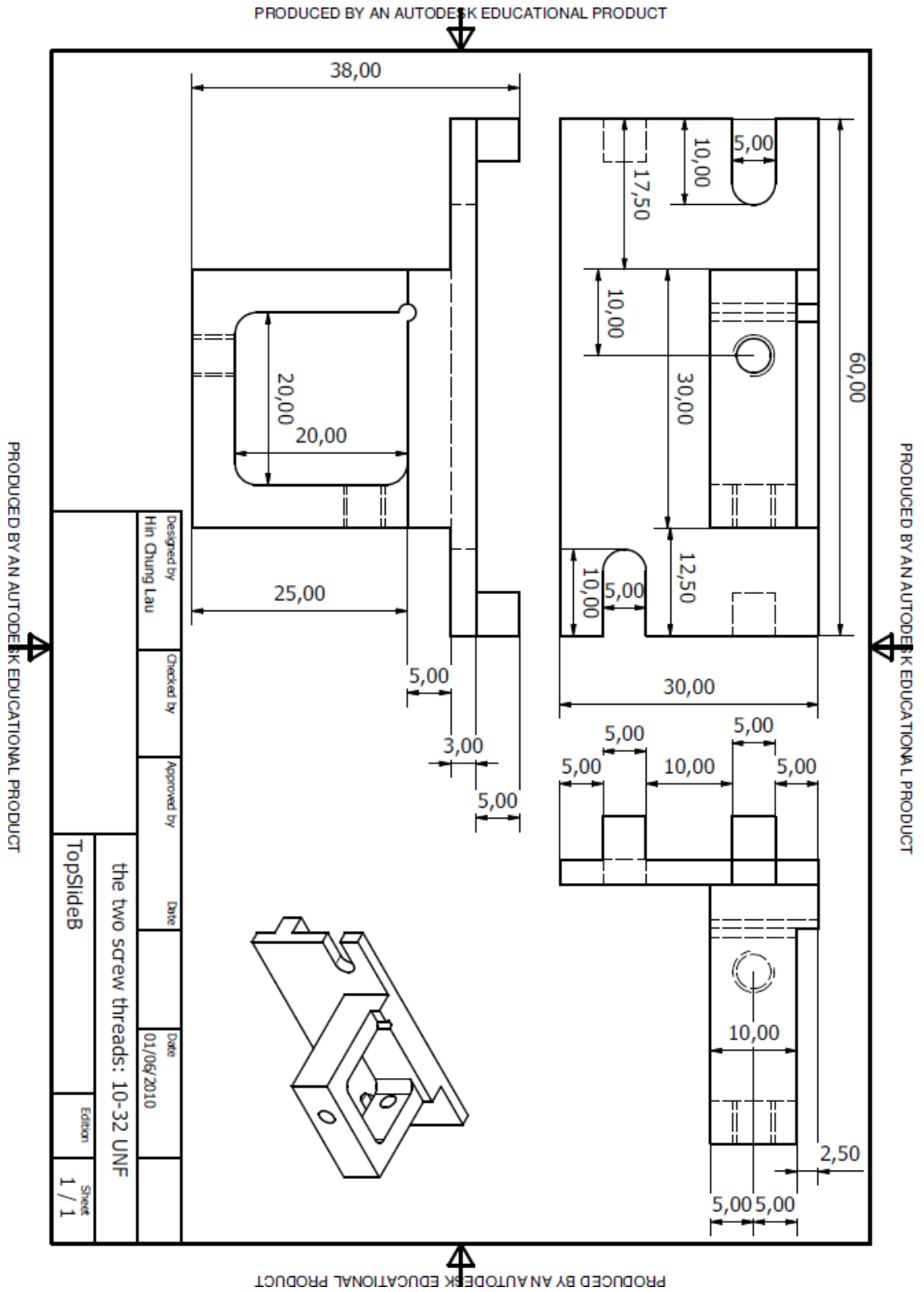
10. Technical drawing of the second adaptor rail system for mounting transducers in the ElectroForce3200 testing system.



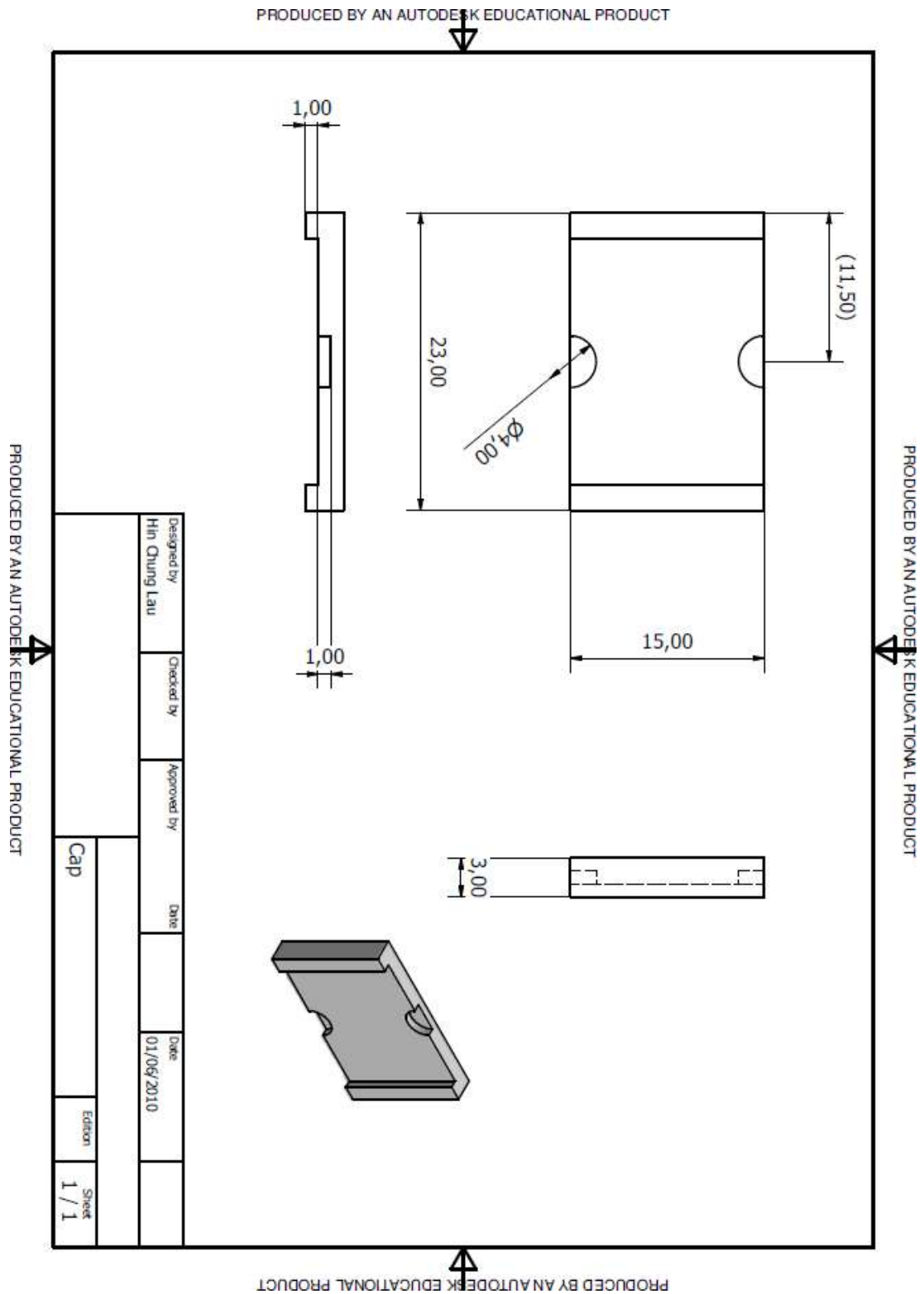
11. Technical drawing of the first mounting adaptors for mounting transducers in the up-right position in the ElectroForce3200 testing system.



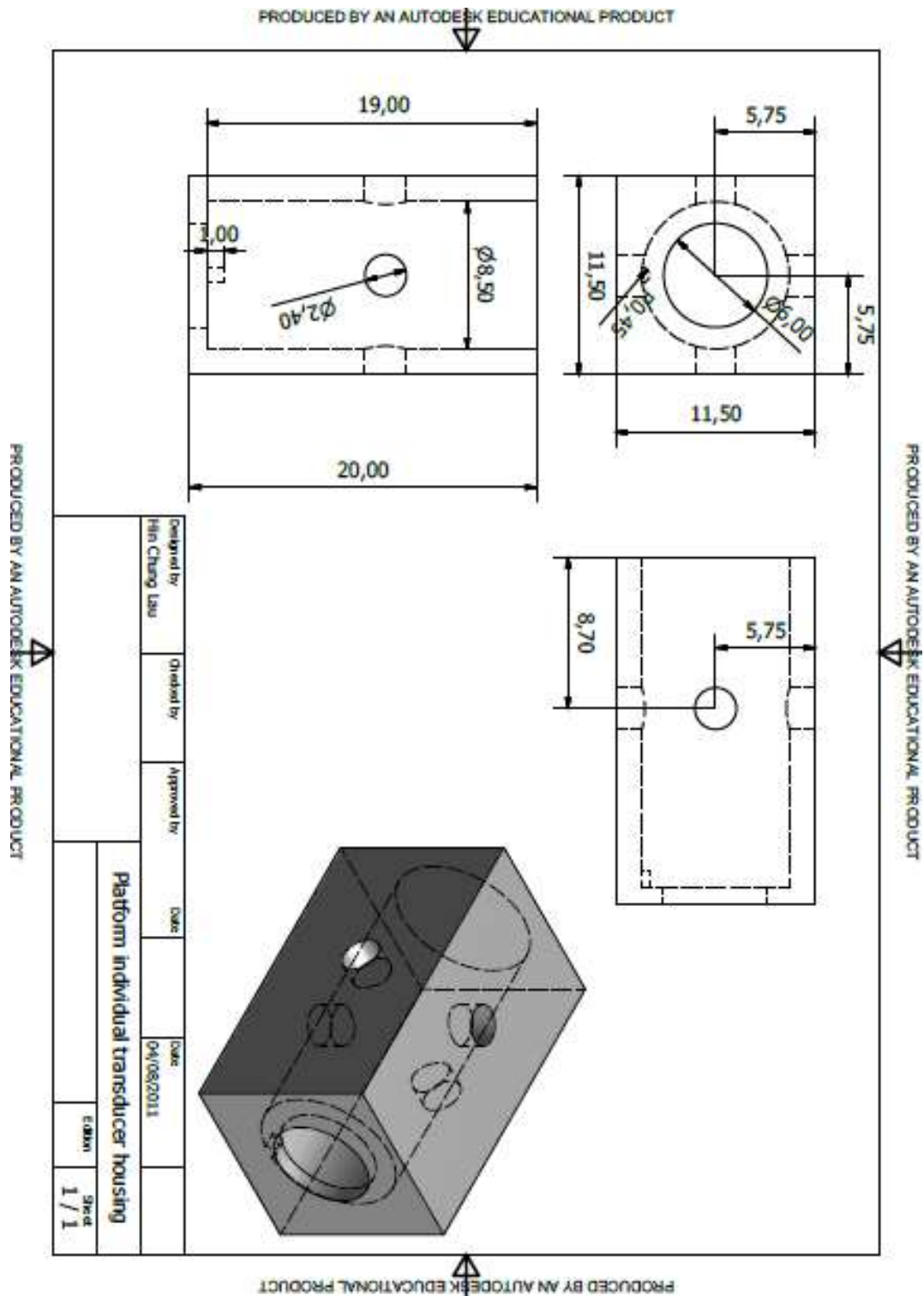
12. Technical drawing of the second mounting adaptors for mounting transducers in side-way position in the ElectroForce3200 testing system.



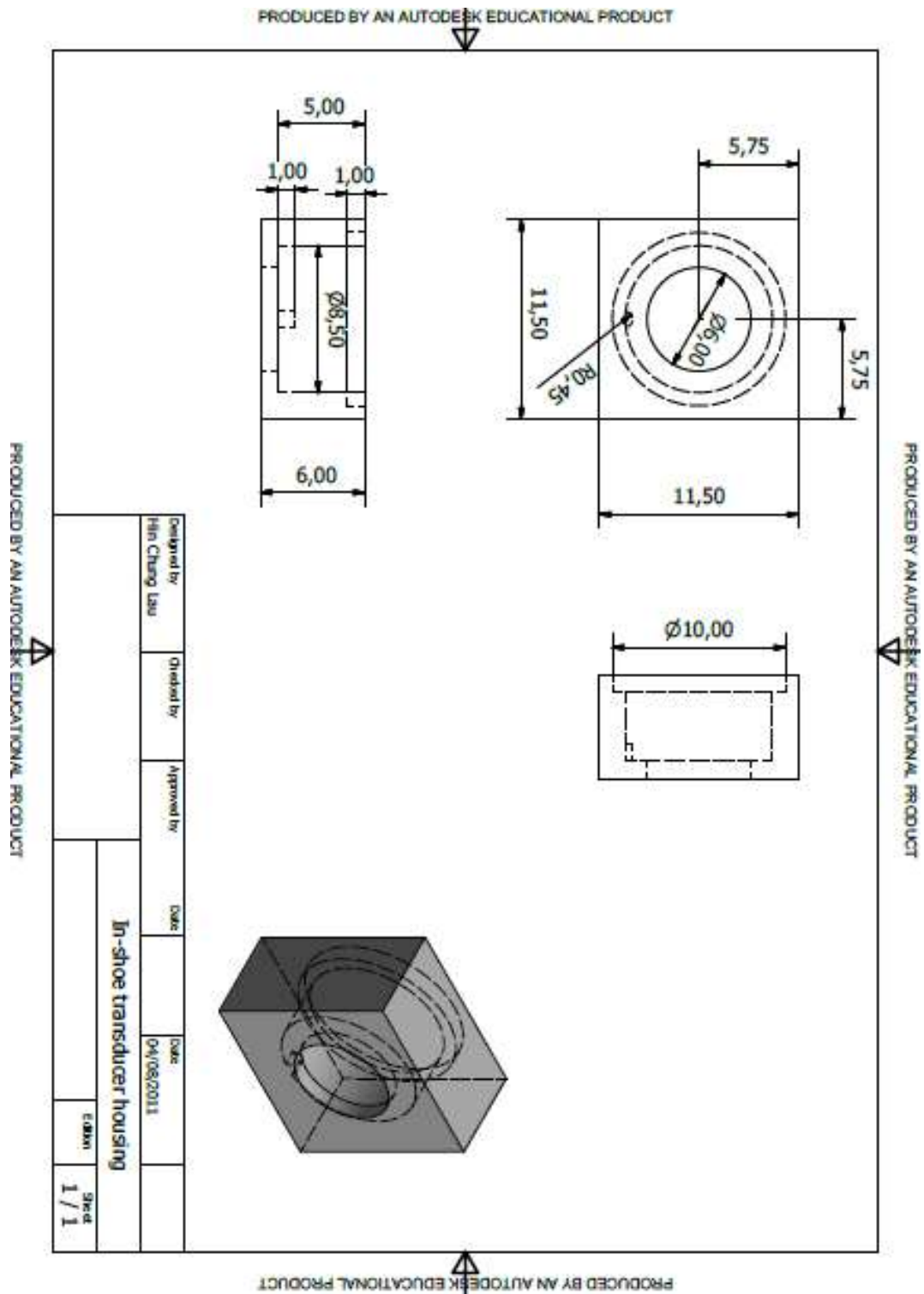
13. Technical drawing of the cap adaptor used for transferring shear load to the transducer during tests in the ElectroForce3200 system.



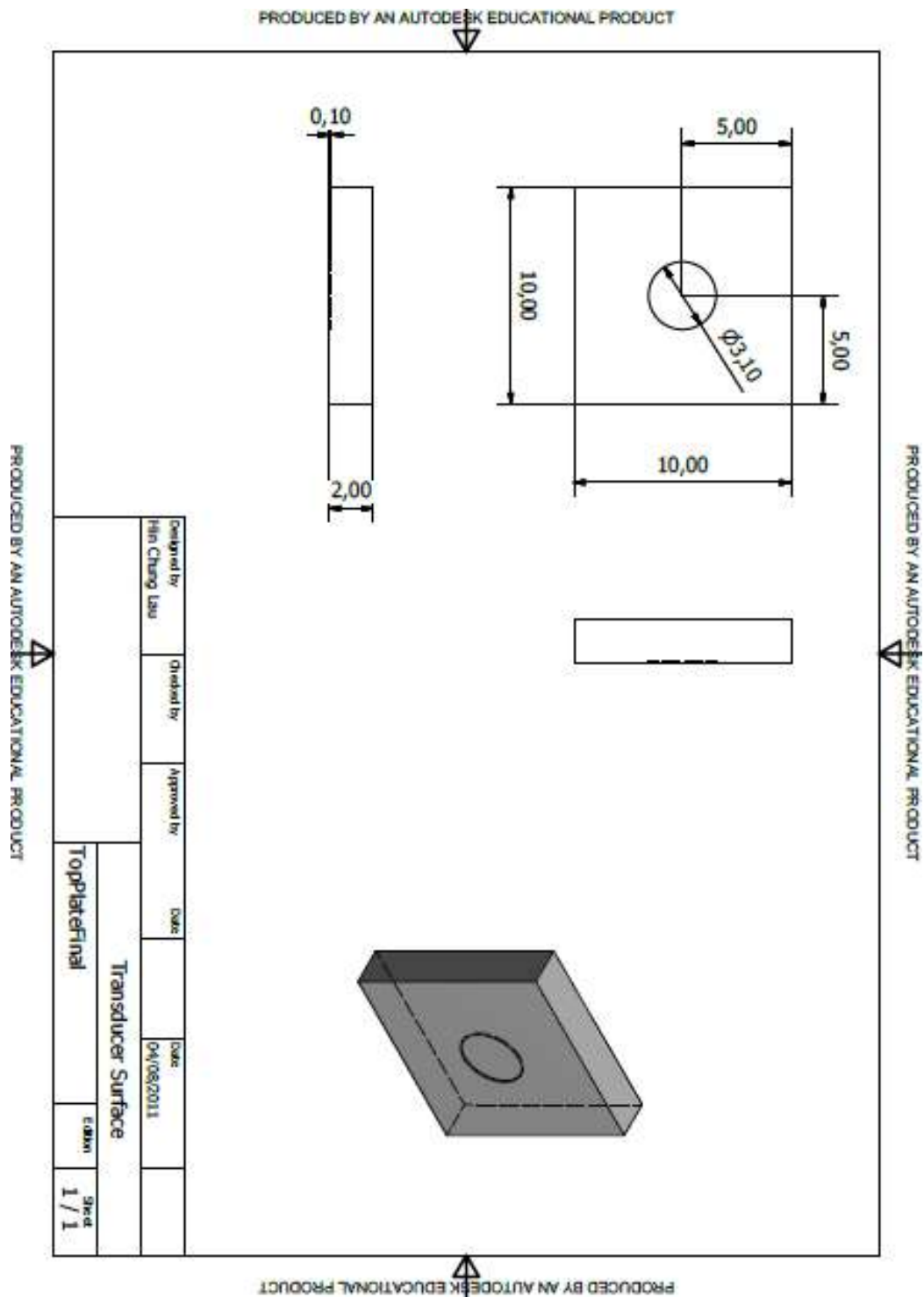
14. Technical drawing of the transducer housing used in the construction of the biaxial shear transducer in the array platform.



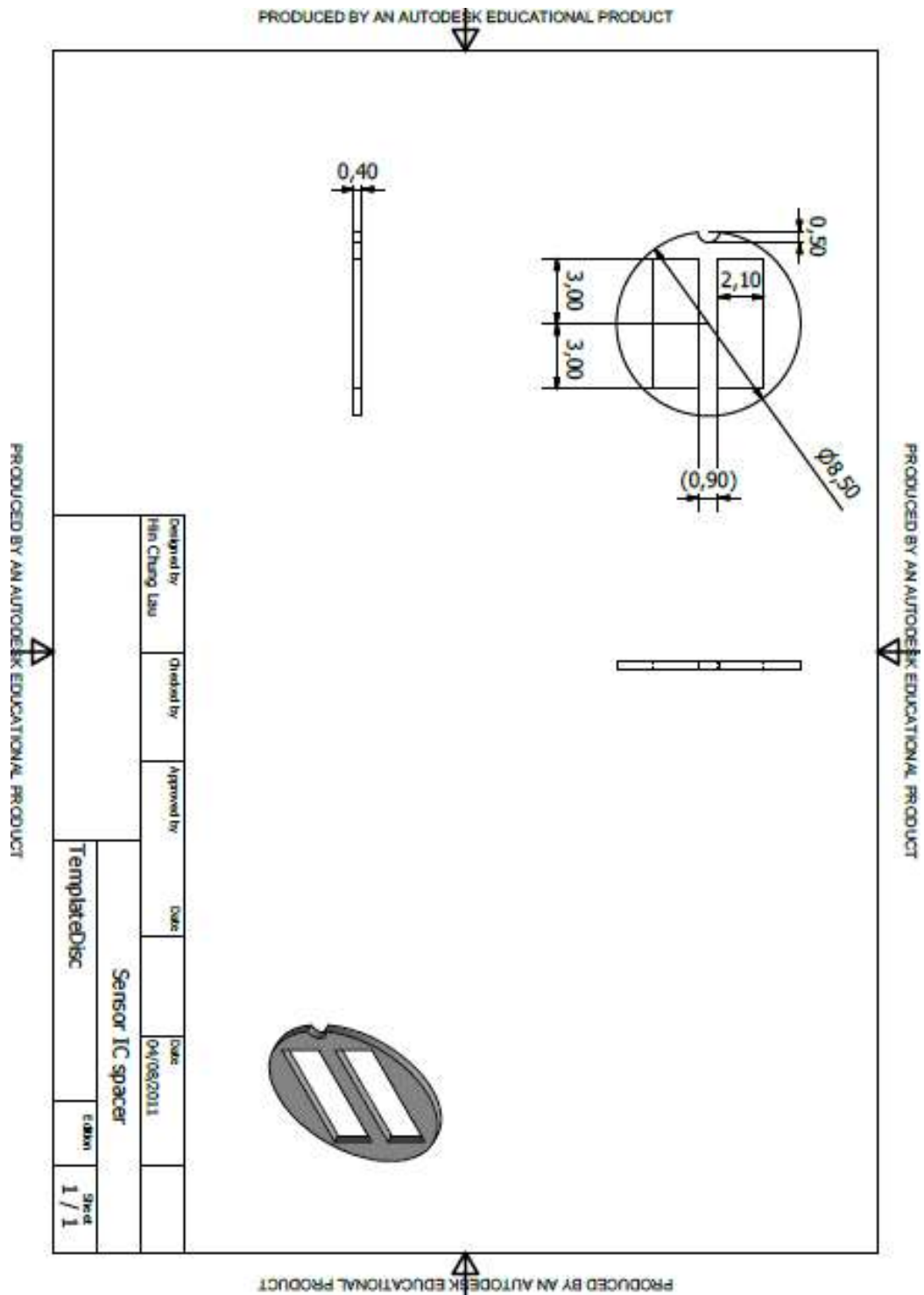
15. Technical drawing of the transducer housing used in the construction of the biaxial shear transducer intended for in-shoe applications.



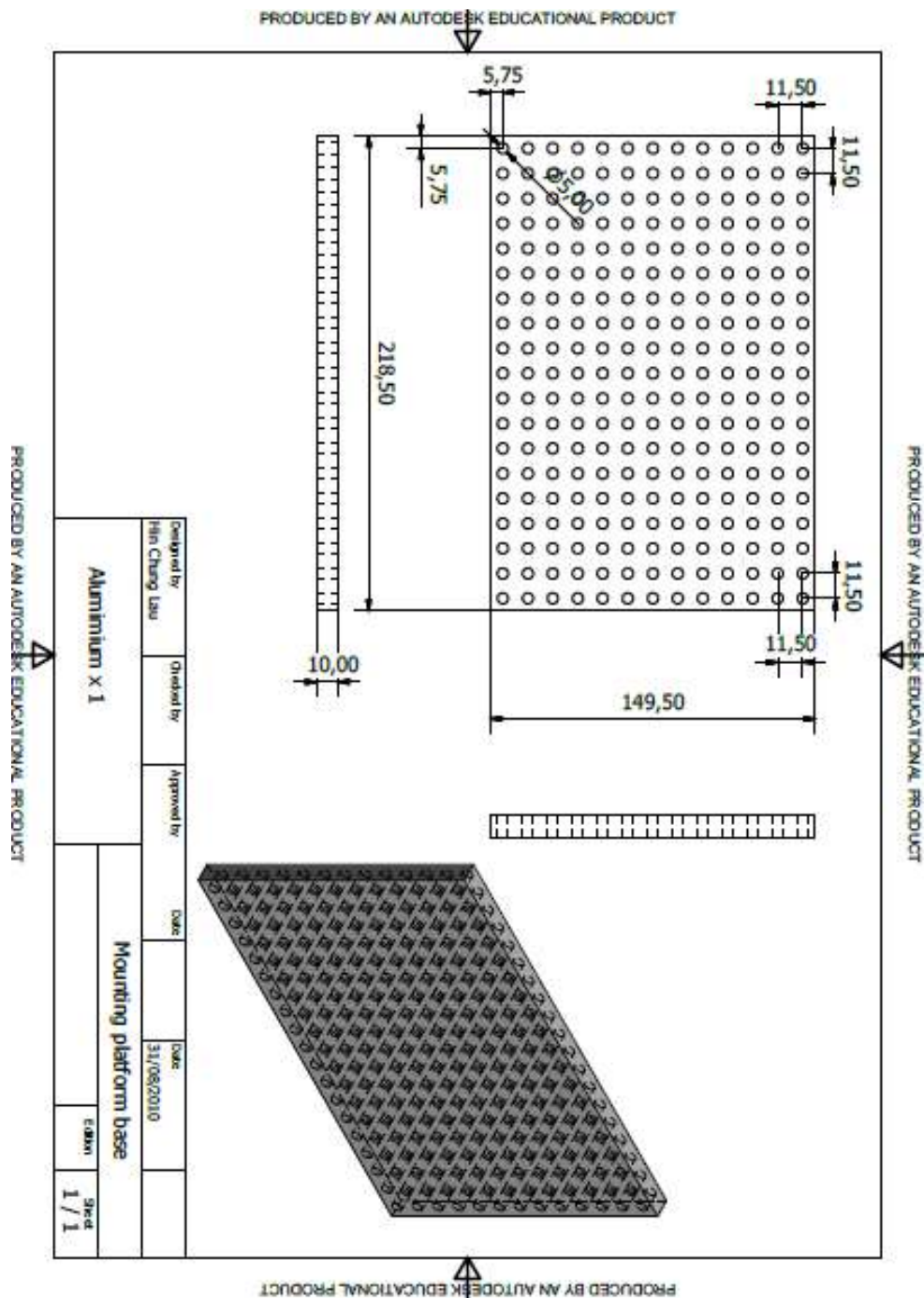
16. Technical drawing of the sensing surface plate of the biaxial shear transducer.



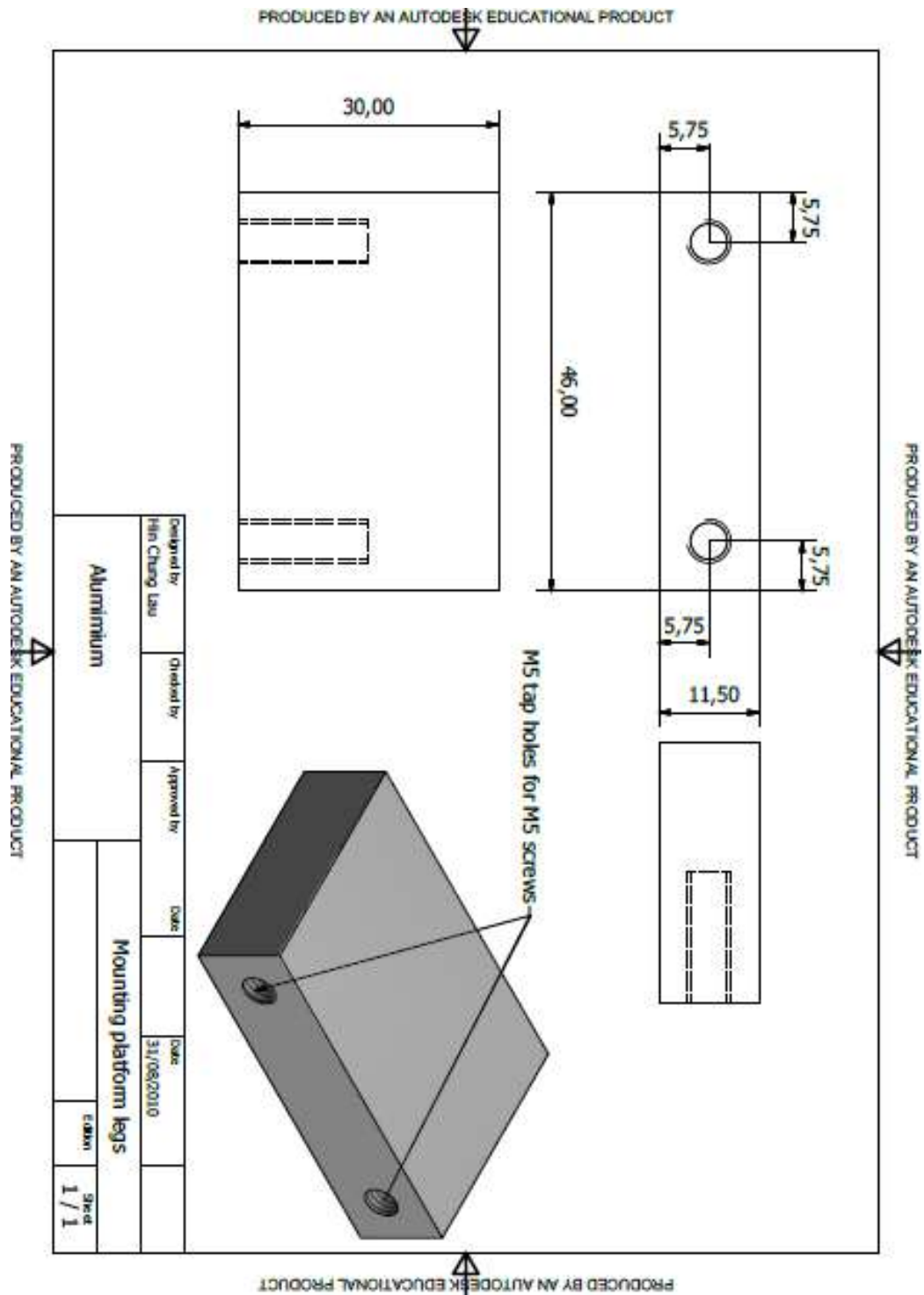
17. Technical drawing of the spacer disc for the alignment of the hall-effect sensor ICs within the transducer housing.



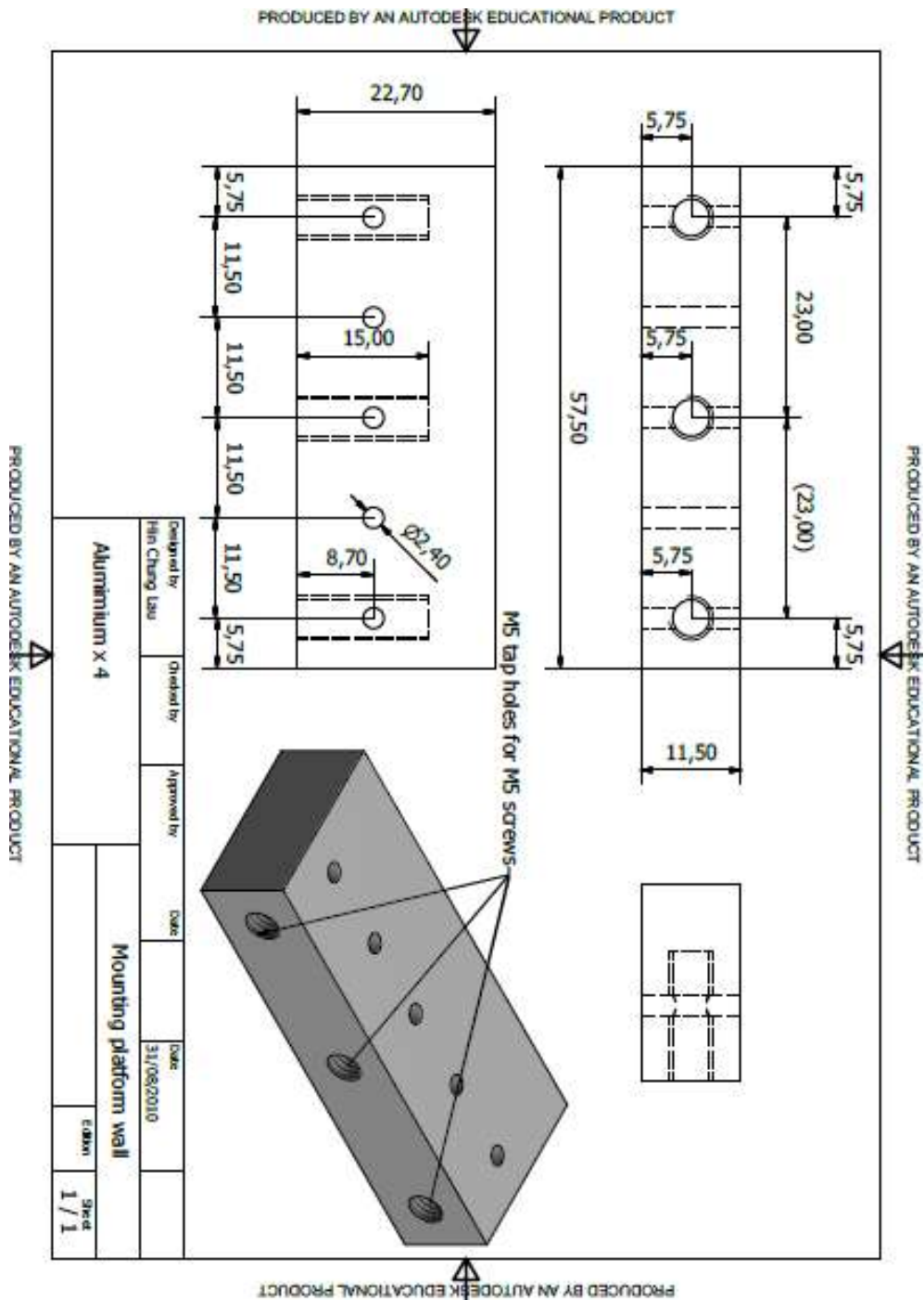
18. Technical drawing of the base plate of the mounting platform for the assembling of a transducer array. The actual base plate manufactured in the study had only 10×10 holes.



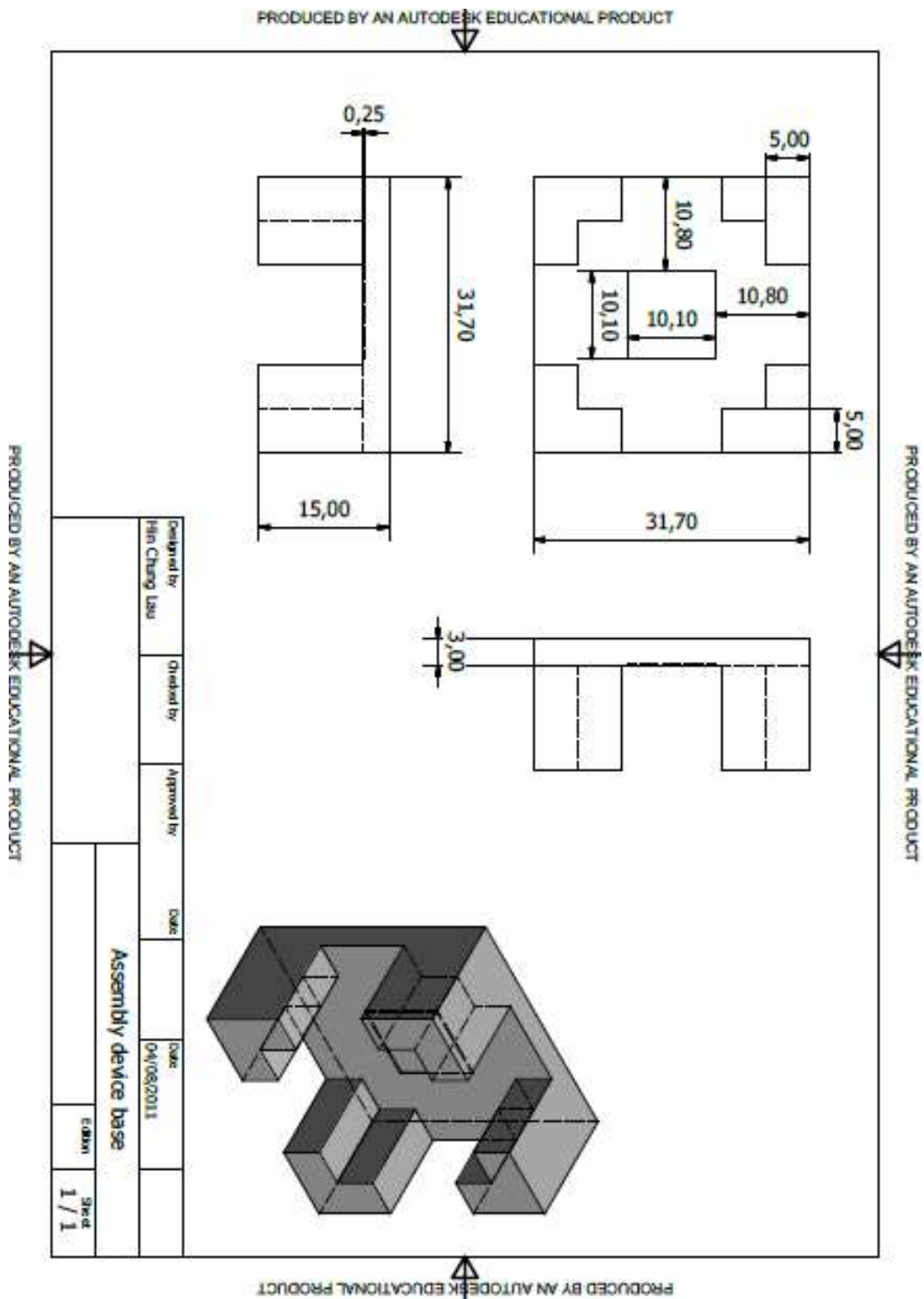
19. Technical drawing of the legs that can be secured to the base of the mounting platform shown above.



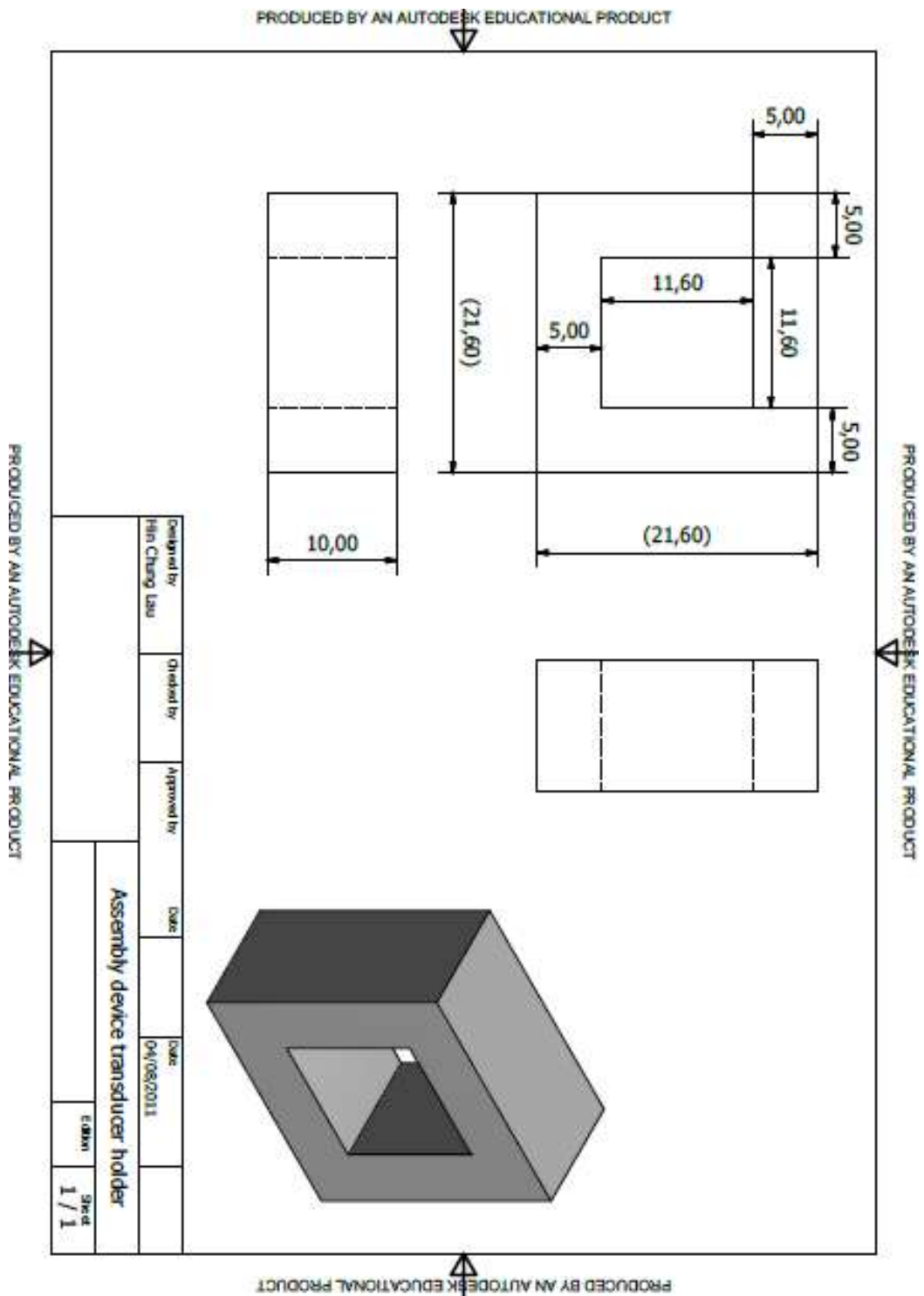
20. Technical drawing of the walls on the mounting platform used to compact the array of transducers together and to secure them in place.



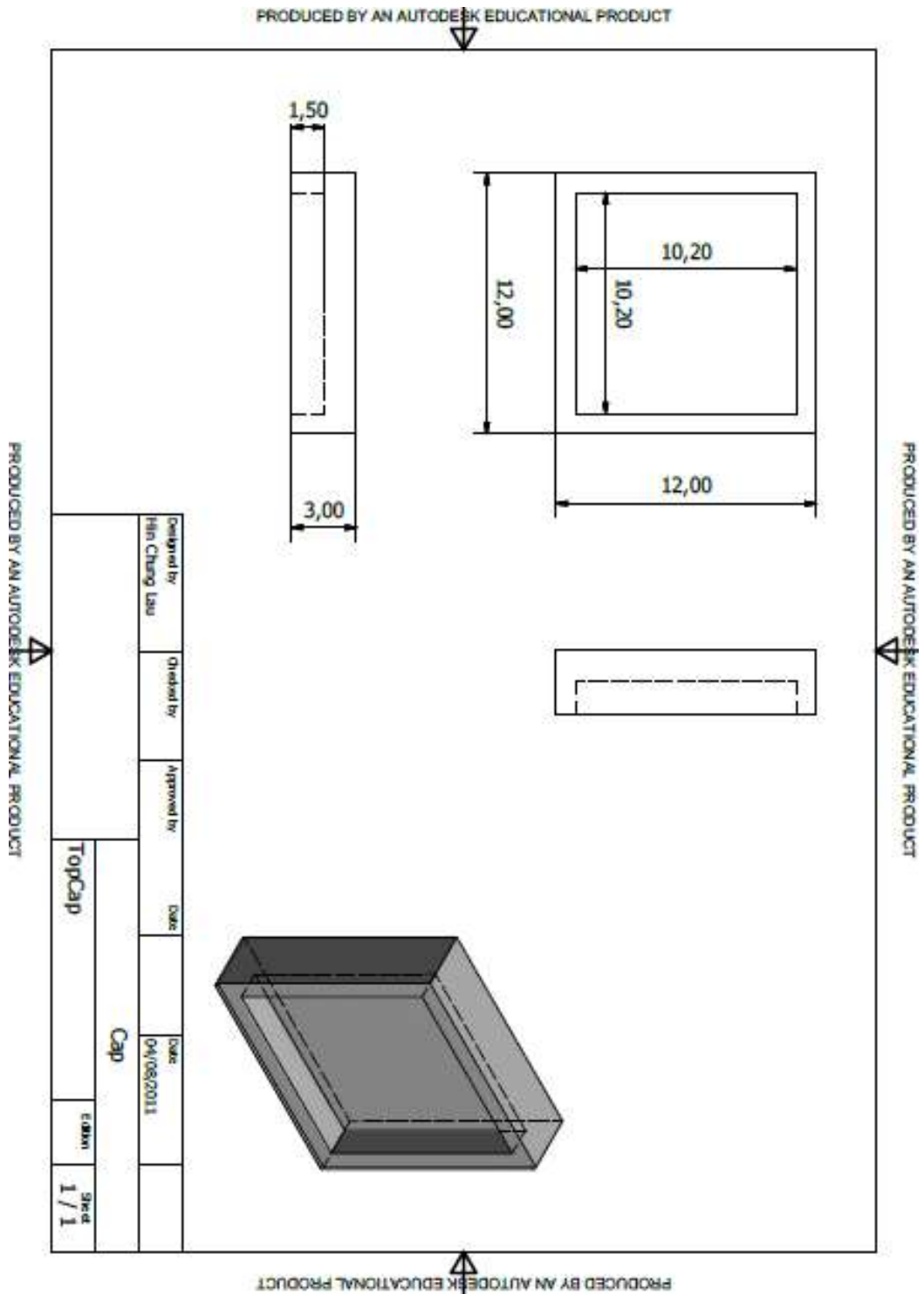
21. Technical drawing of the base of the assembly device used in the assembly of the biaxial shear transducer. The assembly device allowed precise placement of the transducer sensing surface in the centre.



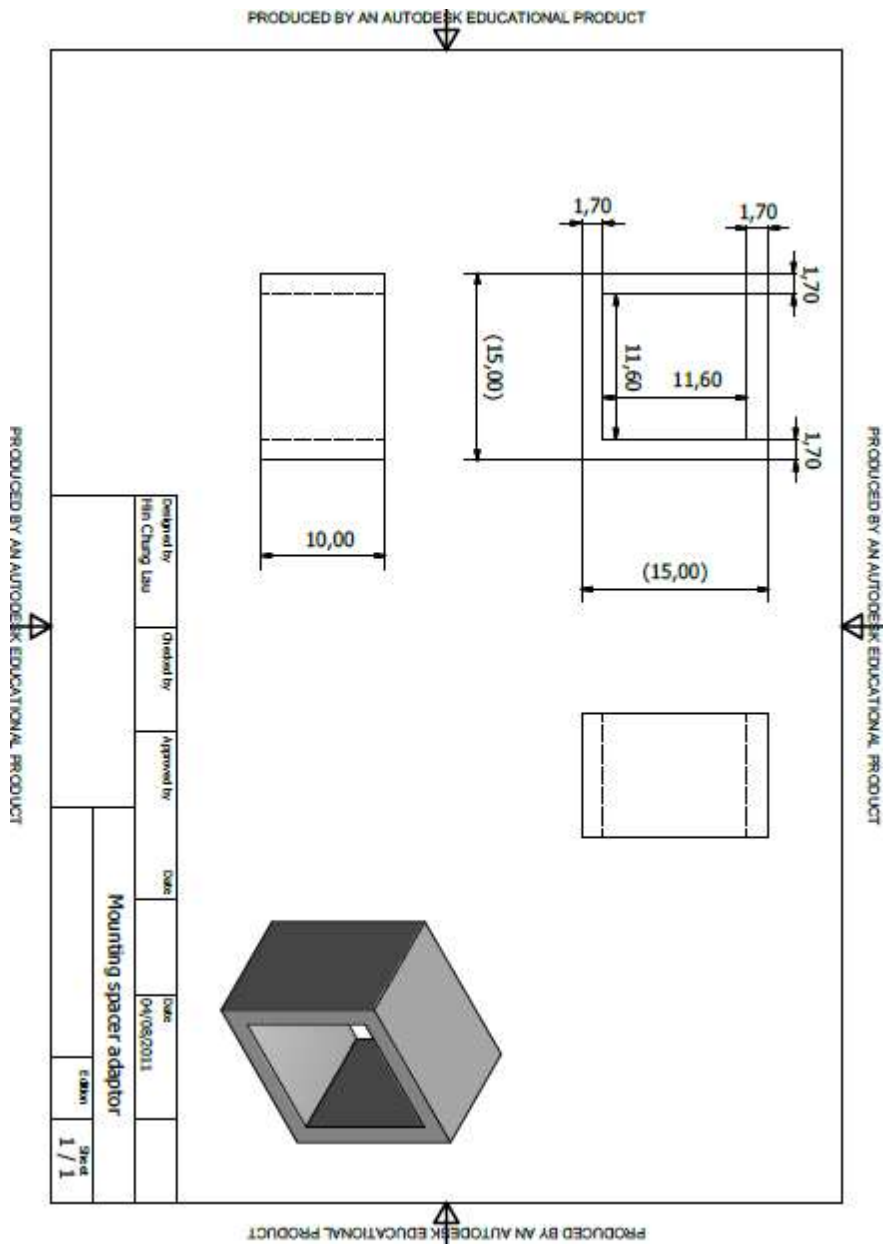
22. Technical drawing of the transducer holder to be used with the assembly device.



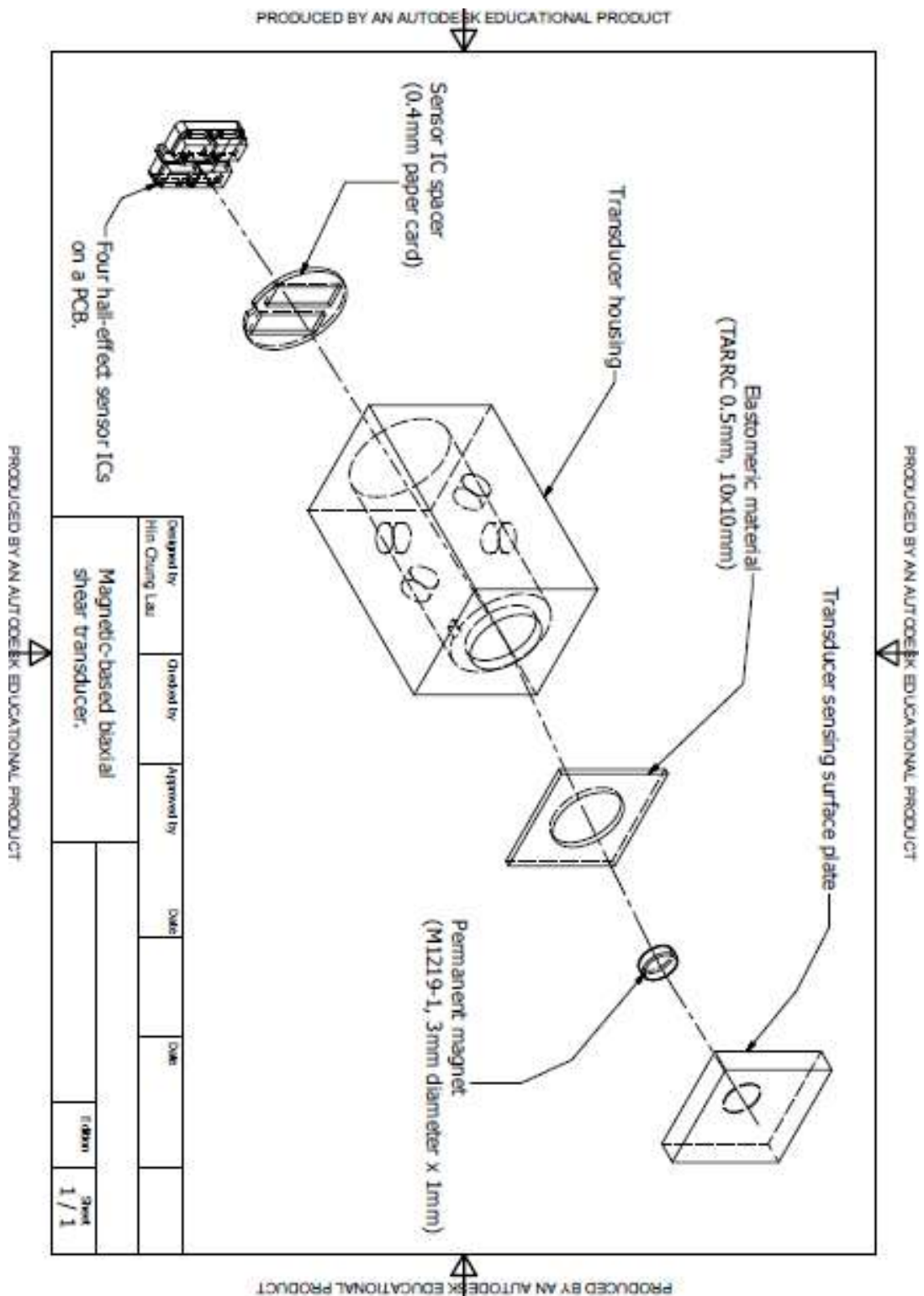
23. Technical drawing of the cap used during the calibration of the biaxial shear transducer for transmitting pure shear force to the surface of the transducer during tests.



24. Technical drawing of the spacer adaptor used in locating the transducer onto the calibration mounting device.



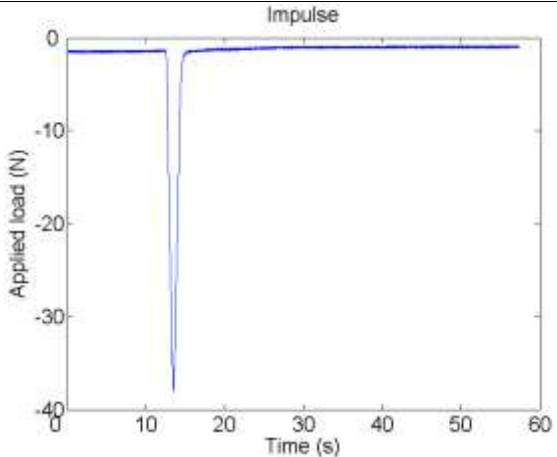
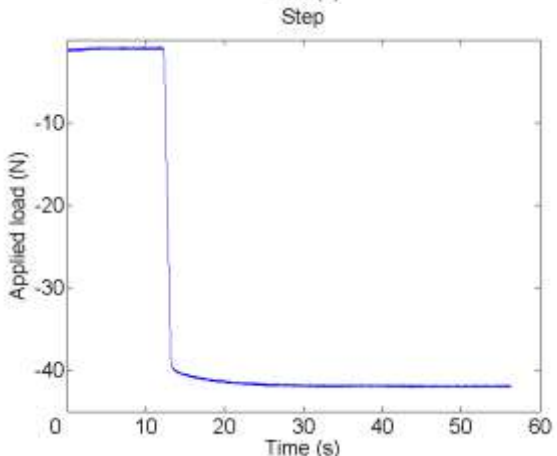
25. Assembly drawing of the magnetic-based biaxial shear load transducer.



Appendix C – Piezoelectric-based triaxial load transducer evaluation results

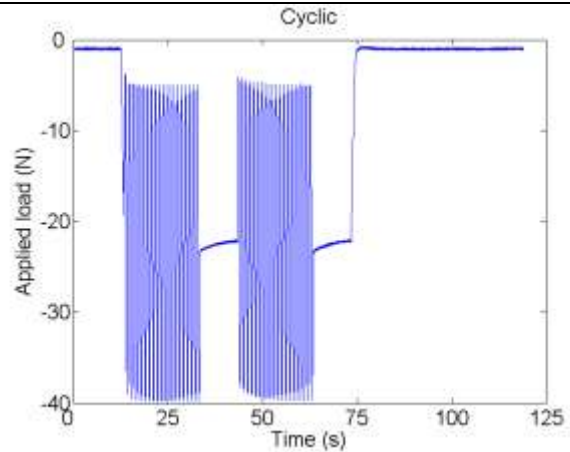
This appendix contains results from the evaluation of the ‘Kent’ piezoelectric based triaxial force transducer system (Section 5.1). Different loading regimes used on the computer controlled material testing machine are described below. Typical output responses from the transducer charge amplifier circuit during different loading regimes have been illustrated. Transducer response plots during calibration on the manually controlled calibration rig are also included.

Different loading regimes applied via the Instron material testing machine:

<p>Impulse load:</p> <ul style="list-style-type: none">• Load hold at 1N for 10s• Absolute ramp to 42N in 1s• Absolute ramp to 1N in 1s• Load hold for 40s <p>(the tensile testing machine was not able to ramp up to exactly 42N)</p>	
<p>Step load:</p> <ul style="list-style-type: none">• Load hold at 1N for 10s• Absolute ramp to 42N in 1s• Load hold for 40s	

Cyclic load:

- Load hold at 1N for 10s
- Absolute ramp to 22N in 1s
- Sine wave +/- 20N about 22N at 1Hz for 20 cycles
- Load hold for 10s
- Sine wave +/- 20N about 22N at 1Hz for 20 cycles
- Load hold for 10s
- Absolute ramp to 1N in 1s
- Load hold for 40s



Typical transducer system outputs:

The raw voltage outputs from the charge amplifier circuits were affected by noise during testing in the material testing laboratory. Consequently, all transducer voltage outputs have been filtered as described earlier (Section 5.1.2.2). Transducer output plots below illustrate both the raw voltage output (BLUE) and the filtered signal (RED). Two data points on each plot have been highlighted to illustrate the peak-to-peak voltage output.

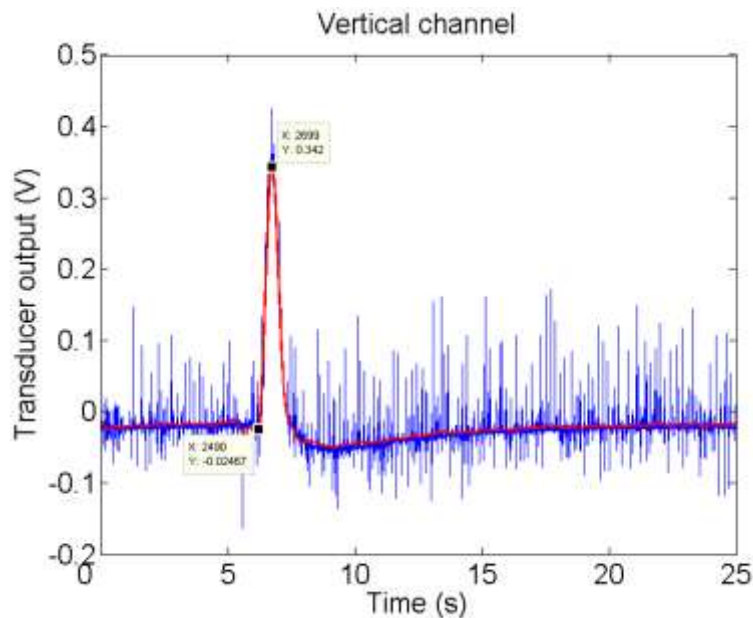


Figure 118 - Typical vertical (Z) output when an impulse vertical load was applied to the transducer.

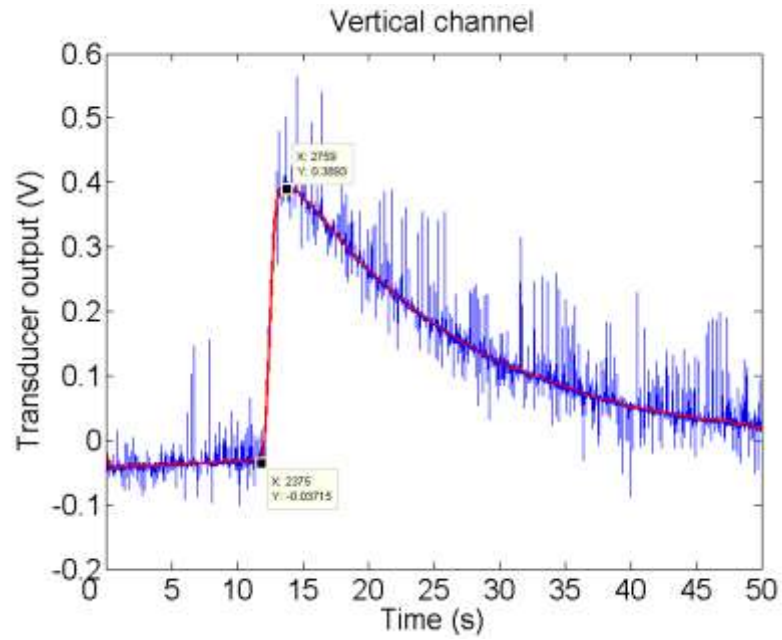


Figure 119 - Typical vertical (Z) channel output when a vertical step load was applied to the transducer.

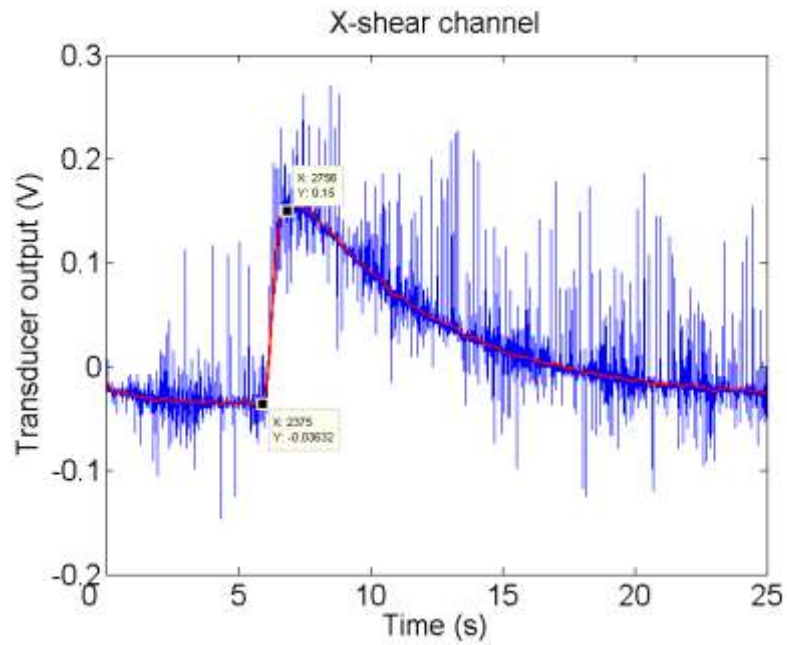


Figure 120 - Typical shear (X) channel output when a vertical step load was applied to the transducer.

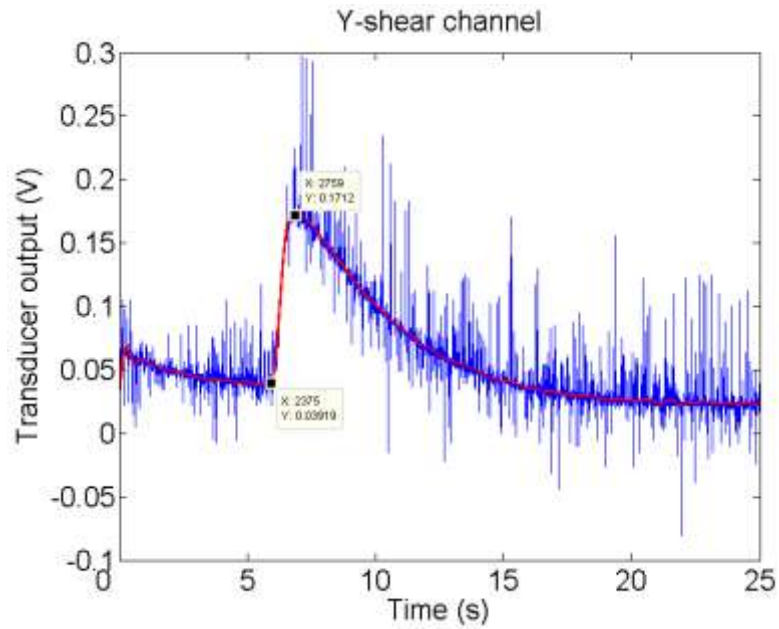


Figure 121 - Typical shear (Y) channel output when a vertical step load was applied to the transducer.

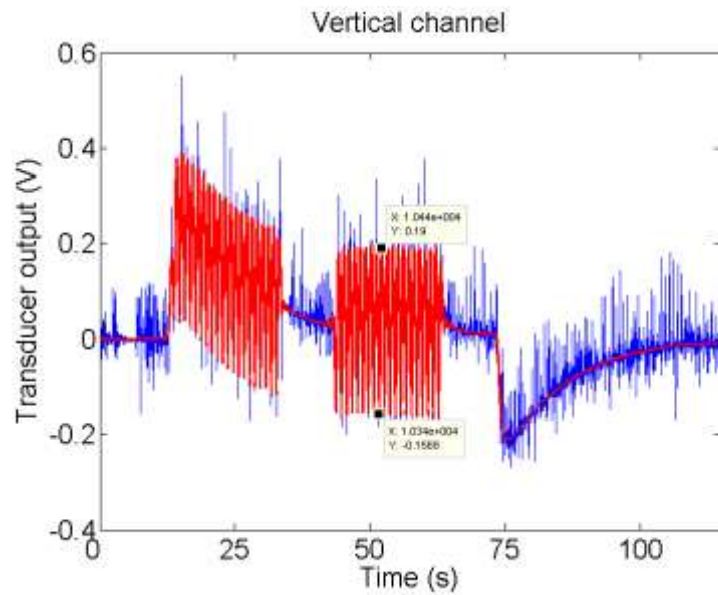


Figure 122 - Typical vertical (Z) channel output when a cyclic load was applied to the transducer.

Typical transducer system response during vertical and biaxial loading:

Plots below illustrate typical transducer system response during vertical and biaxial loading conditions under manual loading using calibration rig. Data signals have

been low-pass filtered as described earlier (Section 5.1.2.2). Transducer response in the shear $\pm X$ axis was evaluated in its intended orientation and the shear $\pm Y$ axis was evaluated with the transducer placed up-side-down. Negative shear data were made positive for the purpose of illustration.

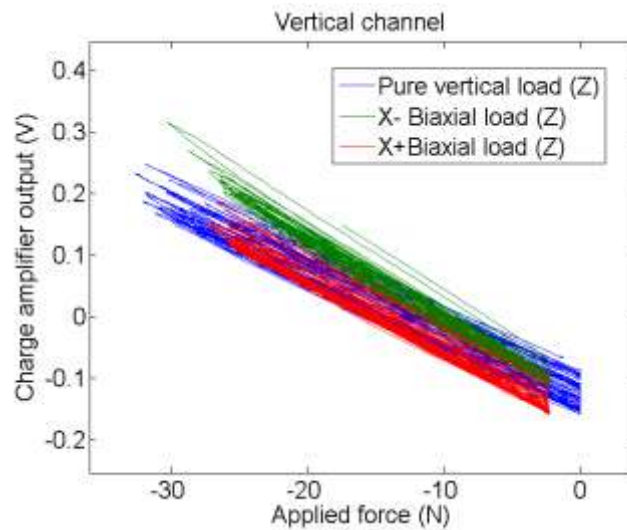


Figure 123 – Transducer response in the vertical (Z) channel during application of pure vertical (Z) load and biaxial (Z and $\pm X$) load.

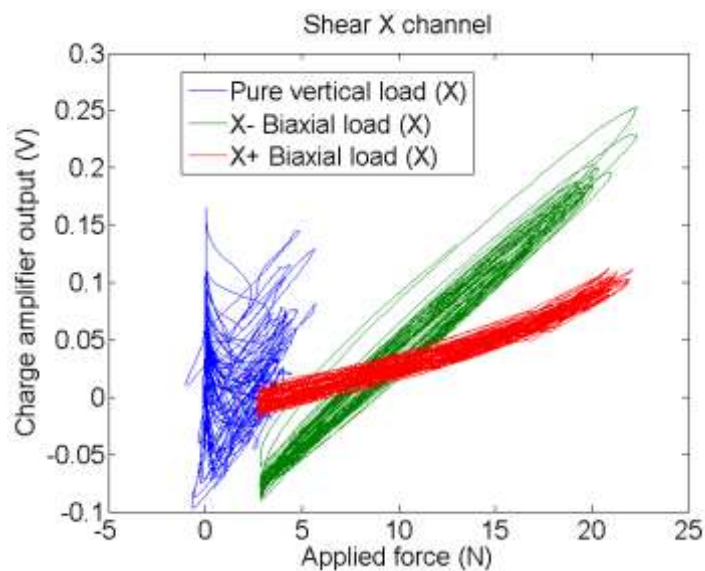


Figure 124 – Transducer response in the shear (X) channel during application of pure vertical (Z) load and biaxial (Z and $\pm X$) load. It was hypothesised that bending of the transducer during pure vertical loading resulted in unexpected crosstalk in the X axis.

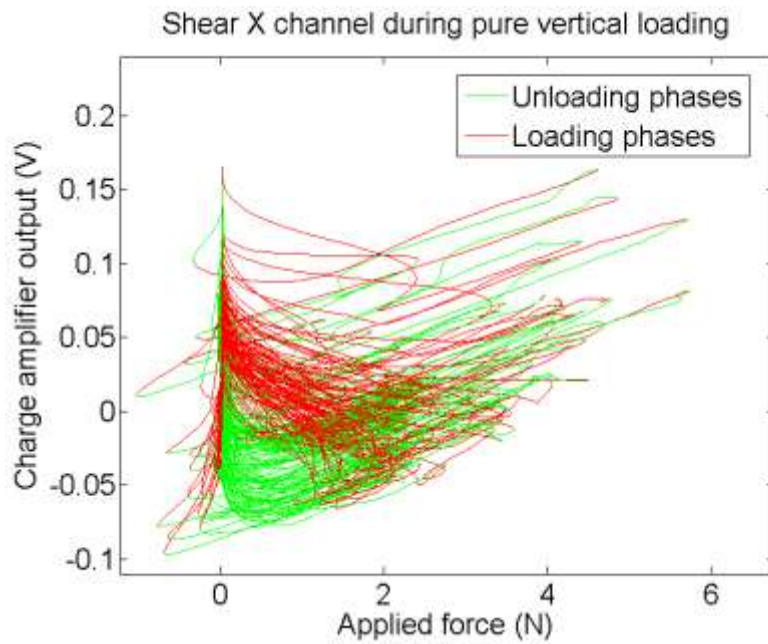


Figure 125 - Transducer response in the shear (X) channel during application of pure vertical (Z) load. It was hypothesised that bending of the transducer during pure vertical loading resulted in unexpected crosstalk in the X axis.

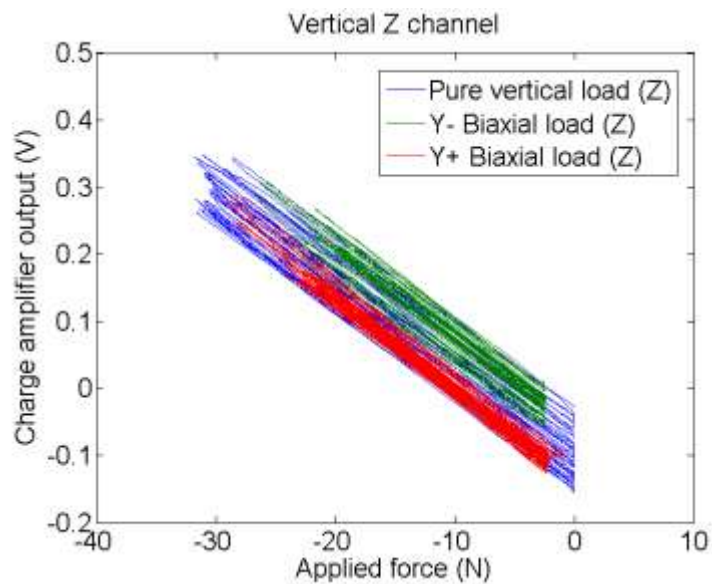


Figure 126 – Transducer response in the vertical (Z) channel during application of pure vertical (Z) load and biaxial (Z and $\pm Y$) load. The transducer was placed up-side-down.

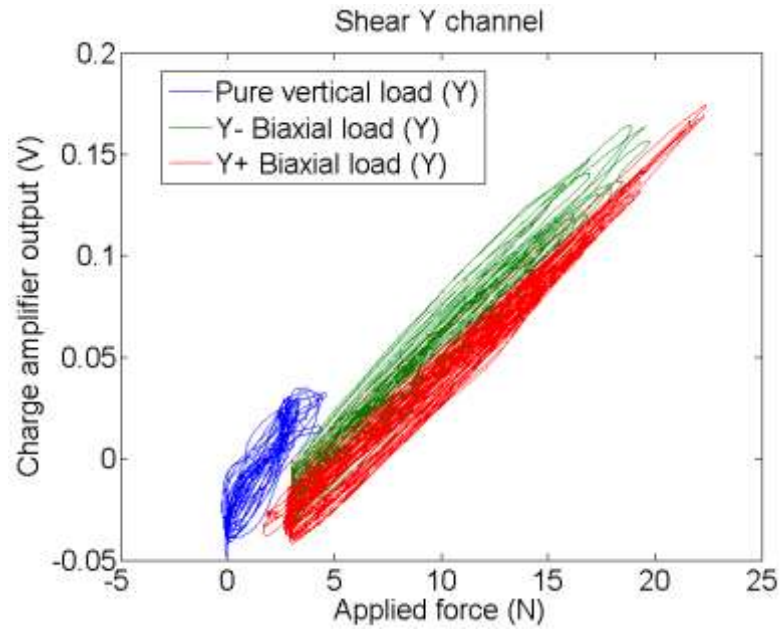


Figure 127 - Transducer response in the shear (Y) channel during application of pure vertical (Z) load and biaxial (Z and $\pm Y$) load. The transducer was placed up-side-down.

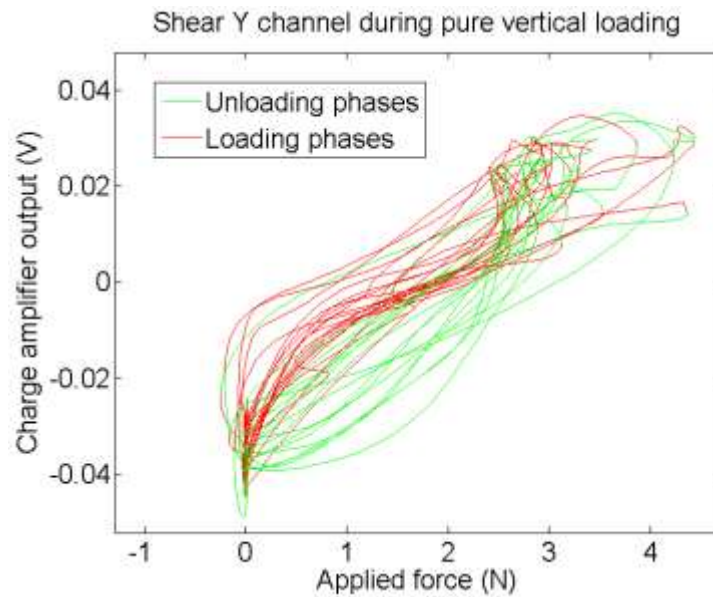


Figure 128 - Transducer response in the shear (Y) channel during application of pure vertical (Z) load. The transducer was placed up-side-down

Appendix D - Rubber manufacture

The Tun Abdul Razak Research Centre (UK), the UK-based research and promotion centre of the Malaysian Rubber Board, kindly provided samples of rubber material based on a standard conventional sulphur vulcanised recipe published earlier (Williams et al., 1992). A variety of spacer plates were put into the mould to achieve the desired sheet thickness. Rubber sheets were cured at 140°C for 40 minutes. Special thanks to J.P. Gladwin (Mill room manager) for manufacturing the material and providing the following photographs of the different stages of the production:

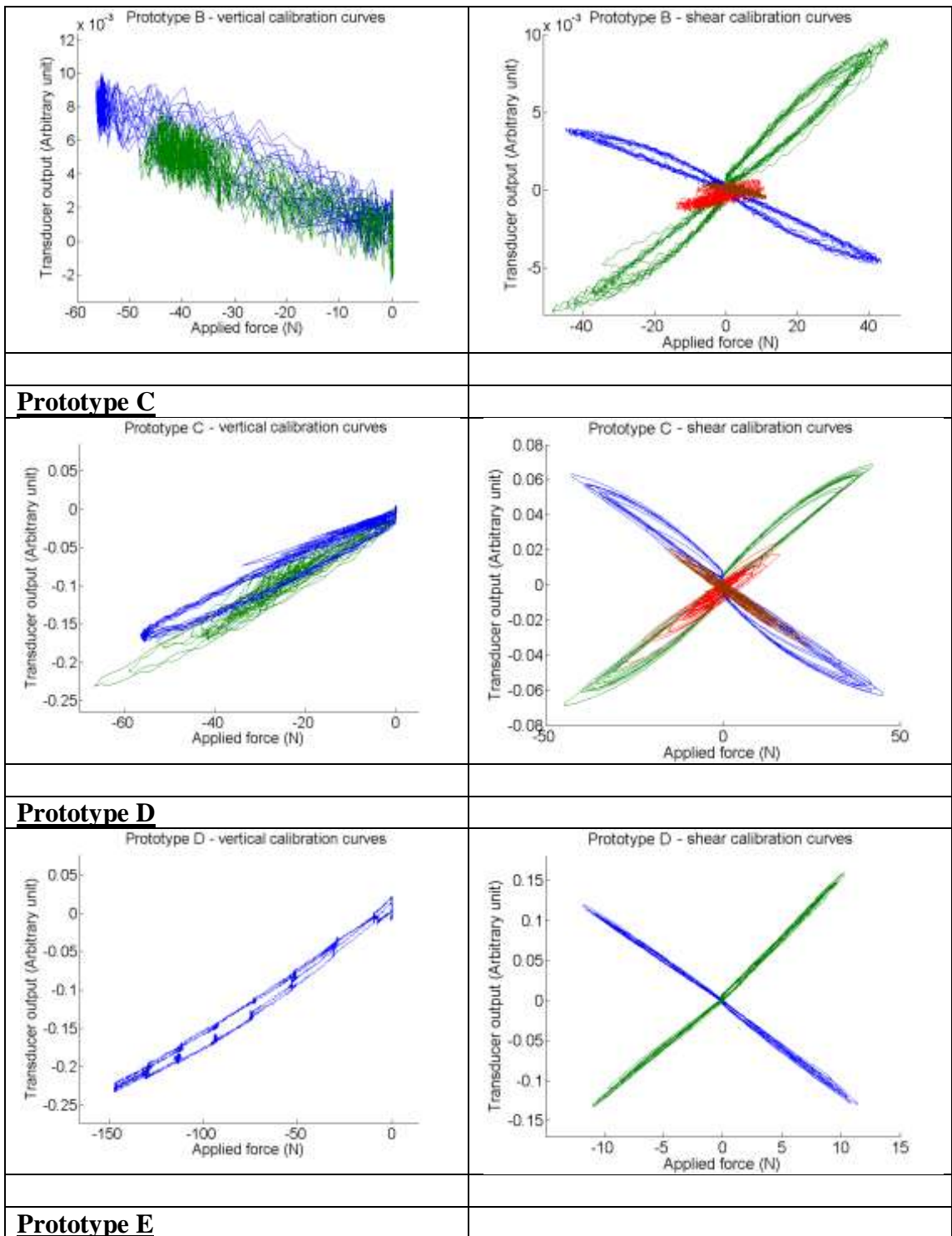
1. The raw rubber used.
2. One of the compounding ingredients.
3. The internal mixer used to compound the batch.
4. The mix once discharged from the mixer.
5. The mill on which the curatives were added.
6. The heated press used to cure the sheets.
7. The mould within which the sheets were cured.
8. The sheeted but unvulcanised (uncured) material.
9. The finished products.

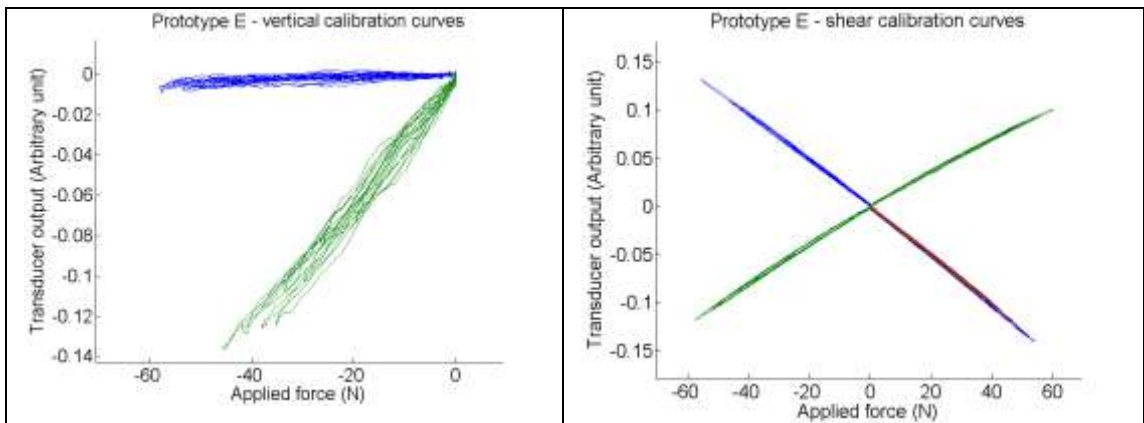


Appendix E – Optoelectronic-based triaxial load transducer calibration results

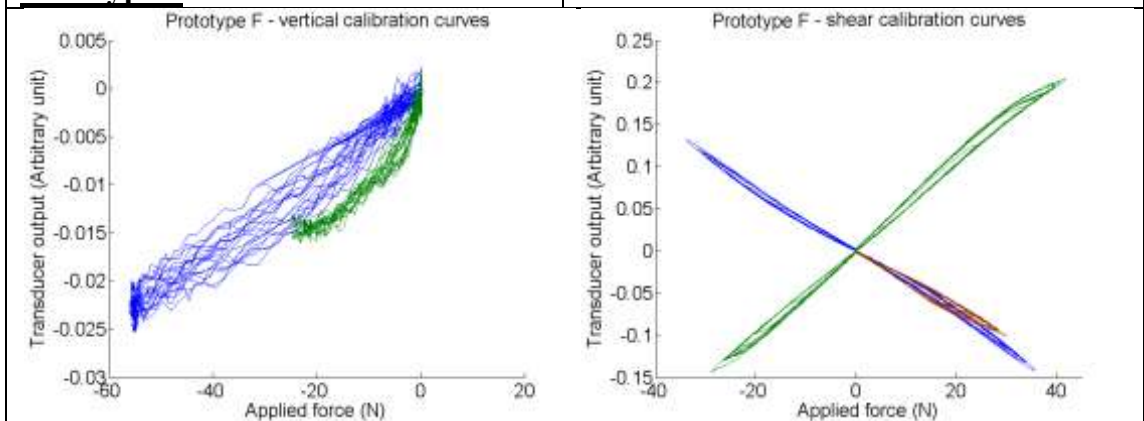
Calibration results on the optoelectronic based load transducer prototypes in Section 5.3.2.7. There were no significant differences between repeated trails on each transducer prototype. So for clarity, calibration plots only display results from one out of the two trails that was conducted per transducer. Transducer responses in each axis during the application of multi-axial loads are also plotted within the figures.

Vertical calibration curve	Shear calibration curves
<p>Key:</p> <ul style="list-style-type: none"> — Vertical (Z) calibration curve — Multi-axial applied force (Z) 	<p>Key:</p> <ul style="list-style-type: none"> — Shear (X) calibration curve — Shear (Y) calibration curve — Multi-axial applied force (X) — Multi-axial applied force (Y)
Prototype A	
<p>Prototype A - vertical calibration curves</p>	<p>Prototype A - shear calibration curves</p>
Prototype B	





Prototype F



Appendix F - Evaluation of permanent magnets

This appendix presents the representative results from the many tests conducted to evaluate the suitability of two permanent magnets for the magnetic based transducer design, as discussed in Section 5.4.2.2.

Results of tests on the M1219-1 magnet in unipolar slide-by mode of operation:

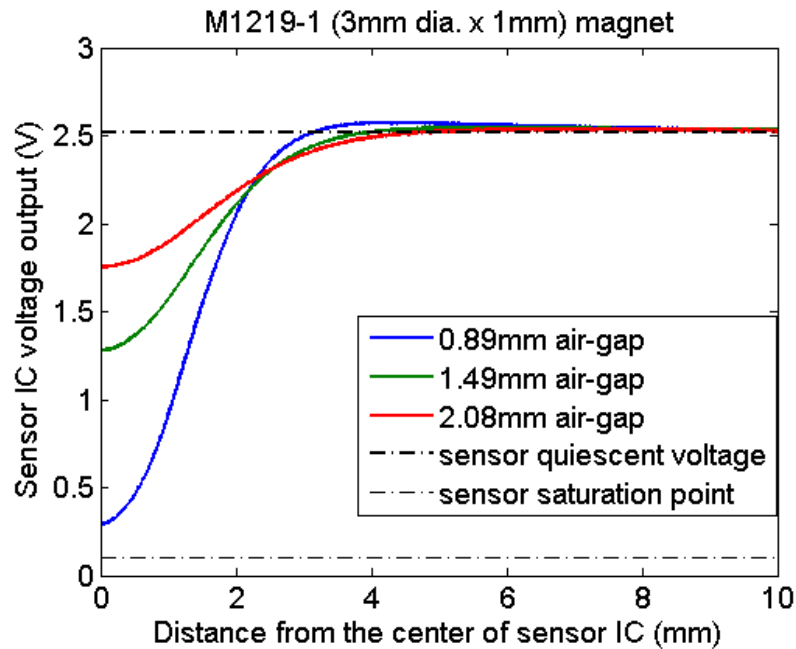


Figure 129 – Sensor voltage output versus the distance between the magnet and the centre of the sensor IC. Tests were conducted with the M1219-1 magnet at different air-gap distances. Dotted lines indicate the sensor saturation voltage (0.1V) and the quiescent voltage (2.52V).

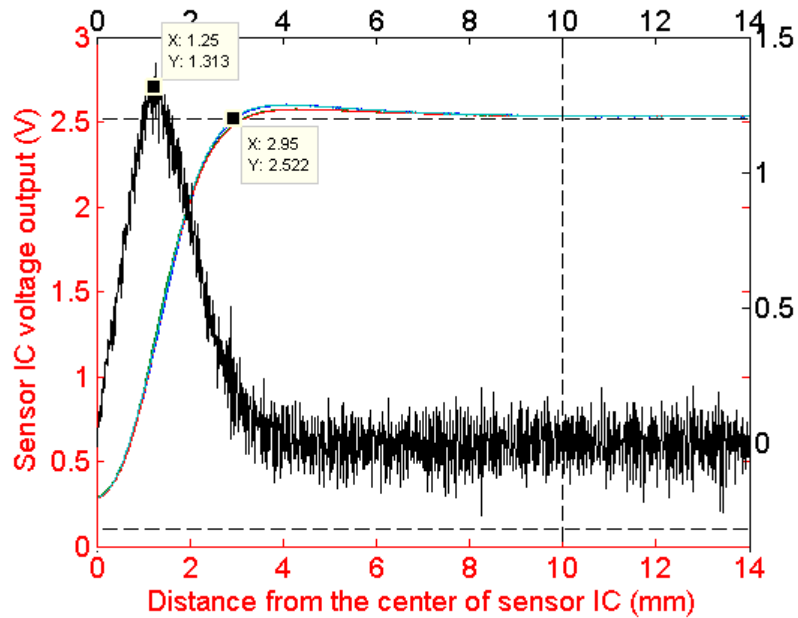


Figure 130 – Sensor voltage output wave from the 0.89mm air-gap data in Figure 129 and its calculated gradient.

Results of tests on the M1219-4 magnet in unipolar slide-by mode of operation:

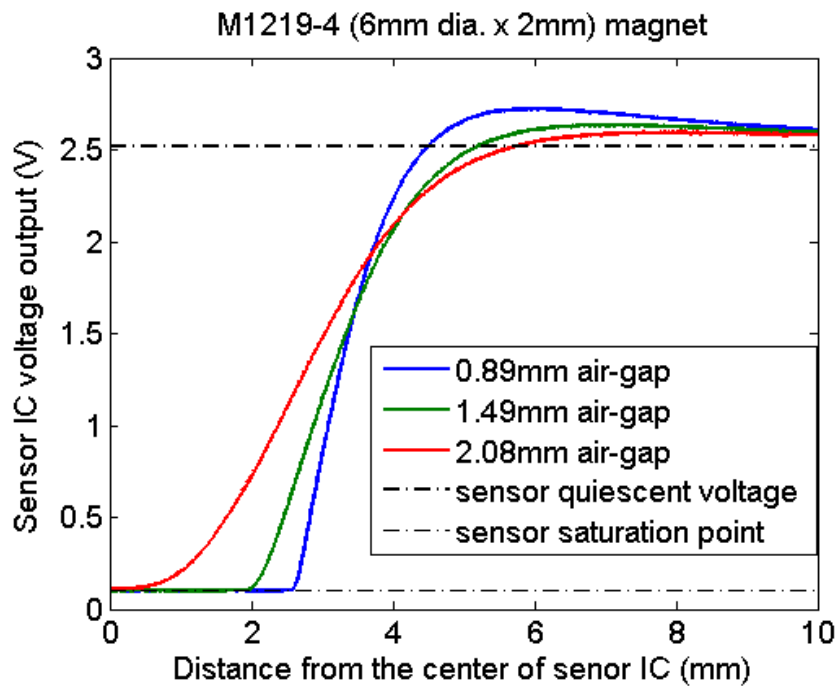


Figure 131 - Sensor voltage output versus the distance between the magnet and the centre of the sensor IC. Test conducted with M1219-4 magnet at different air-gap distances. Dotted lines indicate the sensor saturation voltage (0.1V) and the quiescent voltage (2.52V).

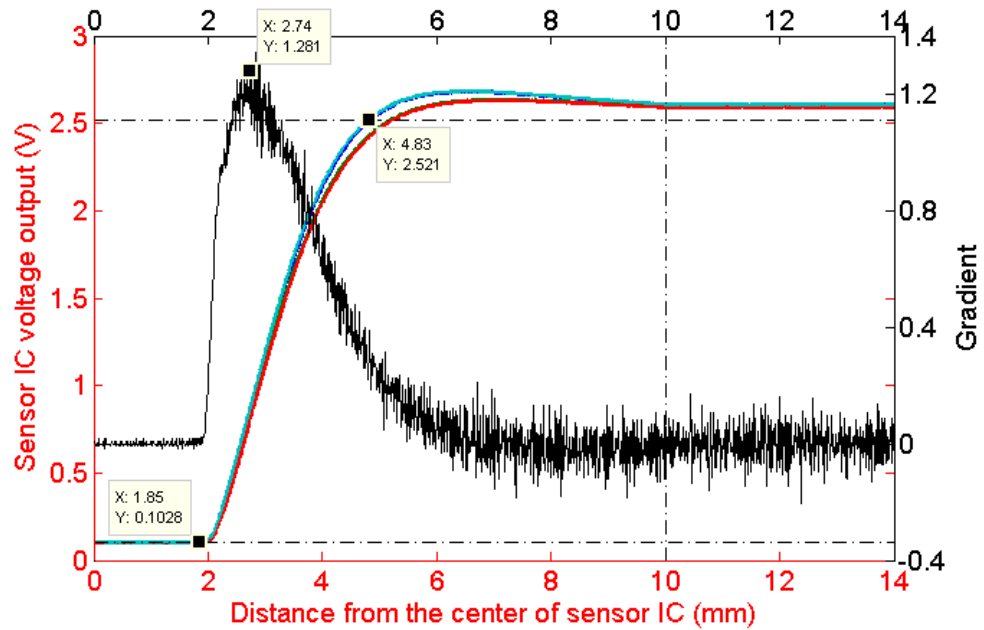


Figure 132 - Sensor voltage output wave from the 0.89mm air-gap data in Figure 131 and its calculated gradient.

Results from tests on the M1219-1 magnet in unipolar head-on mode of operation:

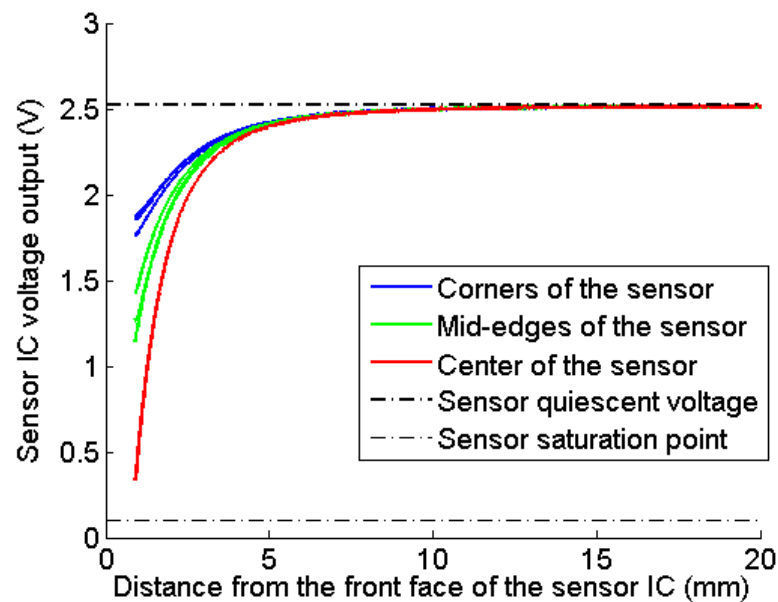


Figure 133 - Sensor voltage output versus the distance between the magnet and the centre of the sensor IC. Test conducted with M1219-1 magnet at different locations on top of the sensor. Dotted lines indicate the sensor saturation voltage (0.1V) and the quiescent voltage (2.52V).

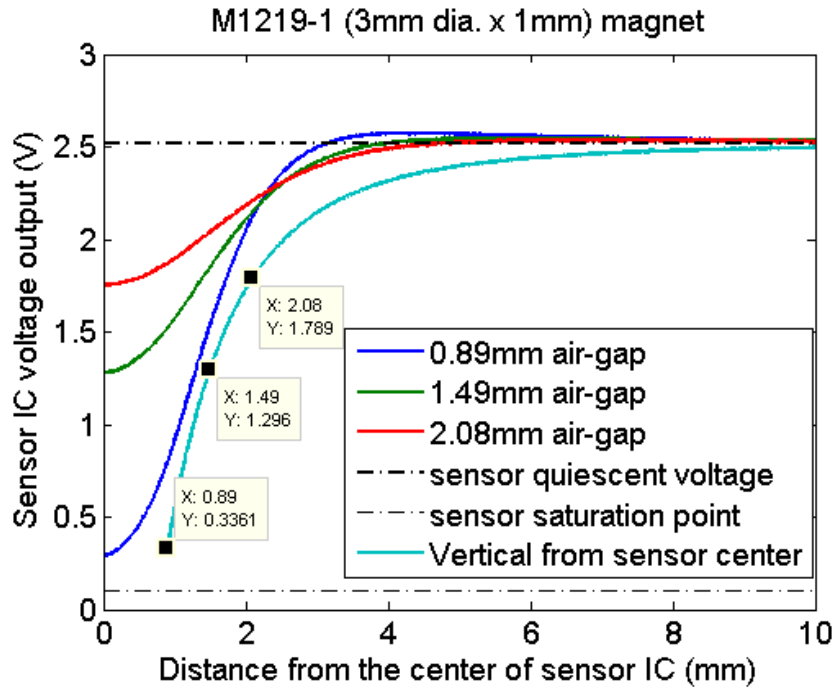


Figure 134 - The closely matching data from the unipolar slide-by tests (Figure 129) and the unipolar head-on test (Figure 133).

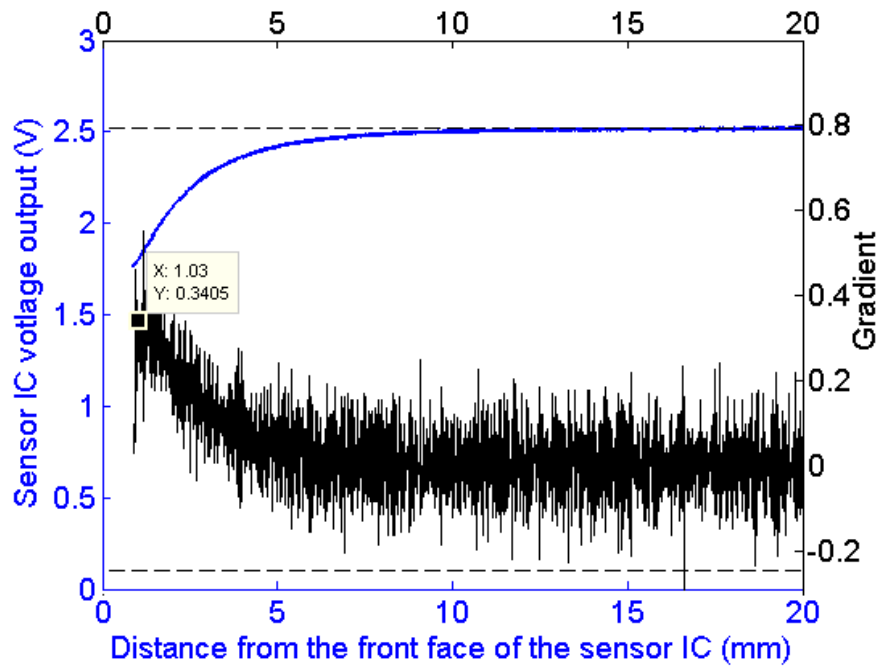


Figure 135 - The gradient of the sensor voltage output waveform when the magnet was at the corner of the sensor in unipolar head-on mode of operation.

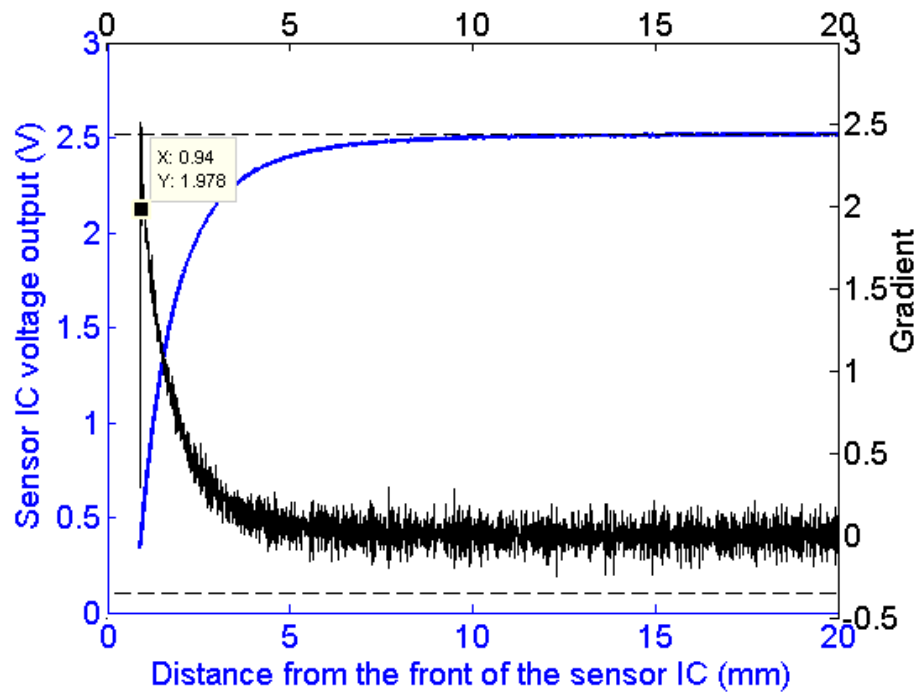
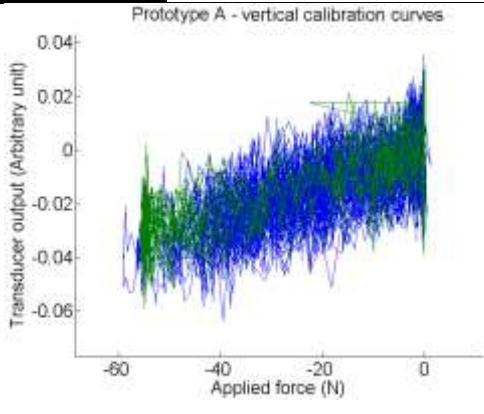
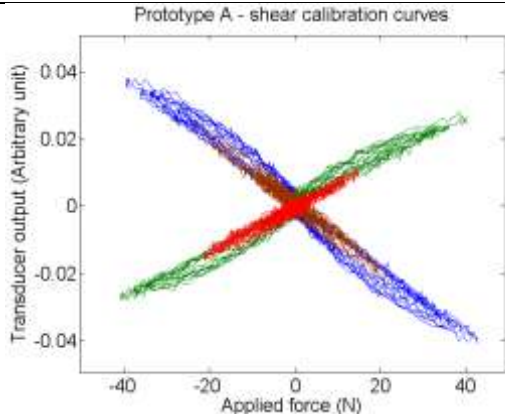
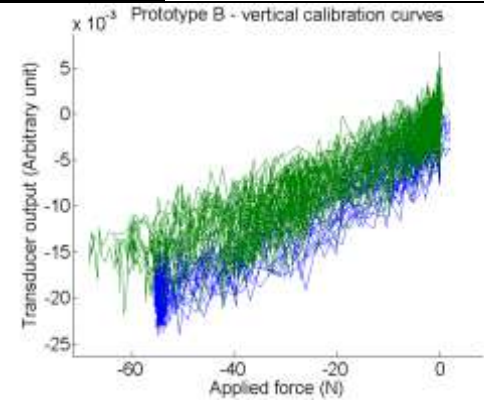
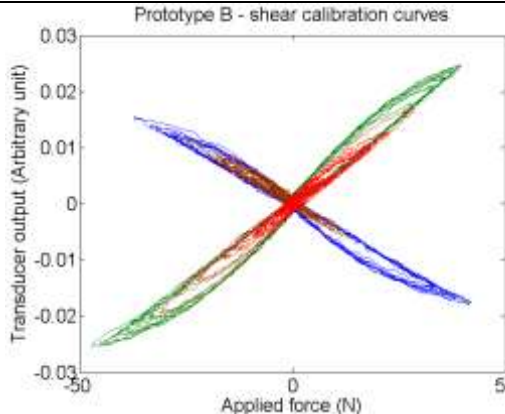


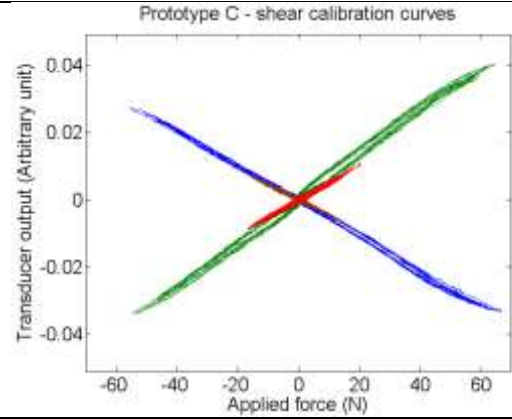
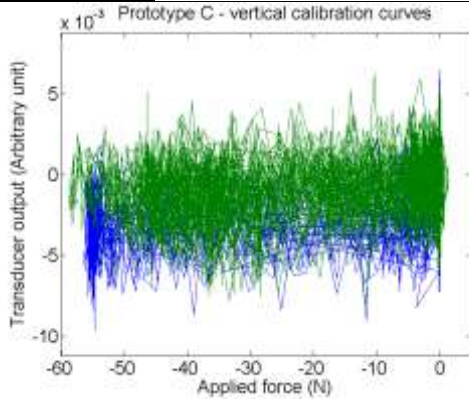
Figure 136 - The gradient of the sensor voltage output waveform when the magnet was at the centre of the sensor in unipolar head-on mode of operation.

Appendix G – Magnetic-based triaxial load transducer calibration results

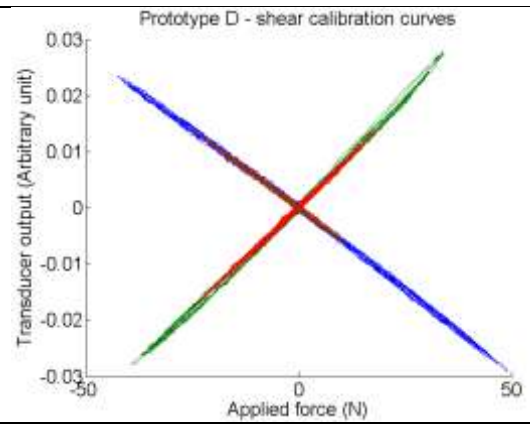
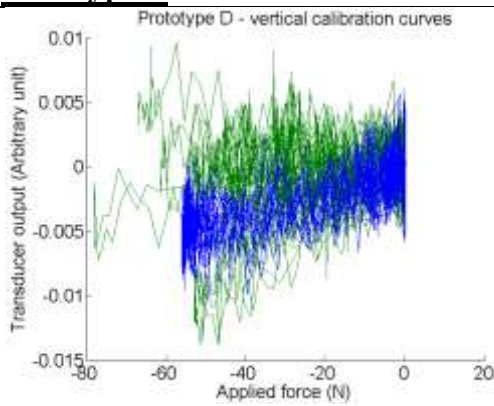
This appendix contains calibration results from the magnetic based load transducer prototypes described in Section 5.4.2.6. Transducer responses in each axis during the application of multi-axial loads were plotted within the figures.

<u>Vertical calibration curve</u>	<u>Shear calibration curves</u>
<p>Key:</p> <ul style="list-style-type: none"> — Vertical (Z) calibration curve — Multi-axial applied force (Z) 	<p>Key:</p> <ul style="list-style-type: none"> — Shear (X) calibration curve — Shear (Y) calibration curve — Multi-axial applied force (X) — Multi-axial applied force (Y)
<u>Prototype A</u>	
<p>Prototype A - vertical calibration curves</p>  <p>The graph shows transducer output (Arbitrary unit) on the y-axis ranging from -0.06 to 0.04, and applied force (N) on the x-axis ranging from -60 to 0. Two data series are plotted: a blue line representing the vertical (Z) calibration curve and a green line representing the multi-axial applied force (Z). Both curves show a noisy, roughly linear relationship that becomes more stable as the force approaches 0.</p>	<p>Prototype A - shear calibration curves</p>  <p>The graph shows transducer output (Arbitrary unit) on the y-axis ranging from -0.04 to 0.04, and applied force (N) on the x-axis ranging from -40 to 40. Four data series are plotted: blue (Shear X), green (Shear Y), red (Multi-axial applied force X), and brown (Multi-axial applied force Y). The curves form an 'X' shape, indicating a linear relationship between shear force and transducer output in both directions.</p>
<u>Prototype B</u>	
<p>Prototype B - vertical calibration curves</p>  <p>The graph shows transducer output (Arbitrary unit) on the y-axis ranging from -25 to 5, with a multiplier of $\times 10^{-3}$ at the top. The x-axis is applied force (N) ranging from -60 to 0. Two data series are plotted: a blue line for the vertical (Z) calibration curve and a green line for the multi-axial applied force (Z). Both curves show a noisy, roughly linear relationship that becomes more stable as the force approaches 0.</p>	<p>Prototype B - shear calibration curves</p>  <p>The graph shows transducer output (Arbitrary unit) on the y-axis ranging from -0.03 to 0.03, and applied force (N) on the x-axis ranging from -50 to 50. Four data series are plotted: blue (Shear X), green (Shear Y), red (Multi-axial applied force X), and brown (Multi-axial applied force Y). The curves form an 'X' shape, indicating a linear relationship between shear force and transducer output in both directions.</p>

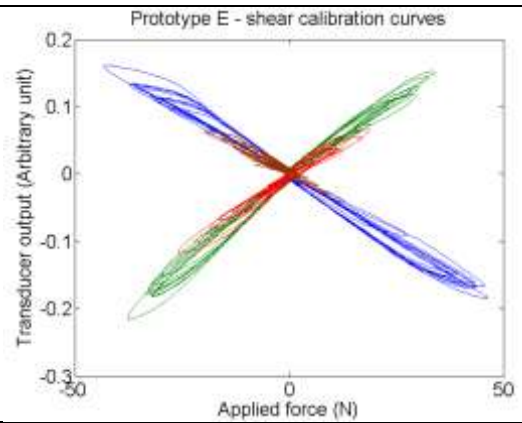
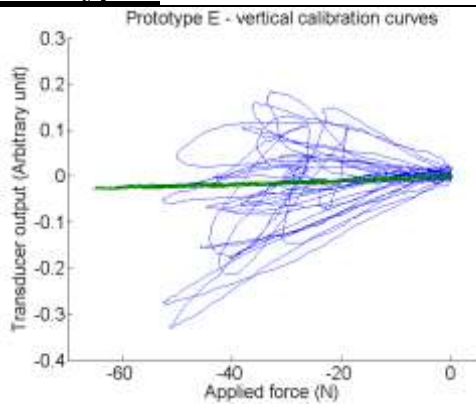
Prototype C



Prototype D



Prototype E

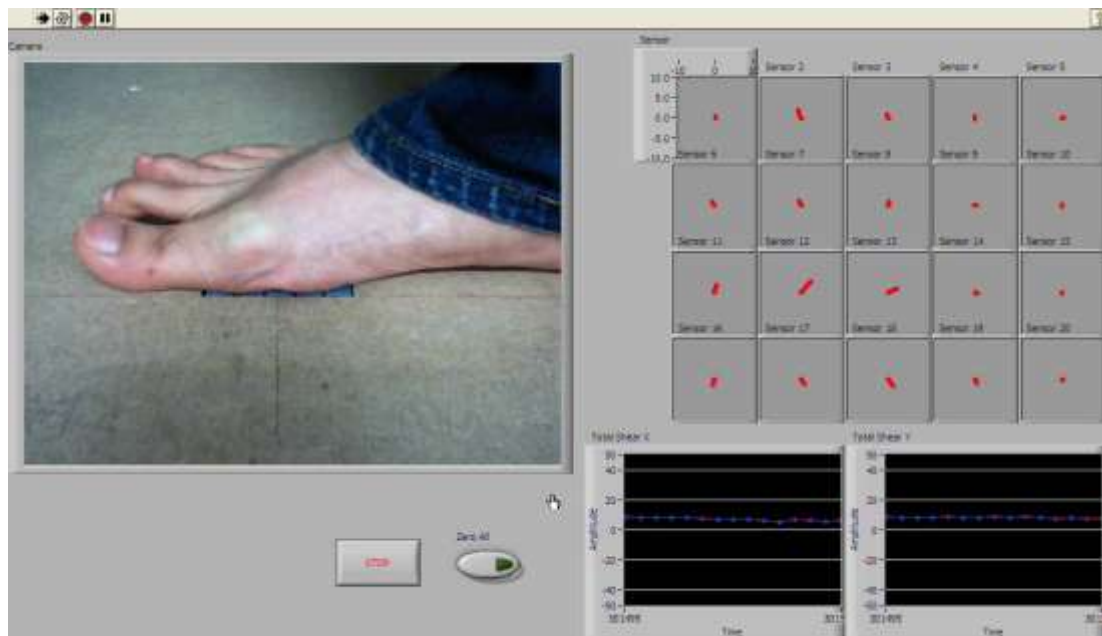


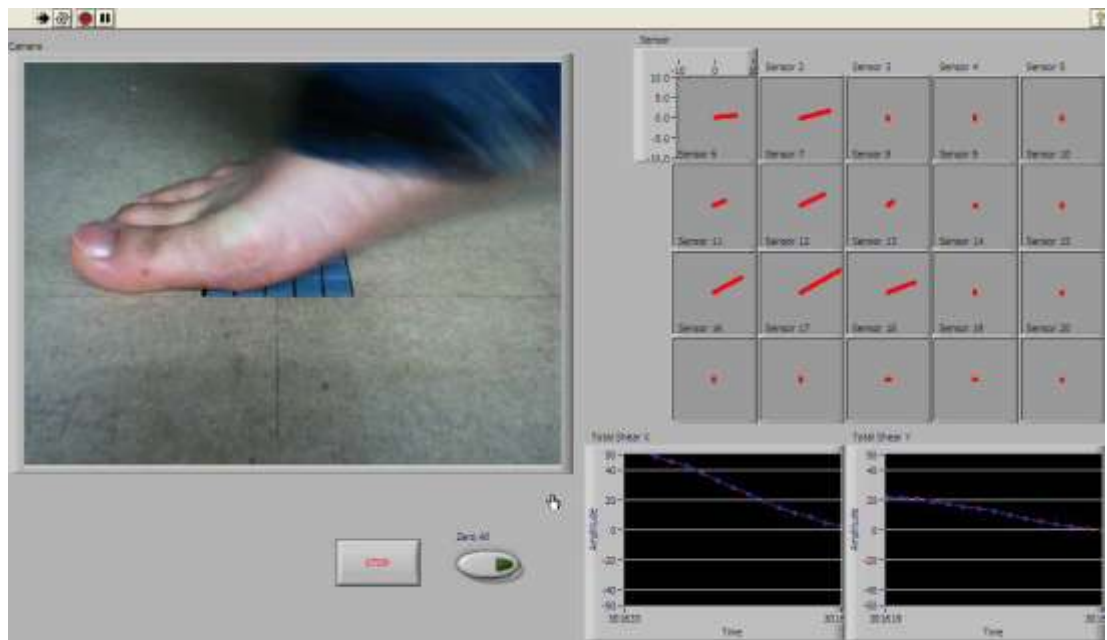
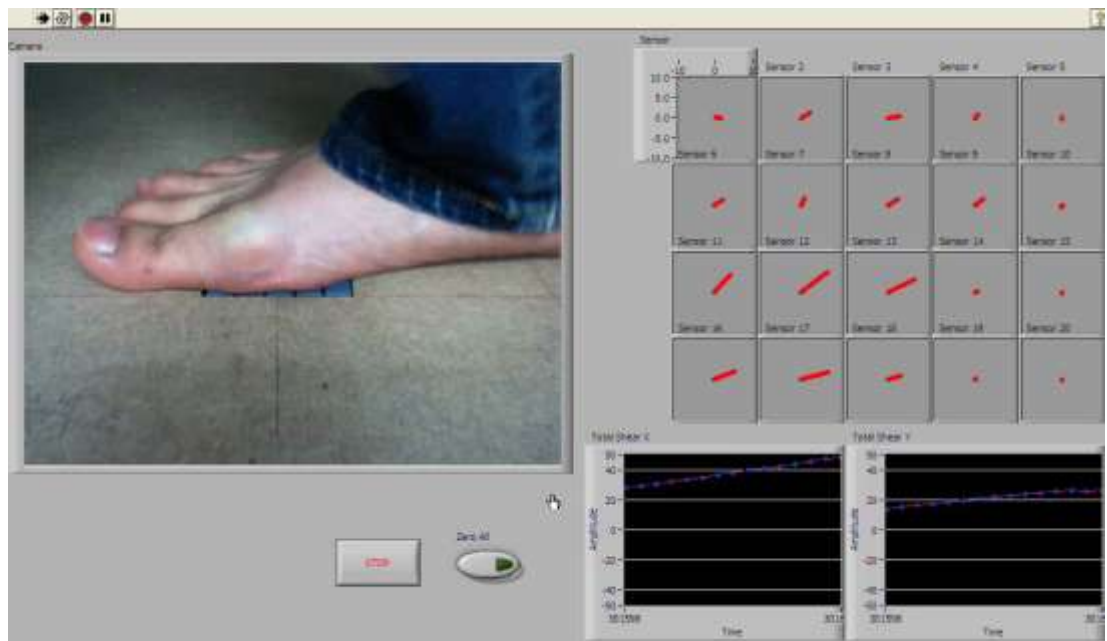
Appendix H - Screenshots of the shear distribution measurement system software

The screenshots below are of a program written in LabVIEW8.6 to demonstrate the biaxial shear distribution measurement system during a subject trial. Screenshots were extracted from screen captured videos created using CamStudio software.

The program was connected with a USB camera that provided real-time video streams of the platform (Top-Left). The program also provided real-time visual display of the direction and magnitude of measured shear load from each transducer (Top-right), as well as the total X-axis and Y-axis shear load measured by all 20 transducers (Bottom-right). It should be noted that the camera had a slow frame rate of 30fps, therefore limited images were obtained.

- **Screenshots sequence during forefoot contact on the transducer array**





- Screenshots sequence during heel contact on the transducer array

